RE-ADHESION CONTROL FOR RAILWAY TRACTION SYSTEMS

Jianhua Yu

Submitted in accordance with the requirements for the degree of
Doctor of Philosophy
The University of Leeds
School of Electronic and Electrical Engineering

September 2007

The candidate confirms that the work submitted is his/her own and that appropriate credit has been given where reference has been made to the work of others

ACKNOWLEDGEMENTS

I would like to thank many people for their kind help with my study and research so that I can finish my dissertation. I sincerely appreciate my supervisor, Dr. T. X. Mei. He always gives me precious instructions of the research methods, enlightens me on solving the problems, shares his valuable experiences in railways and guides me to the right direction.

I am very thankful to my second supervisor, Dr. D. A. Wilson, for his precious time for discussions, valuable ideas and suggestions for every problem, and his angelic patience on revising my report and thesis.

I would like to thank all the people who give me kind support in my life in Leeds, especially to Yongji Zhou and his wife Shiliang with whom I share happiness, sadness and pain, Hong Li who is warm hearted and always gives valuable advices, and also to Xuejun Ding and Xuandi zhao. The school of Electronic and Electrical Engineering at the University of Leeds, gives a bond of a group Chinese students who may never encounter if in China, where I have got a lot of friends。

Finally, I would like to express my appreciation and love to my husband, Tao Tao, who always loves me and stays with me in all the tough times. In addition, I want to thank my parents, and my sister and her husband who took good care of my parents. Special thanks will give to my mother in law for her selfless support and encouragement.

ABSTRACT

Slip is a harmful phenomenon in railway. It causes the wear of wheel rail contact surface and mechanical stress of the traction system. Moreover, it may affect the stability of the whole system. The study is concerned with the development of a novel slip detection and re-adhesion control using practical position encoder.

In detail, this thesis presents a powered wheelset system driven by an induction motor associated with vector control unit. The wheelset models developed from the study include a comprehensive model which involves longitudinal, lateral and yaw dynamics, a distributed parameter model and a lumped parameter model with simplified longitudinal dynamics. The dynamics of a wheelset is studied and compared in normal conditions and slip conditions. Simulation results show typical torsional vibration occurs when slip happens.

Two possible approaches of slip detection based on the vibration phenomenon are discussed. The first one monitors the torsional torque to detect the slip based on the direct torsional torque measurement. In the second approach, a Kalman filter based slip detection method is presented and evaluated in different operation conditions.

Finally a re-adhesion control scheme is developed based on the Kalman filter. The effectiveness of this approach is demonstrated using comprehensive computer simulations.

TABLE OF CONTENTS

LIST OF TABLES

LIST OF FIGURES

1 INTRODUCTION AND LITERATURE REVIEW

1.1 Electrical Traction System

1.1.1 Constitution of a Traction System

The general diagram of a traction system is shown in Figure 1.1. It has been divided into four major parts.

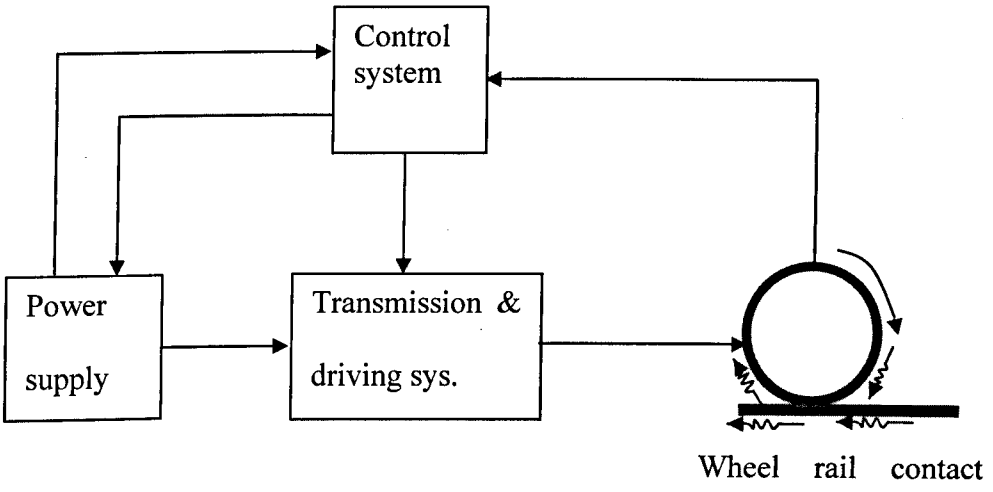

Figure 1.1 General block diagram of a traction system

As the diagram displays, the tractive effort for railway vehicles is generated from wheel-rail contact. It is the most fundamental principle for a conventional railway to utilize a steel wheel on a steel rail to transmit all the forces including traction, braking and guidance [1]. Some power supplies generate either DC or AC power sources for electrical traction systems. Furthermore, the transmission and driving system include driving motors and gear transmissions which are capable of carrying out control actions such as speed varying, torque adjustment etc. Apart from that, a control system is used to control the operational features of power supply, transmission and driving systems to enhance the system stability and protect the system.

1.1.2 Traction Motors

In the early days of electrical traction, both DC motors and AC motors have been used. The smoothly-speed-tuning features of the DC motor made it a favoured choice up to 1960 [2]. However, the commutator of DC motors needs regular maintenance which increases operational costs and reduces the reliability.

With the development of modern power electronics and microprocessor control technology, 3-phase AC motors have become an efficient alternative to DC motors:

Induction Motors

Applications of induction motors in traction systems were once restricted by the constant voltage and frequency power supplies. The development of power electronic converter (PEC), which can provide variable voltage and frequency supplies, make induction motors a more favorable choice for vehicle traction applications than DC motors. Vector control strategies of induction motors allow fast torque dynamics, and give high performance in traction control. Cage induction motors have been widely used in railway systems such as metro railways in Germany & Switzerland and London/Paris/Brussels Eurostar trains [3].

Synchronous Motors

The synchronous motor is another type of AC motor implemented in railway traction. The most well-known application is in the French TGV train. More recently, permanent magnet synchronous motors have been the subject of research interest and have become a strong candidate for railway traction [4].

1.1.3 Traction System with Induction Motors

Traction systems with induction motors can be divided into two different categories: single-inverter single-induction-motor system and single-inverter multiple-induction-motor drive system. Even though there is an increasing research interest in different single-inverter multiple-induction-motor drive systems such as in the Japanese and Korean high speed railway system [5][6], single-inverter single-induction-motor

system is still a conventional driving system utilized in many railway systems [7]. In the latter system, driving the motors individually improves the re-adhesion control performance and makes the maintenance of the wheels easier [8]. Therefore, the research is focused on a single-inverter single-induction-motor system.

One of the main types of induction motor drives is a voltage-source inverter (VSI) fed induction motor drive [3]. The VSI can be switched to generate variable voltage, variable frequency (VVVF) power supply which is often used to realize the speed/torque control of the induction motors together with a vector control unit. The DC link voltages of the VSI vary from 750 V to 3 kV in different countries and regions. According to [3], the widely used VSI fed induction motor traction systems in Europe are fed with DC supply voltages up to 1.5 kV.

1.1.4 Control of Induction Motors

Control schemes for induction motors can be divided into two major categories: scalar control and vector control.

Scalar Control

Scalar control deals with the scalar quantities which are represented by magnitude alone [9]. The popular scalar control method is the coordinated voltage-frequency V_1 / f_1 control which imposes constant relationship between stator frequency and voltage through feed forward control. This control strategy is traditionally used in those occasions which do not require high precision speed control and fast response dynamics.

Vector Control

Vector control strategies make it possible to allow induction motors to achieve a fast dynamic response, in a similar manner of a separately excited DC motor. Vector control is also known as Field Oriented Control (FOC). It was proposed by Hasse [10] and Blaschke [11], and now widely applied in the railway industry [5].

There are three flux space-phasors in the induction motor: rotor flux linkage, air-gap flux linkage and stator flux linkage. The vector controlled induction motor drives can be categorized through the methods of using different flux linkage vector for orientation [12]. Vector control is performed by attaching a rotating frame along one of the flux linkage directions to realize decoupling of torque and flux related current components. Among the three orientations, rotor flux linkage orientation can give a simplified current decoupling [2]. Usually in vector control, the flux is kept constant to give a fast torque response, since flux variation tends to be very slow.

To realize the flux orientation, it is essential to obtain the position of the flux. On one hand, the flux position is either directly measured by using sensors such as Hall sensors [11] and search coils [13], or from the flux estimations. On the other hand, indirect vector control determines the flux position from rotor position and slip frequency. The rotor position can be attained directly through a position sensor and the slip frequency can be calculated from the demand.

Vector control can be also grouped into sensor or sensorless schemes. Control schemes with position sensors use the direct measurement of rotor position to determine flux linkage position, while sensorless control schemes use different speed observers to estimate the rotor speed. Sensorless vector control has earned a lot of research interest, especially by the single-inverter multiple-motor systems as presented in [14].

1.2 Wheelset Arrangement

A wheelset comprises of two wheels being connected onto an axle. Even though there are cases using independent wheels such as in the Spanish high-speed train, the Talgo express and tracked vehicles in coal mines, most conventional rail vehicles use a solid axle wheelset [1]. Each wheel of the wheelset has a coned or profiled tread with a flange on the inside as shown in Figure 1.2. For simplification, the wheel is considered as cone shaped in most wheelset dynamics studies [15]. Meanwhile, as a powered wheelset, a traction motor is mounted on the wheelset to drive the wheels through a gear box.

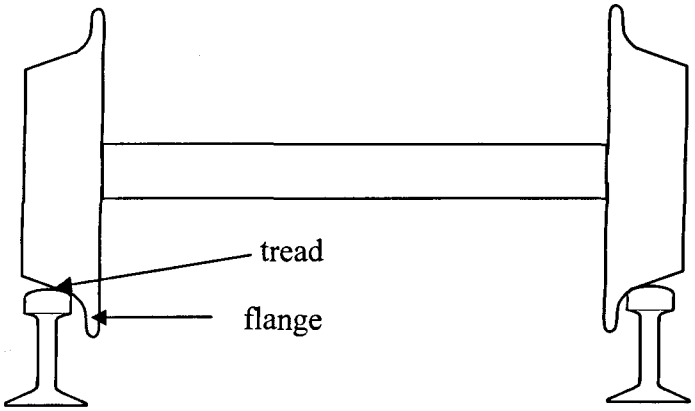

Figure 1.2 Wheelset on rails

As Figure 1.3 shows, the wheel rail contact is simplified to linear profiles with a single contact point [15].

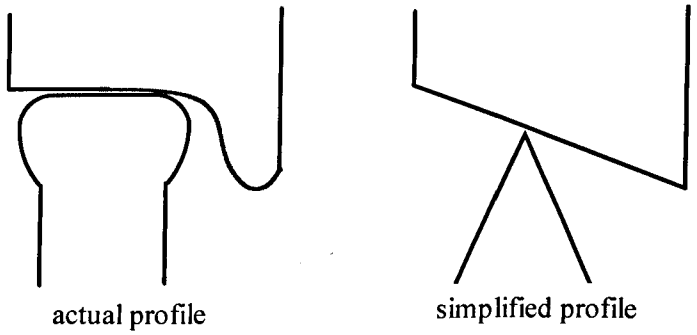

Figure 1.3 Actual and simplified wheel rail contact profile

1.3 Slip Phenomenon and Consequences

1.3.1 Creepages and Creep Forces

As Figure 1.4 shows, the local elastic deformations, such as contractions and expansions of the wheel and rail, generate a tangential force F_t to the wheel rail contact plane [1]. F_t, also known as creep force, induces microslip or creepage. Creepage can be expressed in terms of the velocity difference between two bodies in contact divided by the mean velocity [1]. In this thesis, the creepage in the longitudinal direction is defined as:

$$\lambda = \frac{v_w - v_v}{v_v} \tag{1.1}$$

where, λ is the creepage, v_w is the wheel linear speed and v_v is the vehicle forward speed. λ is also referred to as slip in some works. The creep phenomenon contributes to stable transmissions of the propulsive force [6], and is essential to transmit the motor torque into vehicle movement [16].

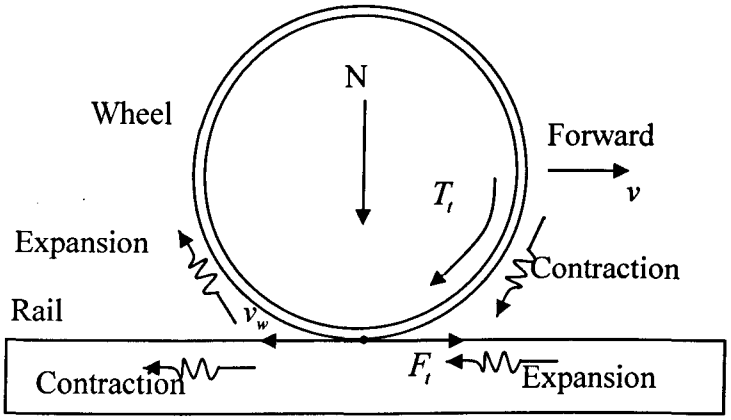

Figure 1.4 Creep phenomenon between wheel and rail

The value of creep force is determined as

$$F_t = \mu N \tag{1.2}$$

where, μ is the creep force coefficient, N is the normal load. Creep force F_t varies in time, even though the normal force N is constant. In practical systems, the creep force is subject to large and uncertain variations due to different contact environments, such as contaminations and weather. The vehicle speed and creepage will affect the resultant creep force as well.

In many railway vehicle modelling for steering or stability control studies, the creep force coefficients are normally taken as constants, for example in steering controls [17], in stability analysis [18] or in bogie fault detections [19] . However, the nonlinear relation of the overall creep force at the contact point with creepage is concerned in the research regarding the re-adhesion control strategies development.

1.3.2 Slip phenomenon and Consequences

Typically, the trend of the fundamental relationship between creep force coefficient μ and creepage λ can be described through different slip curves as show in Figure 1.5 which can be obtained based on a general creep force coefficient model according to [20] and [21]:

$$\mu = \frac{\mu_{s0}}{1+\left(\frac{\lambda}{k_{\mu 1}}\right)^2} + \frac{\mu_{d0}}{1-e^{\left(-\frac{\lambda}{k_{\mu 2}}\right)}} \tag{1.3}$$

where, μ_{s0} and μ_{d0}, $k_{\mu 1}$ and $k_{\mu 2}$ are the curve tuning parameters depending on the rail surface conditions.

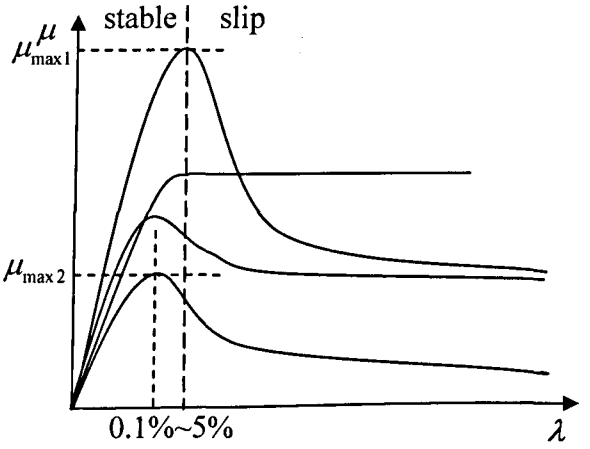

Figure 1.5 Wheel rail contact characteristics

The maximum value of each curve, also known as the adhesion coefficient, gives the adhesion level available at certain contact condition. High adhesion coefficient indicates a dry/good contact condition, while a low adhesion coefficient is related to a poor contact condition such as wet or oily rail. Wheel slip frequently happens in the low adhesion conditions.

Each curve can be partitioned into stable and unstable regions by the maximum point. In the stable region, the curve has positive slope, and vehicle can operate stably in this region. The linear part section of the stable region is also known as low creep section. The nonlinear section of the stable region is known as the large creep section.

In the large creep section, the creep force approaches saturation [22]. By contrast, in the unstable region, also known as the slip region, the curve has negative slopes. The more creepage, the less creep force is obtained in the unstable region. The vehicle is normally required to operate in the low creep section where a stable transmission is guaranteed.

However, the slip curves shown in Figure 1.5 present rather idealized curves. The value of the creep force coefficient varies with external conditions, but measurements from many experimental studies have indicated that the creepage-creep force relations in practice broadly conform to the ideal curves [23]. As a result, the slip curves have been widely used in railway vehicle dynamic studies. In this thesis, look-up tables are generated to represent different wheel rail contact conditions.

Slip happens when the driving torque from the motor is higher than the adhesion level in the present contact condition. In the slip condition, wheel speed will increase much faster than the vehicle's since the creep force is limited by the adhesion level. The excessive slip causes heavy wear of wheel and rail, shortens lives of relevant elements and also brings operational difficulties. Therefore, re-adhesion control is a necessity to ensure stable vehicle performance and prevent excessive wear of wheel and rail.

1.4 Literature Review

Generally, re-adhesion control includes two fundamental issues: the detection of wheel slips and torque control for re-adhesion. Before 1980s, the slip control performance was highly dependent on the driver's skills [16]. With the development of automatic control strategies and electronics technologies, gradually, slip detection and torque adjustment can be controlled by microprocessors with online signal processing which gives good response to the abnormal conditions. Although some measures such as sand or friction modifiers can be applied to wheel rail interface to increase adhesion in traction [24], the re-adhesion controls for the electrical vehicles are implemented associated with torque controllable traction motors, and different approaches have been studied.

1.4.1 Conventional Re-adhesion Control Based on Wheel Speeds

Conventional re-adhesion control schemes, which were developed to detect slip and compensate the poor rail adhesion effort without the exact information of the wheel rail contact condition, use the creep speed criteria or acceleration criterion to detect the slip. The creep speed is defined as the speed difference between the driving wheel and the vehicle. Therefore, the primary important issue for the conventional scheme is the speed measurement. Regularly, the angular speed of a wheel is obtained through a position encoder installed at one end of the wheel axle or traction motor axle [25]. Since it is difficult to obtain vehicle speed appropriately by directly measuring it, the raw train speed is usually taken as the minimum value among several axles. The raw train speed is either used directly to calculate creep speed [7][25][26][27][28] or allowed to increase or decrease by the train acceleration rate when it is lower or greater the trailer car's speed respectively [29][30]. No matter which method is used, the multi position encoder measurement is required for the conventional re-adhesion control.

In the creep speed criteria, the slip condition is indicated when the creep speed is higher than the preset threshold [26][27][28][29][30]. The lower the threshold value, the faster slip condition is detected. Typical threshold value is 0.1 km/h [27]. Some experimental results also show the threshold value may be up to 2 km/h (Shinkansen trains) [26]. A small threshold value may guarantee the vehicle will not slip heavily by scarifying the tractive efficiency where the creepage is far below the adhesion level [22]; meanwhile, high threshold value may result in the delay of slip detection. Different torque control strategies are proposed based on creep speed criteria.

The slip velocity feedback torque control in [27] imposes the torque by feeding back the creep speed through a constant gain. Speed difference control is a method for reducing the torque according to the difference between creep speed and the reference creep speed [25][28]. The reference creep speed can be given fixed based on real field test results [25] or given as a linear function of vehicle velocity [28]. According to [29], the speed difference control only works when the slip speed is very small and suitable for early inhibition of wheel slip development.

Pattern control is used to reduce the torque according to a pre-defined pattern [29][30]. The driving torque is reduced by a certain pre-defined pattern to regain adhesion when a slip conditions is indicated. Once the creep speed is found to be lower than a threshold (usually lower than the one which is used to detect the slip), the re-adhesion is considered to be achieved. The driving torque is either kept at the current level (simplest logic), or gradually increased in a pre-defined pattern to make more utilization of the adhesion condition. The pattern control is also used for small slip corrections and to large extent depends on proper selection of threshold values.

Acceleration criterion is also used to detect the slip especially when all the wheels slip simultaneously in severe slip conditions. In [7], the re-adhesion control is realized by watching the acceleration rate of the wheel speed and reduced the torque by an amount which is proportional to the square of the creep speed.

Based on these conventional anti-slip methods, typical hybrid control re-adhesion control schemes were proposed where conventional re-adhesion control methods are blended as introduced in [29][30]. The control subsystems (speed difference control, pattern control and acceleration criterion) are activated according to different slip levels. Usually, the creep speed threshold for the speed difference control is lower than that of the pattern control. The acceleration criterion is used as the top level of hybrid control. The calculated acceleration rate is compared to the pre set acceleration limit to active a further torque reduction by a certain pattern to secure good adhesion regardless the severity of wheel slip.

1.4.2 Re-adhesion Control Based on Disturbance Observer

A lot of work has been tried to detect the slip and control the torque on the identification of wheel rail contact conditions. The slip condition or the optimal operation region can be pointed out by studying the slope of the creep force. Besides direct measurement of the creep force [31], there are several ways to estimate the creep force as a disturbance to the traction motor.

In [32][33][34], the creep force is considered as the load torque of the motor. Therefore, the creep force can be estimated from the driving torque and the motor

rotating speed with a low pass filter to eliminate the noise caused by taking derivative of wheel speed. In [6][35][36][37], the disturbance observers assume the time derivative of the creep force be zero, and establish full order state space observer to estimate creep force with the wheel angular speed information.

When creep force is known, the creep force coefficient can be calculated as well as the time derivative of the creep force, which can be further used for slip detection and optimal re-adhesion control. The optimal adhesion condition relies on the maximum point of the slip curve, where the derivative of creep force to creepage is zero. According to [33], when the accelerating vehicle encounters a wheel-rail contact condition drop and develops a slip status, the time when the derivative of creep force (dF_t/dt) is equal to zero and the time when the derivative of the creep force to creepage ($dF_t/d\lambda$) is equal to zero are almost identical, so it is possible to examine zero time derivative of creep force to detect the peak point of the slip curve. In [36], a high pass filter is designed to estimate the time derivative of the creep force, but no further anti slip control method is introduced. In most of the works [6][31][34][35], steepest gradient method is proposed to obtain the optimal creep speed, which can be fed to an simple PI controller to derive the torque adjusting amount with extra knowledge of actual creep speed from the measurement. Some others establish a PI controller directly by employing the time derivative of the creep force as the input [32] [33][37].

The advantage of the disturbance observer lies in the fact that it gives the possibility to detect the optimal creepage without the calculation of creepage. However, the time derivative of the creep force can not be estimated correctly when the creep force changes quickly caused by sudden slip [34].

1.4.3 Non-classic Re-adhesion Control Methods

Due to the non-linearity and high noise contaminated facts of slip, there are some non-classical methods to treat this problem such as fuzzy logic based control [38] by examining the time derivative of creep speed together with time derivative of creep force. In [39], wavelet analysis is used to pre-process the data for fuzzy logic

controller, where the wheel acceleration signal is decomposed to a noise-free approximation part and a detail part with noise. Based on the noise free part, the wheel acceleration tendency is estimated and differentiated to identify the slip tendency.

1.4.4 Summary

The strategies of existing re-adhesion control schemes mentioned in the last section mainly rely on

(1) Representative speed variations in slip condition. Since the major driving effect is consumed in speeding up the wheelset speed rather than the vehicle in slip condition, the wheelset speed is to increase much faster than vehicle's. By monitoring speeds of wheelset and vehicle, slip condition can be detected and prevented.

(2) Nonlinear wheel rail contact feature. Wheel rail contact feature can be expressed though slip curves. The maximum points of the curves mean not only optimal operation points but also dividing points of normal conditions and slip conditions. By detecting the turning point of wheel rail contact curves where the slope is zero, the slip can be prevented and the system can be held in optimal operation condition.

The constraints of these approaches are:

(1) Multiple speed sensors are required. Even though some work has been done to estimate train speed directly from wheel velocity measurement [40] and several approaches used GPS [41][42], it is still difficult to obtain vehicle speed properly and precisely. In many applications, several speed sensors are required to be installed other than the powered wheelset. These will increase the cost and the complexity of the tractive unit.

(2) Disturbance sensitivity. Besides the noise caused by the power inverter and position sensor, harsh operation environment and complex operation dynamics of railway vehicle also introduce unwanted disturbances to the system. Therefore, it is difficult to identify the precise dividing point for the normal and slip conditions [23], which results in reiterative action of control system and finally reduces the average tractive effort for the railway vehicle.

1.5 Kalman Filter in Railway Applications

The Kalman filter was developed by both Kalman and Bucy [43][44] to treat "the problem of estimating the state of a linear stochastic system by using measurement that are linear functions of the state" [45]. In railway technologies, the major applications of Kalman filter are in the areas of:

(1) Sensor fusion for train tracking and localization. Kalman filtering is widely used to obtain a robust train speed measurement through a smart fusion of different kind of sensors, such as eddy current sensors [46], odometer and inertial sensors or GPS [47][48], Doppler radar [49], axle-generator [50], or from a Human speaker [51];

(2) Suspension condition monitoring. Kalman filter gives good solutions to monitor the vehicle suspensions conditions and detect the fault based on noisy on-board measurement as presented in [19] and [52];

(3) Active steering issues. In [53], [54], Kalman filters were used to estimate the state variables for active steering controls for railway vehicles;

(4) Wheel-rail adhesion level estimation. In [55], a linear Kalman filter was designed to estimate the wheel-rail low adhesion levels by using the response of vehicle to track irregularities, and the drop of the adhesion level can be indicated based on the estimation results of Kalman filter.

In these applications using Kalman filter, the most relevant ones to the re-adhesion control study are the presented in [50] and [55]. However, in [50], the slip detection and compensation strategies were actually a conventional re-adhesion approach on which finally it was based the speed variation observation. In [55], even though a low wheel-rail adhesion level can be indicated, it cannot figure out whether a slip happens or not.

1.6 Research Approach of This Thesis

The research proposes a novel indirect slip detection and re-adhesion control approach by exploring how wheelset reacts dynamically to the changes in contact conditions. The study starts from the dynamics study of a wheelset model considering the elastic coupling of the shaft, which is different from most of the

existing schemes. The natural torsional modes of the wheelset are studied to find the primary natural mode. Based on the dynamics of the wheelset, several slip detection strategies are introduced and evaluated in different conditions. Special attentions have been given to the Kalman filter based slip detection scheme with the practical position encoder. The further developed re-adhesion control approach based on Kalman filter requires fewer sensors than the existing anti-slip schemes, and robust to noise and external disturbances. All the simulations are carried out in the environment of MATLAB/SIMULINK.

1.7 Thesis structure

There are 7 chapters in this thesis:

Chapter 1 gives a background study of electric traction system, wheelset arrangement and slip phenomena and its consequences. Then the literature review gives a comprehensive introduction of the existing re-adhesion control strategies for electrical vehicle, where the features and limitations of the strategies are summarized. After that, there is a brief review on the Kalman filter applications in railways system, followed by the arrangement of this thesis.

In chapter 2, the induction motor model and its vector controller based on indirect rotor flux linkage oriented control scheme are introduced, which is important for a fast torque response to achieve re-adhesion.

In chapter 3, the wheelset dynamic modelling is presented, where a comprehensive model including longitudinal, lateral and yaw dynamics is firstly introduced and followed by a distributed parameter model and a lumped parameter model with simplified longitudinal dynamics. The natural torsional modes of the wheelset are found based on the distributed parameter model. The dynamics to the external torque of each mode are studied and compared, based on which the primary torsional mode is highlighted. The lumped parameter wheelset model which contains the rotational and primary torsional mode lays the foundation for the further slip detection and controller design. The distributed and lumped parameter models are compared at the end in the dynamic description and simulation results respectively.

Chapter 4 contains the dynamics study of the lumped parameter wheelset model. The dynamics of the wheelset with different natural torsional frequency are studied in different wheel rail contact conditions. The torsional oscillations at the wheelset natural frequency are considered as an indexing phenomenon of the wheelset in slip condition. The stability analyses based on the linearised wheelset model are carried out and indicate the link between the torsional oscillations in slip condition and the system instability.

Chapter 5 deals with the slip detection based on the torsional oscillations. The method of direct monitoring torsional torque based on ideal measurement is introduced, where two post data processing methods treating the vibration signals are introduced and compared. Then a Kalman filter based slip detection scheme is proposed and evaluated with different wheelset axles as well as in different conditions including the cases where a practical position encoder is involved.

In chapter 6, a complete re-adhesion scheme based on Kalman filter is developed and the performances of the scheme are evaluated for different wheels axles and different wheel rail contact conditions. The performances with a practical position encoder are also evaluated. Finally the dynamics of the comprehensive wheelset model which considers the longitudinal, lateral and yaw dynamics couplings are investigated in slip conditions. The feasibility of the re-adhesion scheme is examined in this complex dynamic environment.

Chapter 7 provides the conclusions and suggestions for further study. Here, a summary of this thesis is given. The conclusions are drawn where the novelties and advantages of the developed re-adhesion scheme are put forward. Finally, some suggestions for further work are displayed.

2 MODELLING OF THE INDUCTION MOTOR AND ITS DRIVE

The three phase induction motors are one of the major driving motors for railway traction system nowadays. With the development of power electronic technologies, high performance control unit of induction motors can be implemented at a relatively low cost level [56]. In this study, an induction motor with an indirect vector control scheme acts as the major actuator to carry out the re-adhesion control demand.

In this chapter, the model of a three-phase induction motor is introduced. Indirect rotor flux linkage oriented control (FOC) scheme is presented. Then a position encoder commonly used in railway industry is introduced to the FOC scheme. Finally, a complete tractive unit with a PWM inverter-fed induction motor is presented.

2.1 Modelling of the Induction Motor

2.1.1 Three-Phase Mathematical Model of the induction motor

It is assumed that three-phase stator windings (*A, B, C*) and rotor windings (a_r, b_r, c_r) are distributed symmetrically, and air-gap MMF (magneto-motive force) distribution of any single phase winding is sinusoidal. The permeability of the stator and rotor iron is assumed to be infinite; saturation, iron losses, end-windings and slot-effects are neglected [57].

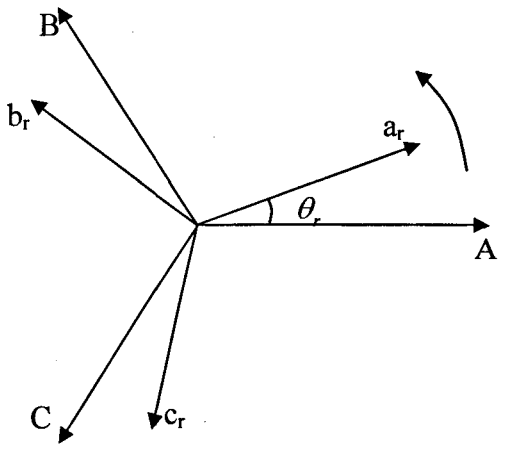

Figure 2.1 ABC (stator) and $a_rb_rc_r$ (rotor) coordinate systems

Figure 2.1 gives a three phase coordinate system for stator and rotor: ABC represents the stator coordinate, which is a static frame with three phases distributed 120° from one another; $a_rb_rc_r$ represent the rotor coordinates, which is a rotating frame with three phases displaced 120°. θ_r is the rotor electrical angle.

Equation of Flux Linkage in Three Phase Coordinate System

The flux equation is given as [58]:

$$\begin{bmatrix} \Psi_{ABC} \\ \cdots\cdots \\ \Psi_{arbrcr} \end{bmatrix} = \begin{bmatrix} L_{ss} & M_{sr} \\ \cdots\cdots\cdots & \\ M_{rs} & L_{rr} \end{bmatrix} \begin{bmatrix} i_{ABC} \\ \cdots\cdots \\ i_{arbrcr} \end{bmatrix} \tag{1.4}$$

In the flux equation:

$\psi_{ABC} = [\psi_A \quad \psi_B \quad \psi_C]^T$ is the array of stator flux linkage;

$\psi_{arbrcr} = [\psi_{ar} \quad \psi_{br} \quad \psi_{cr}]^T$ is the array of rotor flux linkage of referred to stator;

$i_{ABC} = [i_A \quad i_B \quad i_C]^T$ is the array of stator phase currents;

$i_{arbrcr} = [i_{ar} \quad i_{br} \quad i_{cr}]^T$ is the array of rotor phase currents;

L_{ss} is the stator self inductance matrix:

$$L_{ss} = \begin{bmatrix} L_{1m} + L_{1l} & -\frac{1}{2}L_{1m} & -\frac{1}{2}L_{1m} \\ -\frac{1}{2}L_{1m} & L_{1m} + L_{1l} & -\frac{1}{2}L_{1m} \\ -\frac{1}{2}L_{1m} & -\frac{1}{2}L_{1m} & L_{1m} + L_{1l} \end{bmatrix} \tag{1.5}$$

where L_{1m} is the inductance corresponding to air-gap primary flux linkage of the stator; and L_{1l} is the leakage inductances of the stator.

L_{rr} is the rotor self inductance matrix referred to the stator:

$$L_{rr}=\begin{bmatrix} L_{1m}+L_{2l} & -\frac{1}{2}L_{1m} & -\frac{1}{2}L_{1m} \\ -\frac{1}{2}L_{1m} & L_{1m}+L_{2l} & -\frac{1}{2}L_{1m} \\ -\frac{1}{2}L_{1m} & -\frac{1}{2}L_{1m} & L_{1m}+L_{2l} \end{bmatrix} \tag{1.6}$$

where, L_{2l} is the rotor leakage inductance referred to the stator.

M_{sr} is the mutual inductance matrix from the rotor to the stator:

$$M_{sr}=\begin{bmatrix} L_{1m}\cos\theta_r & L_{1m}\cos(\theta_r+120^\circ) & L_{1m}\cos(\theta_r-120^\circ) \\ L_{1m}\cos(\theta_r-120^\circ) & L_{1m}\cos\theta_r & L_{1m}\cos(\theta_r+120^\circ) \\ L_{1m}\cos(\theta_r+120^\circ) & L_{1m}\cos(\theta_r-120^\circ) & L_{1m}\cos\theta_r \end{bmatrix} \tag{1.7}$$

M_{rs} is the mutual inductance matrix from the stator to the rotor:

$$M_{rs}=\begin{bmatrix} L_{1m}\cos\theta_r & L_{1m}\cos(\theta_r-120^\circ) & L_{1m}\cos(\theta_r+120^\circ) \\ L_{1m}\cos(\theta_r+120^\circ) & L_{1m}\cos\theta_r & L_{1m}\cos(\theta_r-120^\circ) \\ L_{1m}\cos(\theta_r-120^\circ) & L_{1m}\cos(\theta_r+120^\circ) & L_{1m}\cos\theta_r \end{bmatrix} \tag{1.8}$$

Equation of Voltage in Three phase Coordinate System

The voltage equations of the stator and rotor windings are [58]:

$$\begin{bmatrix} v_{ABC} \\ \cdots\cdots \\ v_{arbrcr} \end{bmatrix}=\begin{bmatrix} R_1 & 0 \\ \cdots\cdots\cdots \\ 0 & R_2 \end{bmatrix}\begin{bmatrix} i_{ABC} \\ \cdots\cdots \\ i_{arbrcr} \end{bmatrix}+p\begin{bmatrix} \psi_{ABC} \\ \cdots\cdots \\ \psi_{arbrcr} \end{bmatrix} \tag{1.9}$$

where, $v_{ABC}=\begin{bmatrix} v_A & v_B & v_C \end{bmatrix}^T$ is the array of the voltages of the stator;

$v_{arbrcr}=\begin{bmatrix} v_{ar} & v_{br} & v_r \end{bmatrix}^T$ is the array of the voltages of rotor referred to the stator;

$R_1=\begin{bmatrix} r_1 & 0 & 0 \\ 0 & r_1 & 0 \\ 0 & 0 & r_1 \end{bmatrix}$ is the stator resistance matrix, r_1 is the phase resistance of the stator;

$R_2 = \begin{bmatrix} r_2 & 0 & 0 \\ 0 & r_2 & 0 \\ 0 & 0 & r_2 \end{bmatrix}$ is the rotor resistance matrix, and r_2 is the phase resistance of rotor referred to the stator.

Substituting flux equation (1.4) into the voltage equation (1.9) it gives:

$$\begin{bmatrix} v_{ABC} \\ \cdots\cdots \\ v_{arbrcr} \end{bmatrix} = \begin{bmatrix} R_1 & 0 \\ \cdots\cdots\cdots \\ 0 & R_2 \end{bmatrix} \begin{bmatrix} i_{ABC} \\ \cdots\cdots \\ i_{arbrcr} \end{bmatrix} + p \begin{bmatrix} L_{ss} & M_{sr} \\ \cdots\cdots\cdots \\ M_{rs} & L_{rr} \end{bmatrix} \begin{bmatrix} i_{ABC} \\ \cdots\cdots \\ i_{arbrcr} \end{bmatrix} \tag{1.10}$$

or:

$$\begin{bmatrix} v_{ABC} \\ \cdots\cdots \\ v_{arbrcr} \end{bmatrix} = \begin{bmatrix} R_1 + pL_{ss} & pM_{sr} \\ \cdots\cdots\cdots \\ pM_{rs} & R_2 + pL_{rr} \end{bmatrix} \begin{bmatrix} i_{ABC} \\ \cdots\cdots \\ i_{arbrcr} \end{bmatrix} \tag{1.11}$$

Motion Equation of the rotor

The electromagnetic torque of the induction motor T_e is generated by the interactions of stator magnetic field and induced rotor magnetic field and is given as [58]:

$$\begin{aligned} T_e = -n_p L_{1m}[&(i_A i_{ar} + i_B i_{br} + i_C i_{cr})\sin\theta_r + (i_A i_{br} + i_B i_{cr} + i_C i_{ar})\sin(\theta_r + 120^\circ) \\ &+ (i_A i_{cr} + i_B i_{cr} + i_C i_{ar})\sin(\theta_r - 120^\circ)] \end{aligned} \tag{1.12}$$

where, n_p is the pole pair number.

The mechanical dynamics of the motor is governed by [58]:

$$\frac{I_m}{n_p} \cdot \frac{d^2\theta_r}{dt^2} = T_e - T_L - \frac{D}{n_p} \cdot \frac{d\theta_r}{dt} \tag{1.13}$$

where, T_L is the load torque, I_m is the moment inertia of the rotor and D is the windage and viscous damping coefficient.

Usually, the damping torque caused by windage and friction is neglected [59]. Defining rotor electrical angular speed as $\omega_m = \frac{d\theta_r}{dt}$, the final motion equation of the induction motor is:

$$\frac{I_m}{n_p} \cdot \frac{d\omega_m}{dt} = T_e - T_L \tag{1.14}$$

2.1.2 Induction Motor Model in Stationary Two Phase Coordinate System

Equations (1.4), (1.10) and (1.14) are the three basic equations to describe the cage induction motor. The inductances involved are functions of θ_r, and this makes the equations difficult to solve. To simplify the solving process and make the dynamic features more obvious, transformations between different coordinate system are developed. Figure 2.2 defines a stationary $\alpha\beta$ frame which is a two phase coordinate system with axis α being fixed along the stator A axis and the axis β being vertical to the axis α.

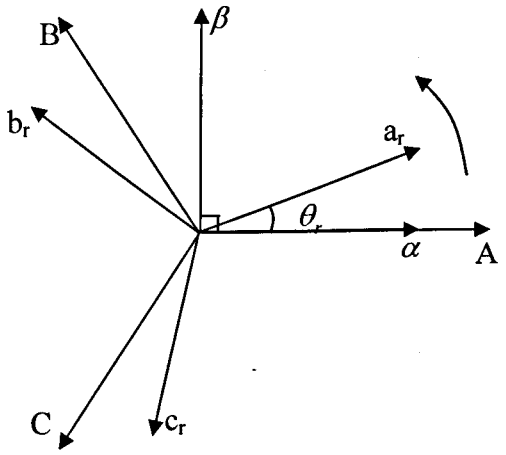

Figure 2.2 ABC/$\alpha\beta$ frame

Transformation Matrix

The variables in these two frames can be transferred using the transformation matrixes. The transformations are made under the restrictions to keep the power unchanged before and after transformation. One of the widely used transformation matrix is to keep the power unchanged before and after the transformation [60]. According to that, the transformation matrix from stator ABC coordinates and $\alpha\beta$ frame is $C_{3s\text{-}2}$:

$$C_{3s-2} = \sqrt{\frac{2}{3}} \begin{bmatrix} 1 & -\frac{1}{2} & -\frac{1}{2} \\ 0 & \frac{\sqrt{3}}{2} & -\frac{\sqrt{3}}{2} \\ \frac{1}{\sqrt{2}} & \frac{1}{\sqrt{2}} & \frac{1}{\sqrt{2}} \end{bmatrix} \tag{1.15}$$

The transformation matrix from $\alpha\beta$ frame to the ABC system is $C_{2\text{-}3s}$:

$$C_{2-3s} = \sqrt{\frac{2}{3}} \begin{bmatrix} 1 & 0 & \frac{1}{\sqrt{2}} \\ -\frac{1}{2} & \frac{\sqrt{3}}{2} & \frac{1}{\sqrt{2}} \\ -\frac{1}{2} & -\frac{\sqrt{3}}{2} & \frac{1}{\sqrt{2}} \end{bmatrix} \tag{1.16}$$

The transformation matrix from rotor $a_rb_rc_r$ coordinates to $\alpha\beta$ frame is $C_{3r\text{-}2}$:

$$C_{3r-2} = \sqrt{\frac{2}{3}} \begin{bmatrix} \cos\theta_r & \cos(\theta_r - 120^\circ) & \cos(\theta_r + 120^\circ) \\ -\sin\theta_r & -\sin(\theta_r - 120^\circ) & -\sin(\theta_r + 120^\circ) \\ 1/\sqrt{2} & 1/\sqrt{2} & 1/\sqrt{2} \end{bmatrix} \tag{1.17}$$

The transformation matrix from $\alpha\beta$ frame to rotor $a_rb_rc_r$ coordinatesis $C_{2\text{-}3r}$:

$$C_{2-3r} = \sqrt{\frac{2}{3}} \begin{bmatrix} \cos\theta_r & -\sin\theta_r & \frac{1}{\sqrt{2}} \\ \cos(\theta_r - 120^\circ) & -\sin(\theta_r - 120^\circ) & \frac{1}{\sqrt{2}} \\ \cos(\theta_r + 120^\circ) & -\sin(\theta_r + 120^\circ) & \frac{1}{\sqrt{2}} \end{bmatrix} \tag{1.18}$$

Equations in $\alpha\beta$ Frame

The equations to describe the induction motor in the $\alpha\beta$ frame are known as Stanley's equation, which is very useful to solve transient problems [61]. The voltage equation is [58]:

$$\begin{bmatrix} v_{\alpha 1} \\ v_{\beta 1} \\ v_{\alpha 2} \\ v_{\beta 2} \end{bmatrix} = \begin{bmatrix} r_1 + pL_s & 0 & pL_m & 0 \\ 0 & r_1 + pL_s & 0 & pL_m \\ pL_m & \omega_m L_m & r_2 + pL_r & \omega_m L_r \\ -\omega_m L_m & pL_m & -\omega_m L_r & r_2 + pL_r \end{bmatrix} \begin{bmatrix} i_{\alpha 1} \\ i_{\beta 1} \\ i_{\alpha 2} \\ i_{\beta 2} \end{bmatrix} \tag{1.19}$$

where.

$$L_m = \frac{3}{2} L_{1m} \; ; \; L_s = L_{1l} + L_m ; \; L_r = L_{2r} + L_m$$

1: suffix for quantities of the stator

2: suffix for quantities of the rotor

For end short circuited squirrel cage induction motor, $v_{\alpha 2} = v_{\beta 2} = 0$.

The flux equations are:

$$\begin{bmatrix} \psi_{\alpha 1} \\ \psi_{\beta 1} \\ \psi_{\alpha 2} \\ \psi_{\beta 2} \end{bmatrix} = \begin{bmatrix} L_s & 0 & L_m & 0 \\ 0 & L_s & 0 & L_m \\ L_m & 0 & L_r & 0 \\ 0 & L_m & 0 & L_r \end{bmatrix} \begin{bmatrix} i_{\alpha 1} \\ i_{\beta 1} \\ i_{\alpha 2} \\ i_{\beta 2} \end{bmatrix} \tag{1.15}$$

Then the stator currents can be given as:

$$i_{\alpha 1} = \frac{1}{R + pL_\sigma} (v_{\alpha 1} + A\psi_{\alpha 2} + B\omega\psi_{\beta 2}) \tag{2.16}$$

$$i_{\beta 1} = \frac{1}{R + pL_\sigma} (v_{\beta 1} + A\psi_{\beta 2} - B\omega\psi_{\alpha 2}) \tag{1.17}$$

where,

$$R = r_1 + \frac{L_m^2}{L_r^2} r_2 ; L_\sigma = L_s - \frac{L_m^2}{L_r} ; A = \frac{L_m}{L_r^2} r_2 ; \; B = \frac{L_m}{L_r}$$

The electromechanical torque is given as:

$$T_e = n_p L_m (i_{\beta 1} i_{\alpha 2} - i_{\beta 2} i_{\alpha 1}) = \frac{n_p L_m}{L_r} (i_{\beta 1}\psi_{\alpha 2} - i_{\alpha 1}\psi_{\beta 2}) \tag{1.23}$$

The motion dynamic equation is the same as equation(1.14).

2.1.2 Simulation Results of an Induction Motor

The correctness of the induction motor model is evaluated by the simulation results. The parameters of the induction motor, which are taken from a practical light duty traction motor, are given in Table 2.1:

Variables	Definitions and values
P_N	Rated power (250 kW)
U_N	Rated voltage (660 V)
f_N	Rated frequency (80 Hz)
r_1	Stator phase resistance (0.0442 Ω)
r_2	Rotor phase resistance referred to the stator (0.0665 Ω)
L_{1m}	Inductance corresponding to air-gap primary flux linkage (1.342×10^{-2} H)
L_{ls}	Stator leakage inductance (6.650×10^{-4} H)
L_{lr}	Rotor leakage inductance referred to the stator (6.680×10^{-4} H)
n_p	Pole pair number (3)
I_m	Rotor (including gearbox) moment of inertia (4.4 kgm^2)

Table 2.1 Parameters of the motor

The model established in MATLAB/Simulink is shown in Figure 2.3. The simulation is carried out under the conditions:

(1) The motor is fed with a three phase balanced power supply with magnitude 380 V and frequency 60 Hz;

(2) The load torque is given as a step signal with a magnitude 800 Nm, stepping at t=1.2 s;

(3) The initial speed of the rotor is 0;

(4) The damping is 0.

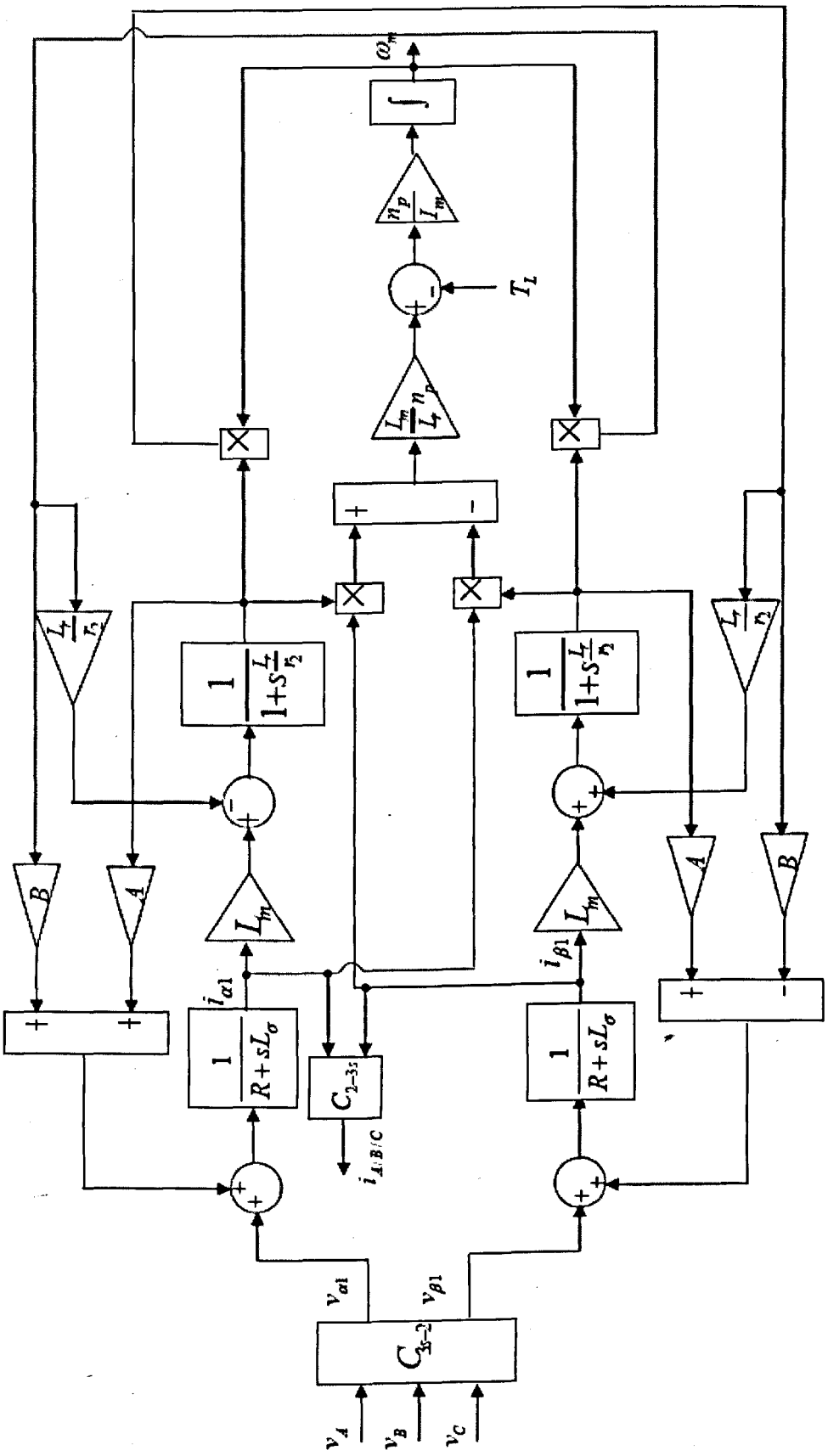

Figure 2.3 Simulation model of the induction motor

The variables observed are the stator currents, electromagnetic torque and rotor speed, which reflect the motor dynamic status and will affect the tractive performance when a mechanical load is included.

Figure 2.4 gives phase A stator current waveform. Figure 2.5 gives the close shot of phase A stator current in time range 0~0.5 s and 1~1.5 s. Figure 2.6 gives the rotor speed waveform.

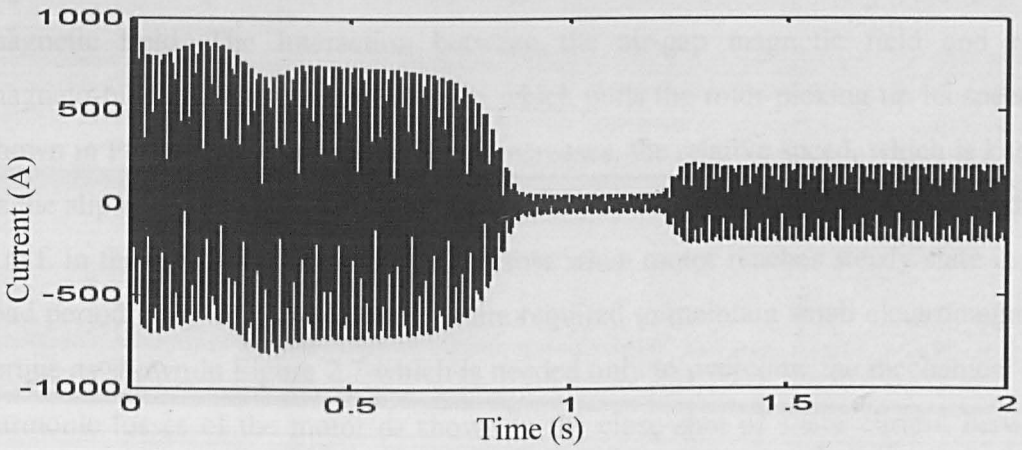

Figure 2.4 Overview the Phase A stator current

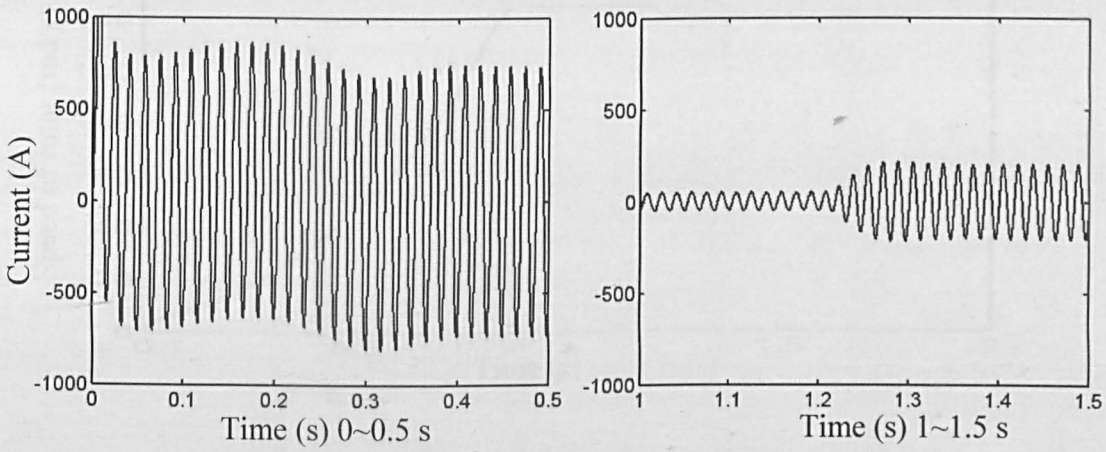

Figure 2.5 Close shot of Stator current 0~0.5 s and 1~1.5 s

When the voltages are first applied, the rotor speed is zero, and the currents running through stator windings build up the fundamental magnetic field which rotates at the

synchronous speed. At the very beginning when rotor is still stationary, the magnetic field cuts the rotor conductors at synchronous speed, which is the highest relative speed. Then the high e.m.f., which is induced by magnetic field cutting the rotor bars, produces high currents in the rotor, so high stator currents are required to balance the rotor currents during starting period as can been seen in close shot 0~0.5 s in Figure 2.5.

The induced currents in rotor generate rotor rotating magnetic field which acts together with original stator rotating magnetic field to produce the air-gap primary magnetic field. The interaction between the air-gap magnetic field and rotor magneto-motive force generates torque which pulls the rotor picking up its speed as shown in Figure 2.6. As the rotor speed increases, the relative speed, which is known as the slip speed between the rotor and the air-gap magnetic field, decreases, and the e.m.f. in the rotor conductor falls. Therefore when motor reaches steady state in no-load period, only small rotor currents are required to maintain small electromagnetic torque as shown in Figure 2.7 which is needed only to overcome the mechanical and harmonic losses of the motor as shown in the close shot of stator current between 1~1.5 s before a load torque is added at t=1.2 s.

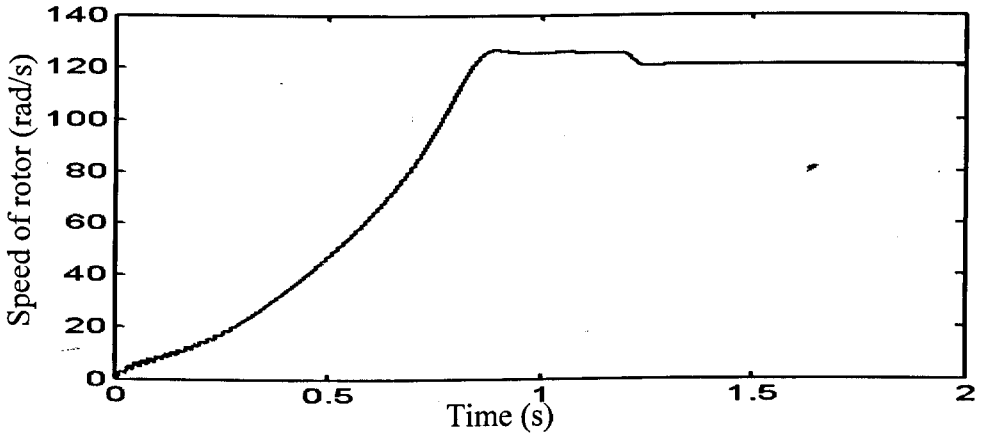

Figure 2.6 Rotor speed

When the mechanical load is added to the motor, the magnetic torque of the motor is temporarily lower than the load torque. The speed of the rotor falls as shown in Figure 2.6 at t=1.2 s when a load torque is added. Then the slip speed increases. The

induced e.m.f. in the rotor increases and so do the induced currents. When the motor reaches the new balanced status, the rotor rotates at a lower speed as shown in Figure 2.6. On the other hand, the stator currents increase to compensate the increase in the rotor currents as shown in the close shot of the stator current in time period 1~1.5 s in Figure 2.5.

Figure 2.7 gives the waveform of the electromagnetic torque of the motor. At the starting period, there is an oscillation due to the alternating cutting of the air-gap magnetic field to the rotor when the rotor speed is low. When the rotor speed is pulled up, the torque rises to a maximum torque known as pull out torque then drops to a low value as the rotor approaches synchronous speed and operates at steady state in the no load condition. When there is load added, the electromagnetic torque is increased to obtain a new balance status.

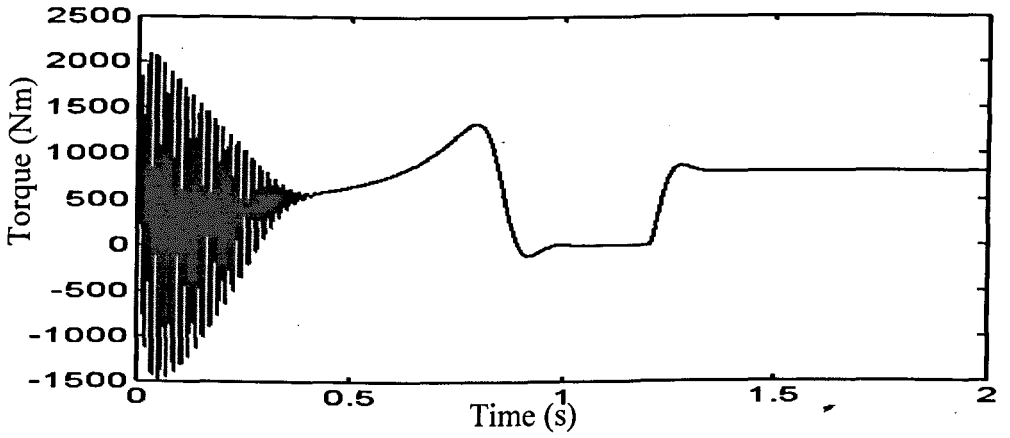

Figure 2.7 Electromagnetic torque

The study of the simulation results of the induction motor gives a physical insight of the induction motor behaviour. Also the results show that the model can deliver anticipated dynamics.

2.2 Field Oriented Control

2.2.1 Rotor Flux Linkage Oriented Vector Control

Field-oriented Control (FOC) is a well developed speed/torque control strategy which is widely used in many applications including railway industry. In this section, the rotor flux linkage orientation control is introduced and will be utilized as a basic torque control unit in the re-adhesion controller design.

In the rotor flux linkage oriented vector control, a rotating d-q frame is defined as: d-axis is fixed along the direction of rotor flux linkage ψ_2 and q-axis is vertical to d-axis as illustrated in Figure 2.8. The transformation from ABC three-phase frame to d-q rotating frame can be carried out in two steps:

(1) transformation from ABC frame to stationary $\alpha\beta$ frame and;

(2) transformation from stationary $\alpha\beta$ frame to rotating d-q frame.

The transformation can be used to decouple the torque and flux related currents so that the induction motor can be controlled like separately excited DC motors.

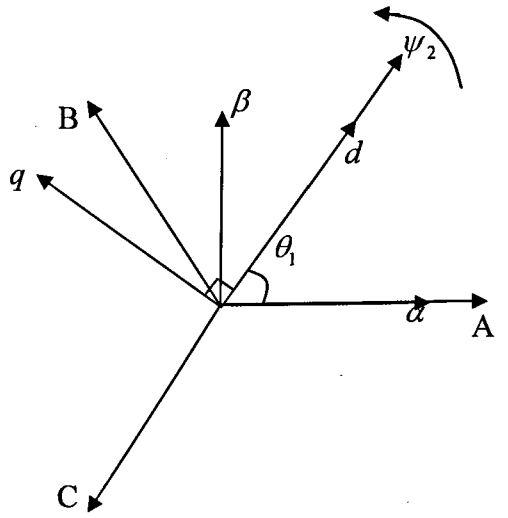

Figure 2.8 dq coordinate system

In the last section, the transformation between ABC frame to $\alpha\beta$ frame has been introduced. Taking the stator current variables for example, the transformation from $\alpha\beta$ frame to d-q frame is:

$$\begin{bmatrix} i_{d1} \\ i_{q1} \end{bmatrix} = C_{\alpha\beta-qd} \begin{bmatrix} i_{\alpha 1} \\ i_{\beta 1} \end{bmatrix} \tag{1.24}$$

where, $C_{\alpha\beta-dq} = \begin{bmatrix} \cos\theta_1 & \sin\theta_1 \\ -\sin\theta_1 & \cos\theta_1 \end{bmatrix}$ is the transformation matrix from $\alpha\beta$ frame to d-q frame.

In d-q frame, the rotor flux linkage component on each axis is given as:

$$\psi_{d2} = L_r i_{d2} + L_m i_{d1} = \psi_2 \tag{1.25}$$

$$\psi_{q2} = L_r i_{q2} + L_m i_{q1} = 0 \tag{1.26}$$

The d-q currents of the stator can be expressed as:

$$i_{d1} = \frac{\psi_2}{L_m} - \frac{L_r}{L_m} i_{d2} \tag{1.27}$$

$$i_{q1} = -\frac{L_r}{L_m} i_{q2} \tag{1.28}$$

The voltage equations of the rotor are described as:

$$v_{d2} = r_2 i_{d2} + p\psi_2 = 0 \tag{1.29}$$

$$v_{q2} = r_2 i_{q2} + \psi_2 \omega_s = 0 \tag{1.30}$$

where,

ω_s: slip angular frequency of the motor.

The d-q currents of the rotor can be derived from equation (1.29) and (1.30):

$$\begin{aligned} i_{d2} &= -\frac{p\psi_2}{r_2} \\ i_{q2} &= -\frac{\psi_2 \omega_s}{r_2} \end{aligned} \tag{1.31}$$

Then i_{q1} can be given as:

$$i_{q1} = \frac{T_2}{L_m} \psi_2 \omega_s \tag{1.32}$$

where,

T_2 : rotor time constant $T_2 = L_r / r_2$;

The electromagnetic torque of the induction motor can be expressed as:

$$T_e = n_p L_m (i_{q1} i_{d2} - i_{q2} i_{d1}) \tag{1.33}$$

For the steady state operation condition, ψ_2 is constant. Hence, i_{d2} is zero according to equation (1.29):

$$i_{d2} = -\frac{p\psi_2}{r_2} = 0 \tag{1.34}$$

The stator current along d axis is:

$$i_{d1} = \frac{\psi_2}{L_m} \tag{1.35}$$

By substituting (1.31) i_{q2} into (1.33) , the torque equation is transformed to:

$$T_e = n_p \psi_2 \cdot \frac{\psi_2 \omega_s}{r_2} = n_p \cdot \frac{L_m^2}{r_2} i_{d1}^2 \omega_s \tag{1.36}$$

By substituting (1.32) ω_s into (1.36), then another form of the torque equation is formed:

$$T_e = n_p \frac{L_m^2}{r_2} i_{d1}^2 \cdot \frac{L_m}{T_2} \cdot \frac{1}{\psi_2} \cdot i_{q1} = n_p \frac{L_m^2}{L_r} i_{d1} i_{q1} = n_p \frac{L_m}{L_r} \psi_2 i_{q1} \tag{1.37}$$

It is obvious that in the steady state operation condition T_e is proportional to the stator current i_{q1} . So the control of the torque can be carried out by controlling i_{q1} and the corresponding q axis stator current is

$$i_{q1} = \frac{L_r}{n_p L_m \psi_2} T_e \tag{1.38}$$

In the d-q frame, the flux and torque of the induction motor can be controlled separately through the control of the related stator currents. Figure 2.9 shows the diagram of rotor flux linkage FOC scheme. There are three basic steps to carry out this scheme:

(1) Generate stator current demands in d-q frame i_{d1}^* and i_{q1}^* according to equations (1.35) and (1.38) based on given flux demand ψ_2^* and torque demand T_2^*;

(2) Generate the stator voltage demands v_d^* and v_q^* from PI controllers on the acknowledgements of real stator currents. Note: in this thesis, the stator currents are assumed to be measured by ideal current sensors.

(3) Transform the voltages v_d^* and v_q^* to ABC three-phase frame on the acknowledgements of the position of rotor flux linkage θ_1.

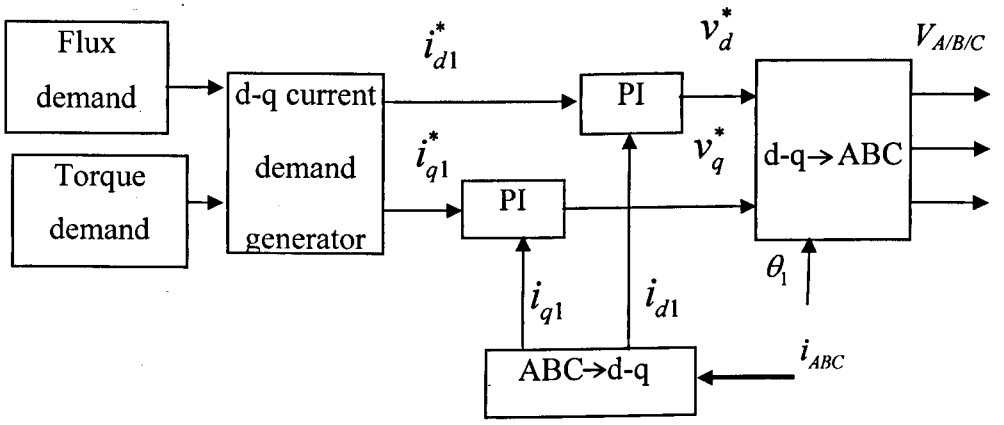

Figure 2.9 Rotor flux linkage FOC scheme

There are different ways to obtain the position of the rotor flux linkage θ_1 : direct or indirect which are distinguished by locating ψ_2 directly calculating it or indirectly from synchronous speed. In this study, the indirect FOC vector control with the use of a position encoder is considered as the drive for induction motor, since railway vehicles are usually equipped with position encoders on the wheel axle ready for use.

2.2.2 Indirect FOC Scheme

The d-q frame rotates synchronously with the rotor flux linkage. The angular position θ_1 can be obtained:

$$\theta_1 = \int \omega_1 dt \tag{1.39}$$

where, ω_1 is the synchronous speed and can be obtained through:

$$\omega_1 = n_p \cdot \omega_{mech} + \omega_s \tag{1.40}$$

where, ω_{mech} is mechanical angular frequency of the rotor.

From equation (1.32), the slip angular frequency can be given as:

$$\omega_s = \frac{L_m}{T_2} \cdot \frac{1}{\psi_2} \cdot i_{q1} \tag{1.41}$$

Usually, ω_s is calculated from the demand value of stator current instead of actual stator current values [62].

Figure 2.10 gives a schematic diagram of the indirect control scheme. Aiming to study the performance of the dynamic response based on this indirect control scheme, simulation is carried out giving the flux demand and torque demand as two step signals: the flux demand stepping at $t = 0.2\ s$ and steady value 1 Wb and the torque command changing at $t = 1.0$ s and steady value 1500 Nm. The initial motor speed is zero.

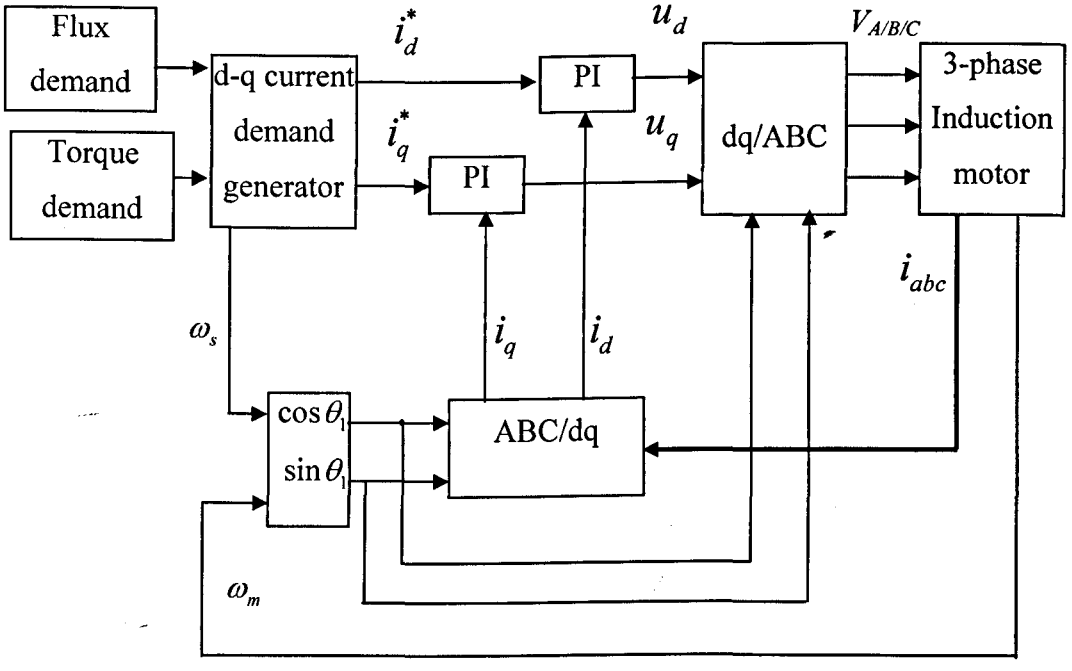

Figure 2.10 Indirect field-oriented control scheme

The flux response and the torque response are shown in Figure 2.11 and Figure 2.12 respectively.

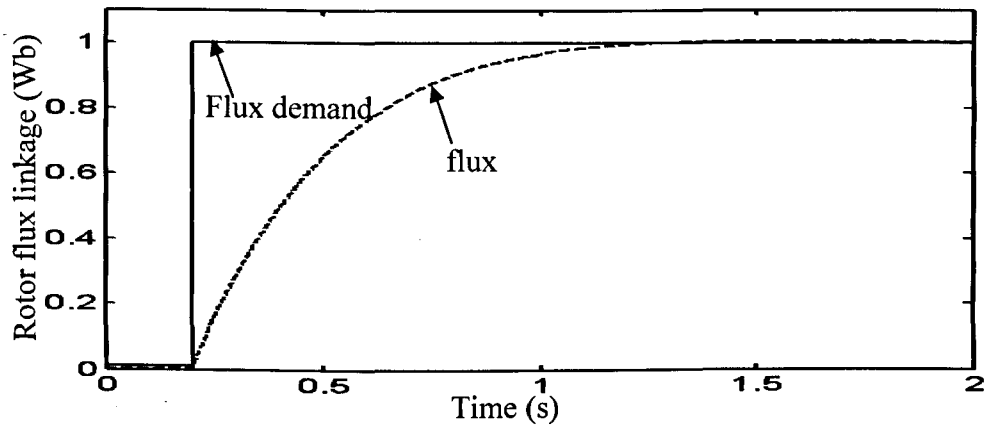

Figure 2.11 Rotor flux linkage demand and observed

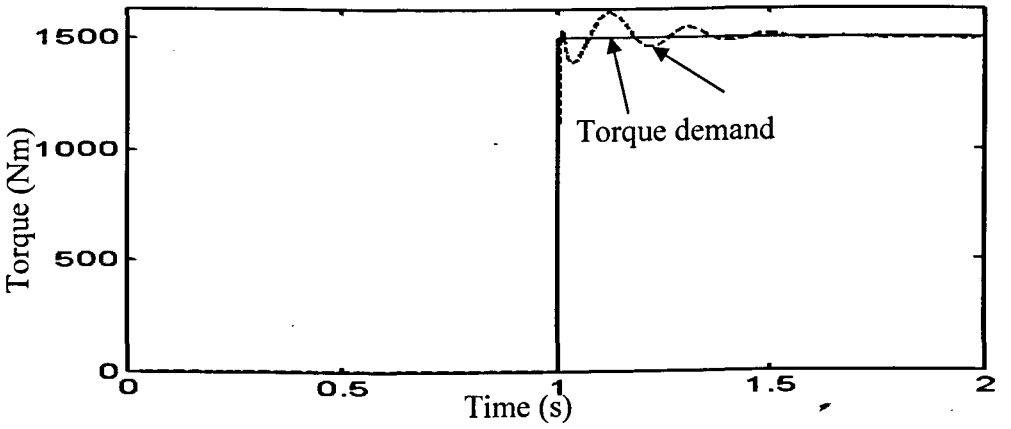

Figure 2.12 Torque demand and torque produced

The flux response shows a time delay about 1 second which is determined by the rotor time constant. The torque response is fast with some pulsations which are the result of compromise between speedy response and lower overshoot. The pulsations of the torque are acceptable in railway application since railway vehicle is a high inertia system.

2.2.3 Modelling of the Position Encoder in FOC Scheme

For the FOC scheme, the rotor position can be obtained through measurement. The most common type of the rotary position sensor is a sensor that scans a toothed wheel on the motor shaft or gearbox [63]. Considering the harsh operation conditions in railway application and for the interest of compact structure and cost, usually it is very difficult to realize a sensor with as many pulses per rotation as the encoder has in other industry applications [30]. Typically the resolution of position encoders used in traction applications is less than 100 pulses per revolution [23]. It is considered that the position encoder is installed on the wheel axle, so the actual rotor position will be proportional to the wheel angular position by the gear ratio R_g.

A position sensor is modelled to include the inaccuracies from actual measurement into the vector control scheme. The real wheel position θ_w information comes from an integration of the wheel speed ω_w, and then the equivalent pulses number N_p can be calculated for a certain position sensor with n_{ps} pulses/rev resolution. The rotor position from the position sensor is given as

$$\theta_{r\_ps} = N_p \cdot R_g \cdot \frac{2\pi}{n_{ps}} \tag{1.42}$$

The maximum absolute error caused by the position sensor is

$$\max(PS\_error) = \frac{2\pi}{n_{ps}} \tag{1.43}$$

Introducing a position encoder with resolution 100 pulses/rev into the indirect FOC scheme shown in Figure 2.10, and carrying out simulation under the same condition, the electromagnetic torque, shown in Figure 2.13, reveals the noise due the truncation errors when counting the pulse number which results in a stepwise waveform of the rotor position.

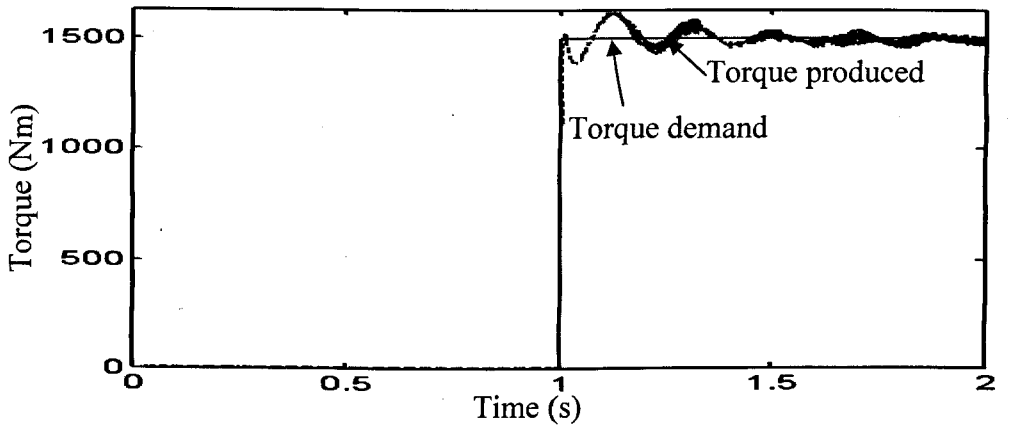

Figure 2.13 Torque demand and torque produced (with position encoder)

2.3 Modelling of a PWM Inverter

As introduced in Chapter 1, the induction motor drive equipped with a voltage source inverter is one of the major types for railways traction. PWM (pulse width modulation) is a key part of vector control with voltage source inverters [56] to provide the voltages according to the demand and thus to realize the control.

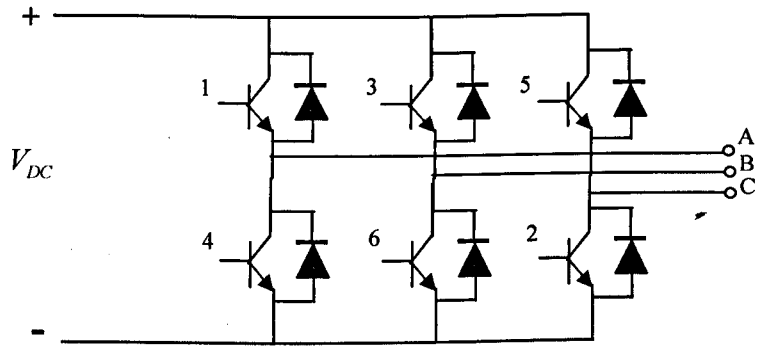

Figure 2.14 PWM inverter

A PWM inverter is modelled as shown in Figure 2.14. The DC link voltage is set as $V_{DC} = 1.5\,\text{kV}$, which is one of the standard DC power supply in railway application as introduced in Chapter 1. The PWM trigger pulses for each leg are generated by comparing a 1 kHz triangular carrier waveform with the corresponding stator voltage demand. The use of fast IGBT switch devices is assumed, and therefore the

switching delays are neglected. The diagram of a PWM inverter-fed induction motor drive is presented in Figure 2.15.

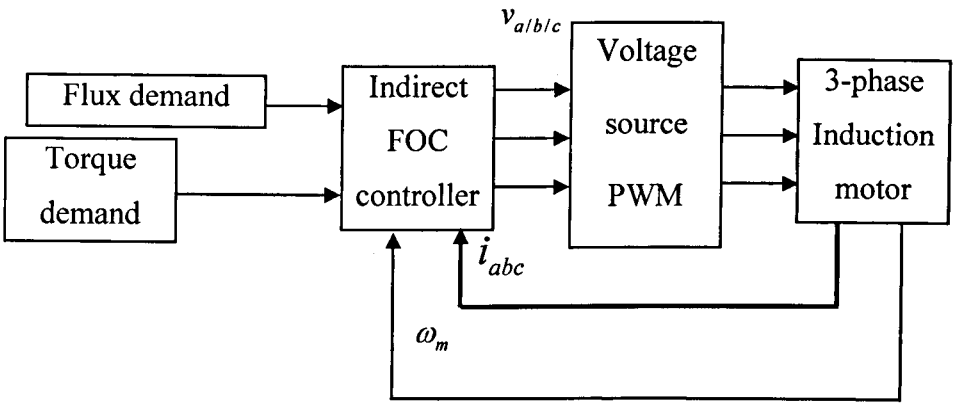

Figure 2.15 PWM inverter-fed induction motor drive

Figure 2.16 presents the torque response for this system. It shows a fast response but with moderate switching noise which are around multiples of 1 kHz generated by the inverter which was studied and proved to have little interference with the further developed slip detection scheme.

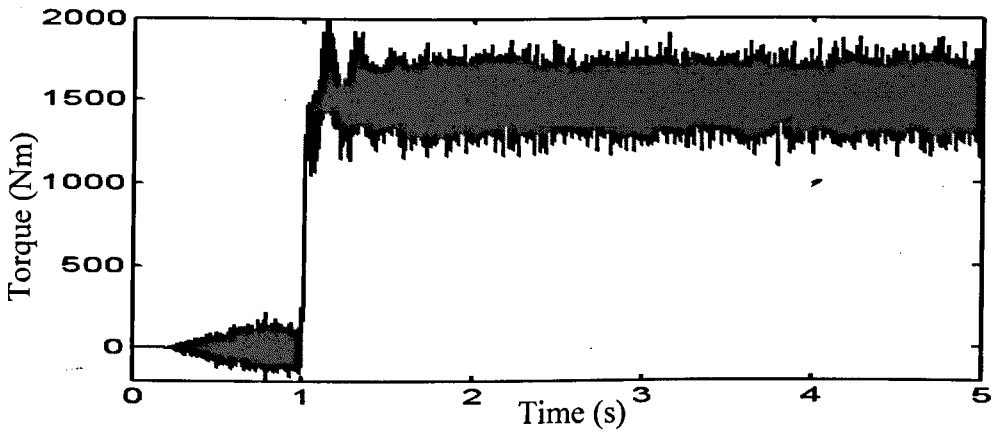

Figure 2.16 Torque generated (Indirect FOC scheme with PWM)

2.4 Summary

Re-adhesion control for AC traction system is ultimately to control the driving motor torque. The vector controlled induction motor can give a fast response for the torque demand and thus to guarantee the torque adjustment from the re-adhesion controller can be carried out in time. The drive system introduced here lays the foundation for further mechanical study and controller development.

3 MECHANICAL MODELLING

For a basic study, a single powered wheelset, with a driving motor mounted on its axle, is used. As Figure 3.1 shows, two wheels are mounted at the ends of an axle. As introduced in Chapter 1, the wheels are considered as two rigid cones. The induction motor is connected to the right hand side wheel through a gearbox, which provides the traction for 1/4 of a typical vehicle. Hence, right hand side has a larger inertia which is the combination of the wheel and driving motor. Connections between the wheelset and bogie in the longitudinal direction are assumed to be solid, as the stiffness is normally very high and the associated dynamics is not of significant relevance to this study [23]. Besides, the mechanical losses and backlash effect of the gear box are considered insignificant [23] and neglected in this study.

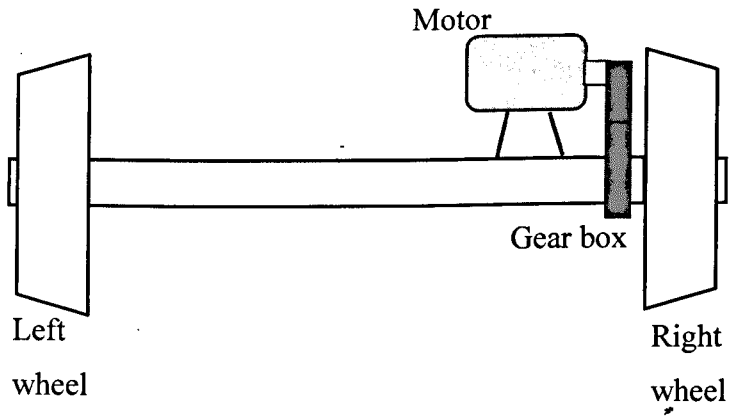

Figure 3.1 Wheelset

In this chapter, the wheel rail contact mechanics is introduced under the consideration of the elastic coupling of the shaft. At first, the wheel rail contact mechanics is introduced. A comprehensive wheelset dynamics which considers the longitudinal, lateral and yaw dynamics is introduced and will be used in comprehensive performance assessments. However, simplifications are introduced where only longitudinal dynamics on straight track is considered in the design of the slip detection and re-adhesion control. Based on the simplifications, the wheelset is treated as a distributed parameter system as well as a lumped parameter system. The

analysis based on the distributed parameter model of the wheelset studies the possible torsional natural modes and their responses to the external torque. The lumped parameter system is developed to consider only the primary torsional mode for the controller design. The two different models of a wheelset are presented and compared, and the analysis shows the consistency of these two models. The significance to clarify the torsional natural modes of the wheelset will become clear in the study of wheelset dynamics in different contact conditions, and further re-adhesion controller development.

3.1 Wheel Rail Contact Laws

Tractive forces of a railway vehicle come from the wheel rail rolling contact. Figure 3.2 shows a wheelset standing on straight rails [15]. The coordinate system *oxyz* moves synchronously with the wheelset: origin *o* is constrained along the central line of the track; the *x*-axis points along the rails in the rolling direction also known as longitudinal direction; the *y*-axis, lateral direction, is 90° lag to complete a right-hand coordinated system; the *z*-axis points vertically upwards. The angular displacement of the wheelset about oz is denoted by the yaw angle ϕ_w, positive anti-clockwise, the correspond velocity is $\dot{\phi}_w$.Let the lateral displacement of the wheelset be denoted by y_w, and then the lateral velocity is $\dot{y}_w$. Track irregularity, also introduces a displacement y_t to the vehicle in the lateral direction, hence velocity $\dot{y}_t$. v is defined as the forward speed of the vehicle. Usually, the track input to the vehicle from the track can be defined in terms of four variables: vertical profile, cross level, lateral alignment and gauge, and can be presented in the form of spectral densities which can be used as inputs to mathematical models [1].

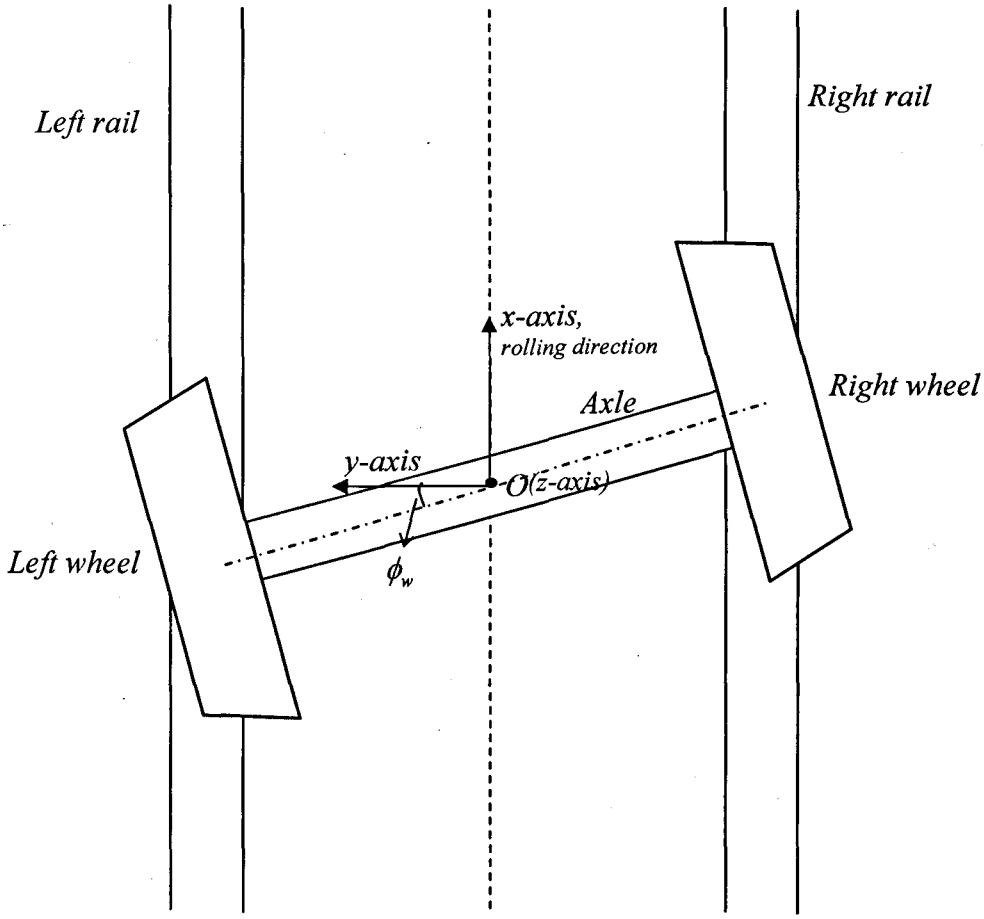

Figure 3.2 Wheelset standing on the rails

3.1.1 Creepage in Longitudinal Direction

The longitudinal creepage depends on whether the left or the right wheel is considered. As shown in Figure 3.3 , a wheelset is depicted by a rigid double cone; the rails are modeled by two parallel cones $2L_g$ apart [15]. The conicity of each wheel is denoted by angle γ.

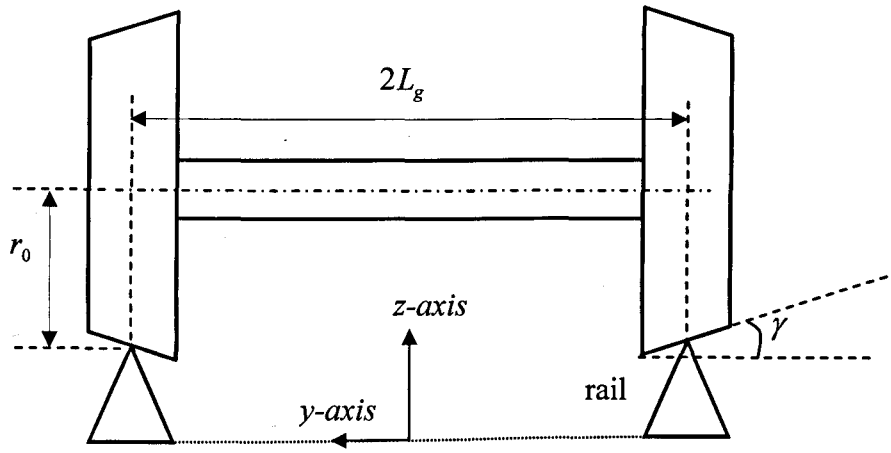

Figure 3.3 Wheelset as a double cone on the cone rails

The radius of each wheel at the center position where $y = 0$ is r_0, so the contact radius of left and right wheels can be given as:

$$Left \quad wheel: \; r_l = r_0 + \gamma(y_w - y_t) \tag{3.1}$$

$$Right\ wheel: \; r_r = r_0 - \gamma(y_w - y_t) \tag{3.2}$$

Considering that the vehicle operates along a straight line, the equivalent linear speed of each wheel is

$$Left \quad wheel: \; v_{wl} = \omega_l \cdot r_l \tag{3.3}$$

$$Right \quad wheel: \; v_{wr} = \omega_r \cdot r_r \tag{3.4}$$

where, ω_l is the angular velocity of the left wheel, and ω_r is the angular velocity of the right wheel.

Based on the definition of longitudinal creepage given in equation (1.1), the basic longitudinal creepages of the two wheels are:

$$Left \quad wheel: \lambda_{xl\_1} = \frac{v_{wl} - v}{v} \tag{3.5}$$

$$Right \quad wheel: \lambda_{xr\_1} = \frac{v_{wr} - v}{v} \tag{3.6}$$

Besides, the yaw movement will contribute to the longitudinal creepages in opposite direction for the two wheels:

$$Left \quad wheel: \lambda_{xl\_2} = \frac{L_g \dot{\phi}_w}{v} \tag{3.7}$$

$$Right \quad wheel: \lambda_{xr\_2} = -\frac{L_g \dot{\phi}_w}{v} \tag{3.8}$$

So the resultant longitudinal creepages of the two wheels are:

$$Left \quad wheel: \lambda_{xl} = \frac{v_{wl} - v}{v} + \frac{L_g \dot{\phi}_w}{v} \tag{3.9}$$

$$Right \quad wheel: \lambda_{xr} = \frac{v_{wr} - v}{v} - \frac{L_g \dot{\phi}_w}{v} \tag{3.10}$$

or

$$\lambda_{xl} = \frac{\omega_l r_o - v}{v} + [\frac{L_g \dot{\phi}_w}{v} - \frac{\omega_l \gamma (y_w - y_t)}{v}] \tag{3.11}$$

$$\lambda_{xr} = \frac{\omega_r r_o - v}{v} - [\frac{L_g \dot{\phi}_w}{v} - \frac{\omega_r \gamma (y_w - y_t)}{v}] \tag{3.12}$$

3.1.2 Creepage in Lateral Direction

The creepage in lateral direction λ_y is formed by two parts [15]. The first part is contributed by the relative lateral velocity of the center of the wheelset along lateral direction. The second part is caused by the yaw movement. So the resultant λ_y is given as

$$\lambda_y = \frac{\dot{y}_w}{v} - \frac{\dot{y}_t}{v} - \phi_w \tag{3.13}$$

Normally, $\frac{\dot{y}_t}{v}$ is ignored when considering lateral creepage in practice. Thus the lateral creepage of the wheels is

$$\lambda_y = \frac{\dot{y}_w}{v} - \phi_w \tag{3.14}$$

3.1.3 Creep Forces and Dynamics

The creep forces of both wheels are given as

$$F_{tl} = \mu_l \cdot N \tag{3.15}$$

$$F_{tr} = \mu_r \cdot N \tag{3.16}$$

where N is the normal force of the wheel, F_{tl} and F_{tr} are the creep forces of left wheel and right wheel respectively; μ_l and μ_r are the creep force coefficients of left wheel and right wheel respectively.

As introduced in Chapter 1, the relationship between creep force ratio μ and creepage λ can be described through slip curves as show in Figure 1.5. In the curve, the creepage λ is the resultant value combined of longitudinal and lateral creepages [64][21]:

$$\lambda = \sqrt{\lambda_y^2 + \lambda_x^2} \tag{3.17}$$

From the contact forces F_{tl} and F_{tr}, their components along longitudinal and lateral directions can be given as:

$$F_{tl\_x} = F_{tl} \cdot \frac{\lambda_{lx}}{\sqrt{\lambda_y^2 + \lambda_{lx}^2}} \tag{3.18}$$

$$F_{tl\_y} = F_{tl} \cdot \frac{\lambda_y}{\sqrt{\lambda_y^2 + \lambda_{lx}^2}} \tag{3.19}$$

$$F_{tr\_x} = F_{tr} \cdot \frac{\lambda_{rx}}{\sqrt{\lambda_y^2 + \lambda_{rx}^2}} \tag{3.20}$$

$$F_{tr\_y} = F_{tr} \cdot \frac{\lambda_y}{\sqrt{\lambda_y^2 + \lambda_{rx}^2}} \tag{3.21}$$

where, F_{tl_x} and F_{tl_y} are the creep forces in the longitudinal direction and lateral direction of the left wheel respectively, F_{tr_x} and F_{tr_y} are the creep forces in the longitudinal direction and lateral direction of the right wheel respectively,

The yaw motion of the wheelset is governed by

$$I_{ws}\ddot{\psi}_w = F_{tr\_x} \cdot L_g - F_{tl\_x} \cdot L_g - k_w \cdot \psi_w \tag{3.22}$$

where I_{ws} is the wheelset yaw inertia, k_w is yaw stiffness of the springs which connect the wheelset to the bogie.

The lateral dynamics are governed by

$$m_{ws}\ddot{y}_w = F_{tr\_y} + F_{tl\_y} + T_c + T_m \tag{3.23}$$

where, m_{ws} is the wheelset mass, T_c is the centrifugal force which is taken into account when the vehicle operates on a curve, T_m is the gravitational force component on a track with a cant angle.

The longitudinal dynamics of the vehicle are:

$$M_v\dot{v} = F_{tr\_x} + F_{tl\_x} \tag{3.24}$$

3.1.4 Simplification of the Wheelset Dynamics

For the re-adhesion control design which is focused primarily on the forward tractive performance, some assumptions are given in the initial stage of the dynamic study:

(1) Vehicle is accelerated along a straight and level track. So there is no T_m and T_c involved for the time being.

(2) The more dominant terms of the longitudinal creepage $\lambda_{xL} = \dfrac{\omega_l r_o - v}{v}$ and $\lambda_{xR} = \dfrac{\omega_r r_o - v}{v}$ are considered.

(3) As the longitudinal dynamics is the major concern, lateral and yaw dynamics are not included at this stage.

In the next two sections, the wheelset is simplified as a system of one shaft with two unequal end inertias, and only the longitudinal and rotational dynamics are considered. To treat the wheelset as a distributed parameter model aims to obtain its natural torsional modes. The dynamics response to the natural modes is also studied which shows the significance of the first order natural torsional mode.

3.2 Distributed Parameter Model of the Axle and Wheels

3.2.1 Natural Modes of the Wheelset

In this section, the wheelset is treated as a shaft having circular cross section with two end inertias as shown in Figure 3.4. In the traction system studied in this thesis, a driving motor is mounted on the right hand side of the wheelset, and hence inertias at the two ends are different.

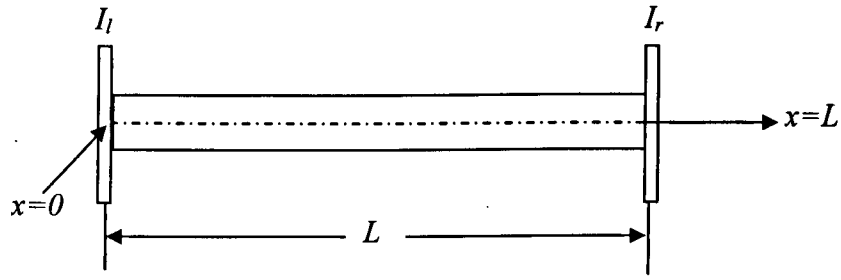

Figure 3.4 Distributed parameter wheelset

For the sake of simplification, it is assumed that only the torsional effects are present, and the shaft is made of homogeneous, isotropic and elastic material. The material variables of this wheelset model used in this section are given in Table 3.1:

Variables	Definitions
ρ	Density
G	Shear modulus
r	Shaft radius
L	Shaft length
$J=(\pi/2)r^4$	Polar moment of area of the shaft
I_l	Left end moment of inertia
I_r	Right end moment of inertia

Table 3.1 Material variables of the wheelset

The free vibration of the shaft is described by the partial differential equation [65]:

$$\rho J \frac{\partial^2 \theta(x,t)}{\partial t^2} = GJ \frac{\partial^2 \theta(x,t)}{\partial x^2} \tag{3.25}$$

where,

θ: angular rotation of shaft

Hence, the resultant problem is given as

$$\frac{\partial^2 \theta(x,t)}{\partial t^2} = \alpha^2 \frac{\partial^2 \theta(x,t)}{\partial x^2} \quad , \alpha = \sqrt{\frac{G}{\rho}} \tag{3.26}$$

The boundary conditions of each end are given separately [66].

On the left hand side, $x = 0$, $\tau_0(t)$ is the external torque acting at left end. For the wheelset studied, $\tau_0(t)$ is from the wheel rail creep force:

$$GJ \frac{\partial \theta(0,t)}{\partial x} + \tau_0(t) = I_l \frac{\partial^2 \theta(0,t)}{\partial t^2} \tag{3.27}$$

Equation (3.27) may be:

$$\frac{\partial \theta(0,t)}{\partial x} + f_0(t) = k_0 \frac{\partial^2 \theta(0,t)}{\partial t^2} \tag{3.28}$$

where, $k_0 = \frac{I_l}{GJ}$ and $f_0(t) = \frac{\tau_0(t)}{GJ}$

Substituting equation (3.26) into equation (3.28), gives:

$$\frac{\partial \theta(0,t)}{\partial x} + f_0(t) = \alpha^2 k_0 \frac{\partial^2 \theta(0,t)}{\partial x^2} \tag{3.29}$$

On the right hand side, $x = L$, $\tau_L(t)$ is the external torque acting at right end which is from the resultant effect of the driving torque from motor and creep force from wheel rail contact:

$$-GJ \frac{\partial \theta(L,t)}{\partial x} + \tau_L(t) = I_r \frac{\partial^2 \theta(L,t)}{\partial t^2} \tag{3.30}$$

Equation (3.30) maybe changed to:

$$-\frac{\partial \theta(L,t)}{\partial x} + f_L(t) = k_L \frac{\partial^2 \theta(L,t)}{\partial t^2} \tag{3.31}$$

where, $k_L = \frac{I_r}{GJ}$ and $f_L(t) = \frac{\tau_L(t)}{GJ}$

Substituting equation (3.26) into equation (3.31), gives:

$$-\frac{\partial\theta(L,t)}{\partial x}+f_L(t)=\alpha^2 k_L\frac{\partial^2\theta(L,t)}{\partial x^2} \tag{3.32}$$

To obtain the natural modes, the external torque is set to zero. The angular function is assumed and a solution is in the form [67]

$$\theta(x,t)=\sum_1^{\infty}\Theta_n(x)p_n(t)\quad(n=1,\cdots\infty) \tag{3.33}$$

For each components in the summation, introducing equation (3.33) to equation (3.25) and separating variables, gives

$$\frac{1}{\Theta_n(x)}\frac{d}{dx}\left[\alpha^2\frac{d\Theta_n(x)}{dx}\right]=\frac{1}{p_n(t)}\frac{d^2p_n(t)}{dt^2},\quad 0<x<L \tag{3.34}$$

or

$$\frac{\ddot{p}_n}{\alpha^2 p_n}=\frac{\Theta_n''}{\Theta_n}=-\beta_n^2 \tag{3.35}$$

where, $-\beta_n^2$ is the separation constant, and can be determined by equation (3.35) with the boundary conditions. There will be a set of infinite number of β values, which relate to the natural modes of the system.

The solutions are of the form

$$p_n(t)=A_n\cos(\alpha\beta_n t)+B_n\sin(\alpha\beta_n t) \tag{3.36}$$

$$\Theta_n(x)=C_n\cos(\beta_n x)+D_n\sin(\beta_n x) \tag{3.37}$$

Moreover, the boundary conditions under free load condition can be expressed in equations (3.38) and (3.39):

Left end $x=0$:

$$\frac{\partial\Theta_n(0,t)}{\partial x}=\alpha^2 k_0\frac{\partial^2\Theta_n(0,t)}{\partial x^2} \tag{3.38}$$

Right end $x=L$:

$$\frac{\partial\Theta_n(L,t)}{\partial x}=-\alpha^2 k_L\frac{\partial^2\Theta_n(L,t)}{\partial x^2} \tag{3.39}$$

Substituting $\Theta_n''=-\beta_n^2\Theta_n$ to the boundary conditions, it gives:

Left end $x=0$:

$$\frac{\partial\Theta_n(0,t)}{\partial x}=-\alpha^2 k_0\beta_n^2\Theta_n(0,t) \tag{3.40}$$

Right end $x = L$:

$$\frac{\partial \Theta_n(L,t)}{\partial x} = \alpha^2 k_L \beta_n^2 \Theta_n(L,t) \tag{3.41}$$

It is obvious that these boundary conditions depend on the eigenvalues β_n.

From the $\Theta_n(x)$ form in equation (3.36), its first derivative is:

$$\Theta'(x) = -\beta_n C_n \sin \beta_n x + \beta_n D_n \cos \beta_n x \tag{3.42}$$

Combining equation (3.42) with the boundary conditions, it can be obtained

$$\frac{C_n}{D_n} = -\frac{1}{\alpha^2 k_0 \beta_n} \tag{3.43}$$

$$\tan(\beta_n L) = \frac{\alpha^2 (k_0 + k_L)\beta_n}{\alpha^4 k_0 k_L \beta_n^2 - 1} \tag{3.44}$$

Then the eigenvalues β_n can be obtained graphically as shown in Figure 3.5 [66]. The intersection of curve 1: $y = \tan(\beta_n L)$ and curve 2: $y = \frac{\alpha^2 (k_0 + k_L)\beta_n}{\alpha^4 k_0 k_L \beta_n^2 - 1}$ determines corresponding β_n, and the natural frequencies (in Hz) is given as

$$f_n = \frac{\alpha \beta_n}{2\pi} \tag{3.45}$$

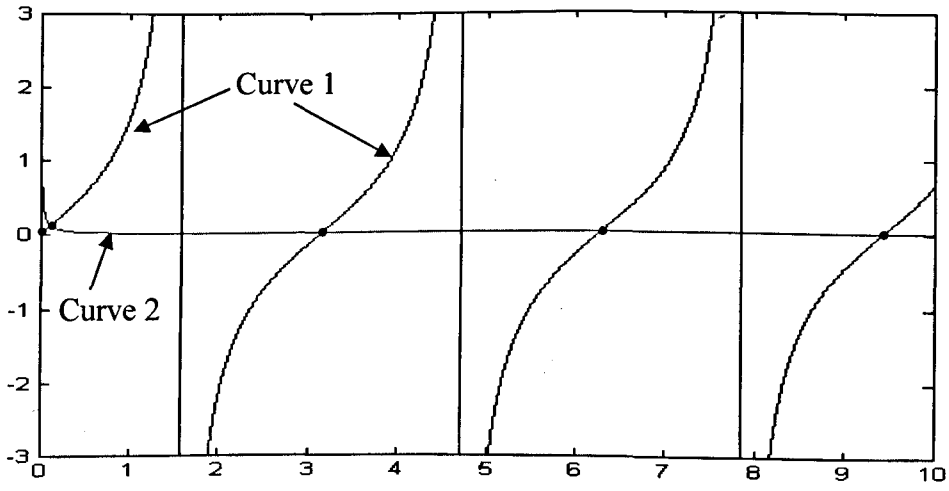

Figure 3.5 Eigenvalue distribution

The resonant frequency of the axle torsional mode in railway vehicle typically ranges between $40-80$ Hz [23]. Here, a wheelset system with natural torsional mode of middle 60 Hz is studied. According to [68], [69], a set of shaft parameters and end inertias are given in Table 3.2 which results in a 60 Hz wheelset shaft. Changing the shaft radius to a lower value leads to a less stiff shaft if the other parameters are kept the same.

Variables	Definitions and values
ρ	Density (7.8×10^3 kg/m^3)
G	Shear modulus (80.77 Gpa)
r	Shaft radius (0.09 m)
l	Shaft length (1.435 m)
$J=(\pi/2)r^4$	Polar moment of area of the shaft
I_l	Left end moment of inertia (62.8 kgm^2)
I_r	Right end moment of inertia (133.2 kgm^2)

Table 3.2 parameters of the 60 Hz wheelset system

The eigenvalues need to be determined. The first ten β_n s obtained graphically are:

$$\begin{bmatrix}0 & 0.1169 & 2.1955 & 4.3848 & 6.5740\\ 8.7633 & 10.9530 & 13.1420 & 15.3310 & 17.5200\end{bmatrix} \tag{3.46}$$

The corresponding natural frequencies (in Hz) of the system are:

$$\begin{bmatrix}0 & 60 & 1.12\times10^3 & 2.24\times10^3 & 3.37\times10^3\\ 4.49\times10^3 & 5.60\times10^3 & 6.73\times10^3 & 7.85\times10^3 & 8.97\times10^3\end{bmatrix} \tag{3.47}$$

So the first torsional natural frequency of this shaft system is 60 Hz. The first ten Θ_n s are given in the form

$$\Theta_n(x)=\cos(\beta_n x)-\alpha^2 k_0\beta_n\sin(\beta_n x) \tag{3.48}$$

3.2.2 Dynamic Response to External Torque

Firstly, no external torque is considered, and $z(x,t)$ satisfies

$$\frac{\partial^2 z}{\partial t^2} = \alpha^2 \frac{\partial^2 z}{\partial x^2} + g(x,t) \tag{3.49}$$

Let $g(x,t)$ can be expanded using $\Theta_n(x)$

$$g(x,t) = \sum_1^\infty \Theta_n(x) g_n(t) \tag{3.50}$$

From equation (3.35), the final dynamic expression for $p_n(t)$ under (3.49) condition will be

$$\ddot{p}_n = -\beta_n^2 \alpha^2 p_n + g_n(t) \tag{3.51}$$

To seek the solutions when considering external input, it is to find functions $h_0(x)$ and $h_L(x)$ such that [67]

$$z(x,t) = \theta(x,t) + h_0(x) f_0(t) + h_L(x) f_L(t) \tag{3.52}$$

and it is required

$$\frac{\partial^2 \theta(x,t)}{\partial t^2} = \alpha^2 \frac{\partial^2 \theta(x,t)}{\partial x^2} \tag{3.53}$$

Hence

$$\frac{\partial^2 z}{\partial t^2} = \alpha^2 \frac{\partial^2 z}{\partial x^2} + \underbrace{(-\alpha^2 h_0'' f_0 + h_0 \ddot{f}_0 - \alpha^2 h_L'' f_L + h_L \ddot{f}_L)}_{g(x,t)} \tag{3.54}$$

To satisfy the boundary conditions

$$k_0 \left.\frac{\partial^2 z}{\partial t^2}\right|_{x=0} = \left.\frac{\partial z}{\partial x}\right|_{x=0} \tag{3.55}$$

$$k_L \left.\frac{\partial^2 z}{\partial t^2}\right|_{x=L} = -\left.\frac{\partial z}{\partial x}\right|_{x=L} \tag{3.56}$$

the following conditions need to be met

$$h_0'(0) f_0(t) + h_L'(0) f_L(t) - k_0 h_0(0) \ddot{f}_0(t) - k_0 h_L(0) \ddot{f}_L(t) = f_0(t) \tag{3.57}$$

and

$$-h_0'(l) f_0(t) - h_L'(L) f_L(t) - k_L h_0(L) \ddot{f}_0(t) - k_L h_L(L) \ddot{f}_L(t) = f_L(t) \tag{3.58}$$

If the initial conditions are zero which are $\theta(x,0)=0$ and $\left.\frac{\partial\theta}{\partial t}\right|_{t=0}=0$, it gives

$$z(x,0)=h_0(x)f_0(0)+h_L(x)f_L(0)=\sum_1^\infty p_n(0)\theta_n(x) \tag{3.59}$$

$$\left.\frac{\partial z}{\partial t}\right|_{t=0}=h_0(x)\dot{f}_0(0)+h_L(x)\dot{f}_L(0)=\sum_1^\infty \dot{p}_n(0)\theta_n(x) \tag{3.60}$$

Since $f_0(t)$ and $f_L(t)$ are independent of each other, and in general there is no constraint on these functions and their derivatives, we must have $h_0(0)=0, h_0'(0)=1, h_0(L)=0, h_0'(L)=0$, $h_L(0)=0, h_L'(0)=0, h_L(L)=0, h_L'(L)=-1$. It is also required that $h_0''(0)=0$, $h_0''(L)=0$, $h_L''(0)=0$ and $h_L''(L)=0$ later. To satisfy these conditions, $h_0(x)$ and $h_L(x)$ can be given as

$$h_0(x)=x-\frac{6x^3}{L^2}+\frac{8x^4}{L^3}-\frac{3x^5}{L^4} \tag{3.61}$$

and

$$h_l(x)=-(x-L)+\frac{6(x-L)^3}{L^2}+\frac{8(x-L)^4}{L^3}+\frac{3(x-L)^5}{L^4} \tag{3.62}$$

These give one group of descriptions how the external torque effects distribute along the shaft, and these can be expanded using $\Theta_n(x)$.

In equation (3.36), $\Theta_n(x)$ is in the form

$$\Theta_n(x)=C_n\cos(\beta_n x)+D_n\sin(\beta_n x) \tag{3.63}$$

In general, it is set $C_n=1$, $n=1,2\ldots$, and then the boundary condition gives $D_n=-\alpha^2 k_0\beta_n$. Defining

$$\langle\Theta_n,\Theta_m\rangle=\int_0^L\Theta_n(x)\Theta_m(x)dx=-\frac{1}{\beta_m^2}\int_0^L\Theta_n(x)\Theta_m''(x)dx \tag{3.64}$$

Integrating by parts twice (when $n\neq m$):

$$\begin{aligned}&(1-\frac{\beta_n^2}{\beta_m^2})\langle\Theta_n,\Theta_m\rangle\\&=-\frac{1}{\beta_m^2}[\Theta_n(L)\Theta_m'(L)-\Theta_n(0)\Theta_m'(0)-\Theta_n'(L)\Theta_m(L)+\Theta_n'(0)\Theta_m(0)]\end{aligned} \tag{3.65}$$

Using the boundary conditions (3.40) and (3.41), equation (3.65) becomes

$$\langle\Theta_n,\Theta_m\rangle=-\alpha^2(k_L\Theta_n(L)\Theta_m(L)+k_0\Theta_n(0)\Theta_m(0)),\quad m\neq n \tag{3.66}$$

Even though $\Theta(x)$ is not orthogonal, a function $h(x)$ can still be expanded in the form

$$h(x)=\sum_{n=1}^{\infty}\gamma_n\Theta_n(x)=\sum_{n\neq m}\gamma_n\Theta_n(x)+\gamma_m\Theta_m(x) \tag{3.67}$$

Then

$$\langle h,\Theta_m\rangle=\sum_{n\neq m}\gamma_n\langle\Theta_m,\Theta_n\rangle+\gamma_m\langle\Theta_m,\Theta_m\rangle \tag{3.68}$$

Using equation (3.66)

$$\langle h,\Theta_m\rangle=-\alpha^2k_l\Theta_m(L)\sum_{n\neq m}\gamma_n\Theta_n(L)-\alpha^2k_0\Theta_m(0)\sum_{n\neq m}\gamma_n\Theta_n(0)+\gamma_m\langle\Theta_m,\Theta_m\rangle \tag{3.69}$$

Using (3.67), and evaluated at $x=0$ and $x=L$,

$$\begin{aligned}&\langle h,\Theta_m\rangle\\&=-\alpha^2k_l\Theta_m(L)(h(L)-\gamma_m\Theta_m(L))-\alpha^2k_0\Theta_m(0)(h(0)-\gamma_m\Theta_m(0))+\gamma_m\langle\Theta_m,\Theta_m\rangle\end{aligned} \tag{3.70}$$

Solving for γ_m, it gives

$$\gamma_m=\frac{\langle h,\Theta_m\rangle+\alpha^2(k_l\Theta_m(L)h(L)+k_0\Theta_m(0)h(0))}{\|\Theta_m\|^2} \tag{3.71}$$

where

$$\|\Theta_m\|^2=\langle\Theta_m,\Theta_m\rangle+\alpha^2(k_L\Theta_m(L)^2+k_0\Theta_m(0)^2) \tag{3.72}$$

Let

$$h_0(x)=\sum_{1}^{\infty}a_n\Theta_n(x) \tag{3.73}$$

$$h_0''(x)=\sum_{1}^{\infty}c_n\Theta_n(x) \tag{3.74}$$

$$h_L(x)=\sum_{1}^{\infty}b_n\Theta_n(x) \tag{3.75}$$

$$h_L''(x)=\sum_{1}^{\infty}b_n\Theta_n(x) \tag{3.76}$$

Using (3.71) and the boundary restrictions of $h_0(x)$ and $h_l(x)$, a_n and b_n are given

$$a_n=\frac{\langle h_0,\Theta_n\rangle}{\|\Theta_n\|^2} \tag{3.77}$$

$$b_n=\frac{\langle h_L,\Theta_n\rangle}{\|\Theta_n\|^2} \tag{3.78}$$

Also

$$c_n = \frac{\langle h_0'', \Theta_n \rangle + \alpha^2 (k_L \Theta_m(L) h_0''(L) + k_0 \Theta_m(0) h_0''(0))}{\|\Theta_n\|^2} \tag{3.79}$$

$$d_n = \frac{\langle h_L'', \Theta_n \rangle + \alpha^2 (k_L \Theta_m(L) h_l''(L) + k_0 \Theta_m(0) h_L''(0))}{\|\Theta_n\|^2} \tag{3.80}$$

By setting $h_0''(0) = 0$, $h_0''(L) = 0$, $h_L''(0) = 0$ and $h_L''(L) = 0$, the expressions of c_n and d_n will be made simple, and those are met by equations (3.61) and (3.62). Then it gives

$$c_n = -\left(\frac{\Theta_n(0) + \beta_n{}^2 \langle h_0, \Theta_n \rangle}{\|\Theta_n\|^2} \right) \tag{3.81}$$

$$d_n = -\left(\frac{\Theta_n(L) + \beta_n{}^2 \langle h_L, \Theta_n \rangle}{\|\Theta_n\|^2} \right) \tag{3.82}$$

Substituting the expansions into $g(x,t)$ in equation (3.54), it gives

$$g(x,t) = \sum_1^\infty (-\alpha^2 (c_n f_0(t) + d_n f_L(t)) + (a_n \ddot{f}_0(t) + b_n \ddot{f}_L(t)) \Theta_n(x) \tag{3.83}$$

Let the Laplace transform of $p_n(t)$ be $P_n(s)$. Then equation (3.51) is transformed to

$$\begin{aligned} s^2 P_n(s) - s p_n(0) - \dot{p}_n(0) &= -\alpha^2 \beta_n^2 P_n(s) - \alpha^2 (c_n F_0(s) + d_n F_L(s)) \\ &+ s^2 (a_n F_0(s) + b_n F_L(s)) - s(a_n f_0(0) + b f_L(0)) - (a_n \dot{f}_0(0) + b \dot{f}_L(0)) \end{aligned} \tag{3.84}$$

But

$$p_n(0) = a_n f_0(0) + b_n f_L(0) \tag{3.85}$$

and

$$\dot{p}_n(0) = a_n \dot{f}_0(0) + b_n \dot{f}_L(0) \tag{3.86}$$

Hence

$$P_n(s) = \frac{s^2}{s^2 + \alpha^2 \beta_n^2} (a_n F_0(s) + b_n F_L(s)) - \frac{\alpha^2}{s^2 + \alpha^2 \beta_n^2} (c_n F_0(s) + d_n F_L(s)) \tag{3.87}$$

Rearrange equation (3.87), it gives

$$P_n(s) = (1 - \frac{\alpha^2 \beta_n^2}{s^2 + \alpha^2 \beta_n^2})(a_n F_0(s) + b_n F_L(s)) - \frac{\alpha^2}{s^2 + \alpha^2 \beta_n^2} (c_n F_0(s) + d_n F_L(s)) \tag{3.88}$$

Using

$$\theta(x,s) = \sum_1^\infty \Theta_n(x) P_n(s) - h_0(x) F_0(s) - h_L(x) F_L(s) \tag{3.89}$$

and $f_0(t)=\frac{\tau_0(t)}{GJ}$, $f_l(t)=\frac{\tau_L(t)}{GJ}$, it is obtained

$$\theta(x,s)=\sum_1^{\infty}-\frac{1}{J\rho}\left(\frac{c_n+\beta_n^2 a_n}{s^2+\alpha^2\beta_n^2}\tau_0(s)+\frac{d_n+\beta_n^2 b_n}{s^2+\alpha^2\beta_n^2}\tau_L(s)\right)\Theta_n(x) \tag{3.90}$$

Finally using (3.77) and (3.81)

$$\theta(x,s)=\frac{1}{J\rho}\sum_1^{\infty}\left(\frac{\Theta_n(0)}{\|\Theta_n\|^2}\frac{\tau_0(s)}{s^2+\alpha^2\beta_n^2}+\frac{\Theta_n(L)}{\|\Theta_n\|^2}\frac{\tau_L(s)}{s^2+\alpha^2\beta_n^2}\right)\Theta_n(x) \tag{3.91}$$

Based on the 60 Hz wheelset which is introduced in the last section, the dynamic response is studied considering the first ten modes given in equation (3.48). Since the higher order modes are out the frequency range of interest. Using equation (3.91), the general solution is given as

$$\begin{aligned}\theta(x,s)&\approx\frac{1}{J\rho}\sum_1^{10}\left(\frac{\Theta_n(0)}{\|\Theta_n\|^2}\frac{\tau_0(s)}{s^2+\alpha^2\beta_n^2}+\frac{\Theta_n(L)}{\|\Theta_n\|^2}\frac{\tau_L(s)}{s^2+\alpha^2\beta_n^2}\right)\Theta_n(x)\\&=\sum_1^{10}\left(\frac{\varphi_{n0}}{s^2+\alpha^2\beta_n^2}\tau_0(s)+\frac{\varphi_{nL}}{s^2+\alpha^2\beta_n^2}\tau_L(s)\right)\Theta_n(x)\end{aligned} \tag{3.92}$$

The first ten φ_{n0} s and φ_{nL} s are given in Table 3.3.

φ_{n0}	φ_{nL}
0.0050694	0.0050694
0.0107082	-0.0050642
0.0000220	0.0000103
0.0000055	-0.0000106
0.0000024	0.0000082
0.0000014	-0.0000066
0.0000009	0.0000055
0.0000006	-0.0000046
0.0000004	0.0000040
0.0000003	-0.0000035

Table 3.3 First ten φ_{n0} and φ_{nL} values

It shows that the major effective modes are the first two. Even the third one has little effect on the dynamics. The first one, zero mode, describes the constant torsional angle and fixing distributions along the shaft. The second one is the major torsional mode which is considered in the lumped parameter model.

3.3 Lumped Parameter Model of a Wheelset

From the analysis of the wheelset dynamics using distributed parameter model, it is shown that only the linear and the first torsional modes of the wheelset are the primary dynamics motions. Therefore, a simplified lumped parameter system will make it easier for slip dynamic study and further controller design.

3.3.1 Lumped Parameter Model

In the lumped parameter model of the wheelset, the shaft is considered as a spring with finite torsional stiffness k_s as shown in Figure 3.6.

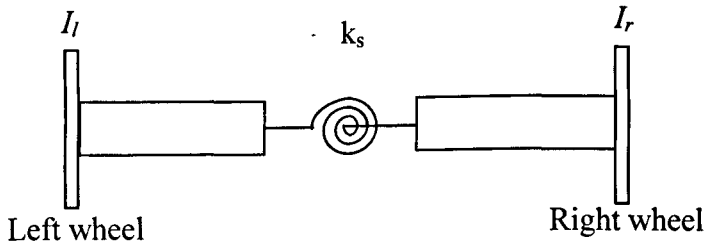

Figure 3.6 Lumped parameter wheelset

The right wheel is driven directly by an induction motor, and its dynamics are given as

$$T_m - T_s - T_{tr} = I_r \frac{d\omega_r}{dt} \tag{3.93}$$

where T_m is the driving torque fed by the induction motor, T_s is the torsional torque along the shaft, T_{tr} is the tractive torque contributed by the wheel-rail contact force on the right hand side, and ω_r is the angular velocity of the right wheel.

The left wheel is driven by the torsional torque,

$$T_s - T_{tl} = I_l \frac{d\omega_l}{dt} \tag{3.94}$$

where T_{tl} is the tractive torque from the wheel-rail contact on the left hand side, and ω_l is the angular velocity of the left wheel.

The torsional torque along the shaft is determined by the difference in rotation between the two wheels

$$T_s = k_s \int(\omega_r - \omega_l)dt + C(\omega_r - \omega_l) \tag{3.95}$$

where C is the material damping of the shaft, usually very small, and considered as zero in the following analysis if not specially indicated.

The vehicle is driven by the total tractive effort:

$$M_v \frac{dv_v}{dt} = (T_{tr} + T_{tl}) \Big/ r_0 \tag{3.96}$$

where r_0 is the wheel radius, and v_v is the forward vehicle speed.

Choosing state variable as $\mathbf{x} = [\omega_r \ \omega_l \ \theta_s]^T$, where $\theta_s = \int(\omega_r - \omega_l)dt$, then the system can be described as:

$$\begin{bmatrix} \dot{\omega}_r \\ \dot{\omega}_l \\ \dot{\theta}_s \end{bmatrix} = \underbrace{\begin{bmatrix} 0 & 0 & -\frac{k_s}{I_r} \\ 0 & 0 & \frac{k_s}{I_l} \\ 1 & -1 & 0 \end{bmatrix}}_{A_1} \begin{bmatrix} \omega_r \\ \omega_l \\ \theta_s \end{bmatrix} + \underbrace{\begin{bmatrix} \frac{1}{I_r} \\ 0 \\ 0 \end{bmatrix}}_{B_1} T_m + \underbrace{\begin{bmatrix} -\frac{1}{I_r} & 0 \\ 0 & -\frac{1}{I_l} \\ 0 & 0 \end{bmatrix}}_{C_1} \begin{bmatrix} T_{tr} \\ T_{tl} \end{bmatrix} \tag{3.97}$$

The torsional natural frequency can be found using

$$f_n = \frac{1}{2\pi} \sqrt{k_s \frac{I_l + I_r}{I_l I_r}} \tag{3.98}$$

3.3.2 Comparisons of Two Wheelset Models

Comparisons of a 60 Hz wheelset are carried out as follows to show the consistency of the distributed parameter model and the lumped parameter model. The end inertias of both models are the same. For numerical comparisons, the results of the left wheel dynamics are given. Similar outcome can be obtained for the right wheel.

From the mathematical descriptions of the lumped parameter model, the left wheel rotational speed is given as

$$\omega_{l\_Lumped}(s) = -\frac{I_r s^2 + k_s}{s[I_l I_r s^2 + k_s(I_l + I_r)]} T_{tl} + \frac{k_s}{s[I_l I_r s^2 + k_s(I_l + I_r)]}(T_m - T_{tr}) \tag{3.99}$$

or

$$\omega_{l\_Lumped}(s) = -\frac{\frac{1}{I_l} s^2 + \frac{k_s}{I_l I_r}}{s[s^2 + \frac{k_s(I_l + I_r)}{I_l I_r}]} T_{tl} + \frac{\frac{k_s}{I_l I_r}}{s[s^2 + \frac{k_s(I_l + I_r)}{I_l I_r}]}(T_m - T_{tr}) \tag{3.100}$$

For the distributed parameter model of the wheelset, only considering the first two modes, the left wheel rotational speed, which is the derivative of its left end angular displacement, is given as

$$\omega_{(x=0)\_Distributed}(s) = s\sum_{1}^{2}\left(\frac{\varphi_{n0}}{s^2 + \alpha^2\beta_n^2}\tau_0(s) + \frac{\varphi_{nL}}{s^2 + \alpha^2\beta_n^2}\tau_L(s)\right)\Theta_n(0) \tag{3.101}$$

That is

$$\begin{aligned}\omega_{(x=0)\_Distributed}(s) = &\frac{[\varphi_{01}\Theta_1(0) + \varphi_{02}\Theta_2(0)]s^2 + \alpha^2\beta_2^2\varphi_{01}\Theta_1(0)}{s[s^2 + \alpha^2\beta_2^2]}\tau_0 \\ &+ \frac{[\varphi_{L1}\Theta_1(0) + \varphi_{L2}\Theta_2(0)]s^2 + \alpha^2\beta_2^2\varphi_{L1}\Theta_1(0)}{s[s^2 + \alpha^2\beta_2^2]}\tau_L\end{aligned} \tag{3.102}$$

where, β_n is given in (3.46), φ_{n0} and φ_{nL} are given in Table 3.3, $\tau_0 = -T_{tl}$, and $\tau_L = T_m - T_{tr}$.

The data shown in Table 3.4 give the comparison of coefficients of the corresponding terms in equation (3.99) and (3.101). The relative errors of corresponding coefficients between the distributed model and lumped parameter

model are lower than 0.05%. The errors come from the calculation errors when obtaining the natural modes of the distributed parameter system.

Distributed parameter system	lumped parameter system
$\varphi_{01}\Theta_1(0)+\varphi_{02}\Theta_2(0)=0.0158$	$1/I_l$ =0.0159
$\alpha^2\beta_2^2\varphi_{01}\Theta_1(0)=717.3727$	$k_s/I_lI_r=721.98$
$\varphi_{L1}\Theta_1(0)+\varphi_{L2}\Theta_2(0)=0$	
$\alpha^2\beta_2^2\varphi_{L1}\Theta_1(0)=717.3727$	$k_s/I_lI_r=721.98$
$\sqrt{k_s(I_l+I_r)/I_lI_r}=376.17$	$\alpha\beta_2=376.17$

Table 3.4 Comparison of two wheelset models

Time history simulations are also carried out to compare these two models. Figure 3.7 shows a diagram of the lumped parameter model and Figure 3.8 shows that of the distributed parameter model.

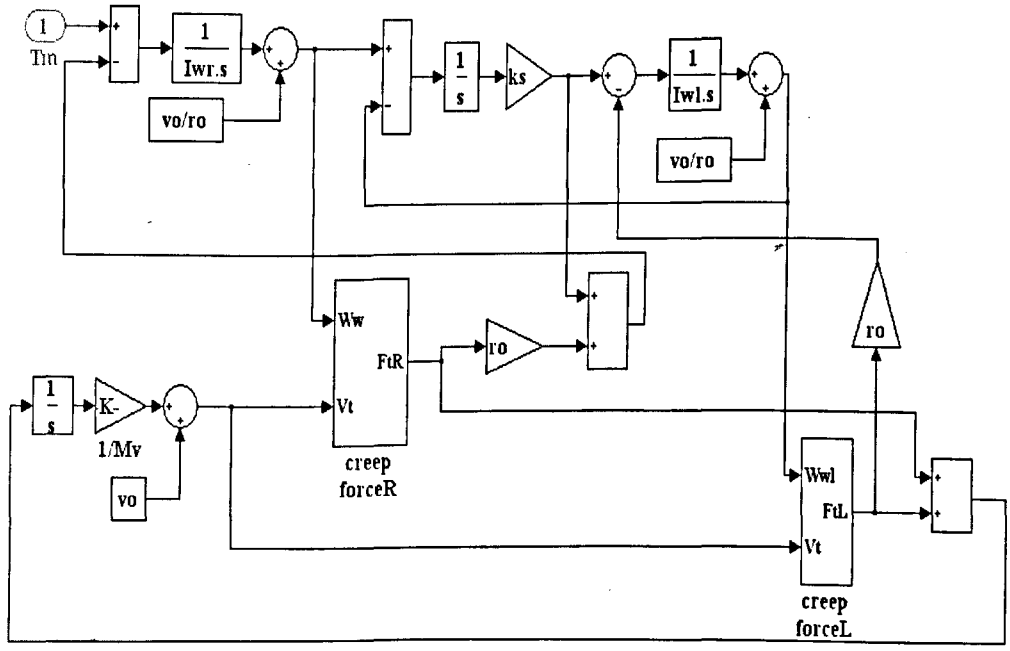

Figure 3.7 Simulation model of the wheelset as a lumped parameter model

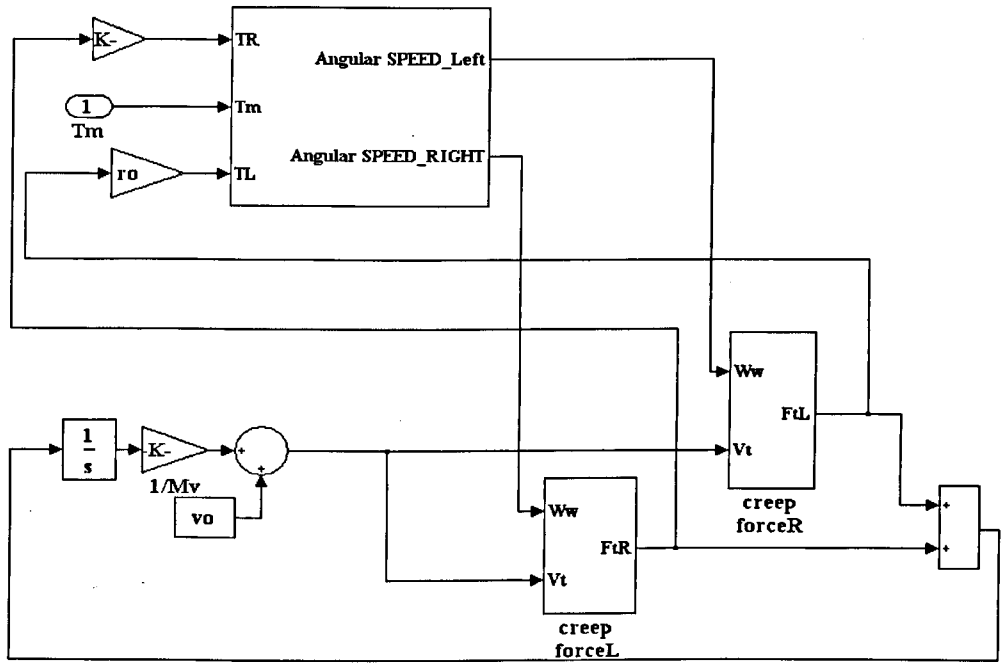

Figure 3.8 Simulation model of the wheelset as a distributed parameter model

The same driving torque is fed to the lumped parameter model and distributed parameter model respectively. The contact conditions are the same for both systems, and slips happen after $t = 4\,\mathrm{s}$. The right wheel and left wheel speeds are obtained from lumped parameter model and right end ($x = L$) and left end ($x = 0$) are calculated from distributed model for making comparisons.

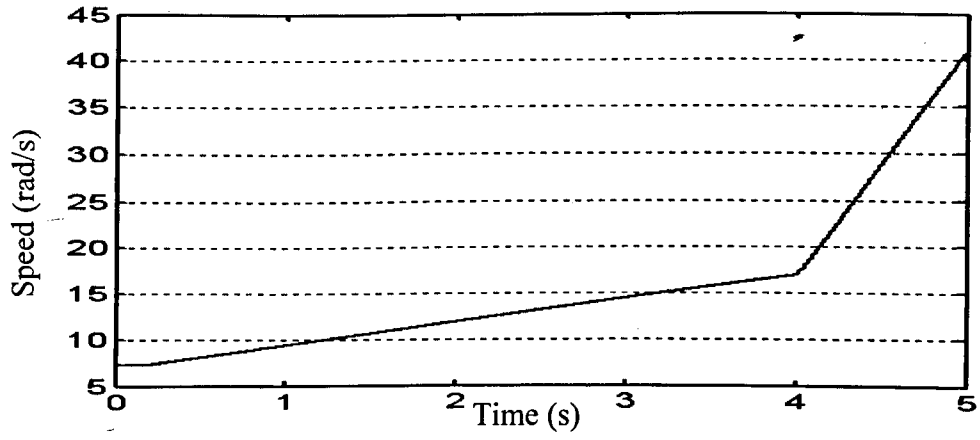

Figure 3.9 Wheel speeds from lumped model

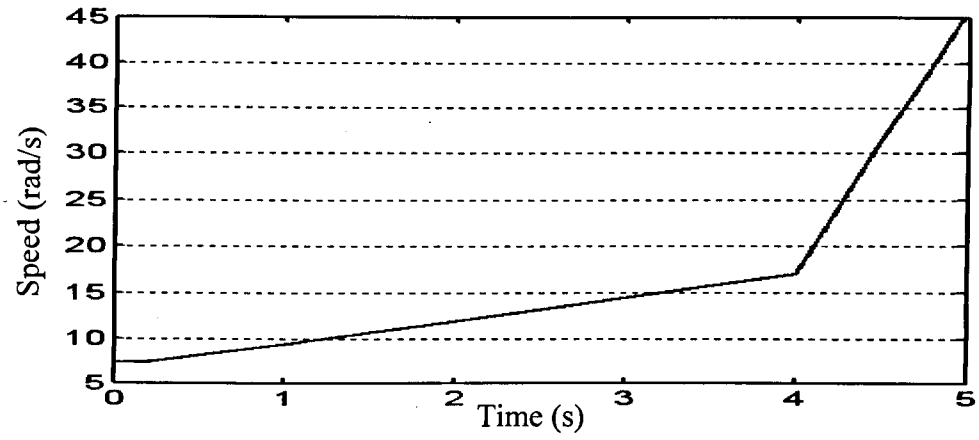

Figure 3.10 Wheel speeds from distributed model

Figure 3.9 and Figure 3.10 give the speeds from which it can be found that the speeds of both wheels are so close to each that they overlap each other. The results show that the dynamics of the two systems are close to each other in normal condition, where the difference is kept about 0.05%. After a slip occurs, the speed of the distributed parameter model increases faster than that of the lumped parameter model. It is because the negative slope of the contact slip curve expedites the reduction of creep force, thus even a small difference between the speeds at the beginning of slip occurrence will be widened when the speeds increase in the slip condition.

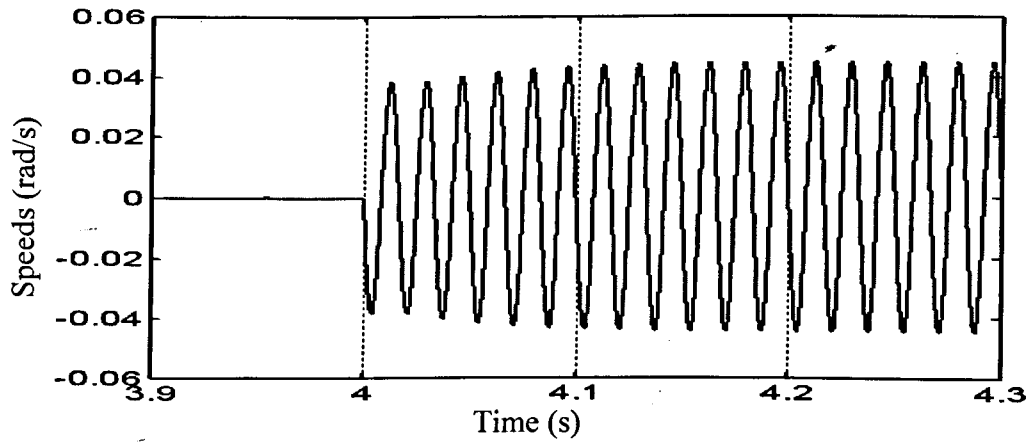

Figure 3.11 Wheel speed difference ($\omega_r - \omega_l$) from the lumped model

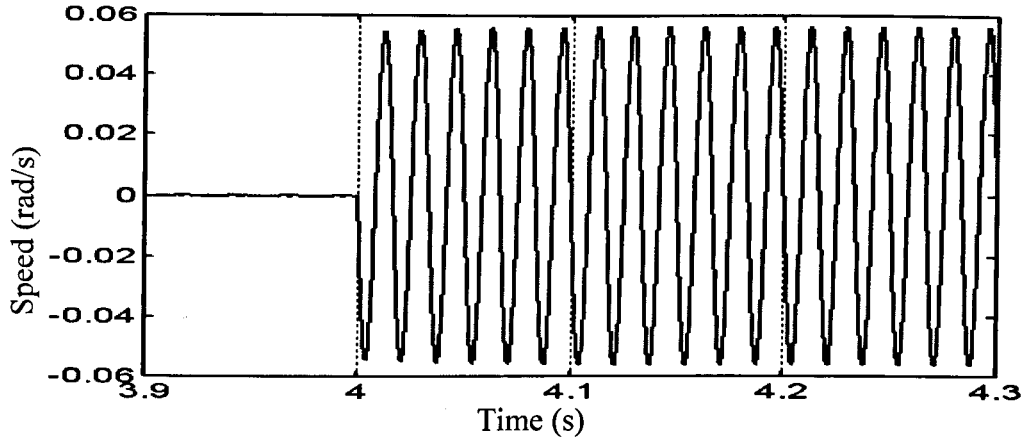

Figure 3.12 Wheel speed difference ($\omega_{x=L} - \omega_{x=0}$) from the distributed model

Figure 3.11 and Figure 3.12 give the speed differences between two end wheels from the lumped parameter system and distributed parameter system respectively. In both figures, there are oscillations when contact conditions are changed. The frequencies of the oscillation for both systems are the same, which is 60 Hz, but the oscillation from the distributed parameter model is of a higher magnitude than that of the lumped parameter model because of the higher creepage of the distributed parameter model.

3.4 Summary

In this chapter, the comprehensive wheelset model which contains longitudinal, lateral and yaw dynamics are introduced which will be used for the evaluation of the further developed re-adhesion scheme. Some simplifications are given to emphasize the forward tractive performance. Then a distributed parameter wheelset model is studied to find the possible torsional modes and followed by an introduction of a lumped parameter model which contains the rotational mode and the primary torsional mode. The comparisons of the distributed parameter model and the lumped parameter model of the wheelset show a high level of consistency. So the following dynamic study will focus on the lumped model of the wheelset which is adequate for the controller design.

4 ASSESSMENT OF WHEELSET DYNAMICS

Based on the lumped parameter model of the wheelset given in Chapter 3, the dynamics of the wheelsets with different natural torsional modes between 40-80 Hz are studied and compared in normal and slip conditions, which provides a basis for the proposed slip detection approach. In the end, eigenvalue distributions of different operation points are studied to show a vital link between the dynamics in slip conditions and the system stability.

4.1 Dynamics of the Wheelset Driven by an Induction Motor

4.1.1 Simulation Model of the Wheelset Driven by an Induction Motor

The diagram of the wheelset system driven by an induction motor is shown in Figure 4.1.

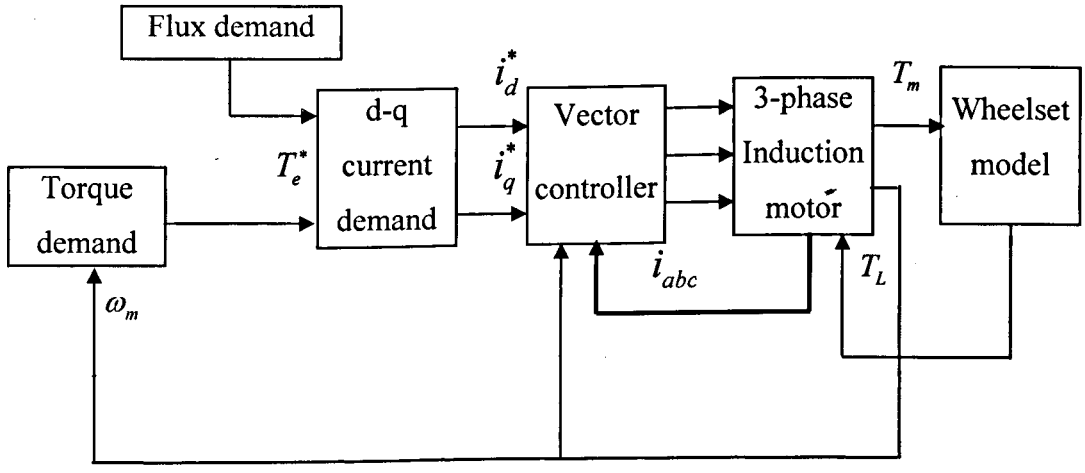

Figure 4.1 Diagram of the wheelset system driven by an induction motor

In this model, the electromagnetic torque produced by the induction motor is fed to the wheelset though a gearbox with gear ratio R_g :

$$T_m = T_e \cdot R_g \tag{4.1}$$

The motor is mounted on the right hand side of the shaft as introduced in Chapter 3, driving right wheel directly. So the load torque of the motor will be the sum of the tractive torque due to right hand side wheel rail contact and the torsional torque along the shaft divided by gear ratio:

$$T_L = (T_{tr} + T_s) / R_g \tag{4.2}$$

4.1.2 Demands and Parameters Used in the Simulation

The torque demand is designed in a manner as shown in Figure 4.2, which includes a jerk limited period. The jerk of the vehicle will be restricted within a certain service value which will not cause passenger discomfort [70]. In some papers and works, the upper limit of the jerk is suggested to set as 0.5 m/s^3 or 0.45 m/s^3 [71] [72]. After the jerk limited period, the torque demand is kept constant for a constant acceleration of the vehicle. When the speed exceeds the base speed, the torque is reduced inversely to the speed which lies in the constant power region for further speed increasing until the vehicle reaches its expected operation speed.

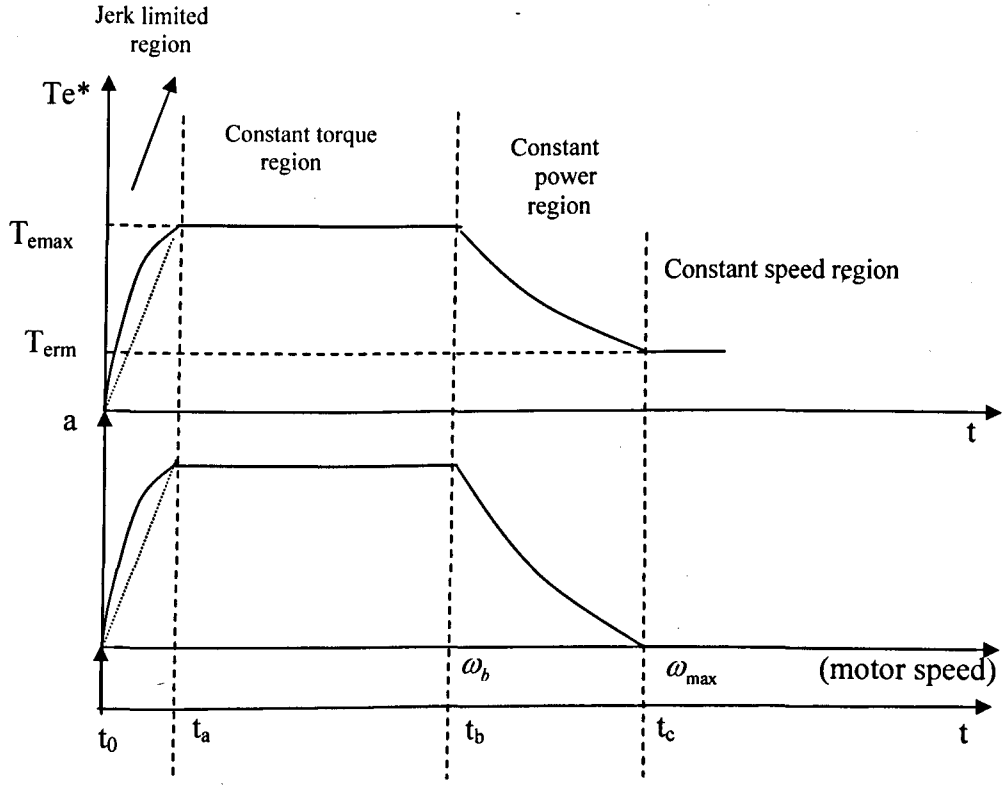

Figure 4.2 Torque demand profile

In Figure 4.2, the torque demand is divided into four different regions in the time sequence:

(1) $t_0 \sim t_a$: jerk limited region.

(2) $t_a \sim t_b$: constant torque region, hence constant vehicle acceleration until driving motor reaches its base speed ω_b ;

(3) $t_b \sim t_c$: constant power region, torque demand decreased inversely proportional to the motor speed until the motor reaches it maximum speed $\omega_{\max}$, maximum power $P = T_{e\max} \cdot \omega_b = T_{erm} \cdot \omega_{\max}$;

(4) $\geq t_c$: constant speed region, constant vehicle speed, and also constant motor speed.

In the simulations, a torque demand shown in Figure 4.3, is used unless specified otherwise. In Figure 4.3, t_0 is set as 1.5 s to give enough time for the flux building up to its demand value. There is $t_a - t_0 = 2$ s jerk limited period with the jerk value 0.38 m/s^3 . Usually t_0, t_a are kept fixed in the simulations, but t_b and t_c are varied according to different operation conditions. In constant torque region, the torque value is1500 Nm .

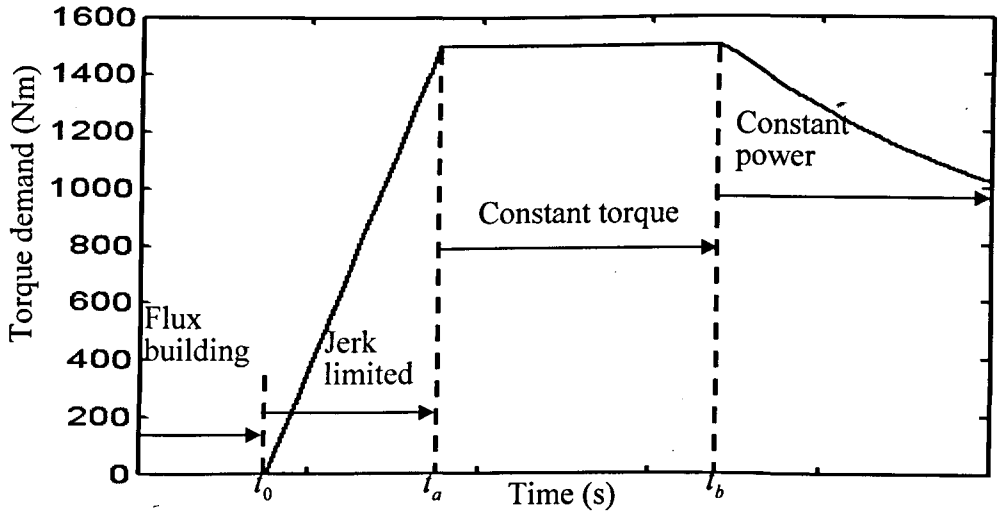

Figure 4.3 Torque demand

The flux demand is a step signal, stepping at t=0.2 s with steady state value 1 Wb.

In the simulation, look-up tables are used to model different slip curves shown in Figure 4.4 to Figure 4.6. There are three groups of curves: c11 and c12, c21 and c22, c31 and c32. Each group describes one specified wheel rail contact condition. In each group, the one with the higher value is related to a good contact condition, and the other is related to a poor contact condition.

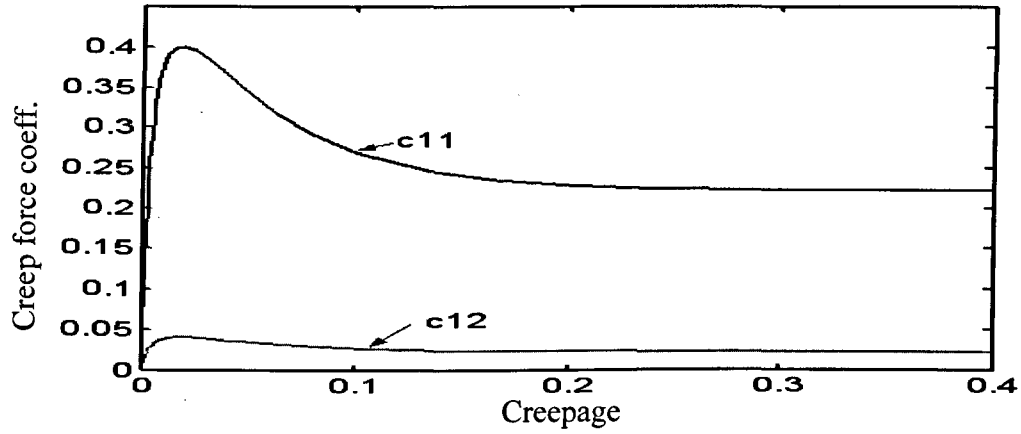

Figure 4.4 Slip curves group 1

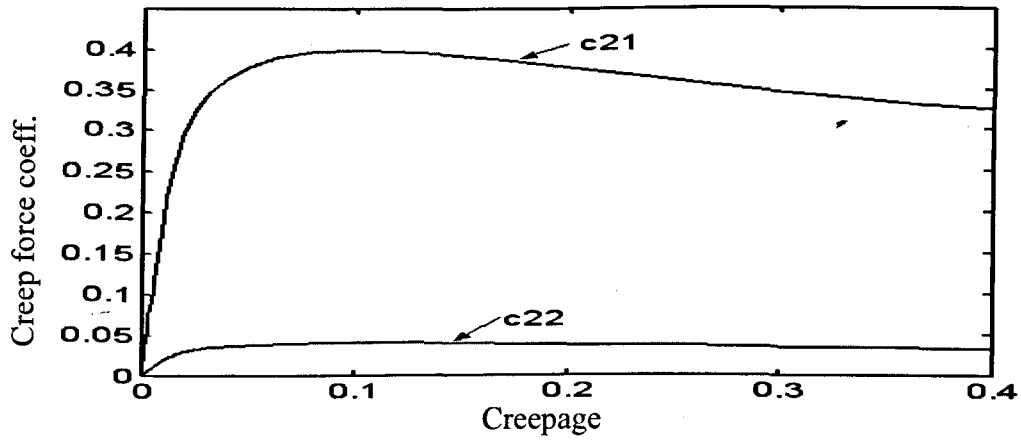

Figure 4.5 Slip curves group 2

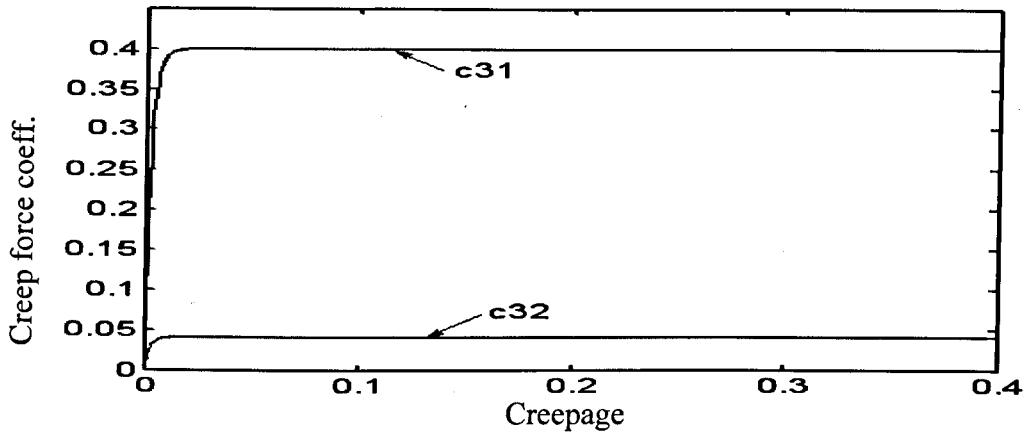

Figure 4.6 Slip curves group 3

4.1.3 Simulation Results of Wheelset Dynamics

In this section, dynamics of the wheelset with 60 Hz torsional mode is studied in different contact conditions and speeds followed by the studies of different wheelsets which is 40 Hz and 80 Hz.

Firstly, the dynamics of the wheelset system with a torsional natural frequency of 60 Hz are studied. The wheel rail contact condition is given by the slip curves shown in Figure 4.4. c11 is given as the initial contact condition. At $t = 4\,\mathrm{s}$, the contact condition is switched from c11 to c12. Then a slip occurs. The contact conditions of the left and right wheel rail contact are kept the same. The initial speed of the vehicle is set to10 km/h.

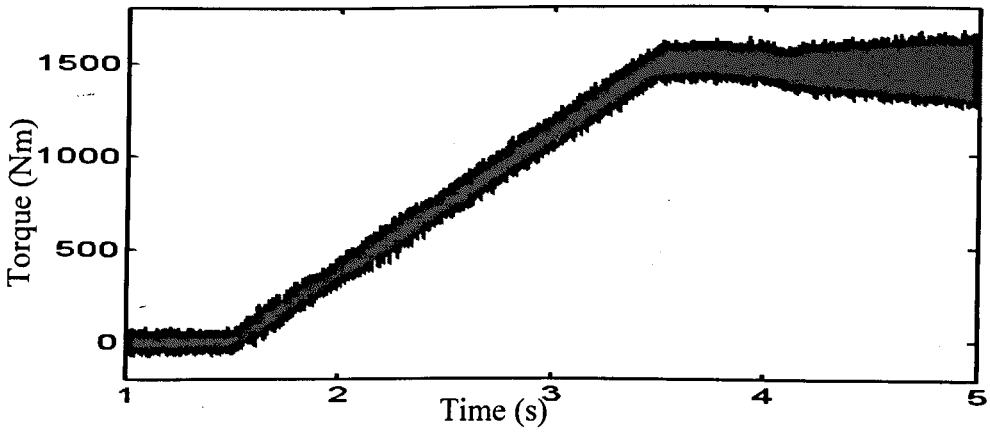

Figure 4.7 Motor torque (60 Hz, sudden change,10 km/h)

Figure 4.7 shows the motor output torque. Due to the effect of the vector control unit of the induction motor, the output torque follows the torque demand shown in Figure 4.3 well, but contains a lot of noise due to the PWM inverter and the position sensor.

Angular velocities of both wheels and equivalent vehicle angular velocity are shown in Figure 4.8. When the slip occurs, the wheel velocities rise much faster than that of the vehicle. Most of the driving energy is consumed in accelerating the wheel instead of the vehicle which is one of the typical features of the slip phenomenon. The creepage is much higher in the slip condition than that in the normal condition, hence the term slip ratio. The wheel velocities keep on increasing if there are no anti-slip measures as shown in Figure 4.9. Many anti-slip controllers use this feature to detect slip: when the measured slip ratio is higher than a pre-defined threshold, a slip condition is assumed.

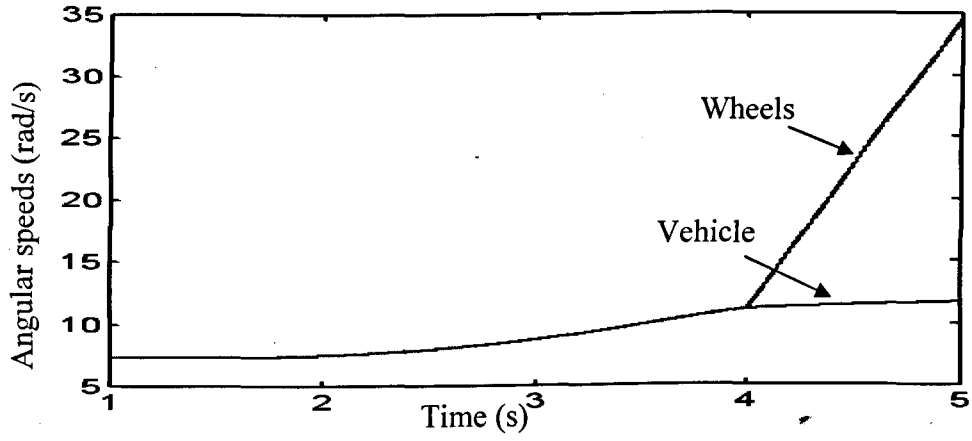

Figure 4.8 Wheel and vehicle angular velocities (60 Hz, sudden change,10 km/h)

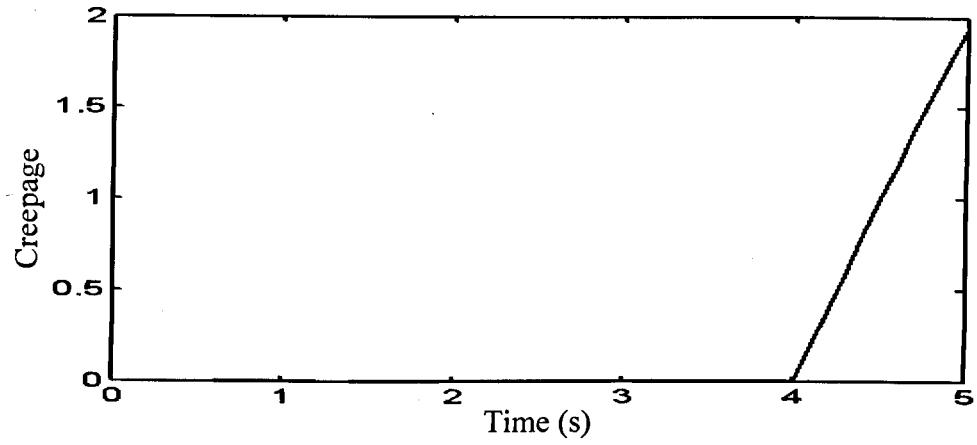

Figure 4.9 Creepage (60 Hz, sudden change,10 km/h)

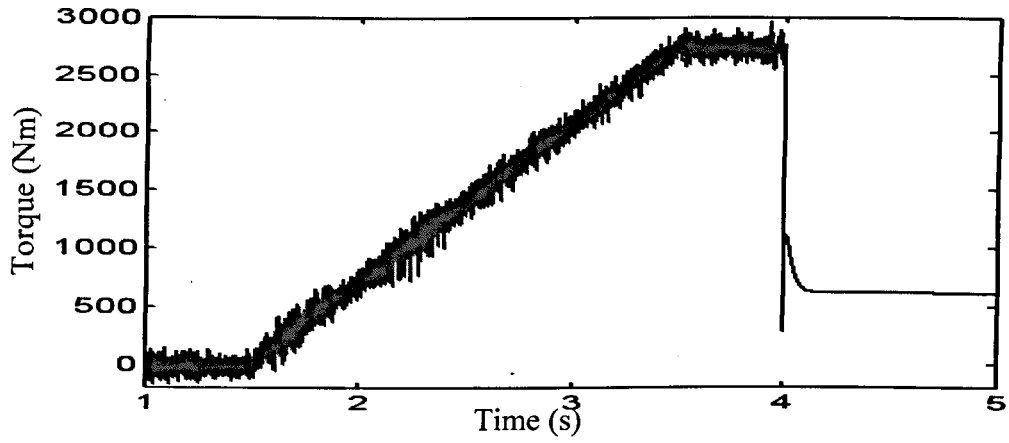

Figure 4.10 Right side tractive torque (60 Hz, sudden change,10 km/h)

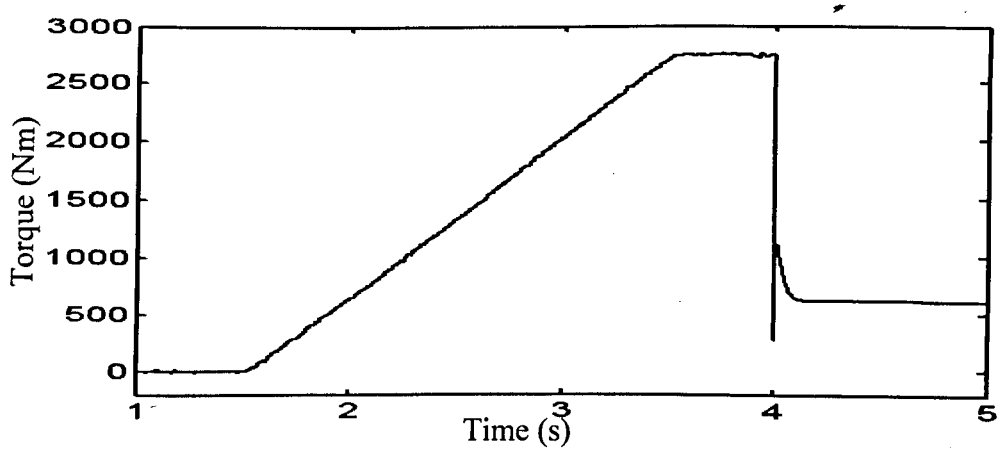

Figure 4.11 Left side tractive torque (60 Hz, sudden change,10 km/h)

Figure 4.10 and Figure 4.11 show the tractive torque from the right hand side and the left hand side respectively. They follow a similar pattern due to the same contact condition set in the simulation. Tractive torque from right hand side contains a lot of noise, because the right wheel is driven directly by the motor torque. The tractive torque of the left wheel is much cleaner than that of the right hand side due to the filter effect of the wheelset shaft.

It is clear that before a slip occurs, the majority effort of the motor torque is applied to drive the vehicle. When the wheel rail contact condition is changed, the adhesion level limits the torque that can be delivered to the vehicle. The tractive torque at the wheels drops to a very low level initially and then increases slightly due to the increased creepage, after which the creepage is increased beyond the maximum adhesion point and the tractive torque reduces due the negative slope of the slip curve.

It can be noticed that there is a region after $t = 4\,\mathrm{s}$ in which the tractive torque becomes a straight line. The reason is that in the serious slip conditions when creepage is higher than the limit of the slip curve (0.4 here), the tractive torque is kept as the final value coming from the slip curve. It is true that from the equation (1.3) it can be seen that when creepage λ approached infinite, the creep force coefficient approaches a constant value.

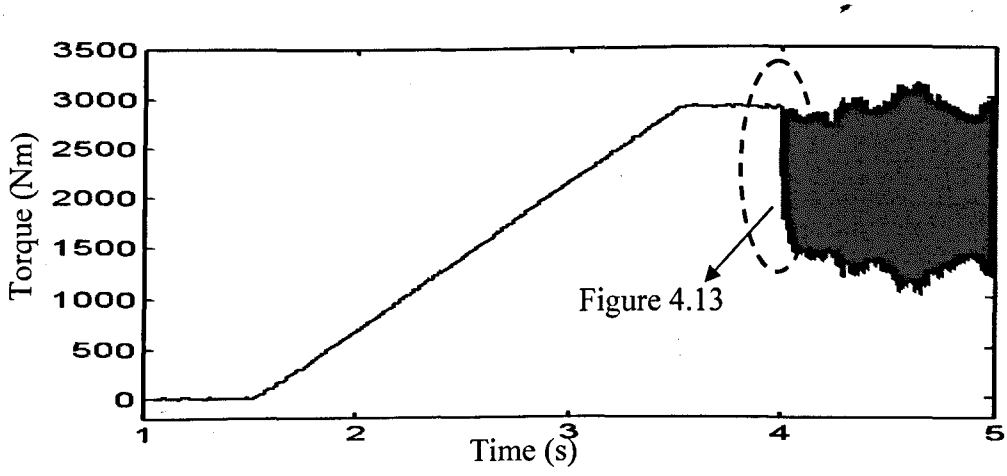

Figure 4.12 Torsional torque overview (60 Hz, sudden change,10 km/h)

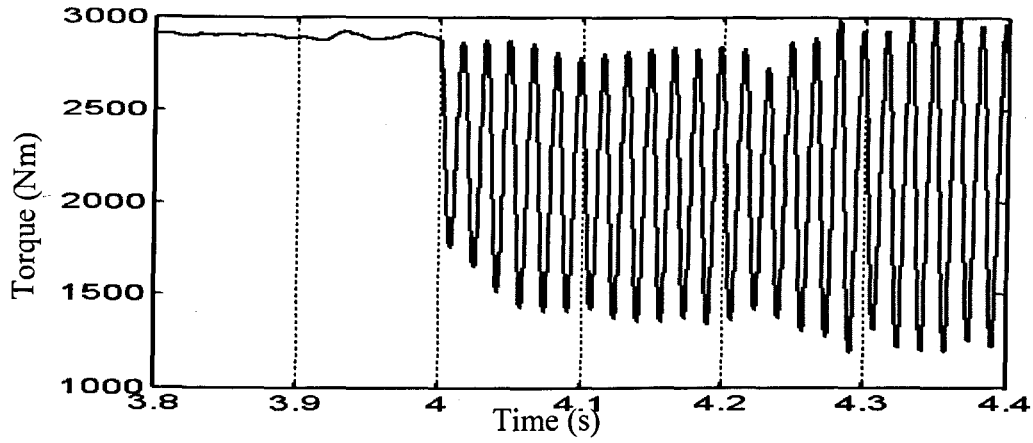

Figure 4.13 Torsional torque close shot 3.8~4.5 s (60 Hz, sudden change,10 km/h)

However, in slip conditions, the wheelset operates in the unstable region of the creepage-creep force coefficient curve, where the damping effect of the creep forces to the wheelset dynamic modes becomes negative, leading to sustained oscillations in the system. Figure 4.12 shows the overview of the torsional torque of the wheelset shaft. Before $t = 4$ s, when the vehicle operates in normal condition, the torsional torque delivers the driving toque to the left wheel stably and closely follows the pattern of the driving torque. After $t = 4$ s, when the slip occurs, the torsional torque loses the ability to stably transfer the driving toque. Torsional vibrations occur as can be seen from the close shot of the torsional torque between 3.8-4.5 s shown in Figure 4.13. The vibrations are at the natural frequency of the wheelset shaft which is 60 Hz.

The observation of occurrence of the torsional vibrations in slip conditions leads to the development of a completely new approach for the wheel slip detection, which is the main innovation of the study. The phenomenon has been reported in the past [73]. However, more rigorous checks and theoretical analysis are first conducted to confirm the link between torsional stability and contact conditions.

To confirm that the frequency of torsional vibration occurring in the slip condition is purely determined by the wheelset system natural frequency, two more wheelset models are tested: one with natural frequency 40 Hz and the other 80 Hz. The simulations are carried out using the same contact conditions which are given in

Figure 4.4, and the initial speed is 10 km/h. The torsional torque in the time period 3.8-4.5 s of 40 Hz system is shown in Figure 4.14. It shows that after $t = 4$ s, when slip occurs, torsional vibration appears, and the frequency is 40 Hz. A similar result is obtained from the model of 80 Hz as shown in Figure 4.15.

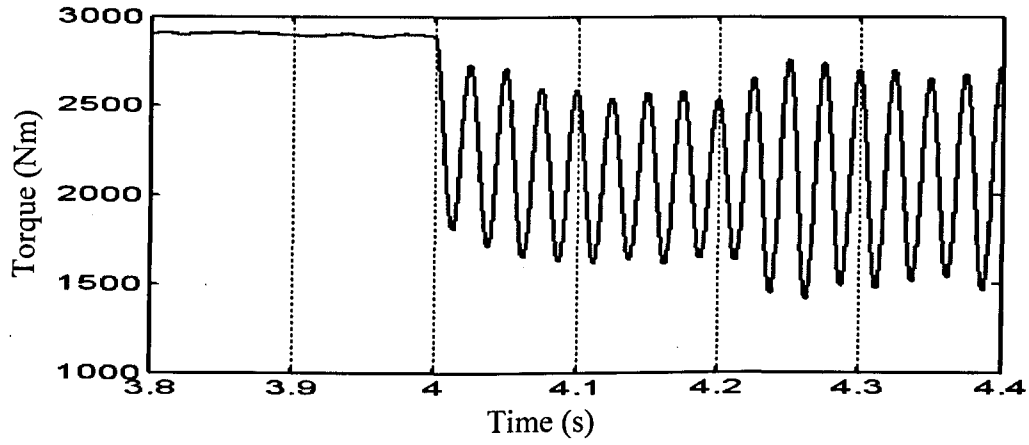

Figure 4.14 Torsional torque close shot (40 Hz, sudden change,10 km/h)

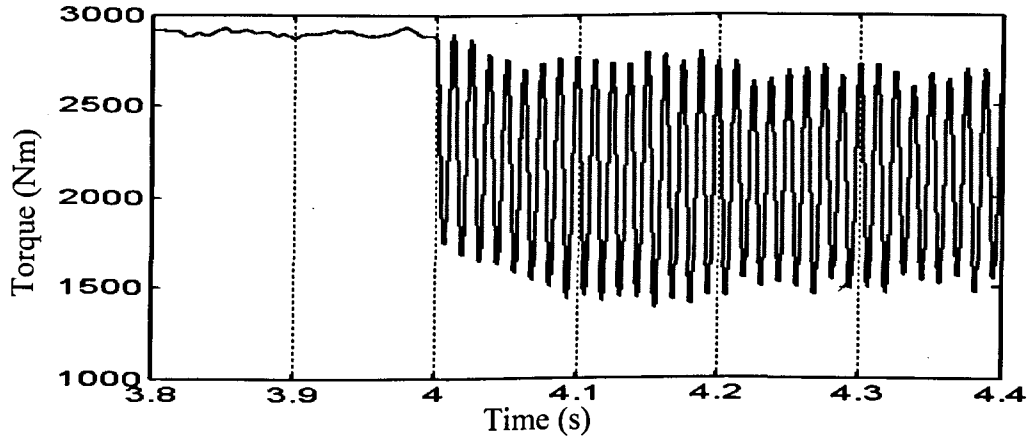

Figure 4.15 Torsional torque close shot (80 Hz, sudden change,10 km/h)

Simulations are also carried out to confirm that the torsional vibrations occur in different slip conditions. Based on the wheelset system with 60 Hz natural frequency, wheelset dynamics will be studied in different wheel rail contact profiles: c21 and c22 given in Figure 4.5, c31 and c32 given in Figure 4.6. The simulations are carried out using these two different groups of slip curves, switching from higher one to the

corresponding lower curve at $t = 4\,\mathrm{s}$ to develop slip conditions, and the initial speed is 10 km/h. The torsional torque in each case is shown in Figure 4.16 and Figure 4.17. The close shot of each torsional torque shows the torsional vibrations of 60 Hz after $t = 4\,\mathrm{s}$. So it is clear that, for the different contact profiles, torsional vibrations appear at the natural frequency of the wheelset when there is a wheel slip.

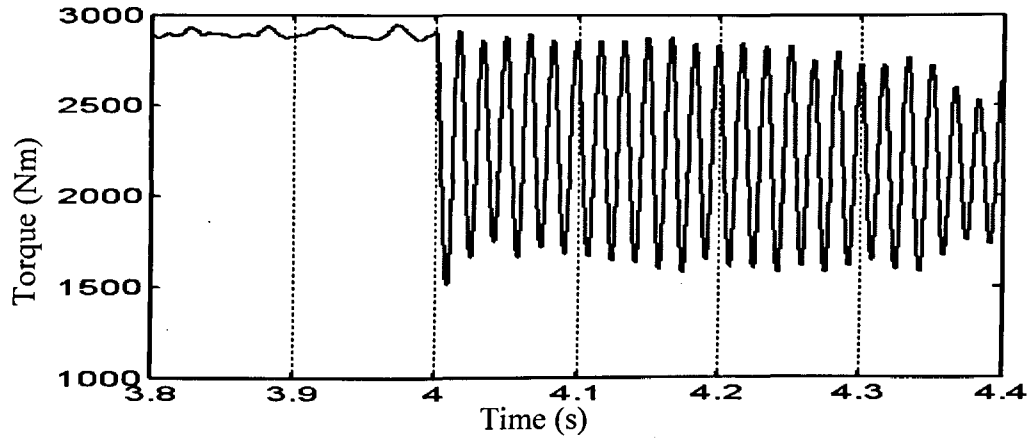

Figure 4.16 Torsional torque close shot (60 Hz, c21)

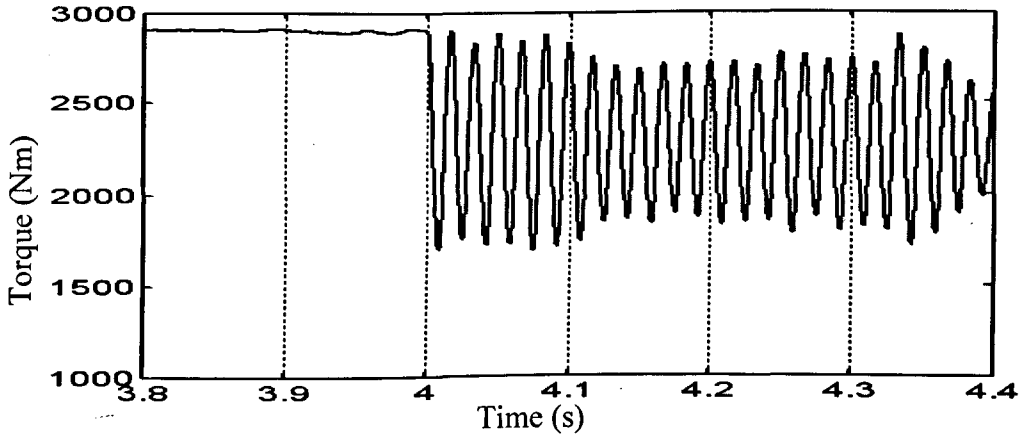

Figure 4.17 Torsional torque close shot (60 Hz, c31)

Furthermore, the study checks the cases where the wheel rail contact condition is always kept poor rather than a sudden change. Simulations are carried out with a 60 Hz wheelset model, initial speed10 km/h, but the wheel rail contact is kept low as defined by curve c12 in Figure 4.4. Figure 4.18 gives the wheels' and vehicle's

angular velocities and Figure 4.19 gives the torsional torque waveform in this condition. It shows that due to the poor wheel rail contact condition, slip happens shortly after the torque demand is added, and the wheel shaft starts to oscillate at the natural frequency.

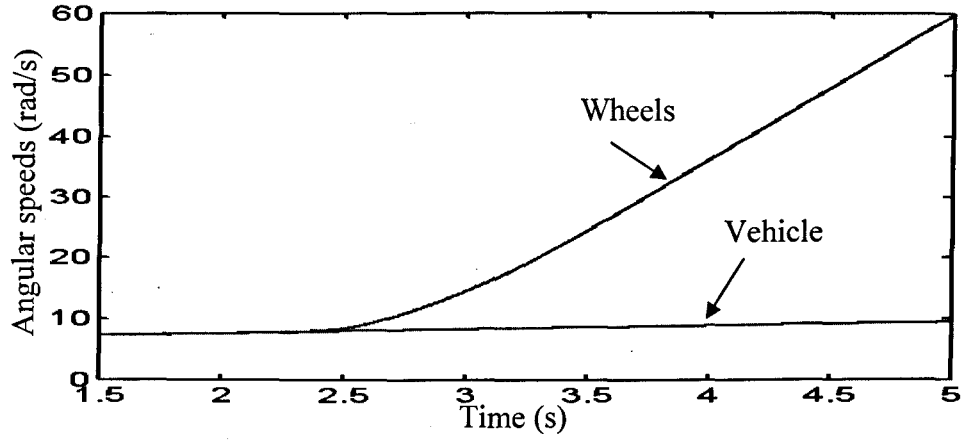

Figure 4.18 Wheel and vehicle angular velocities (low condition, c12,10 km/h , 60 Hz)

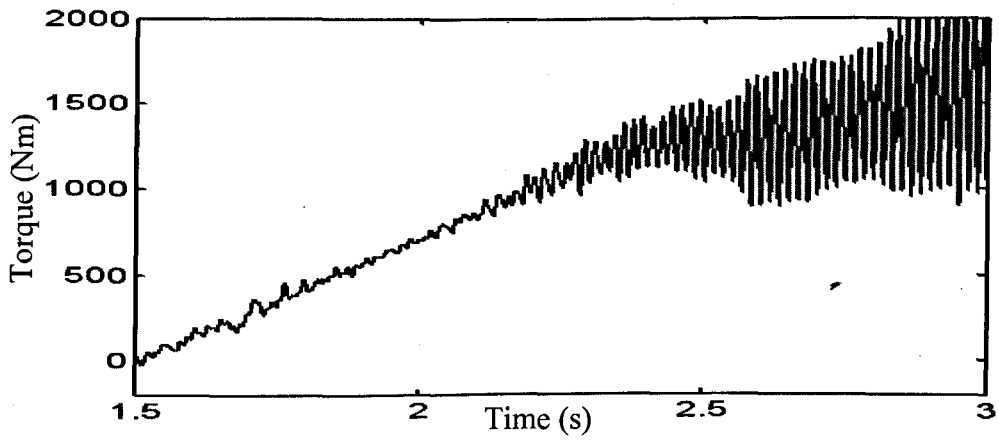

Figure 4.19 Torsional torque (low condition, c12,10 km/h , 60 Hz)

Figure 4.20 gives the wheels and vehicle angular velocities and Figure 4.21 shows the torsional torque when the initial speed is100 km/h. The vibration at the natural frequency shows up as well, and the slip occurs almost as soon as the motor torque is applied. It appears that the slip is more likely to occur at a higher speed for the same conditions as suggested in [74].

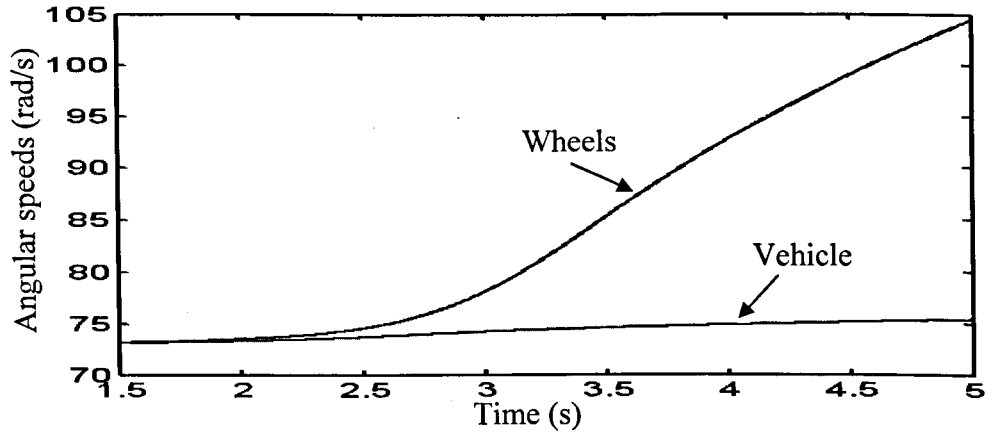

Figure 4.20 Wheel and vehicle angular velocities (low condition, c12,100 km/h , 60 Hz)

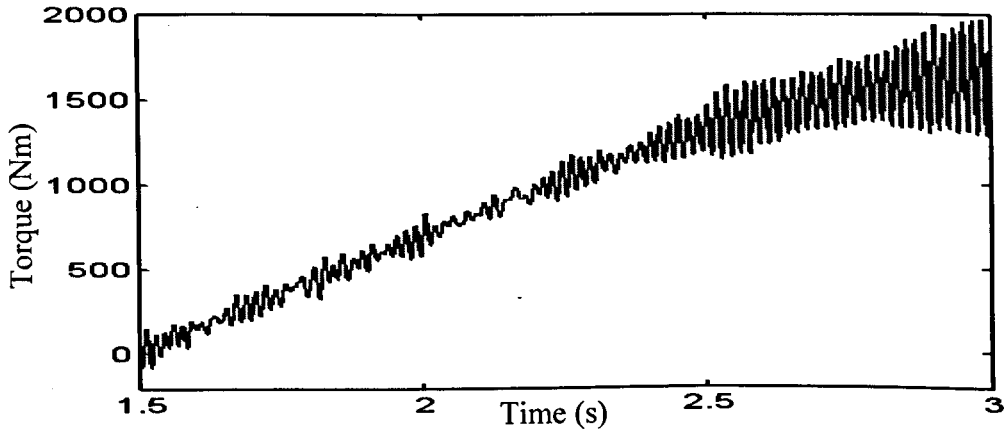

Figure 4.21 Torsional torque (low condition, c12,100 km/h , 60 Hz)

4.2 Dynamic Analysis of the Wheelset in Different Conditions

Theoretical analyses based on linearised contact models are carried out to support the findings from the computer simulations. The locus of the eigenvalue is studied when the operation points are moved along the slip curve in different conditions.

4.2.1 Linearization of the Wheelset Model

In equation (3.97), T_{lr} and T_{ll} have nonlinear relationships with creepage λ which are determined by the wheel and vehicle speeds. Since the vehicle inertia is much

larger that of the wheels, the vehicle speed may be considered constant. Expanding Taylor series about an operation point of λ_{r0} and λ_{l0} , gives

$$right\ wheel: T_{tr} = T_{tr}\Big|_{\lambda=\lambda_{r0}} + \frac{dT_{tr}}{d\lambda}\Big|_{\lambda=\lambda_{r0}} \cdot \Delta\lambda_r \tag{4.3}$$

or

$$T_{tr} = T_{tr0} + k_r \cdot \Delta\lambda_r \tag{4.4}$$

and

$$left\quad wheel: T_{tl} = T_{tl}\Big|_{\lambda=\lambda_{l0}} + \frac{dT_{tl}}{d\lambda}\Big|_{\lambda=\lambda_{l0}} \cdot \Delta\lambda_l \tag{4.5}$$

or

$$T_{tl} = T_{tl0} + k_l \cdot \Delta\lambda_l \tag{4.6}$$

where k_r and k_l are the slopes of the slip curve at the operation points of the right and left wheel respectively.

Considering $\Delta\lambda_r = \frac{\omega_r - \omega_{r0}}{\omega_v}$ *and* $\Delta\lambda_l = \frac{\omega_l - \omega_{l0}}{\omega_v}$, then equations (4.4) and (4.6) can be changed to:

$$right\ wheel: T_{tr} = T_{tr1} + k_1\omega_r \tag{4.7}$$

$$left\quad wheel: T_{tl} = T_{tl1} + k_2\omega_l \tag{4.8}$$

where

$$T_{tr1} = T_{tr0} - k_r\frac{\omega_{r0}}{\omega_v} \quad and \quad T_{tl1} = T_{tl0} - k_l\frac{\omega_{l0}}{\omega_v}$$

$$k_1 = \frac{k_r}{\omega_v} \quad and \quad k_2 = \frac{k_l}{\omega_v}$$

Substituting T_{tr} and T_{tl} into equation (3.97), leads to

$$p\begin{bmatrix}\omega_r\\ \omega_l\\ \theta_s\end{bmatrix} = \underbrace{\begin{bmatrix}-\frac{k_1}{I_r} & 0 & -\frac{k_s}{I_r}\\ 0 & -\frac{k_2}{I_l} & \frac{k_s}{I_l}\\ 1 & -1 & 0\end{bmatrix}}_{A_2}\begin{bmatrix}\omega_r\\ \omega_l\\ \theta_s\end{bmatrix} + \underbrace{\begin{bmatrix}\frac{1}{I_r} & -\frac{1}{I_r} & 0\\ 0 & 0 & -\frac{1}{I_l}\\ 0 & 0 & 0\end{bmatrix}}_{B_2}\begin{bmatrix}T_m\\ T_{tr0}\\ T_{tl0}\end{bmatrix} \tag{4.9}$$

Characteristic polynomial of $\mathbf{A}_2$ is given as:

$$|s\mathbf{I}-\mathbf{A}_2| = s^3 + (\frac{k_1}{I_r}+\frac{k_2}{I_l})s^2 + (\frac{k_s}{I_r}+\frac{k_s}{I_l}+\frac{k_1k_2}{I_rI_l})s + k_s\frac{k_1+k_2}{I_rI_l} \tag{4.10}$$

There are three eignvalues of the characteristic equation. Since it is difficult to give the general polynomial expressions of these eigenvalues, the eigenvalues are calculated out using different sets of k_1 and k_2, and hence to give the root locus of the system as follows.

4.2.2 Dynamic Analysis Based on the Linearized Wheelset Model

Stability analysis is carried out through studying the eigenvalue migration in different conditions, based on linearised models at different operating points along the creep-creep force curve as illustrated in Figure 4.22

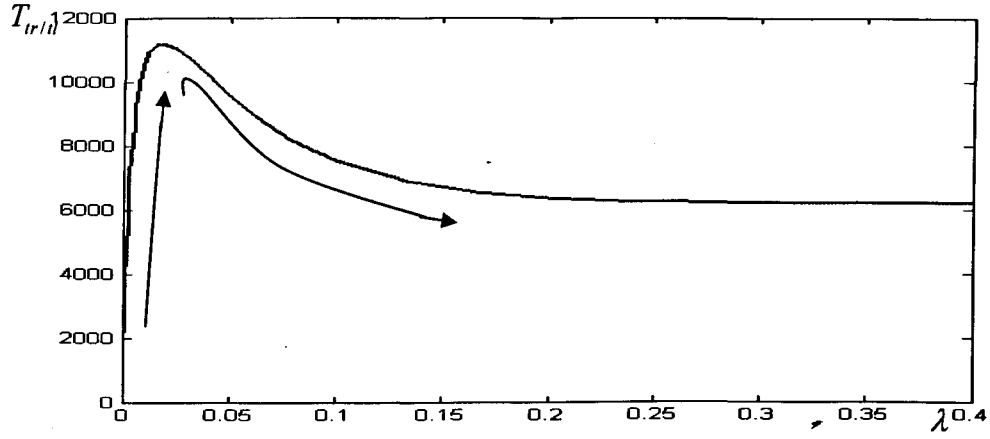

Figure 4.22 Relationship of tractive torque and slip ratio

Firstly, it is assumed that the left and the right wheel rail contact conditions are the same, the vehicle speed is 10 km/h and the natural frequency of the wheelset is 60 Hz. Figure 4.23 shows the movements of the eigenvalues when the operating points moves along the curve as the arrows orientate. In the stable region where the curve has a positive slope, the positive damping keeps all the modes concerned stable (as indicated by '*'). However, when the operating point moves beyond the maximum adhesion value, there are two unstable modes (as indicated by 'o'). One is the torsional mode of the axle which is indicated by a pair of unstable conjugate poles,

and the other is the common rotation of the two wheels indicated by the unstable pole on the real axis.

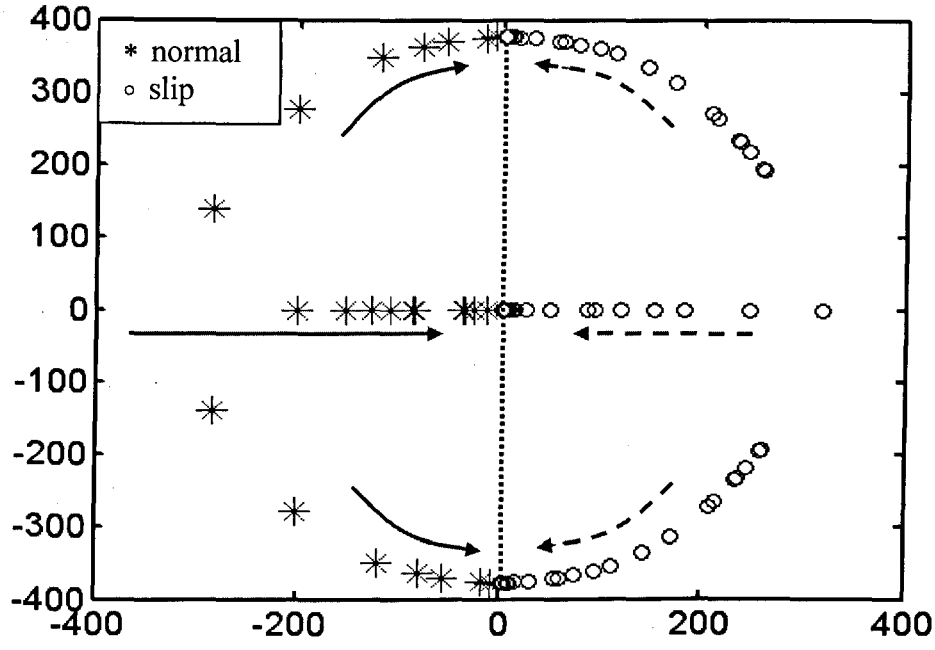

Figure 4.23 Eigenvalue migrations with contact conditions (10 km/h , 60 Hz)

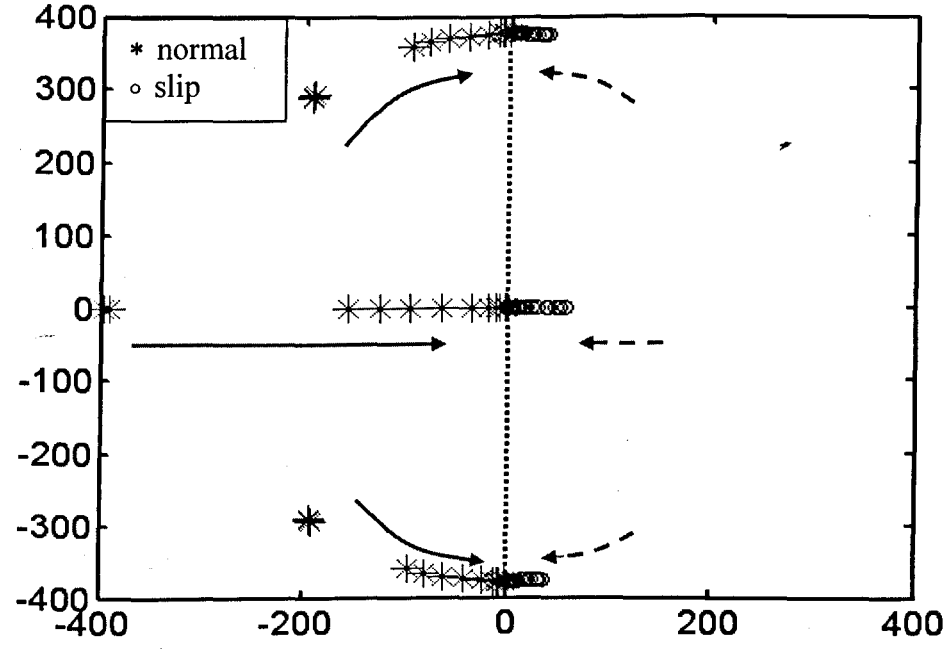

Figure 4.24 Eigenvalue migrations with contact conditions (100 km/h , 60 Hz)

Figure 4.24 gives the eigenvalue movements when the speed is at 100 km/h . A similar result is obtained, but it appears that the dynamic modes are closer to the imaginary axis at higher speeds and therefore the torsional mode is easier to excite.

On the other hand, a less rigid axle brings lower natural modes of the system. Figure 4.25 gives the eigenvalue distribution at the same condition of Figure 4.23, but with a 40 Hz wheelset model. It shows a similar trend of the destabilizing effect as the operation point moves into the slip region.

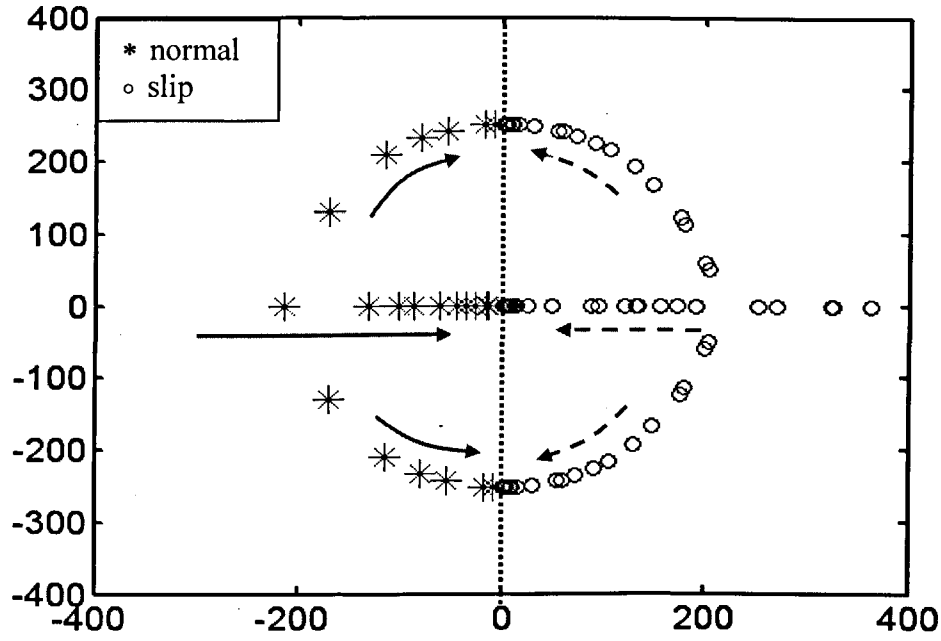

Figure 4.25 Eigenvalue migrations with contact conditions (10 km/h , 40 Hz)

When the two wheels operate in different conditions, e.g. one side of the wheelset operates at stable region while the other in the slip region, the stability will be determined by the overall effect of contact conditions. It is possible that the wheelset system will become unstable even though one side is working within the stable region. Figure 4.26 gives the eigenvalue distributions in such conditions. There are two different trends of the migrations which relate to the two contact conditions at wheels. The ones indicated by ' * ' in Figure 4.26 describe the eigenvalue distribution when the left wheel operates in slip condition but the right wheel operates in normal condition. The ones indicated by '□' are obtained in the condition

where the right wheel slips but the left wheel does not. Overall, the side slip is more difficult to excite and sustain: it only happens when the stable operating side has much higher $dT_t/d\lambda$ value.

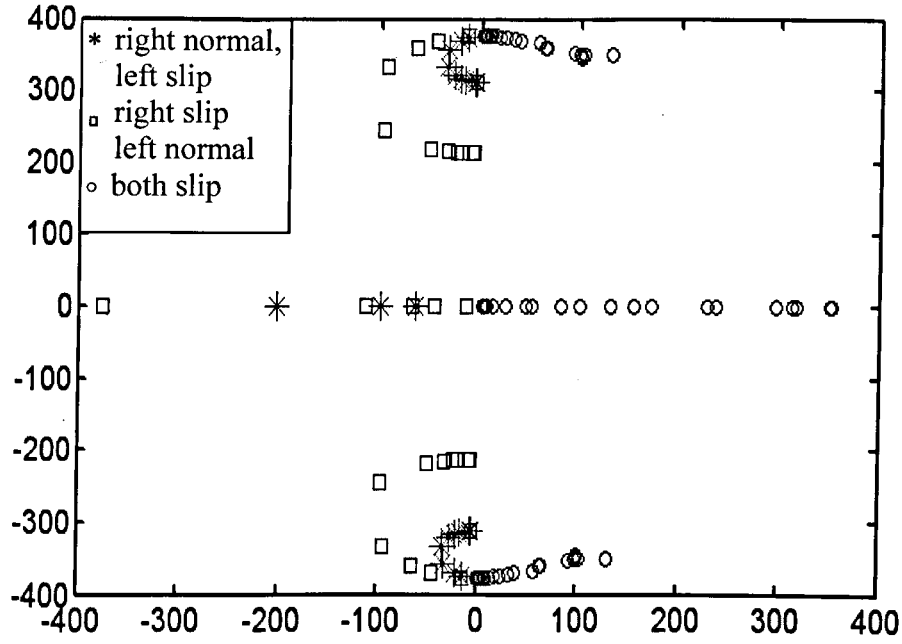

Figure 4.26 Eigenvalue migrations with wheels on different conditions (10 km/h)

4.3 Summary

From the simulation results and the dynamic analysis of the wheelset dynamics in different conditions, it is obvious that there is a close link between the wheel slip and the wheelset torsional vibration. Some previous work also suggested that wheelset torsional vibrations would be caused by the loss of adhesion [73][75]. This link is explored in this study to develop a new and effective slip detection scheme.

5 SLIP DETECTION

As introduced in Chapter 4, the torsional mode of a wheelset is severely affected by the contact conditions. Thus, the slip condition can be detected via monitoring torsional vibration information. It is therefore possible to detect the slip conditions by monitoring the status of the torsional mode.

In this chapter two approaches are studied. One is based on the direct measurement of the torsional torque, and the other is concerned with the development of a Kalman filter that estimates the torsional torque variations from wheel speed measurements. The signals (either measured or estimated) are then processed to extract the component at the frequency of the dominant torsional mode. No re-adhesion control is used in this chapter, which will be presented in chapter 6.

5.1 Slip Detection via Monitoring Torsional Torque

Torque sensors will be required to measure the torsional torque. Strain gauges are widely used in railway vehicle status monitoring [76], and non-contact digital rotary torque measurement solutions with high accuracy and resolution, using "Surface Acoustic Wave" technology is becoming available for railway applications as well [77] where a piezoelectric device is sticked on the surface of the shaft to pick up the torsional deformations. In the following analysis, it is assumed that the torsional torque is measured through a rather accurate torque sensor.

Figure 5.1 shows a measured torsional torque for the wheelset with a torsional mode of 60 Hz. The result is obtained under the contact condition shown in Figure 4.4 where the adhesion coefficient is reduced from 0.4 to 0.04 at $t = 4\,\mathrm{s}$, and the initial speed is 10 km/h.

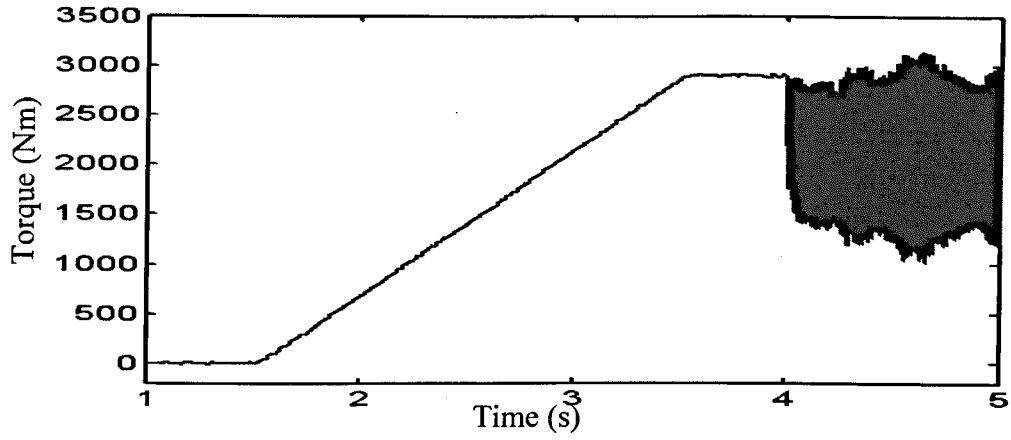

Figure 5.1 Torsional torque measured (60 Hz, sudden change,10 km/h)

The vibration is obvious in the measured torsional torque waveform, but post processing is needed to detect the natural frequency component. Two methods are studied. One is based on frequency domain analysis using the running FFT method, and the other uses a combination of filters.

5.1.1 Running FFT Method

Running FFT analysis carries out FFT analysis over a windowed section of the measured signal. From the spectrum of each FFT analysis, the component at the natural frequency is picked out. By comparing the time history of the magnitude at the specified natural frequency, the slip condition can be detected.

The outcome of the running FFT processing on the torsional torque signal in Figure 5.1 results in the time history of the magnitude at the natural frequency, which is 60 Hz here as shown in Figure 5.2. The FFT analysis is computed over a 0.2 s time windowed signal which is updated every 0.05 s. In each frame of the FFT analysis result, the component of the natural frequency component is picked up. It is obvious that when slip happens after $t = 4$ s , the magnitude increases rapidly due the appearance of torsional oscillations. By setting a threshold, e.g. 50 Nm, the slip condition can be indicated within 0.5 s.

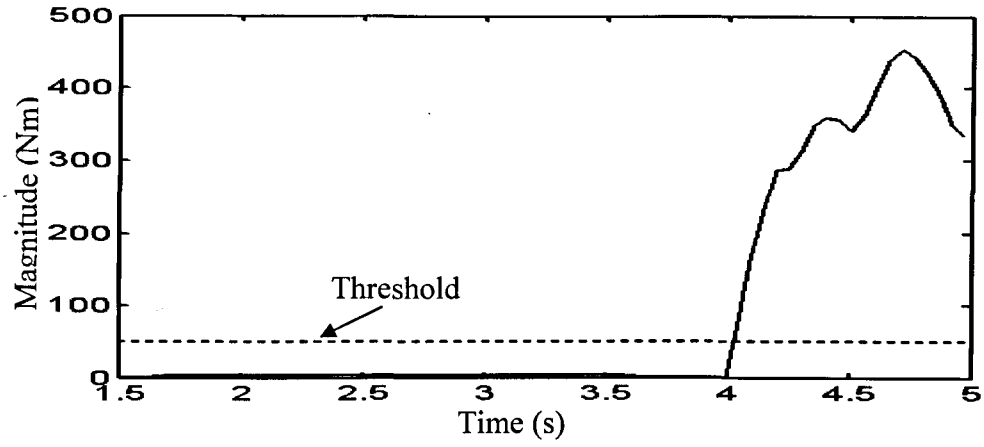

Figure 5.2 Magnitude information of torsional torque of specified natural frequency using running FFT (60 Hz)

The running FFT method is a widely used method to deal with vibration signals. It is effective and most straight forward, but it is also computationally intensive and increases the complexity of the control system, compared to the time domain filtering as shown in the next section.

5.1.2 Filter Combination Method

As shown in Figure 5.3, the torsional torque signal is fed to a band-pass filter, which is designed to extract the component at the natural frequency. Then through a rectifier and a low-pass filter with a low bandwidth, the magnitude of the natural frequency component can be obtained.

Figure 5.3 Filter combination method

The band-pass filter is designed as a basic second order band-pass filter

$$BP = \frac{H_0 \beta s}{s^2 + \beta s + \omega_0^2} \tag{4.11}$$

where, ω_0 is the centre frequency, β is the bandwidth, and H_0 is the maximum magnitude of the filter. For the 60 Hz wheelset shaft, the bandwidth is set as 3 Hz, $H_0 = 1$, the bode plot of which is shown in Figure 5.3. The bandwidth of the low pass filter is set as 1 Hz.

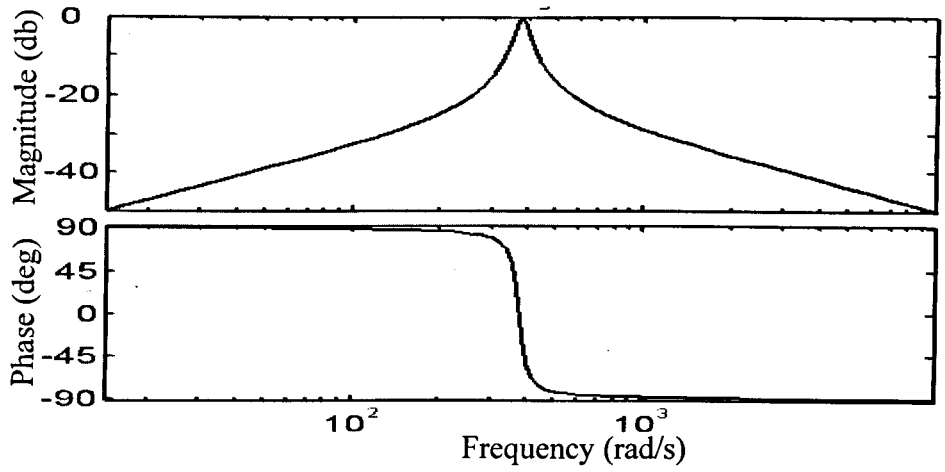

Figure 5.4 Bode diagram of a band-pass filter

For the input signal given in Figure 5.1, the final magnitude at the output of the low pass filter is shown in Figure 5.5. It is again clear that the magnitude of the natural frequency component increases in the slip condition while it is nearly zero in the stable operation condition.

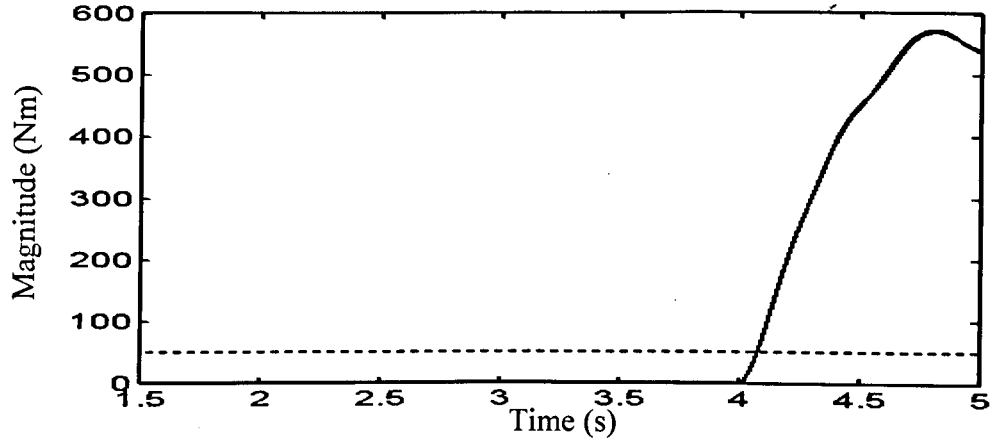

Figure 5.5 Magnitude result of torsional torque of the natural frequency using filter combination method (60 Hz, sudden change,10 km/h)

5.1.3 Evaluation of Different Wheelset and in Different Conditions

Firstly, wheelset shafts with two different natural frequencies are studied: one is a 40 Hz shaft and the other is an 80 Hz shaft. In both simulations, the contact condition is set as defined in Figure 4.4, and the condition is changed from a good case to a poor case at $t = 4$ s to initialize slip conditions. The initial speed for both cases is 10 km/h. In the simulations, the running FFT analysis and the bandpass filter centre frequencies are tuned to the corresponding wheelset natural frequency.

For the 40 Hz wheelset, the torsional torque is given in Figure 4.14, and the magnitudes of the natural frequency component using the running FFT method and the filter method are shown respectively in Figure 5.6 and Figure 5.7. Those show the consistency of these two methods, there is a clear increase in the vibration magnitude in slip condition after $t = 4$ s.

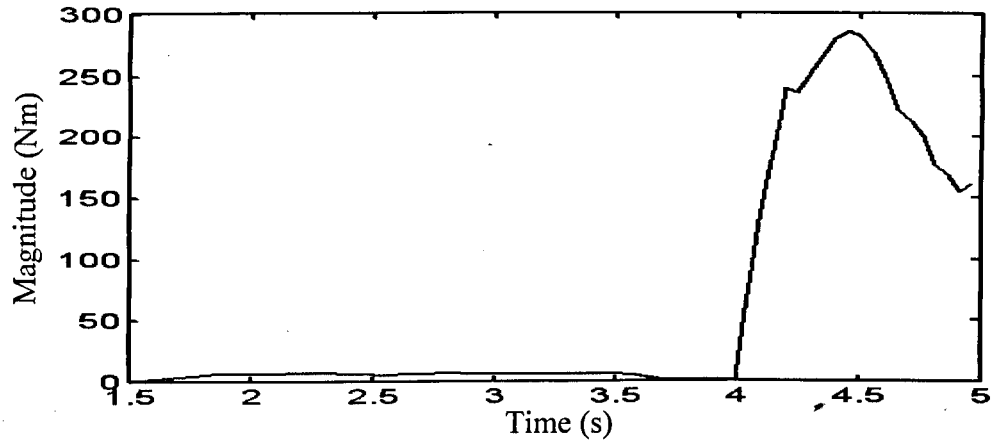

Figure 5.6 Magnitude information of torsional torque of specified natural frequency using running FFT (40 Hz, sudden change,10 km/h)

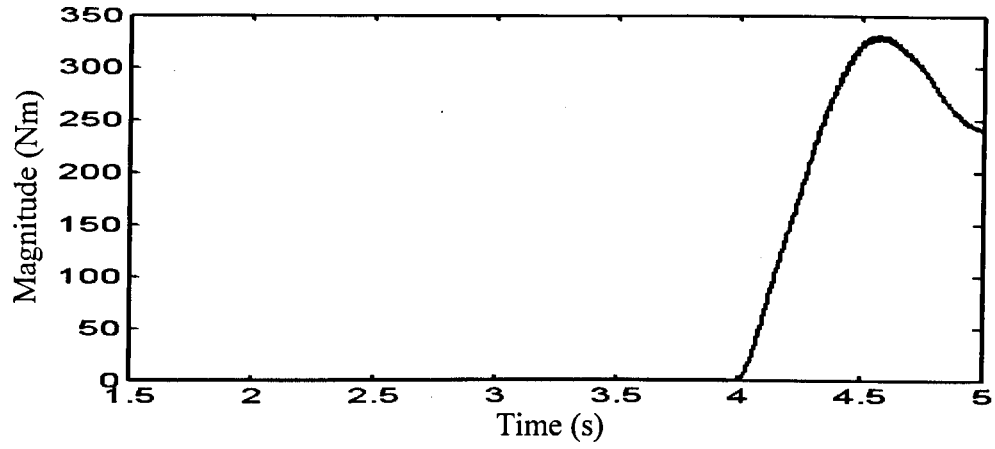

Figure 5.7 Magnitude result of torsional torque of the natural frequency using filter combination method (40 Hz, sudden change,10 km/h)

For the 80 Hz wheelset, the torsional torque is shown in Figure 4.15, and the magnitudes of the natural frequency component using the running FFT method and the filter method are shown respectively in Figure 5.8 and Figure 5.9. Again the results show that either of the methods is expected to give the magnitude information for slip detection.

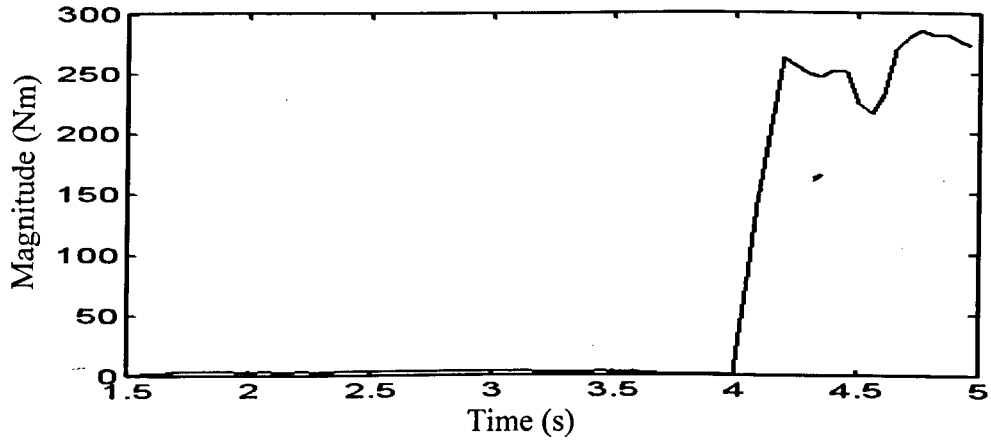

Figure 5.8 Magnitude information of torsional torque of specified natural frequency using running FFT (80 Hz, sudden change,10 km/h)

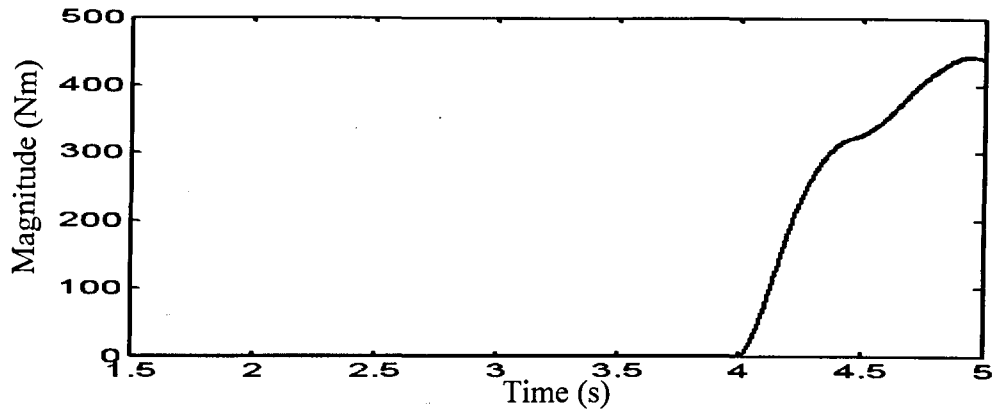

Figure 5.9 Magnitude result of torsional torque of the natural frequency using filter combination method (80 Hz, sudden change,10 km/h)

Secondly, the performances are assessed at different speeds and with tractive effort is applied when the vehicle is already on a track with poor contact conditions. Figure 5.10 and Figure 5.11 give the magnitude of the natural frequency component when the initial speed of the vehicle is 10 km/h. Figure 5.12 and Figure 5.13 give the magnitude of the natural frequency component when the initial speed of the vehicle is 100 km/h. For both cases, using either the running FFT method or the filtering method the occurrence of the torsional vibration due to slip can be detected in time by observing the magnitude variation. It is also noticed that the rate of the increase of the magnitude in these two cases are lower that those of the sudden change cases, which is because of the lower driving torque in the jerk limited region.

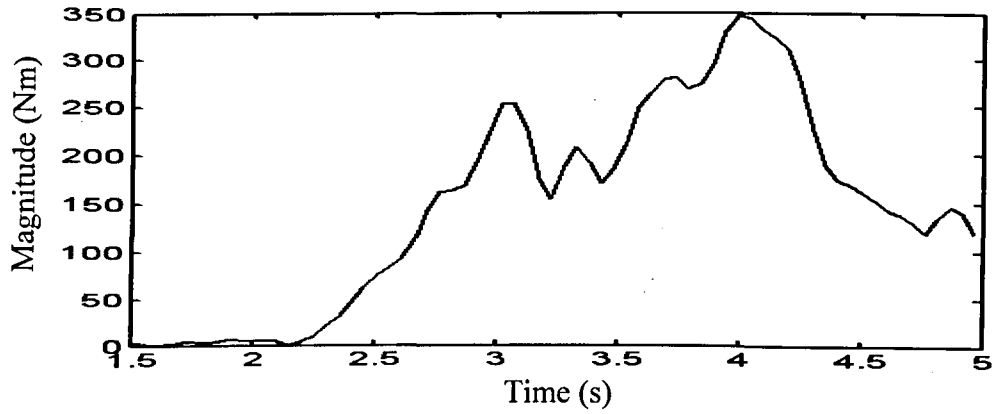

Figure 5.10 Magnitude information of torsional torque of specified natural frequency using running FFT (60 Hz, low contact condition,10 km/h)

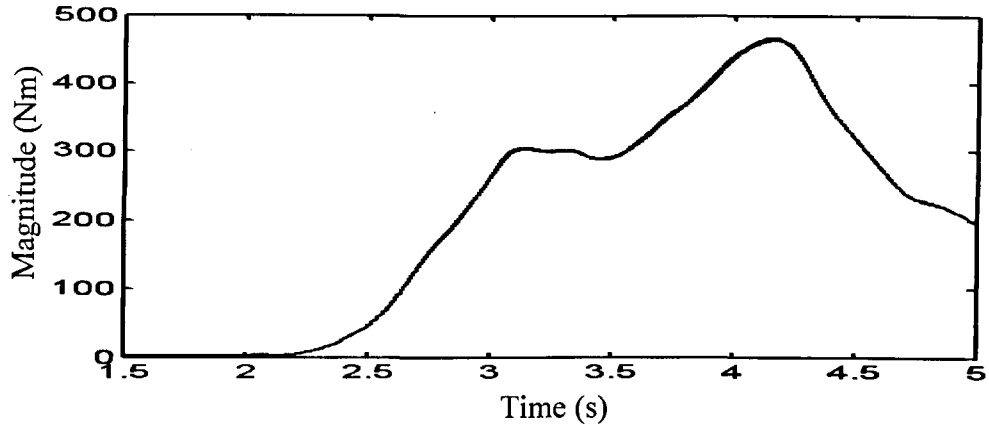

Figure 5.11 Magnitude result of torsional torque of the natural frequency using filter combination method (60 Hz, low contact condition,10 km/h)

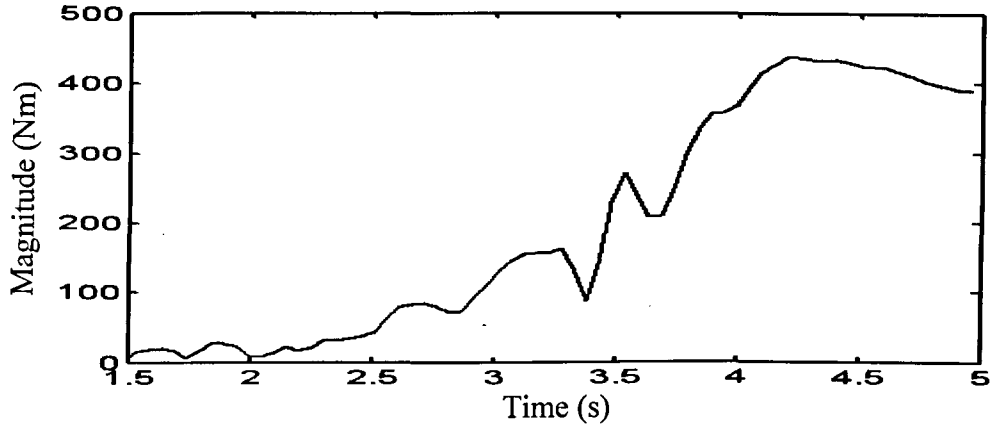

Figure 5.12 Magnitude information of torsional torque of specified natural frequency using running FFT (60 Hz, low contact condition,100 km/h)

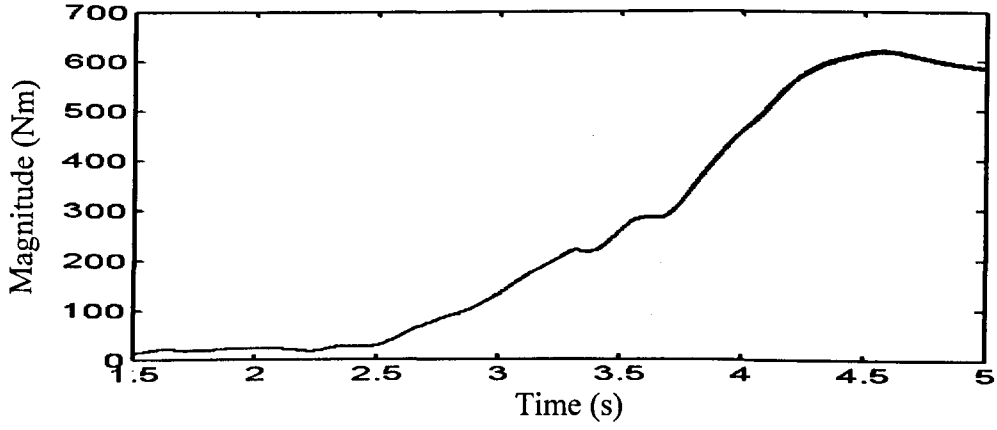

Figure 5.13 Magnitude result of torsional torque of the natural frequency using filter combination method (60 Hz, low contact condition,100 km/h)

The magnitude analyses in different conditions show the effectiveness of the idea to detect the slip based on the torsional vibrations in slip conditions. Both data processing methods presented give consistent results of the magnitude at the natural frequency. However, the time domain filtering method is probably preferred in practice for its simplicity and will be used as the main magnitude extraction method in the following analysis.

Although the torsional torque gives a good and direct possibility for slip detection, it requires torque measurement instrumentation which will increase the cost and structure complexity. Thereafter, a Kalman filter is developed to provide an estimation of the vibration signals from the measurement of wheel speed which is normally available in modern traction systems.

5.2 Slip Detection based on the Kalman Filter

5.2.1 Principle of the Kalman filter

The Kalman filter is an effective technique to estimate the states of a dynamic system. The measuring devices give the required measurements with certain noise. With the knowledge of the inputs and outputs from the physical system, a Kalman filter can give the optimal estimation of the system states.

Given an observable linear control system

$$\dot{\mathbf{x}} = \mathbf{A}\mathbf{x} + \mathbf{B}\mathbf{u} + w \tag{4.12}$$

$$\mathbf{y} = \mathbf{C}\mathbf{x} + \mathbf{D}\mathbf{u} + \upsilon \tag{4.13}$$

where, the dynamics are subject to random disturbances w and the measurements are subject to random noise v. Kalman filter is designed to solve the optimal estimator problem: Construct a full state observer which minimizes the combined effect of the disturbances and the noise, thus providing a "most likely" estimate of the system state [78]. The processes are Gaussian white noise processes which means firstly null mean value

$$E(w) = 0 \qquad E(\upsilon) = 0 \tag{4.14}$$

Secondly, fixed covariance value

$$E(ww^T) = Q_{kf} \tag{4.15}$$

$$E(\upsilon\upsilon^T) = R_{kf} \tag{4.16}$$

and mutually uncorrelated

$$E(w\upsilon^T) = 0 \tag{4.17}$$

Then the problem is to construct a state estimate $\hat{x}$ that minimizes the steady state error covariance

$$P = \lim_{t\to\infty} E\{(\mathbf{x} - \hat{\mathbf{x}})(\mathbf{x} - \hat{\mathbf{x}})^T\} \tag{4.18}$$

The optimal solution is the Kalman Filter which constructs an output injection:

$$\dot{\hat{\mathbf{x}}} = \mathbf{A}\hat{\mathbf{x}} + \mathbf{B}\mathbf{u} + \mathbf{L}(\mathbf{y} - \mathbf{C}\hat{\mathbf{x}} - \mathbf{D}\mathbf{u}) \tag{4.19}$$

where the filter gain L is determined by solving an algebraic Riccati equation.

5.2.2 Small Signal Model for the Wheelset System

Wheel rail contact laws are highly nonlinear, but linearised models are desired for the Kalman filter design. Recalling the wheel set model given in equation (3.97), the state space description of the wheel set system is

$$\dot{\mathbf{x}} = \mathbf{A}_1\mathbf{x} + \mathbf{B}_1\mathbf{u} + \mathbf{C}_1\mathbf{u}_2 \tag{4.20}$$

where $\mathbf{x} = [\omega_r \ \omega_l \ \theta_s]^{\mathrm{T}}$, the input vector $\mathbf{u} = [T_m \quad 0 \quad 0]^T$, and $\mathbf{u}_2 = [T_{tr} \quad T_{tl}]^T$.

Let $\mathbf{x}_0$ be the static operation point, then

$$\dot{\mathbf{x}}_0 = \mathbf{A}_1\mathbf{x}_0 + \mathbf{B}_1\mathbf{u}_0 + +\mathbf{C}_1\mathbf{u}_{20} \tag{4.21}$$

Let the transient variables be $\mathbf{x} = \mathbf{x}_0 + \Delta\mathbf{x}$, and input be $\mathbf{u} = \mathbf{u}_0 + \Delta\mathbf{u}$ and $\mathbf{u}_2 = \mathbf{u}_{20} + \Delta\mathbf{u}_2$. Then the variation is described:

$$\Delta\dot{\mathbf{x}} = \mathbf{A}_1\Delta\mathbf{x} + \mathbf{B}_1\Delta\mathbf{u} + \mathbf{C}_1\Delta\mathbf{u}_2 \tag{4.22}$$

From equation (4.3), ΔT_{tr} and ΔT_{tl} are given as $k_r \cdot \Delta\lambda_r$ and $k_l \cdot \Delta\lambda_l$. As the vehicle speed can be considered constant, ΔT_{tr} and ΔT_{tl} are written as:

$$\Delta T_{tr} = k_r \cdot \frac{\Delta\omega_r}{\omega_v} = k_1 \cdot \Delta\omega_r \tag{4.23}$$

$$\Delta T_{tl} = k_l \cdot \frac{\Delta\omega_l}{\omega_v} = k_2 \cdot \Delta\omega_l \tag{4.24}$$

Finally, the linear small signal model is given as:

$$\Delta\dot{\mathbf{x}} = \begin{bmatrix} \Delta\dot{\omega}_r \\ \Delta\dot{\omega}_l \\ \Delta\dot{\theta}_s \end{bmatrix} = \underbrace{\begin{bmatrix} -\frac{k_1}{I_2} & 0 & -\frac{k_s}{I_2} \\ 0 & -\frac{k_2}{I_1} & \frac{k_s}{I_1} \\ 1 & -1 & 0 \end{bmatrix}}_{\mathbf{A}} \begin{bmatrix} \Delta\omega_r \\ \Delta\omega_l \\ \Delta\theta_s \end{bmatrix} + \underbrace{\begin{bmatrix} \frac{1}{J_r} \\ 0 \\ 0 \end{bmatrix}}_{\mathbf{B}} \Delta T_m \tag{4.25}$$

The measurement available is the rotational speed of the wheel on the traction motor side and therefore the output equation is:

$$y = \underbrace{\begin{bmatrix} 1 & 0 & 0 \end{bmatrix}}_{\mathbf{C}} \begin{bmatrix} \Delta\omega_r \\ \Delta\omega_l \\ \Delta\theta_s \end{bmatrix} \tag{4.26}$$

To simplify, re-define $\mathbf{x} = [\Delta\omega_r \ \Delta\omega_l \ \Delta\theta_s]^{\mathrm{T}}$ and $\mathbf{u} = \begin{bmatrix} \Delta T_m & 0 & 0 \end{bmatrix}^T$. The small signal model can be expressed as

$$\dot{\mathbf{x}} = \mathbf{A}\mathbf{x} + \mathbf{B}\mathbf{u} \tag{4.27}$$

$$\mathbf{y} = \mathbf{C}\mathbf{x} \tag{4.28}$$

where matrixes $\mathbf{A}$, $\mathbf{B}$ and $\mathbf{C}$ are given in equations (4.25) and (4.26).

5.2.3 Kalman Filter Based on the Small Signal Model

Based on the small signal model described in equations (4.27) and (4.28), a Kalman filter as shown in Figure 5.14 is constructed according to equation (4.19). The input of the system is the driving torque variation ΔT_m. The measurement input is the right wheel speed variation $\Delta\omega_r$. Zero initial conditions are considered. The outputs of the Kalman filter are the variations of the three state variables: the right wheel speed variation $\Delta\hat{\omega}_r$, the left wheel speed variation $\Delta\hat{\omega}_l$ and the torsional torque variation $\Delta\hat{T}_s$. With some loss of dynamic accuracy, but great savings in

computational effort, it is often possible to use a stationary Kalman filter, with which the Kalman gain is pre-computed and held constant in the filtering process [79]. So in the following study, the Kalman gain L is pre-computed based on the model equation and a set of covariance values Q_{kf} and R_{kf} which are given as $Q_{kf} = 1\times10^{6}$ and $R_{kf} = 1\times10^{-6}$.

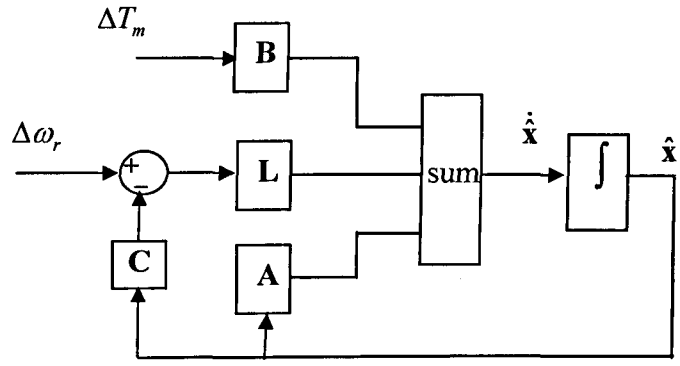

Figure 5.14 Estimation based on Kalman filter

In matrix $\mathbf{A}$, k_1 and k_2 values are determined by the slope of slip curves and the vehicle speed. So these may results in different sets of data. Through simulations, it is found that the smaller k_1 and k_2 which are determined by the regions near the peak of slip curves can bring better estimation results which will be proved in the next section. In the following study, k_1 and k_2 are kept fixed unless especially specified as

$$k_1 = k_2 = 2\times10^{3} \tag{4.29}$$

5.2.4 Estimation Results of the Kalman filter

The performance of the Kalman filter is assessed using the contact condition defined by Figure 4.4 which is changed from the good one to the poor one at $t = 4$ s, and the initial speed is 10 km/h. The sampling interval is set as 1ms.

Figure 5.15 shows the right wheel speed variation which is fed to the Kalman filter as the measurement input.

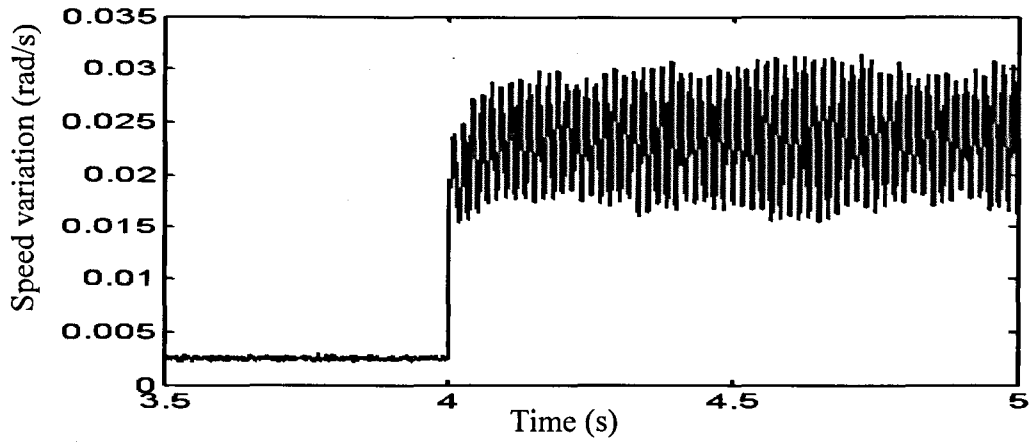

Figure 5.15 Right wheel speed variation $\Delta\omega_r$ (60 Hz, sudden change,10 km/h)

Figure 5.16 is the driving torque variation ΔT_m that may be used as the input of the Kalman filter. As it shows, ΔT_m contains primarily noise which is caused by the PWM and the position sensor in the vector control scheme. The mean value of this signal is 2 Nm which is very close to zero. Therefore ΔT_m is set to zero in the Kalman filter directly. This procedure will reduce the noise of the estimation and complexity of the filter structure without affecting the correctness of the estimation.

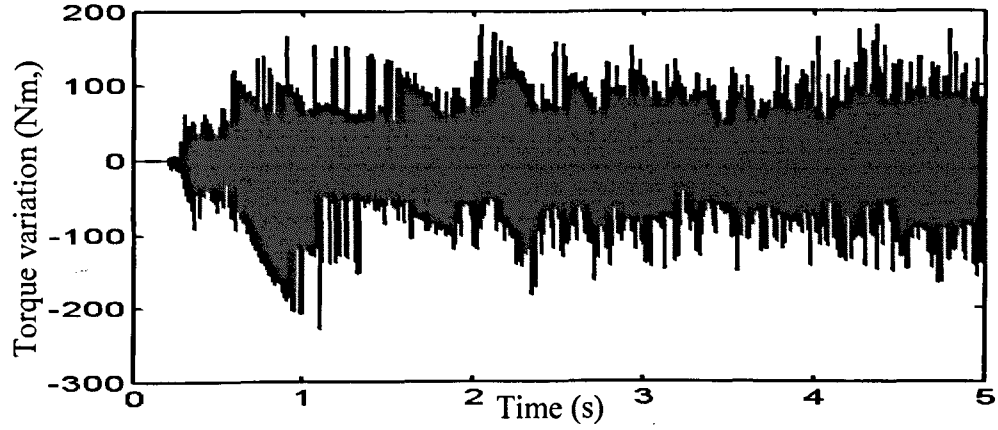

Figure 5.16 Driving torque variation ΔT_m (60 Hz, sudden change,10 km/h)

Figure 5.17 shows the estimation of right wheel speed variation. Compared with the the original results of the right wheel speed variation obtained by simulation of the drive system given in Figure 5.15, it shows a good match.

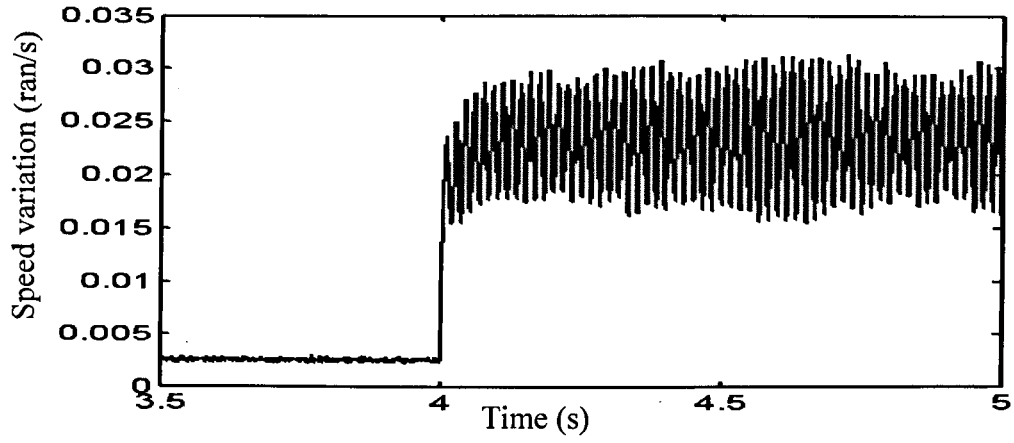

Figure 5.17 Estimation of right wheel speed variation (60 Hz, sudden change,10 km/h)

Figure 5.18 and Figure 5.19 compare the original result of the left wheel speed variation obtained by simulation of the drive system and estimated left wheel speed variation. It can be seen that the estimation suppresses the magnitude but still retains the oscillation information.

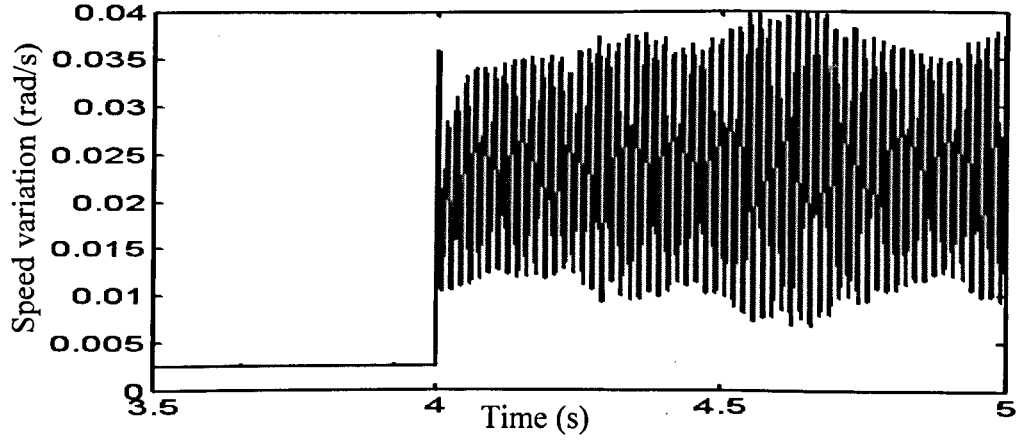

Figure 5.18 Original left wheel speed variation (60 Hz, sudden change,10 km/h)

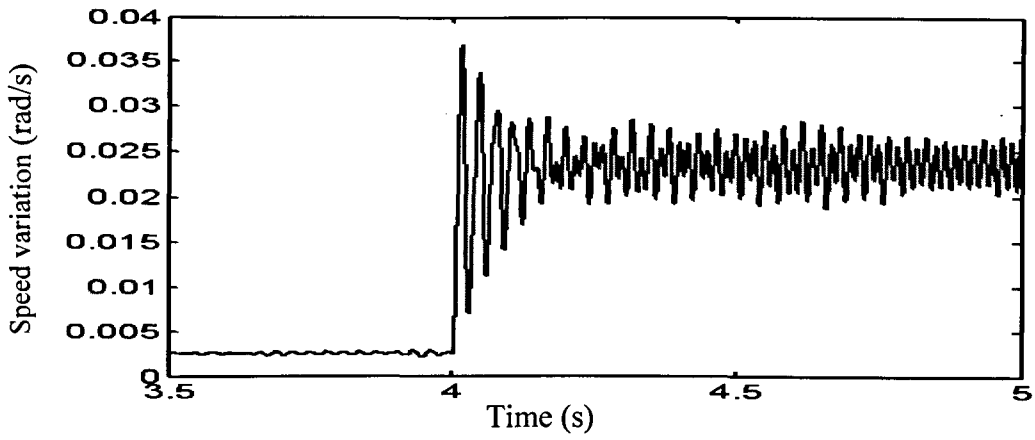

Figure 5.19 Estimation of left wheel speed variation (60 Hz, sudden change,10 km/h)

Figure 5.20 is the original torsional torque variation obtained by the simulation and Figure 5.21 gives the estimation result of torsional torque variation. Although the oscillation magnitude is also attenuated, the estimation gives the torsional vibration information in the slip condition which can be proved to be sufficient for the detection as shown later.

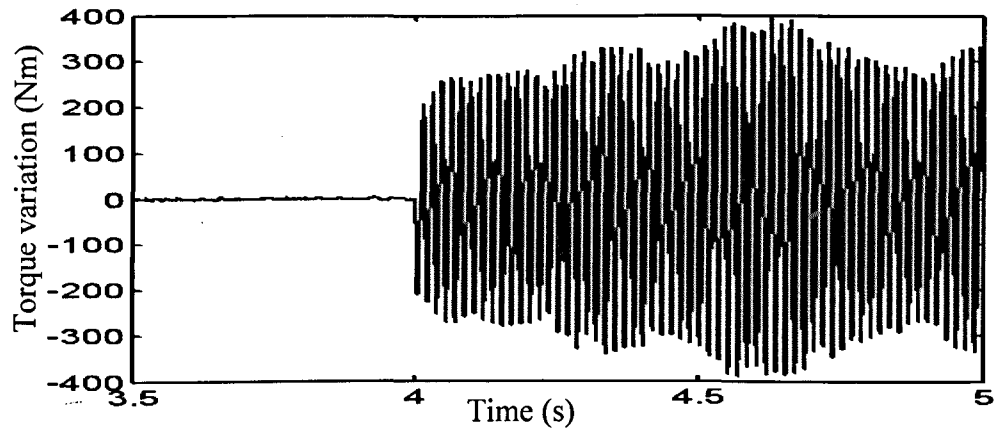

Figure 5.20 Original torsional torque variation (60 Hz, sudden change,10 km/h)

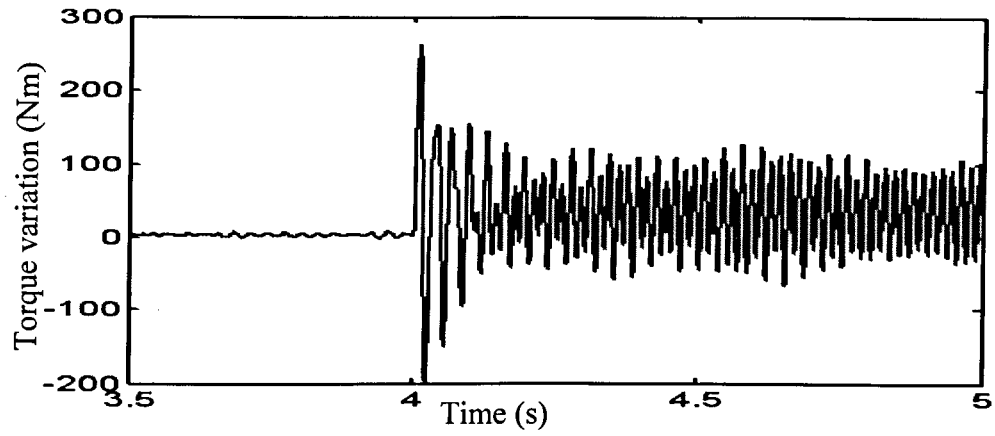

Figure 5.21 Estimation of torsional torque variation (60 Hz, sudden change,10 km/h)

A comparison study is carried out to investigate the effect of different k_1 and k_2 values to the estimation results. Another two sets of k_1 and k_2 values are tried. The large value set is derived from the linear region of the creep-creep force curve as

$$k_1 = k_2 = 2\times10^4 \tag{4.30}$$

The estimation of the torsional torque variation based on this set of date is given in Figure 5.22. It shows a fast response but with large offset of the results. Since the system matrix determined by this set of data is far different from the one in slip conditions where k_1 and k_2 are smaller.

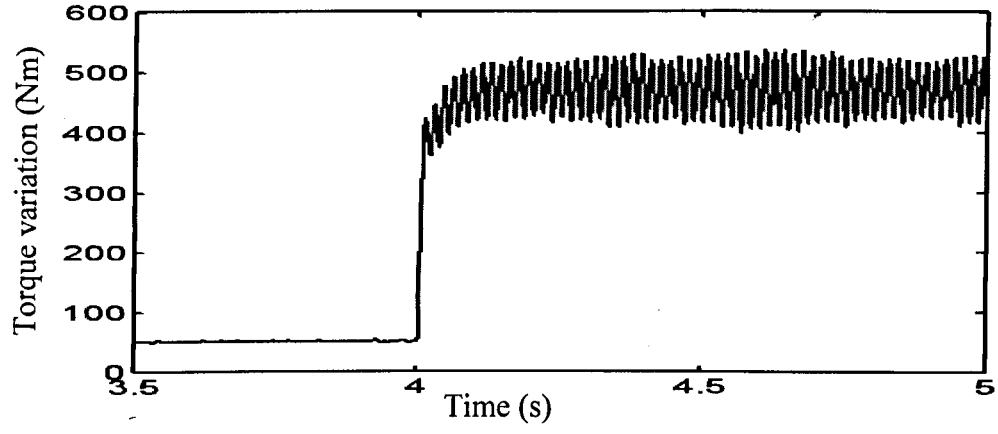

Figure 5.22 Estimation of torsional torque variation

(60 Hz, sudden change,10 km/h, $k_1 = k_2 = 2\times10^4$)

The other lower value set comes from the saturation region as

$$k_1 = k_2 = 0.8 \times 10^3 \tag{4.31}$$

The estimation of the torsional torque variation based on this set is given in Figure 5.23. It shows a similar result as in Figure 5.21 but with a slower response. From the comparison, it can be seen that choosing k_1 and k_2 values from the saturation region can give a better result than those in the linear region.

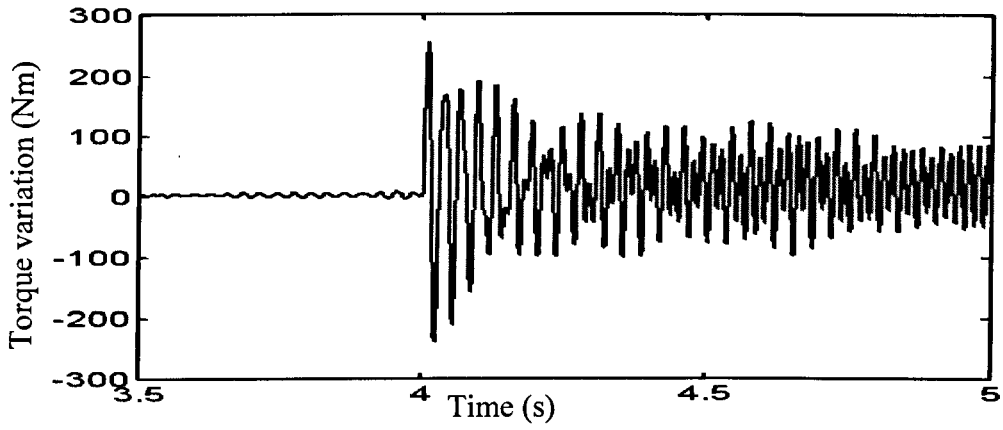

Figure 5.23 Estimation of torsional torque variation

(60 Hz, sudden change,10 km/h, $k_1 = k_2 = 0.8 \times 10^3$)

Then, the 40 Hz and 80 Hz system are considered. Running the simulations considering the contact conditions given in Figure 4.4 with sudden changes at $t = 4$ s and initial speed 10 km/h, the original torsional torque variations obtained by simulation are shown in Figure 5.24 and Figure 5.26 respectively. The Kalman filter estimating results are shown in Figure 5.25 and Figure 5.27 respectively. Both the results confirm that the Kalman filter can work properly in different wheelset model with different natural frequency.

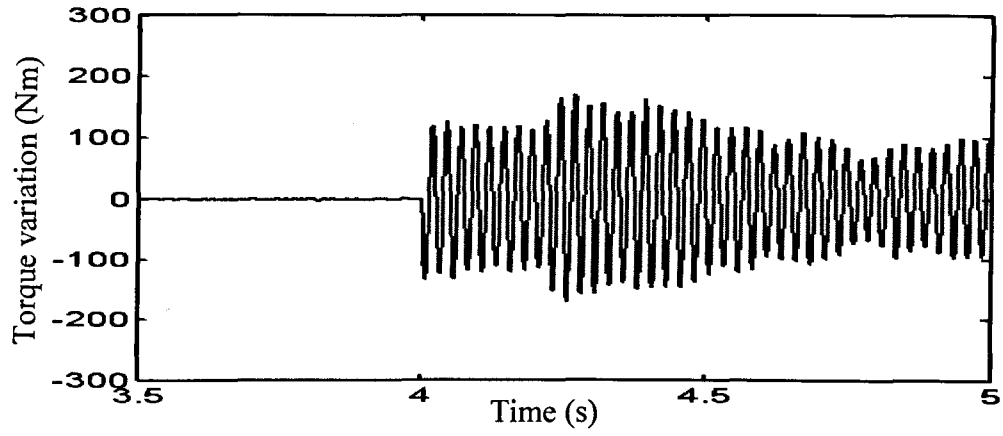

Figure 5.24 Original torsional torque variation (40 Hz, sudden change, 10 km/h)

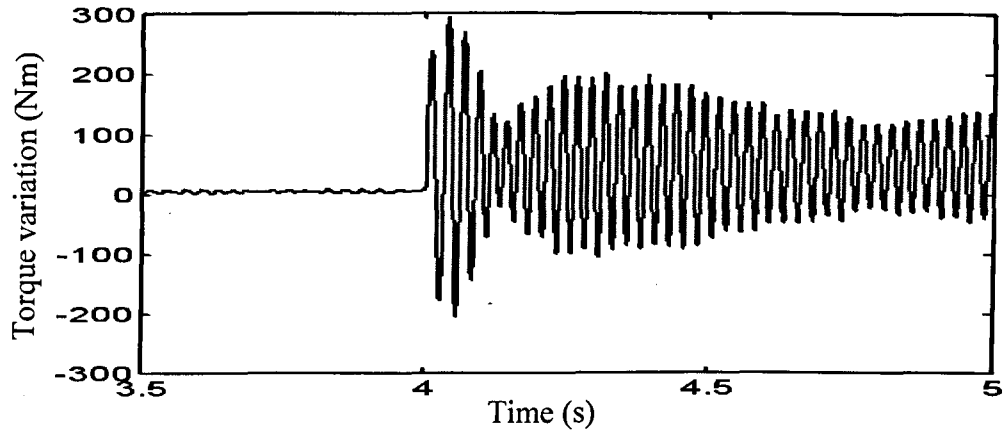

Figure 5.25 Estimation of torsional torque variation (40 Hz, sudden change, 10 km/h)

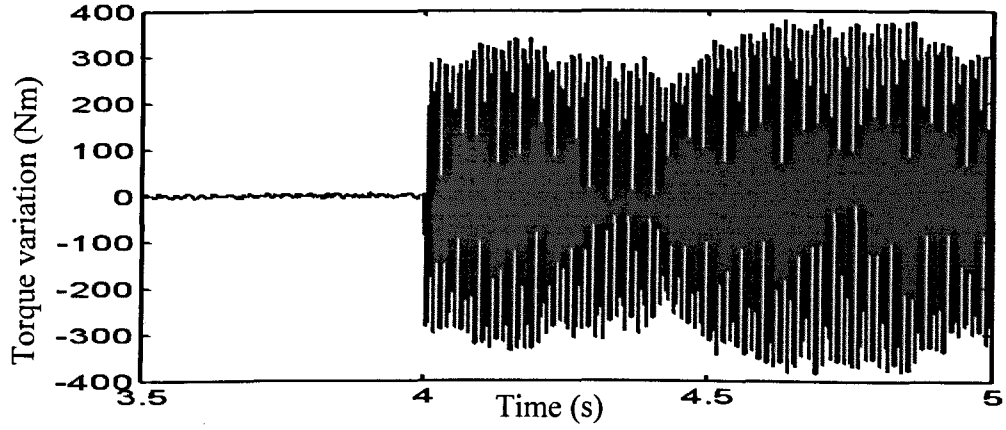

Figure 5.26 Original torsional torque variation (80 Hz, sudden change, 10 km/h)

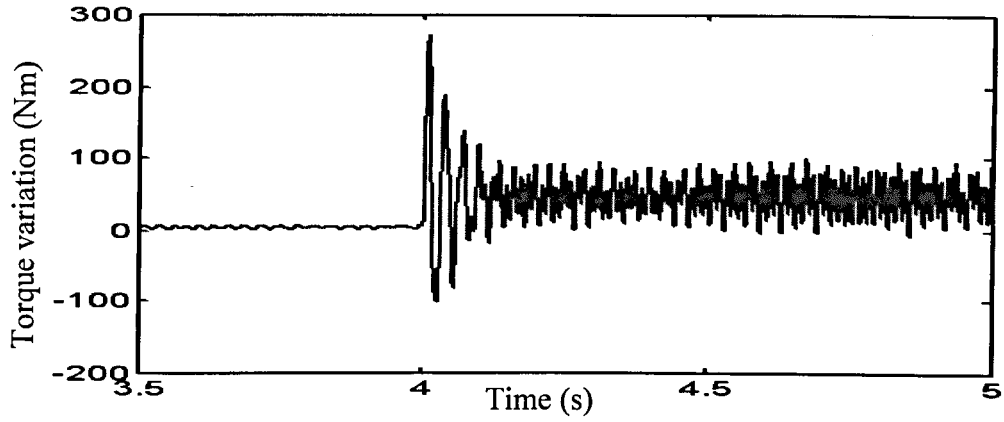

Figure 5.27 Estimation of torsional torque variation (80 Hz, sudden change, 10 km/h)

5.2.5 Slip Detection Based on the Kalman Filter

The estimated torsional torque can be used to replace the direct measurement from the axle. The filter method which is introduced to extract the magnitude information from oscillation signals can be also used to deal with the estimated torsional torque variation information.

Figure 5.28, Figure 5.29 and Figure 5.30 give the magnitude of the natural frequency component based on the estimation of torsional torque variation from the Kalman filter for the wheelset axles at different torsional frequencies. The increase of the magnitude in the slip condition is clear and the trend is consistent with the result shown in Figure 5.5.

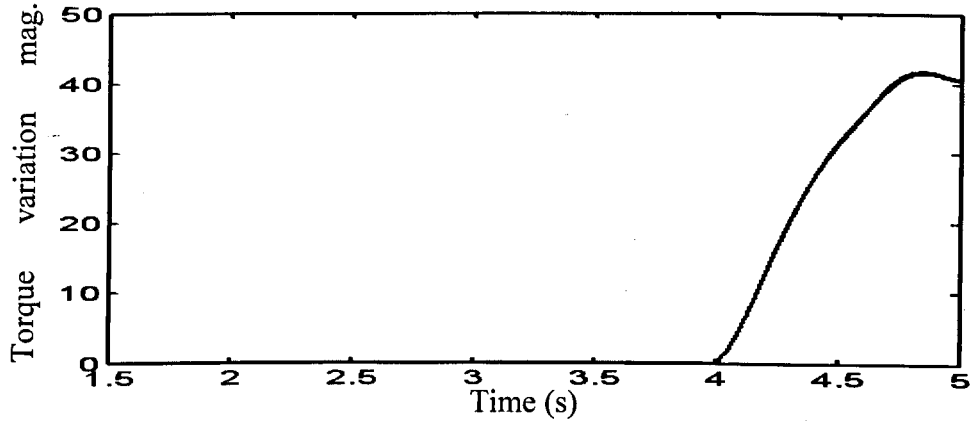

Figure 5.28 Natural frequency component magnitude of torsional torque estimation from filter method (60 Hz, sudden change,10 km/h)

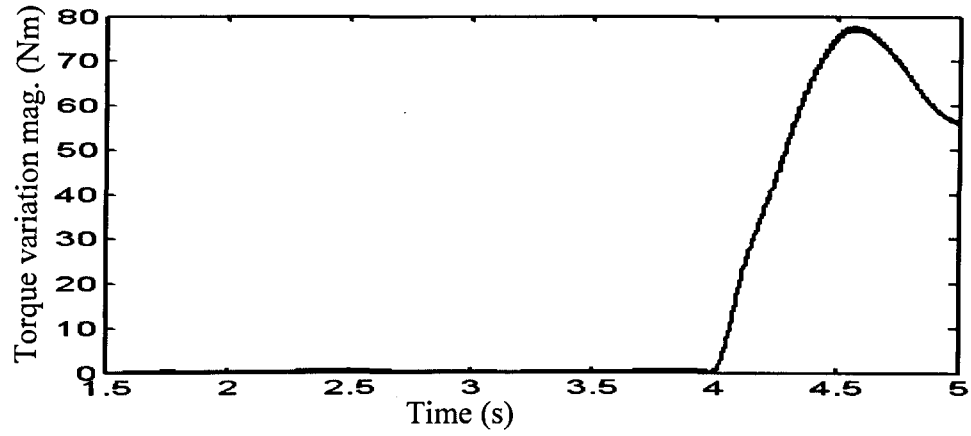

Figure 5.29 Natural frequency component magnitude of torsional torque estimation from filter method (40 Hz, sudden change, 10 km/h)

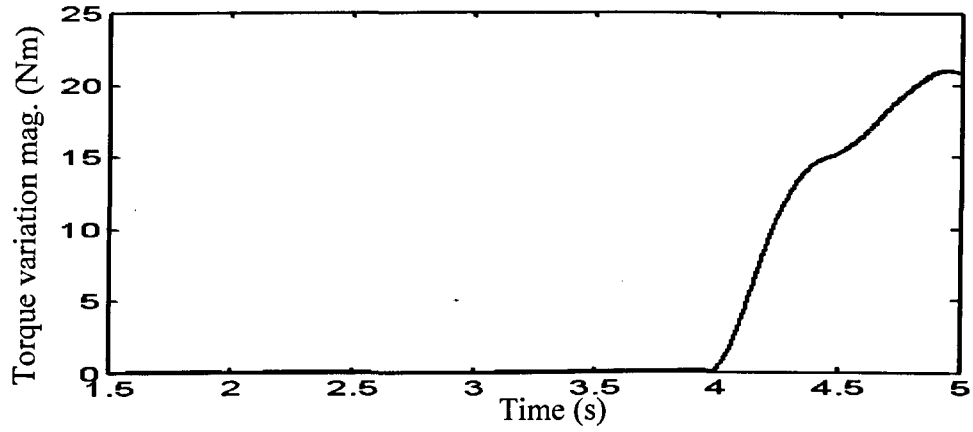

Figure 5.30 Natural frequency component magnitude of torsional torque estimation from filter method (80 Hz, sudden change, 10 km/h)

Similar simulations are carried out by keeping the contact conditions always low instead of sudden changes. Figure 5.31, Figure 5.32 and Figure 5.33 give the actual torsional torque variation, estimated torsional torque variation using Kalman filter and the magnitude history of the natural frequency component respectively with the initial speed 10 km/h. For the initial speed to 100 km/h, the corresponding results are shown in Figure 5.34,Figure 5.35 and Figure 5.36. The results confirm again that the Kalman filter based method can give enough information to detect the torsional vibration appearance in slip conditions.

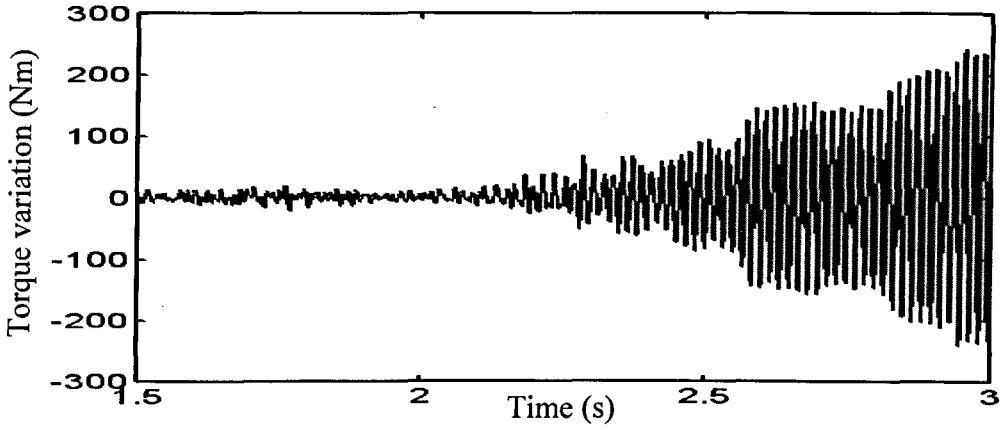

Figure 5.31 Original torsional torque variation (60 Hz, low contact condition, 10 km/h)

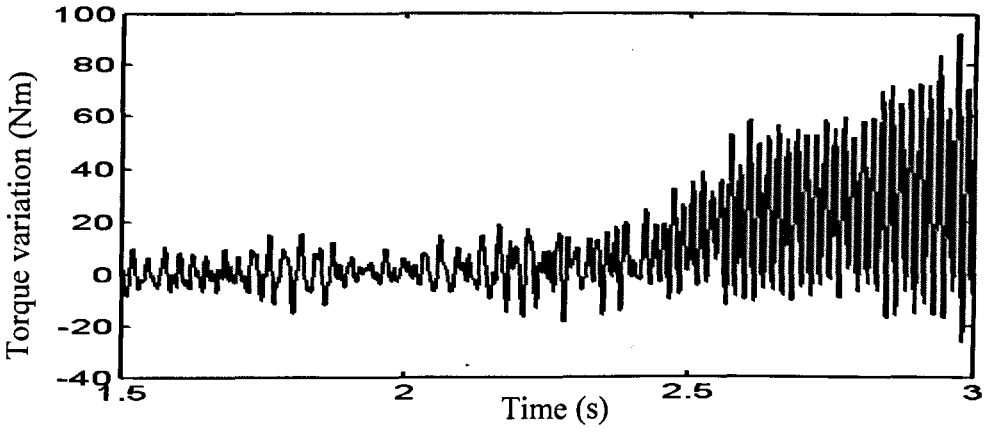

Figure 5.32 Estimation of torsional torque variation (60 Hz, low contact condition, 10 km/h)

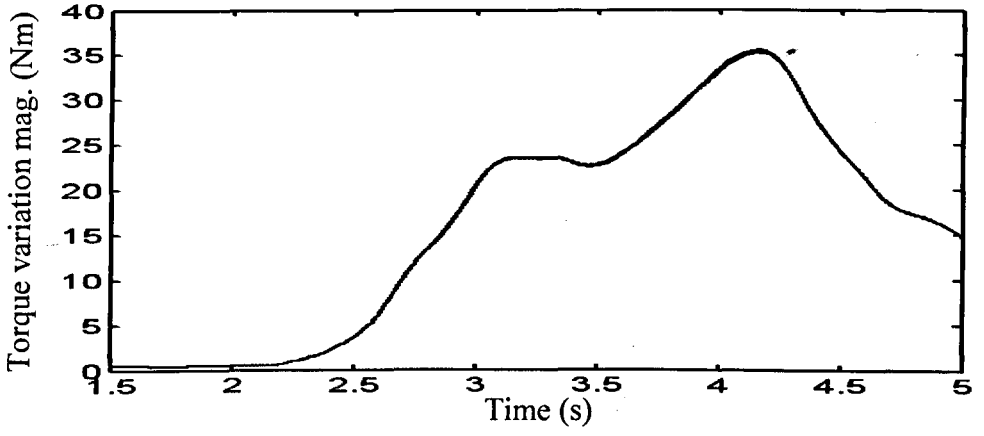

Figure 5.33 Natural frequency component magnitude of torsional torque estimation from filter method (60 Hz, low contact condition, 10 km/h)

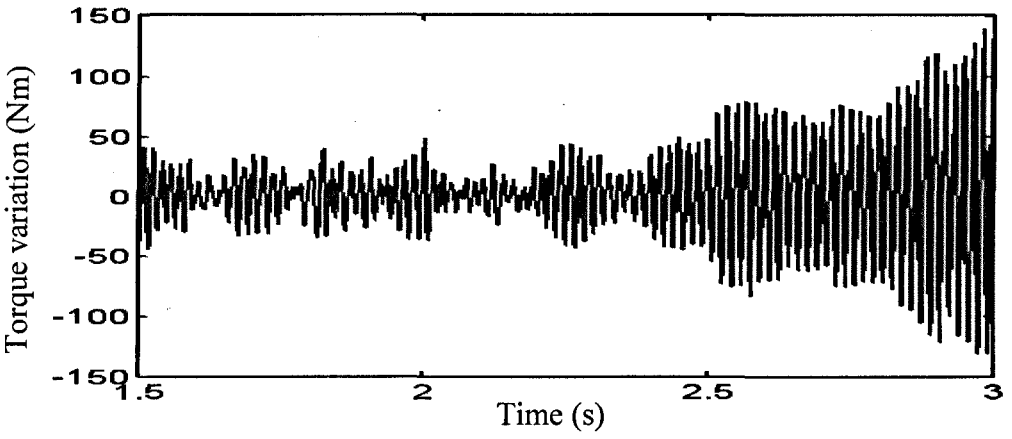

Figure 5.34 Original torsional torque variation (60 Hz, low contact condition, 100 km/h)

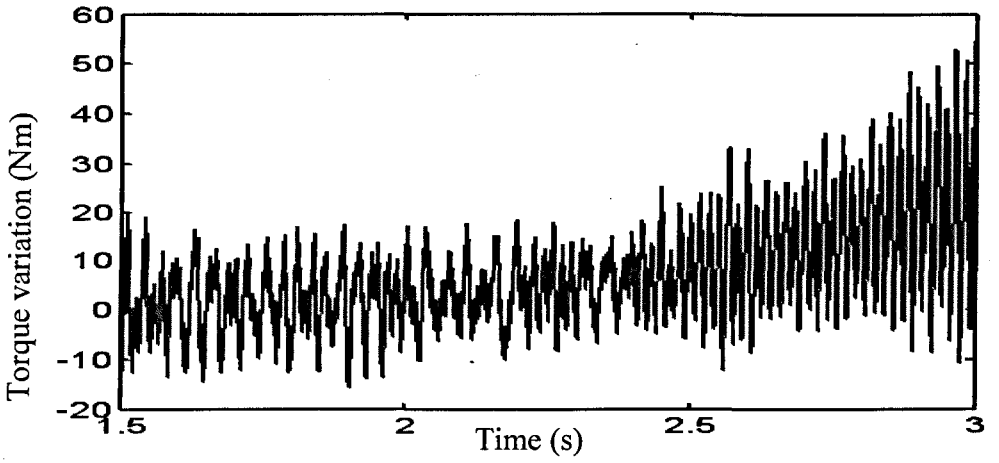

Figure 5.35 Estimation of torsional torque variation (60 Hz, low contact condition, 100 km/h)

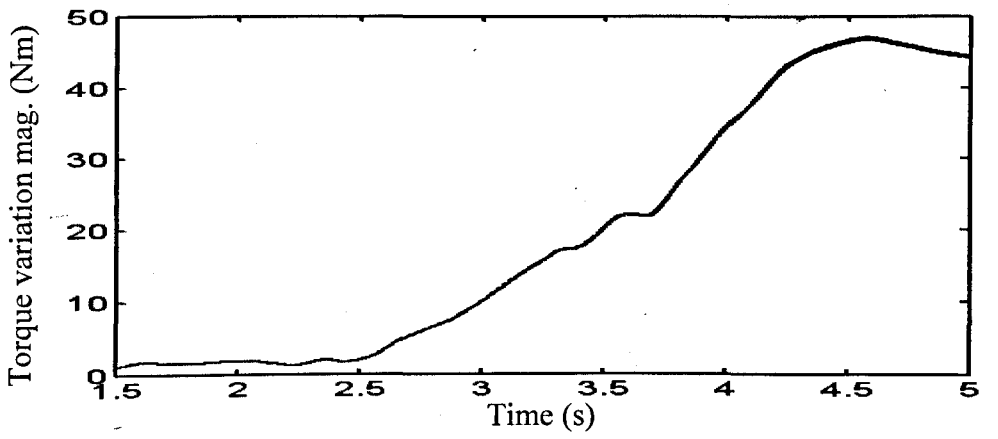

Figure 5.36 Natural frequency component magnitude of torsional torque estimation from filter method (60 Hz, low contact condition, 100 km/h)

5.3 Effect of Practical Position Encoder

5.3.1 Speed Calculation Based on Position Encoder

As introduced in the FOC control strategies for induction motors, a position sensor is used to obtain the rotor speed/position. Because of the harsh operational conditions for railway vehicles and the issue of cost, it is very difficult to realize a sensor with as many pulses per revolution as the encoder has in other industrial applications [25]. In the following studies, a 100 pulse/rev encoder is considered.

A basic way to calculate speed is to count pulses over a fixed time period. The pulse counted from the encoder is sampled at a fixed rate as 1ms.

By differentiating the encoder pulse in each sampling period, the motor speed can be obtained [80]. The block diagram of this method is shown in Figure 5.37.

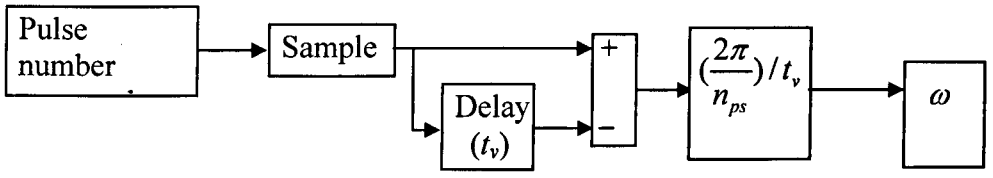

Figure 5.37 Basic velocity calculation method

The speed is given as

$$\omega = (N_p \cdot \frac{2\pi}{n_{ps}})/t_v \tag{4.32}$$

where, N_p is the pulse number counted in a fixed period, t_v is the time interval to update N_p value, n_{ps} is the resolution of the position encoder.

The performance of this method is evaluated using a testing ramp speed signal and the results is shown in Figure 5.38 where t_v is set as 5 ms and the resolution of the position sensor is 100 pulses/rev.

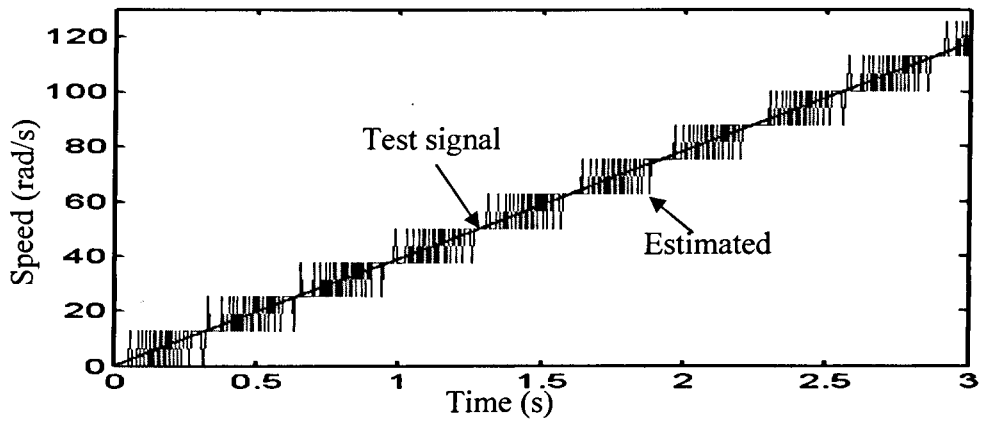

Figure 5.38 Velocity estimation against test speed signal (method 1)

The second method shown in Figure 5.39 is developed from the first one: calculating speed using average pulse number change in a fixed interval, for example 1 ms, defined as t_{v0}. The average is calculated in a longer time window $M \cdot t_v$ (M is an integer), for example 5 ms. In a consecutive $M \cdot t_{v0}$ time window, the information of the pulse number is updated every t_{v0} interval. That means the latest pulse number information is used to calculate the speed.

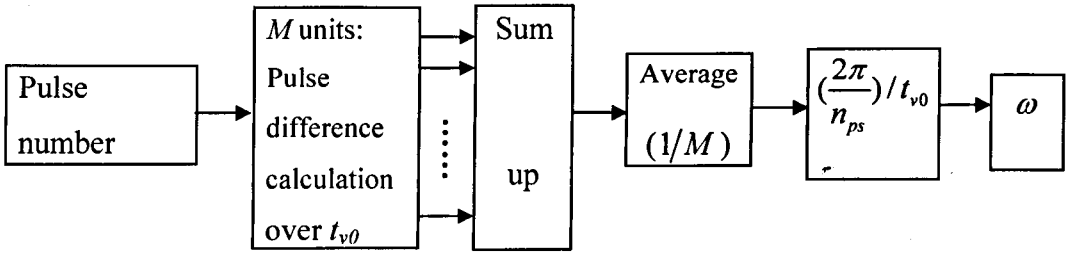

Figure 5.39 Velocity calculation using average pulse number variation

Figure 5.40 gives the estimation results using the same ramp test signal and same position sensor of resolution of 100 pulses/rev, and t_{v0} is set as 1ms, M is taken as 5.

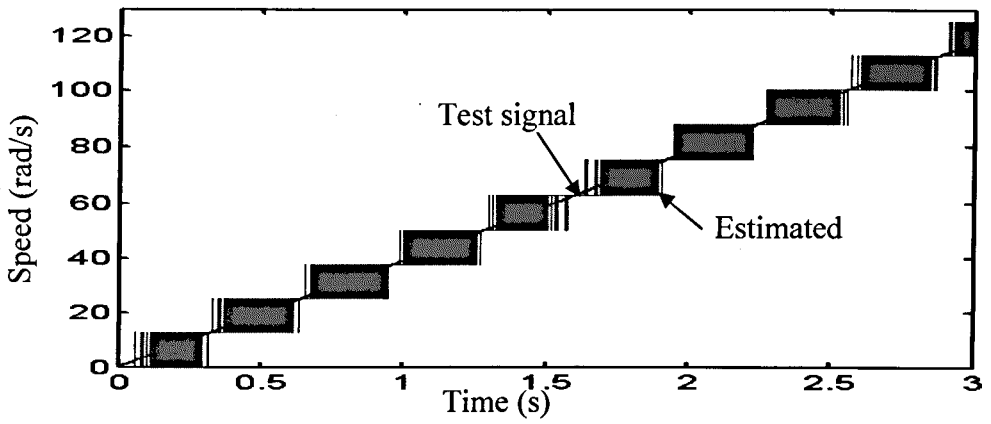

Figure 5.40 Velocity estimation against test speed signal (method 2)

The third method is to estimate the velocity based on the pulse width. The pulse width is measured using a high frequency clock with period T_c. The resultant velocity is given as

$$\omega = \frac{2\pi / n_{ps}}{N_c \cdot T_c} \tag{4.33}$$

where, N_c is the pulses counted from the high frequency clock. Setting T_c as 0.01ms, the estimated result is given in Figure 5.41. It shows a good estimation of the velocity speed in a certain speed range which is lower than 100 rad/s in this case.

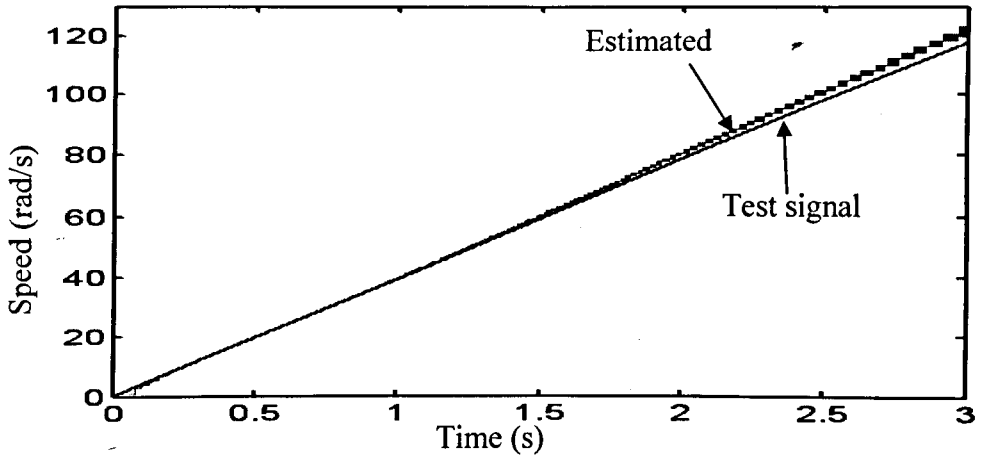

Figure 5.41 Velocity estimation against test speed signal (method 3)

The error between the test signal and the estimated result is increasing with the speed which is due to the limitation of the clock frequency. The accuracy of speed estimation in the higher speed range can be improved by increasing the frequency of the clock or measuring pulse width between two or more pulses of the encoder as illustrated in Figure 5.42. By taking into account the time interval between pulses in addition, the position sensor resolution can be also doubled shown in Figure 5.42 which is useful for low speed measurement. So for the n_{ps} pulses/rev position sensor, it can be actually used as a position sensor with $2n_{ps}$ pulses/rev resolution. On the other hand, in the high speed range, the n_{ps} pulses/rev position sensor can be used as equivalent position sensor with resolutions of $\frac{1}{2}n_{ps}$ pulses/rev, $\frac{1}{3}n_{ps}$ pulses/rev and so on.

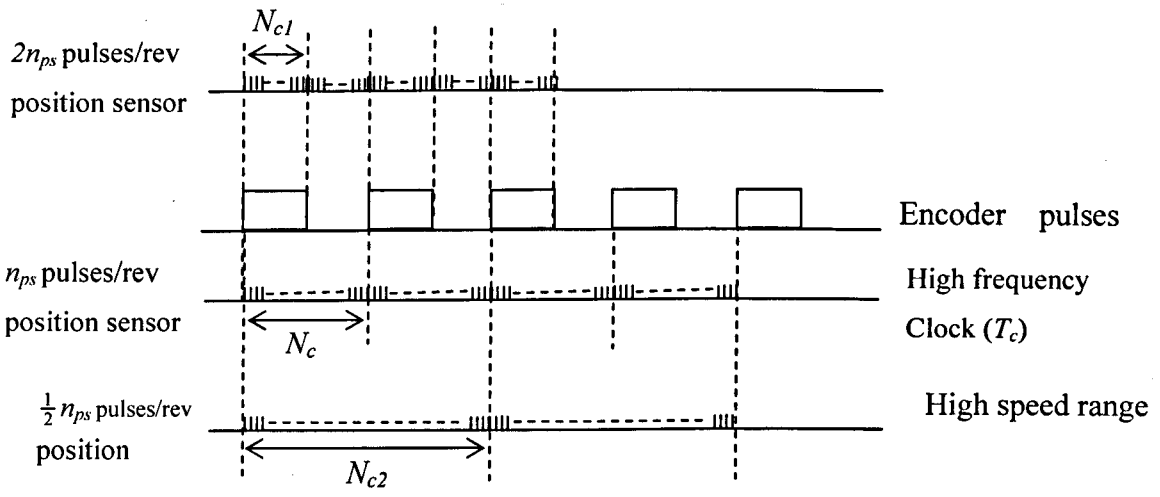

Figure 5.42 Counting method in different speed range

The comparison of the velocity estimations shows that the first two methods introduce a lot of resolution noise, but the third one gives better estimation and less noise. So the third method will be used to estimate the driving wheel speed in the following evaluation.

5.3.2 Slip detection based on Kalman Filter using Practical Sensor

Even though the third method can give a good estimation of the speed, there is still some resolution noise. The noise can be reduced by adding a low pass filter before the speed signal is fed to the Kalman filter [81].

The estimated torsional torque variation using the encoder is given in Figure 5.43 where there is a sudden reduction of the adhesion coefficient at $t = 4\,\mathrm{s}$. Compared with the one without the position sensor in Figure 5.21, it shows that the position sensor introduces a lot of noise in the Kalman filtering. However, the trend of increase of the magnitude in the slip condition is consistent with the one without encoder.

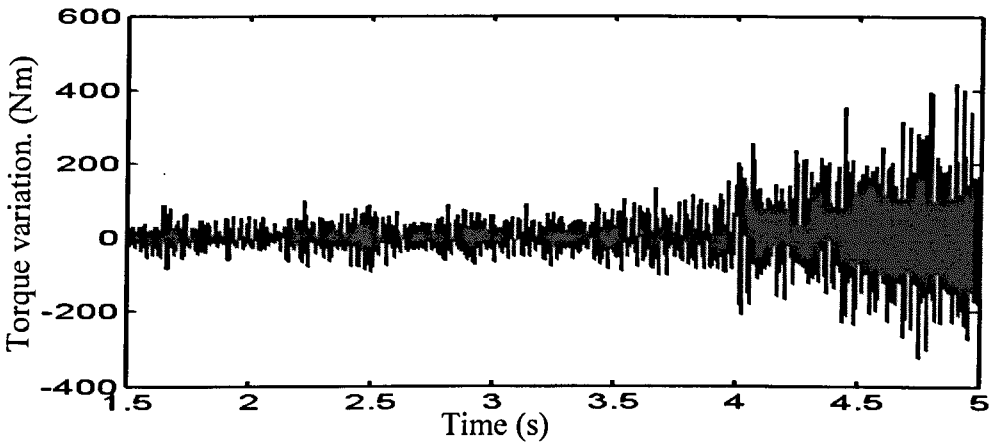

Figure 5.43 Estimation of torsional torque variation with position sensor (60 Hz, sudden change, 10 km/h)

After post data processing using the filtering method, the magnitude of the natural frequency component of the estimated torsional torque variation is given in Figure 5.44. It shows that magnitude increases obviously in slip condition which is consistent with the result shown in Figure 5.28 but with a higher value in normal condition due to the introduction of position sensor. By setting a proper threshold, a slip condition can be indicated in time.

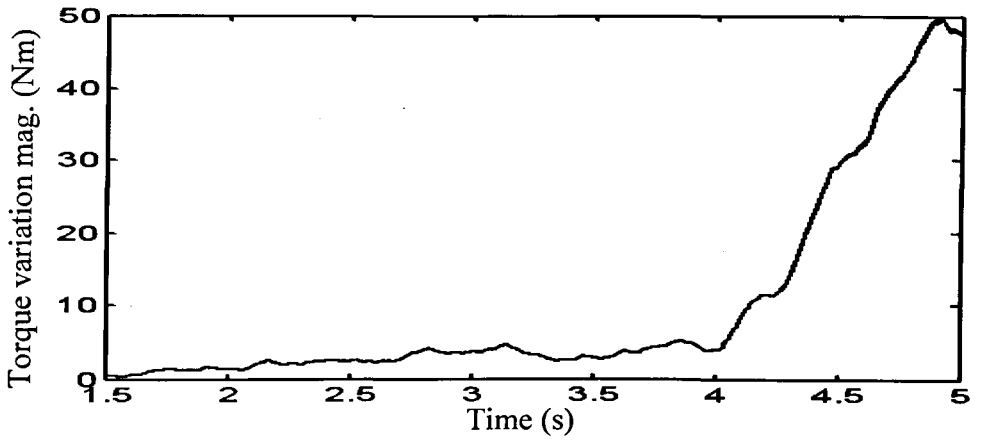

Figure 5.44 Natural frequency component magnitude of torsional torque estimation from filter method with position encoder (60 Hz, sudden change, 10 km/h)

A comparison of different position sensors is carried out under the same condition obtaining the result in Figure 5.44. The natural frequency component magnitudes of torsional torque estimation with position encoders with resolution of 60 pulses/rev, 100 pulses/rev, 200 pulses/rev are compared as shown in Figure 5.45. The high frequency clock is 0.01ms. It shows that all these sensors can generate a proper calculation of the magnitude in this speed range. In the following study, a position sensor with 100 pulses/rev is used.

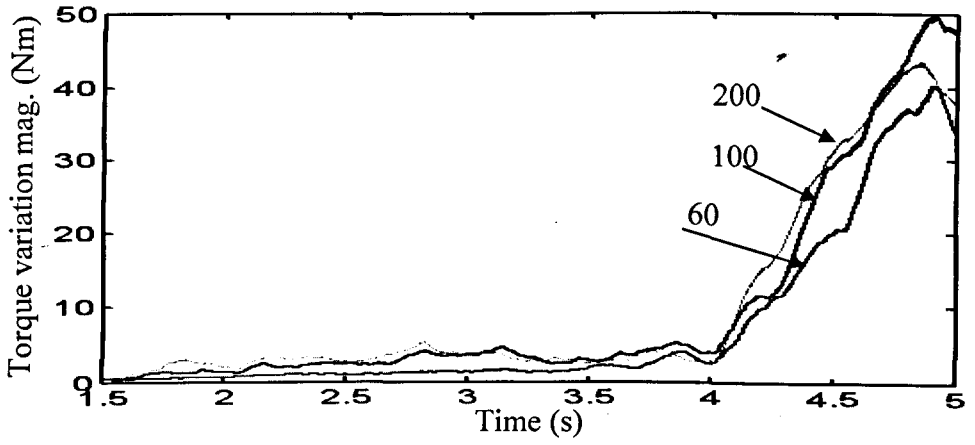

Figure 5.45 Comparison of different position sensors

For the wheelset with different torsional stiffness, the magnitudes of the natural frequency components are shown in Figure 5.46 and Figure 5.47 respectively. The results show that, even with the position encoder, the magnitude trends are consistent with the previous corresponding results without position encoder.

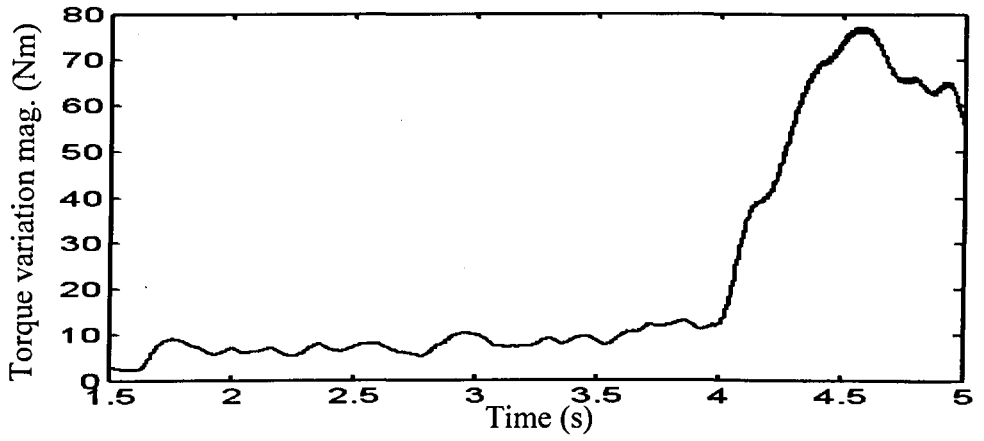

Figure 5.46 Natural frequency component magnitude of torsional torque estimation from filter method with position sensor (40 Hz, sudden change, 10 km/h)

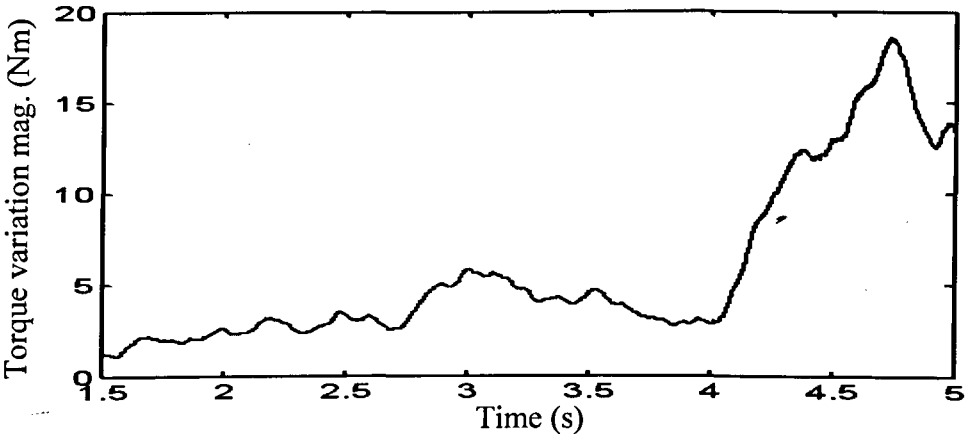

Figure 5.47 Natural frequency component magnitude of torsional torque estimation from filter method with position sensor (80 Hz, sudden change, 10 km/h)

Similar conclusions can also be drawn for the conditions where the adhesion level is always low on the track. Figure 5.48 gives the magnitude of the natural frequency

component when the initial speed is set as 10 km/h. Figure 5.49 gives the magnitude of the natural frequency component when the initial speed is set as 100 km/h.

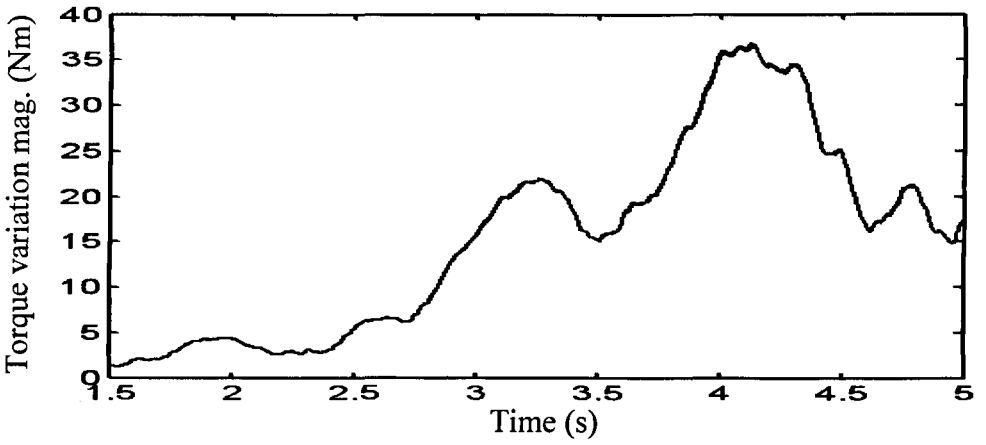

Figure 5.48 Natural frequency component magnitude of torsional torque estimation from filter method with position sensor (60 Hz, low contact condition, 10 km/h)

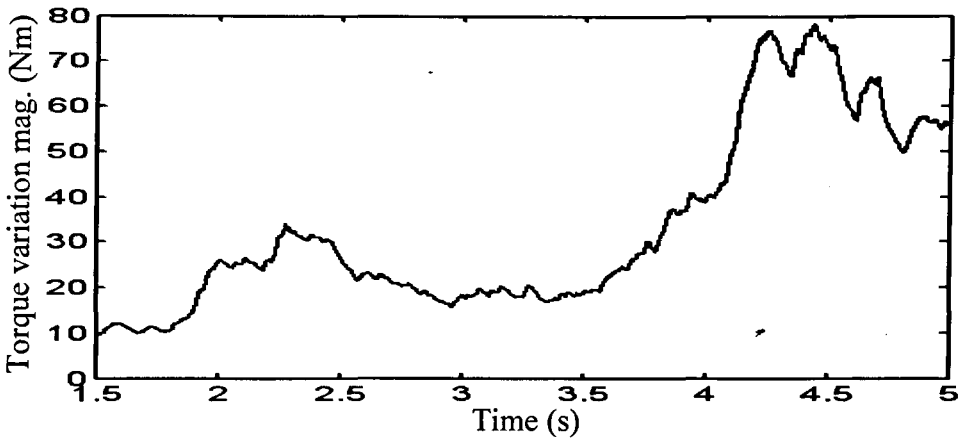

Figure 5.49 Natural frequency component magnitude of torsional torque estimation from filter method with position sensor (60 Hz, low contact condition, 100 km/h)

The results confirm clearly the feasibility and consistency of detecting the slip by monitoring the magnitude of the natural frequency component based on the Kalman filter with practical sensors. For practical applications, a threshold must be selected carefully and probably tuned on line to determine the level of the magnitude above which wheel slip is considered to have occurred.

5.4 Summary

Two slip detection methods are presented and evaluated in different conditions. The results show the consistency and feasibility of both methods. Special attention has been given to the Kalman filter based slip detection with the practical position encoder, and it shows the slip condition can be indicated in time when the threshold is set properly.

6 RE-ADHESION CONTROL SCHEMES

A re-adhesion control scheme is proposed based on the vibration phenomenon. When slip condition is detected from monitoring the vibration signal, it enables a torque control unit to generate a torque reduction command which is fed back to the vector control unit of the induction motor. When the symbolic vibration disappears, it indicates that the system has recovered from the slip condition and regained adhesion in the current wheel rail contact condition.

To realize a re-adhesion control, the critical issue is to determine how much torque needs to be reduced. In this chapter, a torque reduction rule is firstly introduced. Then the performances of the re-adhesion scheme are evaluated with ideal and practical encoders respectively. Finally, the performances are studied based on the comprehensive wheelset dynamics.

6.1 Re-adhesion Control based on Kalman filter

In this section, the basic idea of the re-adhesion control scheme is presented and initially assessed using the ideal position measurement.

6.1.1 Re-adhesion Control model based on Kalman filter

As introduced in Chapter 5, a properly designed Kalman filter can give good estimation of torsional torque variation which provides an important index of slip condition. It is clear that the magnitude in normal condition is close to zero, while in the slip condition, the magnitude increases due to the occurrence of the torsional oscillations. A reduction of the tractive effort applied to below the level of the adhesion is clearly necessary, but the amount of the torque reduction must be set properly. A PI control unit is developed to perform this function. The diagram of the re-adhesion control scheme is given in Figure 6.1.

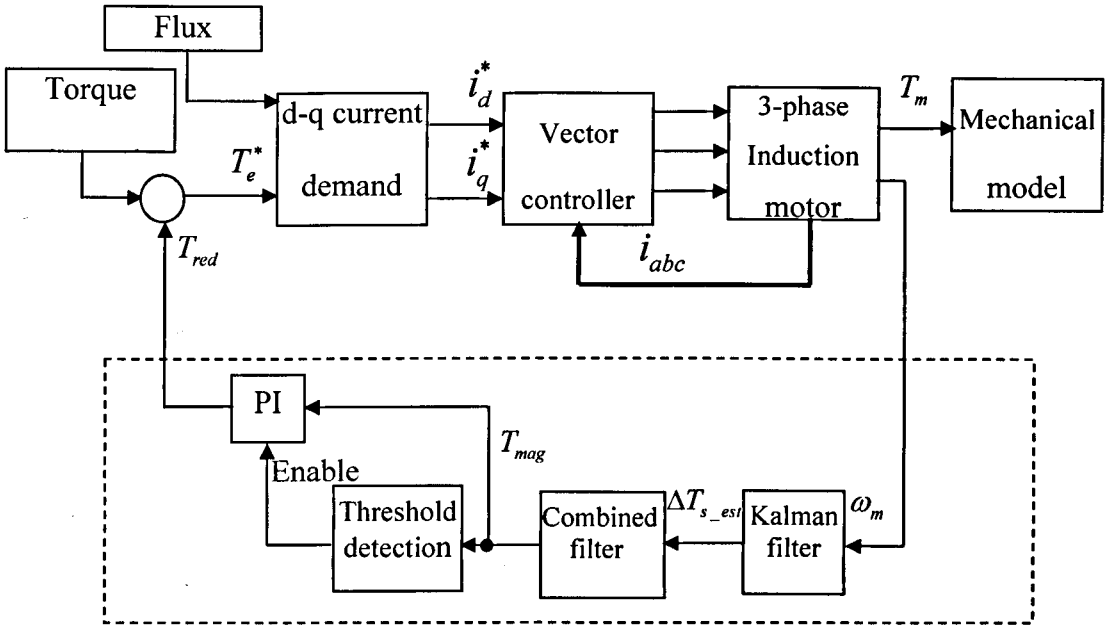

Figure 6.1 Block diagram for re-adhesion control based on Kalman filter

The dashed framed part is the re-adhesion controller based on the Kalman filter. The motor speed is fed to the Kalman filter. The estimated torsional torque variation ΔT_{s_est} is then fed to the combined filtering unit to extract the magnitude of the natural frequency component T_{mag}. In the threshold detection unit, T_{mag} is compared to a rather small threshold which can be set to 5~10 Nm. An enabling command will be generated and fed to the PI controller when T_{mag} is greater than the threshold. Through a PI controller, a torque reduction amount is determined from T_{mag}:

$$T_{red}(s) = (K_P + \frac{K_I}{s})T_{mag}(s) \tag{6.1}$$

6.1.2 Re-adhesion Performance

A simulation is carried out using the wheelset with the torsional mode of 60 Hz. The contact condition is given in Figure 4.4 with a sudden change from a good case to a poor one at $t = 4$ s. The magnitude of the natural frequency component used for slip detection and torque reduction is shown in Figure 6.2.

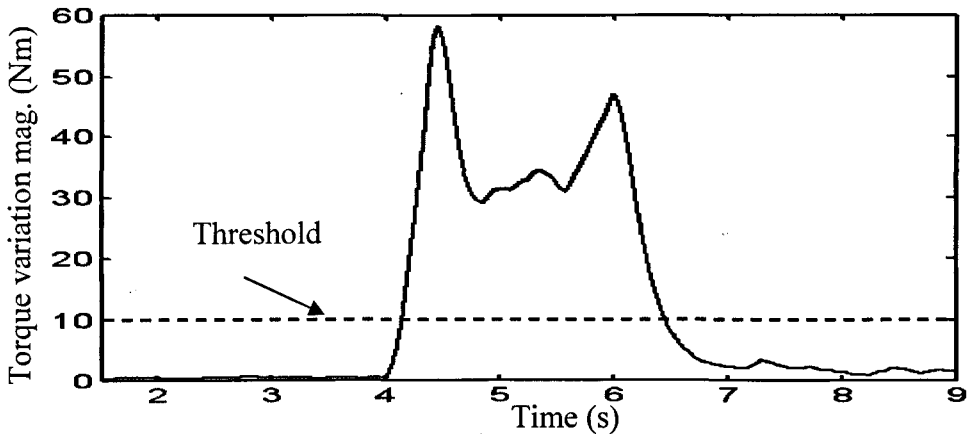

Figure 6.2 Natural frequency component magnitude

of torsional torque variation estimation (60 Hz, sudden change,10 km/h)

By choosing suitable threshold value (10 Nm in this case) and PI controller parameters, a torque reduction demand is generated and sent to the input of the motor controller. Hence the motor output torque which drives the wheel is reduced as shown in Figure 6.3.

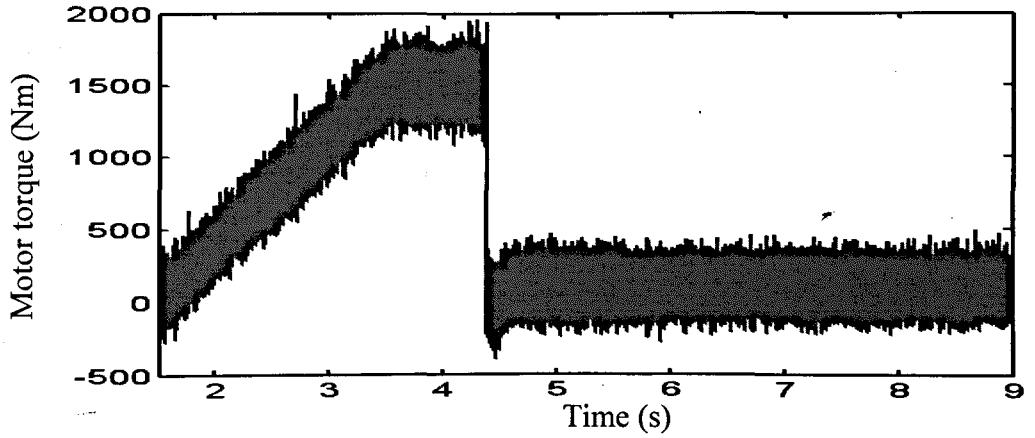

Figure 6.3 Motor torque (60 Hz, sudden change, 10 km/h)

The resultant effect of the re-adhesion can be observed from the speeds signals as shown in Figure 6.4. It can be seen that after slip happens, the creepage reaches as much as 70% within 0.4 s before being detected. Once the slip condition is detected, the motor torque is reduced due to the fast response of vector controller. It takes

about 1.6 s to withdraw the splitted wheel speed back to the vehicle speed due to the action of the re-adhesion scheme, and then the vehicle is accelerated stably in the new contact condition.

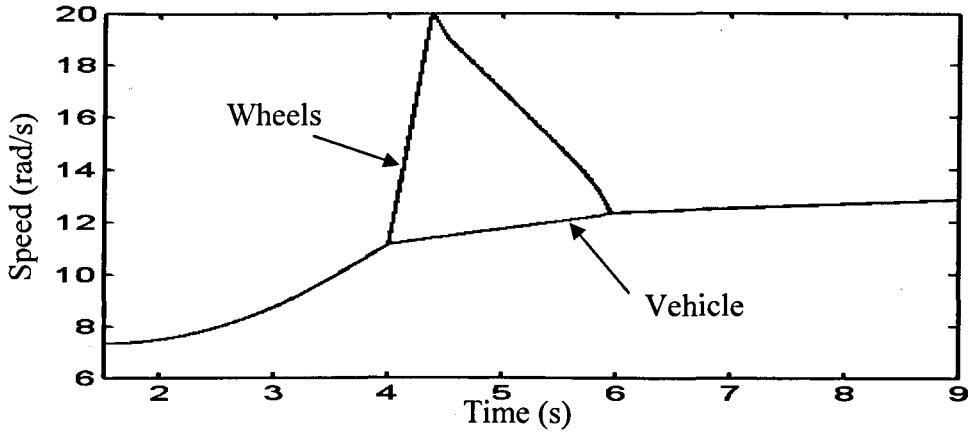

Figure 6.4 Wheels and vehicle angular speeds (60 Hz, sudden change, 10 km/h)

Figure 6.5 presents an overview of the torsional toque variation. From the close shot of the time period 3.8-4.4 s given in Figure 6.6, it is clear that, after the contact condition is suddenly changed at $t = 4$ s, torsional vibrations appear which indicates a slip condition. Figure 6.7 gives the close shot of the torsional torque during the time period 5.5-6.1 s where the system regains adhesion. The absence of the torsional torque vibration after about 5.96 s indicates that the system is no longer slipping due to the effect of the re-adhesion control scheme. The waveform of the torsional torque confirms that the torsional torque vibrations will only appear in the slip conditions.

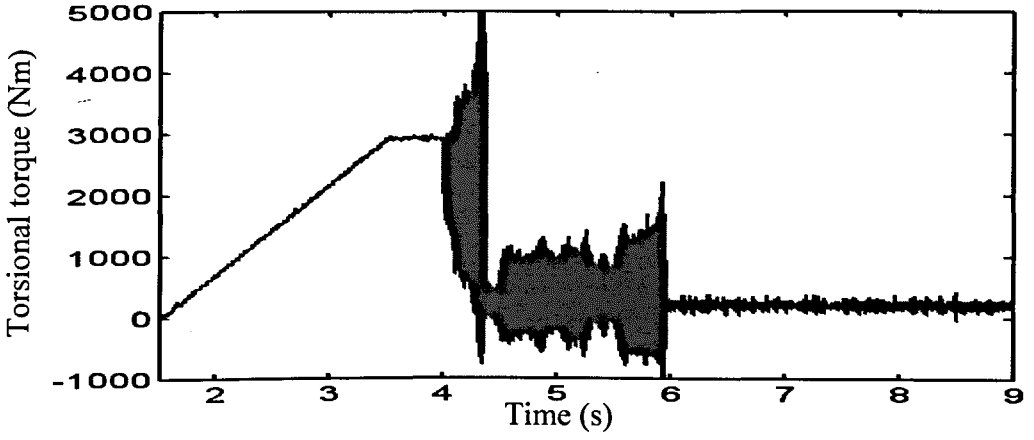

Figure 6.5 Torsional torque (60 Hz, sudden change, 10 km/h)

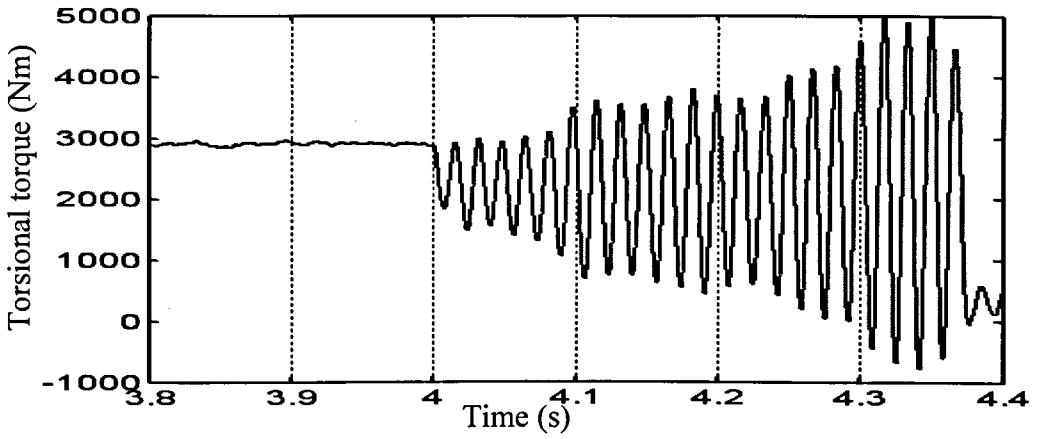

Figure 6.6 Close shot of the torsional torque (3.8-4.4 *s*, 60 Hz, sudden change, 10 km/h)

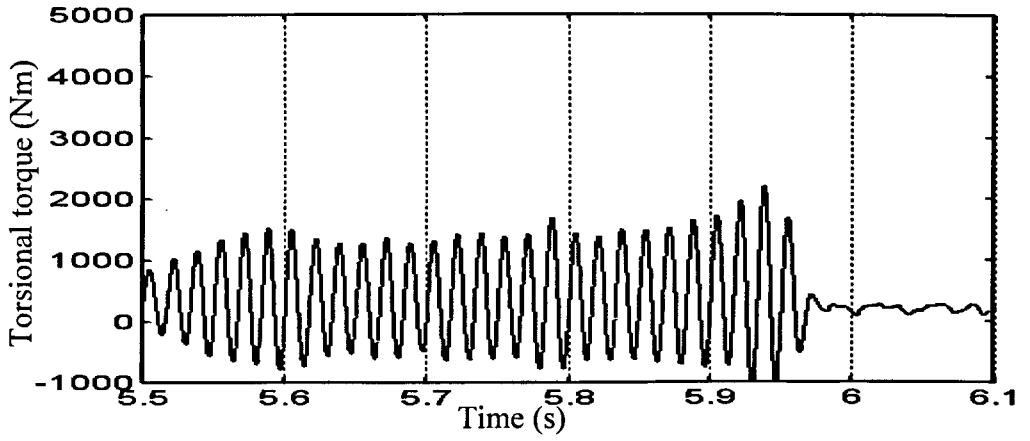

Figure 6.7 Close shot of the torsional torque (5.5-6.1 s, 60 Hz, sudden change, 10 km/h)

Figure 6.8 illustrates the effectiveness of the re-adhesion scheme for the wheelset with a softer shaft where the Kalman filter related parameters and the filter parameters are tuned to extract the 40 Hz component, the wheels' speed and vehicle speed are shown in Figure 6.8. The slip condition is detected almost as soon as the condition changes within 0.1 s. It takes a bit longer to actually reduce the wheel speed where the maximum creepage reaches about 120%. However, once the amount of torque is reduced enough, it only takes 0.8 s for the wheel speeds to be drawn back to the speed of vehicle.

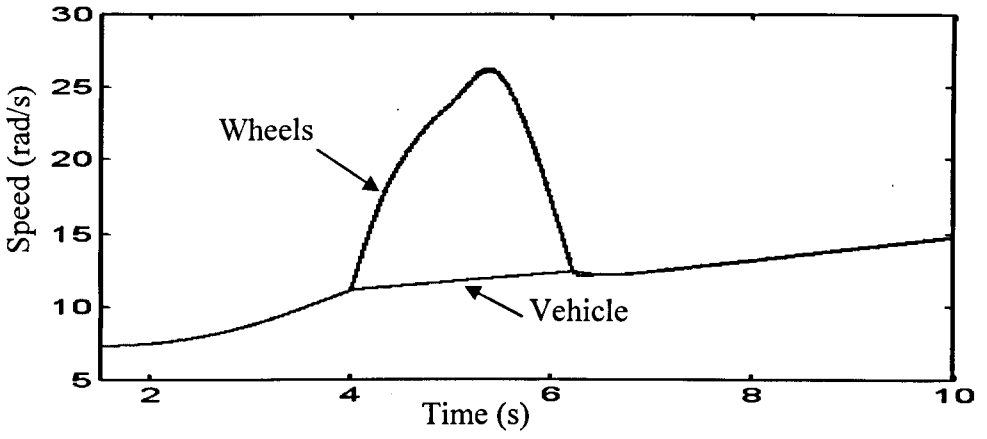

Figure 6.8 Wheels and vehicle angular speeds (40 Hz, sudden change, 10 km/h)

Similarly, Figure 6.9 confirms that this re-adhesion control scheme can work for the 80 Hz system as well. As it shows, the wheel slip is detected and a complete re-adhesion is achieved within 2 seconds. In this case, a second (smaller) slip occurs but is quickly detected and eliminated by the controller, which is clearly evidence that the system works very closely to the optimal point of the slip curves.

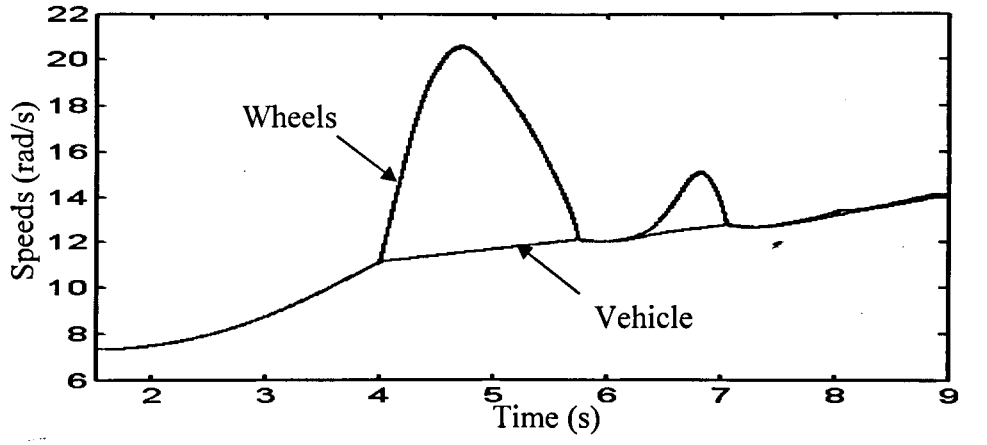

Figure 6.9 Wheels and vehicle angular speeds (80 Hz, sudden change,10 km/h)

Finally, considering the initially low contact condition, the re-adhesion control scheme can also work in cases where the initial speed is set to 10 km/h and 100 km/h respectively. Figure 6.10 gives the performance of the re-adhesion scheme when the initial speed of the vehicle is 10 km/h and Figure 6.11 shows the performance when the initial speed is 100 km/h. It is noticed that the wheel slips tend to be less severe

than the sudden change conditions where the maximum creepages are less than 15% because of the relative low driving torques to the wheelset. On the other hand, the torsional vibrations are smaller and less sensitive to the slip conditions. However, the results show that the proposed re-adhesion scheme delivers a robust performance.

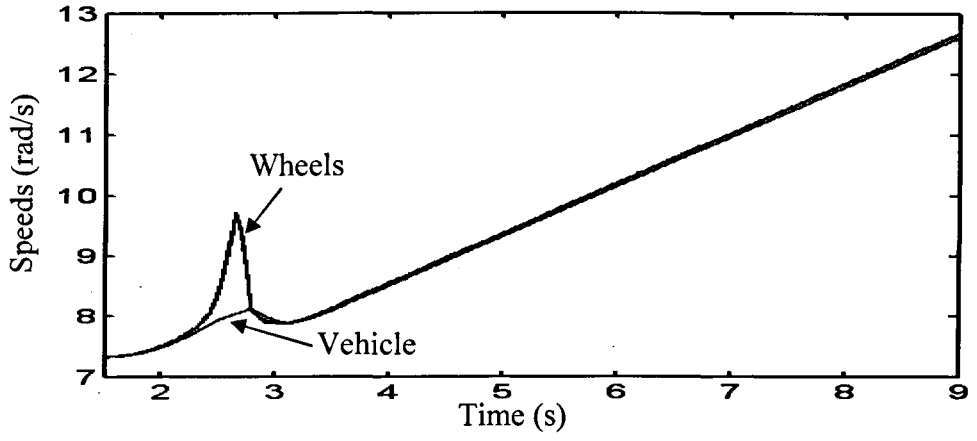

Figure 6.10 Wheels and vehicle angular speeds (60 Hz, low contact condition, 10 km/h)

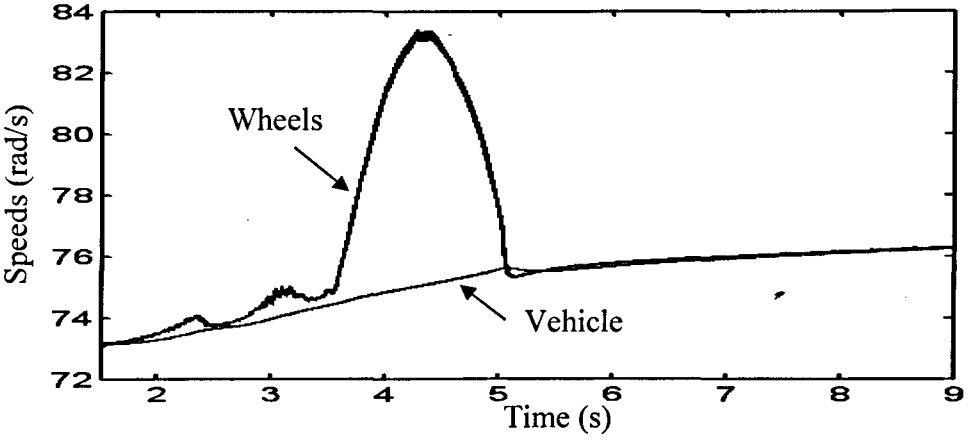

Figure 6.11 Wheels and vehicle angular speeds (60 Hz, low contact condition, 100 km/h)

6.2 Assessment with Practical Sensing

In this section, the re-adhesion scheme based on Kalman filter will be evaluated under the consideration of practical sensing. The resolution the position encoder used in the study is 100 pulses/rev.

The position encoder introduces resolution noise into the scheme, the Kalman filter estimated results have higher value than those with ideal position sensors stated in Chapter 5. Therefore a higher threshold value is needed. By properly setting the threshold and tuning the PI controller for torque reduction control, satisfactory re-adhesion performances can be achieved.

Figure 6.12 presents the re-adhesion scheme performance with the practical encoder, where the shaft torsional mode is set to 60 Hz. The simulation is carried out with a 60 Hz system. The contact condition is defined by Figure 4.4 with a sudden change from a good condition to a poor condition at $t = 4$ s, and the initial speed is 10 km/h. The results shows that the total recovery only takes less than 1.5 s with the maximum creepage less than 70%, which delivers a faster re-adhesion performance without the position sensor.

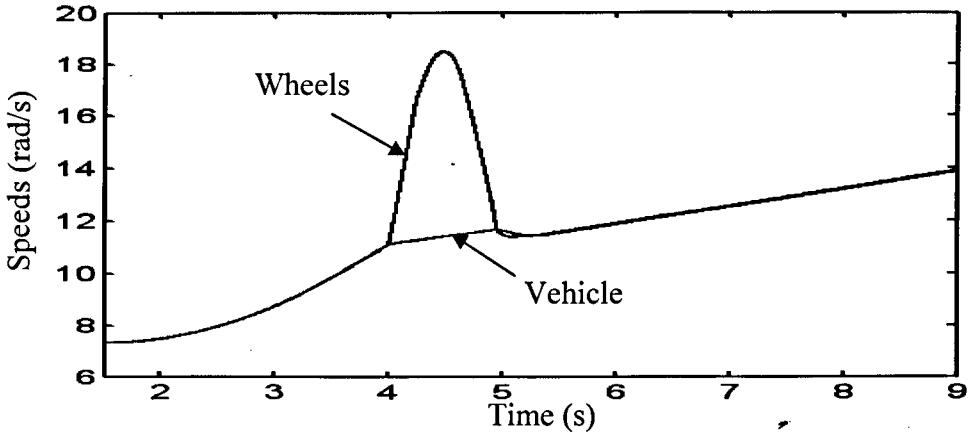

Figure 6.12 Wheels and vehicle angular speeds with practical sensor (60 Hz, sudden change, 10 km/h)

Figure 6.13 and Figure 6.14 present the performance of the re-adhesion control scheme with practical sensors for 40 Hz and 80 Hz axles respectively. Both cases show the re-adhesion can be achieve within 1.5 s, which are faster than those without position sensors. The faster response is mainly due the higher value of the estimation output from the Kalman filter based on the practical position sensor which results a higher output of the PI controller for the torque reduction.

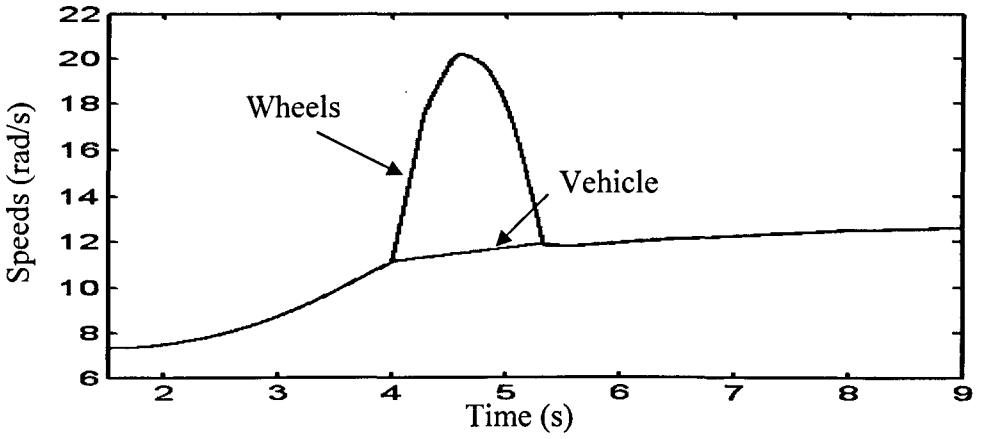

Figure 6.13 Wheels and vehicle angular speeds with practical sensor (40 Hz, sudden change, 10 km/h)

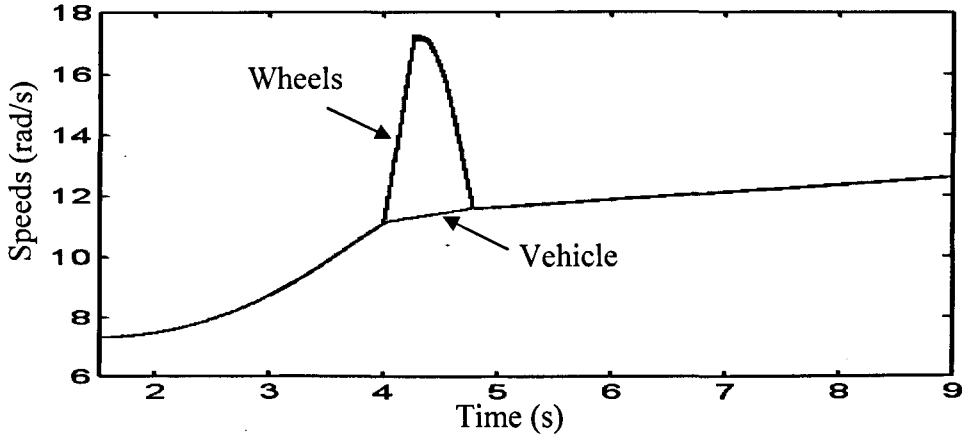

Figure 6.14 Wheels and vehicle angular speeds with practical sensor (80 Hz, sudden change, 10 km/h)

Figure 6.15 and Figure 6.16 give the results for the 60 Hz axle with initially low contact condition but different initial speeds. One is 10 km/h and the other is 100 km/h. Both the results show that the re-adhesion control scheme can work properly. The slip conditions can be detected and be recovered within 2 seconds.

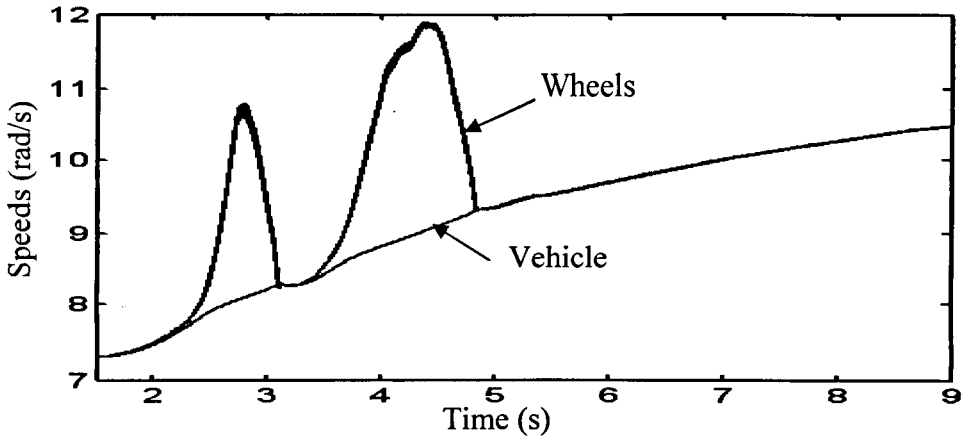

Figure 6.15 Wheels and vehicle angular speeds with practical sensor (60 Hz, low contact condition, 10 km/h)

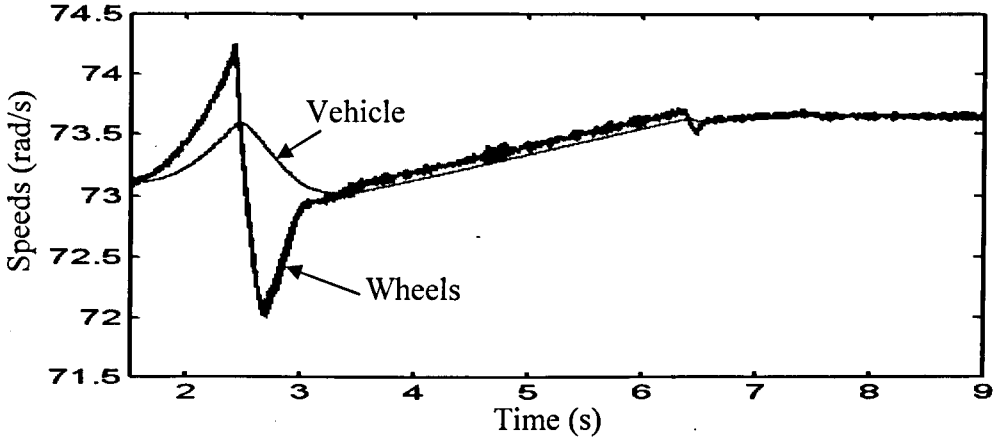

Figure 6.16 Wheels and vehicle angular speeds with practical sensor (60 Hz, low contact condition, 100 km/h)

6.3 Assessment with the Comprehensive Wheelset Model

A comprehensive wheelset model has already been introduced in Chapter 3, although a wheelset model with simplified longitudinal dynamics is used to develop re-adhesion controller. In this section, the dynamics of a comprehensive wheelset model, where the yaw and lateral dynamics are taken into account, will be used to evaluate the performance of the developed re-adhesion controller.

6.3.1 Wheelset Dynamics based on Comprehensive Wheelset Model

The complete dynamic model of the wheelset as described in Chapter 3 is built in Simulink, a block diagram of which is shown in Figure 6.17. The additional parameters of the model are given in Table 6.1.

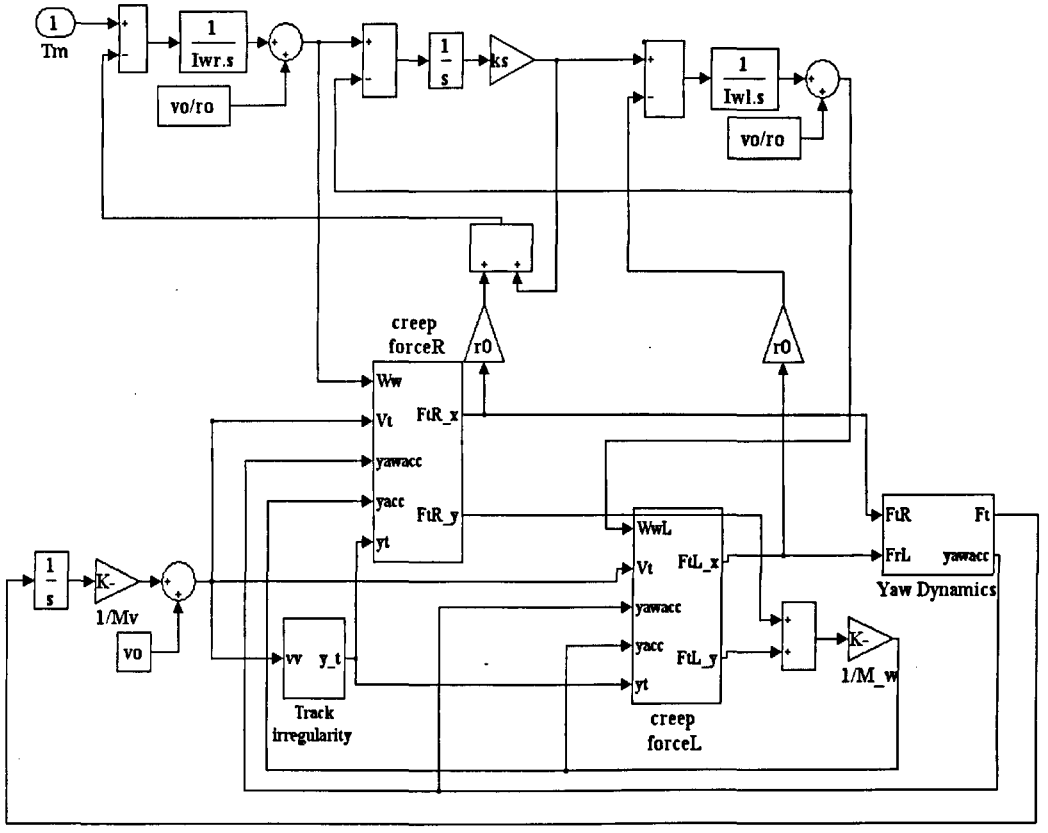

Figure 6.17 Simulation model for the comprehensive wheelset model

Variables	Definitions and values
m_{ws}	Wheelset mass (2714 kg)
I_{ws}	Wheelset yaw inertia (1397 kgm^2)
k_w	Yaw spring stiffness (5×10^6 N/m)
γ	Conicity of wheel (0.2)
L_g	Half gauge length (0.7175 m)

Table 6.1 Parameters for comprehensive wheelset model

In addition to the longitudinal and rotational motions, the dynamics of the wheelset yaw and lateral modes are also included in the comprehensive model. The creepages and hence creep forces in the yaw and lateral directions are results of the wheelset responding to the track input excitation and will affect the performance of the re-adhesion control, as the total contact force is limited by the maximum adhesion available a the same wheel-rail contact point.

Simulation is carried out using the contact condition defined in Figure 4.4 with a sudden change at $t = 4\,s$. The initial speed of the vehicle is set at 10 km/h. The track irregularity shown in Figure 6.18 is generated to represent the track misalignment y_t of a typical mainline [82] and the corresponding velocity $\dot{y}_t$ given in Figure 6.19.

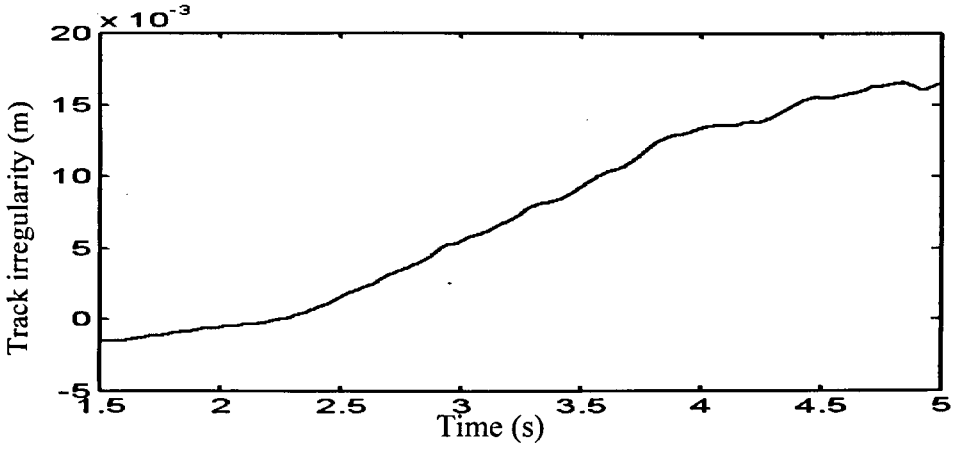

Figure 6.18 Track irregularity y_t

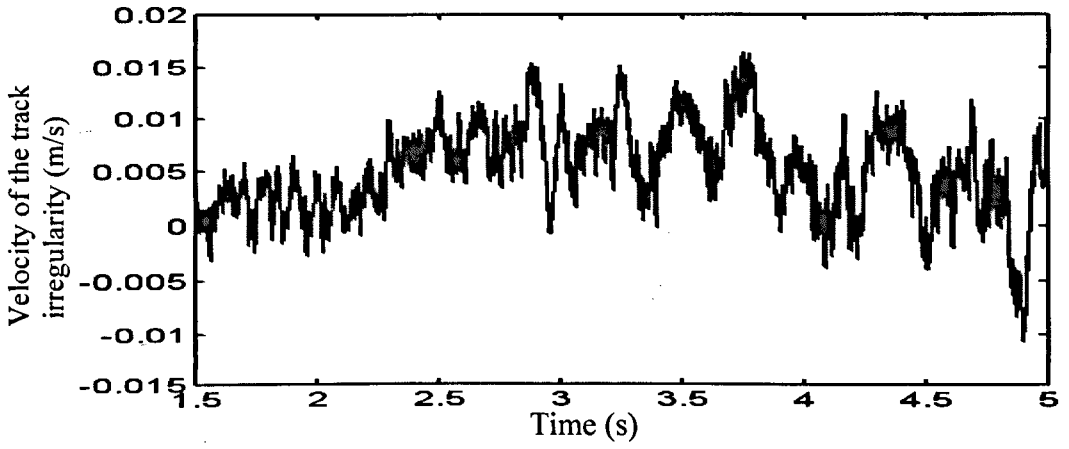

Figure 6.19 Velocity of the track irregularity $\dot{y}_t$

Figure 6.20 gives the resultant disturbances to the longitudinal creepage. It shows that in the stable operation condition before $t = 4\,\mathrm{s}$, the disturbance is very small. When a slip condition is developed, a vibration appears. This vibration reflects a sustained yaw and lateral oscillations. The oscillations with a frequency of 9.5 Hz show that, the loss of adhesion also causes the instabilities in lateral and yaw motions. Therefore a good re-adhesion control scheme is also desirable in the point of view of vehicle stability.

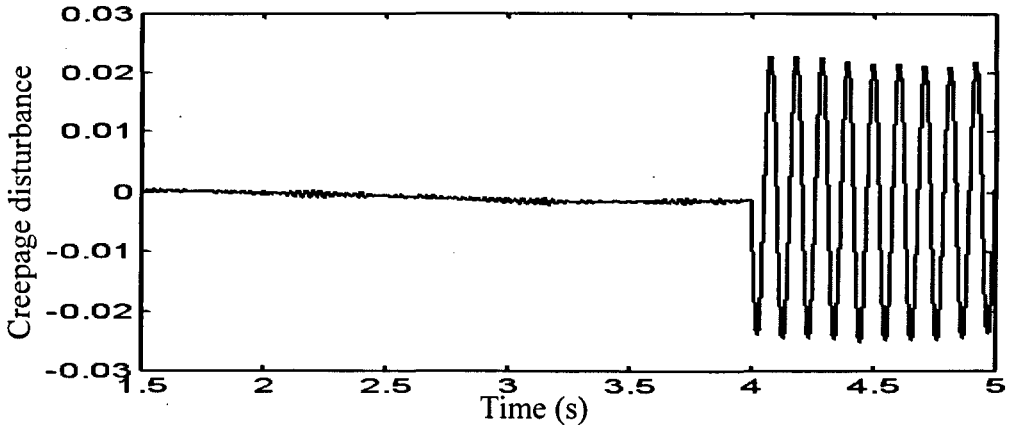

Figure 6.20 Longitudinal creepage disturbance (60 Hz, sudden change, 10 km/h)

However, the longitudinal creepage is still dominated by the wheel spinning in the slip condition as shown Figure 6.21. The trend of the longitudinal creepage is consistent with the one with the simplified wheelset model: rather small in normal conditions and increasing in slip conditions. It is clear that additional wheelset instability does introduce obvious pulsations in longitudinal creepage which is not revealed in the simplified wheelset model.

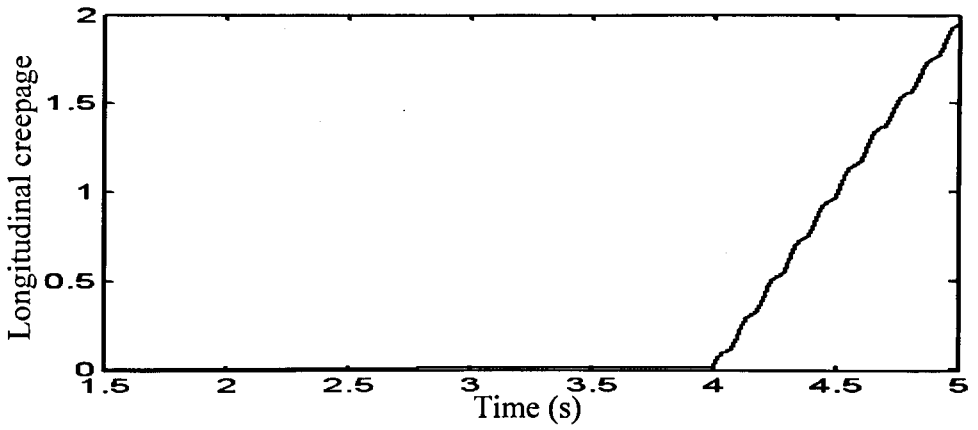

Figure 6.21 Longitudinal creepage (60 Hz, sudden change, 10 km/h)

Figure 6.22 presents the waveform of the torsional torque. Due to the interactions between lateral, yaw and longitudinal motions, the torsional torque in the stable condition is subjected to large variations which are different from the one based on the simplified model. Also certain oscillations show up in the torsional torque which is due to fact that two wheels of the wheelset operate at different contact conditions. However, the indexing oscillation at the wheelset torsional natural frequency still happens when slip occurs, which can be seen in the close shot given in Figure 6.23. So it is expected that the re-adhesion control scheme based on torsional vibration phenomenon will still work properly in the conditions where substantial interferences exits.

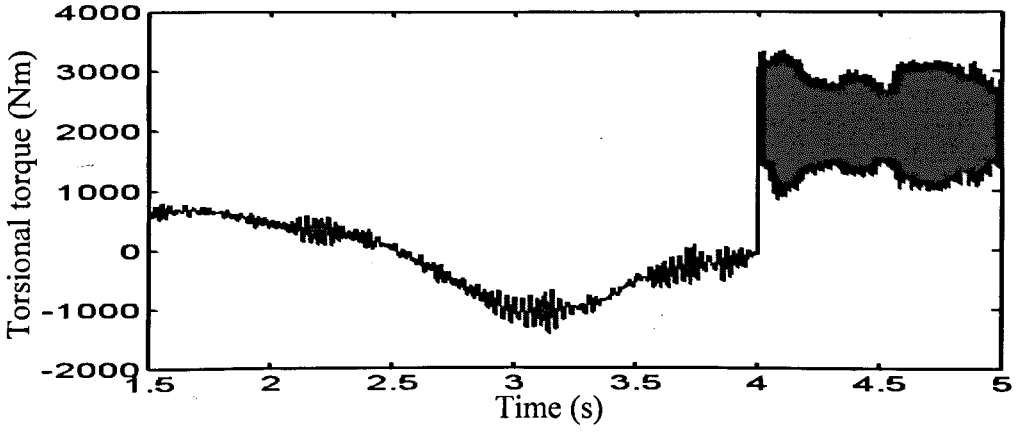

Figure 6.22 Torsional torque with longitudinal disturbance (60 Hz, sudden change, 10 km/h)

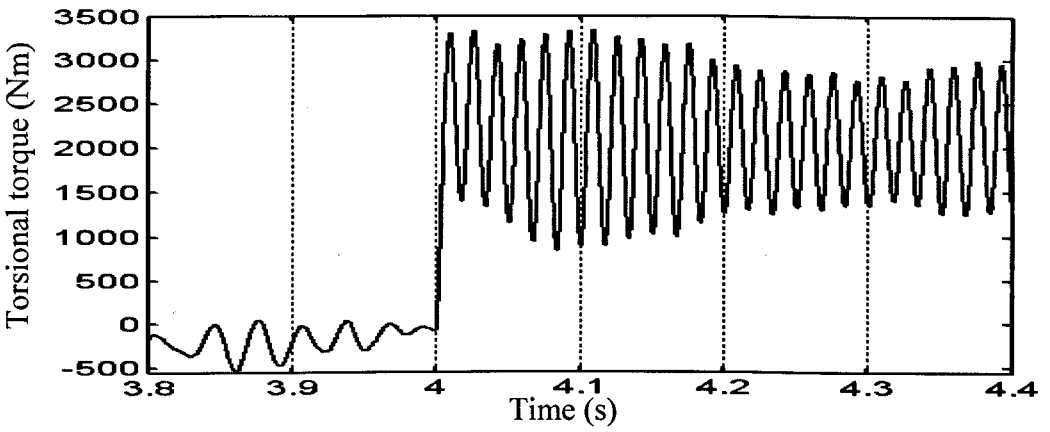

Figure 6.23 Close shot of torsional torque with longitudinal disturbance (60 Hz, sudden change, 10 km/h)

6.3.2 Re-adhesion Control Performance for the Comprehensive Wheelset Model

Figure 6.24 shows that the re-adhesion control scheme based on Kalman filter works in comprehensive operation conditions of railway vehicle.

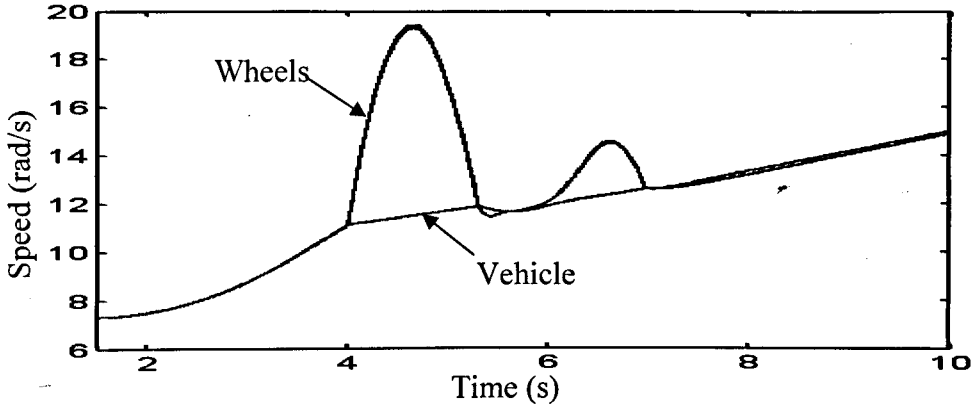

Figure 6.24 Wheels and vehicle angular speeds with disturbances (60 Hz, sudden change, 10 km/h)

The results show that the first slip condition is detected and get recovered within 2 seconds with the maximum creepage less than 70%, and it takes about 1 second to recover from the second small slip.

6.4 Summary

A re-adhesion control scheme is developed based the estimation from the Kalman filter. The effectiveness of this scheme is evaluated in different conditions and with practical sensors. The results show that the re-adhesion can be achieved within 2 seconds after slip happens in most cases. Furthermore, an assessment has been carried out based on the comprehensive model which shows that the developed re-adhesion scheme can work effectively even though there are dynamic disturbances.

7 CONCLUSIONS AND FURTHER WORK

7.1 Conclusions

The aim of this research is to carry out the dynamic study of a wheelset, which is driven by a vector controlled induction motor in different conditions and develop a novel re-adhesion control approach that uses imperfect position sensors. The task is fulfilled by several steps as summarized here.

At the first step, an induction motor is modelled, and its drive based on an indirect vector control scheme is developed. Vector controlled induction motors are widely used in railway AC traction systems, and are normally capable of delivering fast and accurate torque dynamic responses which are essential to ensure a rapid torque reduction in the latest re-adhesion control techniques.

The second step is concerned with the modelling of the wheelset. The study of the distributed parameter model of the wheelset reveals the natural torsional modes of the system, and the numerical analysis of the system dynamic response to the external torque excludes the higher order torsional mode (second and higher) since the angular responses of higher order torsional modes are nearly zero. Based on these results, a lumped parameter model of the wheelset which pays special attention to the first order natural torsional mode is introduced. The numerical comparison of the dynamic response of the distributed parameter model and the lumped parameter model is carried out as well as the comparison of simulation results and shows the consistency of the two models. A comprehensive model which includes the longitudinal, lateral and yaw dynamics is also introduced. Some simplifications were given to the comprehensive model for the convenience of controller design. Therefore, the lumped parameter system was taken as the basis for further dynamic study and controller design.

Additionally, based on the lumped parameter model of the wheelset, the dynamics in different wheel rail contact condition are investigated. The torque demand to the motor is given in a predefined pattern which includes a jerk limit period. Through

comparing the dynamics in normal and slip statuses, it is found that intensive torsional oscillation appearance in the slip condition is a typical phenomenon for slip status. Further studies are carried out in different conditions such as wheelsets with different torsional stiffness, different wheel rail contact conditions and different speeds. The results show that the torsional vibrations occurring in slip condition are the intrinsic torsional modes which are determined by the wheelset construction and independent of vehicle operation conditions. The stability analyses based on the linearised wheelset model illustrate the link between the torsional vibration and the system instability.

Then, two methods dealing with vibration signals are introduced. Running FFT method is a straight forward method to analyze vibration signals but computing intensive. Time domain filtering method is more suitable for industry application because it is effective, easy to implement and costs less. Both of these methods are capable of extracting the magnitude information of the component at the torsional vibration frequency.

Two approaches are studied to detect the slip based on the torsional vibration information. The first approach is based on the measurement of the torsional torque, but requires extra torque measurement instrumentation. The slip detection is carried out by observing the magnitude of the torsional torque component at the wheelset natural frequency. The feasibility of slip detection using torsional torque measurement is studied in different conditions, such as wheelsets with different stiffness, different contact conditions and different speeds. The simulation results show that the slip conditions can be detected very fast based on torque measurement.

The second approach, a Kalman filter is designed to estimate torsional torque variation which contains enough torsional vibration information for slip detection. The design of the Kalman filter is investigated by considering the wheel rail contact nonlinearities, and shows that the coefficients near the saturation region of the slip curve can give a better matched estimation. The validity of the slip detection scheme based on Kalman filter is evaluated in different conditions with ideal position encoders initially. Then the scheme is further evaluated on the practical position encoders where the estimated results have higher magnitude than those with ideal

position sensors. The simulation results in different conditions show that even with practical position sensors, the Kalman filter based slip detection can indicate the slip condition in good time.

Finally, a re-adhesion control scheme is developed based on the Kalman filter. The estimated torsional torque variation from the Kalman filter is not only used to indicate the slip condition but also fed to a PI controller to determine the torque reduction amount. The generated torque reduction amount is fed back to the vector control unit of the induction motor to adjust the motor output until a re-adhesion status is achieved. The performances of the re-adhesion scheme are evaluated in different conditions with practical sensors, and show that the re-adhesion can be achieved within 2 seconds in most cases and the wheelset operates at an optimal status thereafter. Furthermore, dynamics of the comprehensive wheelset model where complex dynamics is involved are studied and the feasibility of the re-adhesion scheme is also evaluated in return. However, there are difficulties to achieve a good re-adhesion performance in the high speed range based on the comprehensive model.

The most relevant results and conclusions that have been drawn from this work are:

(1) The first order torsional mode is the primary torsional mode of a wheelset shaft.

(2) Self-excited torsional vibration appears in slip conditions. The frequency of the vibration is purely determined by the primary torsional mode of the wheelset shaft.

(3) A slip condition can be detected rapidly and directly by monitoring torsional torque based on the torque measurement in different operation conditions and for different wheelset axles.

(4) A proper designed Kalman filter can give good estimation of the torsional torque variation which contains the torsional vibration information. The detection method based on Kalman filter can detect the slip condition in time and requires only one position measurement which is usually equipped in railway vehicles.

(5) The developed re-adhesion control scheme based on the Kalman filter can help the system regain adhesion shortly after a slip condition is detected and

optimal (or nearly optimal) adhesion is attained in the re-adhesion status in different operation conditions.

(6) The re-adhesion scheme based on Kalman filter can work properly with practical position sensor and also under dynamic disturbances.

The contribution of this work is to shed light on the wheelset mechanical dynamics rather than study the speeds which are widely used in conventional re-adhesion schemes. In the wheelset dynamics study, the elastic coupling of the shaft is considered which makes it different from most re-adhesion control scheme considering rigid shafts. The developed re-adhesion approach only requires a single position encoder with low resolution which is commonly used in railway vehicles, and immune from the noise and disturbances which are unavoidable in practical operation. Furthermore, the proposed scheme can work properly in different conditions, whether the slip develops slowly or occurs severely by sudden change.

7.2 Further Work

It is considered that the following work would be interesting for future research:

(1) Further study on the re-adhesion characteristic based on comprehensive model especially in high speed range.

(2) Suitability studies in different railway bogies. Different mounting methods of the driving and transmission unit may result in different damping effect to the torsional mode. The damping effect in this thesis was considered neglectable which was suitable for a specified group of railway vehicles, while some others may have extra damping used to protect the system from excessive vibrations. So it is useful to carry out some comparison studies of different systems to define the applicability and expansibility of this approach.

(3) Experimental verification. It is important to verify scheme's validity through experiments. On a hardware platform, practical issues of the scheme such as Kalman filter implementation and tuning of control parameters will need to be examined carefully.

(4) Optimization study. This aspect of work is aimed to achieve a fast and optimal re-adhesion dynamics which may include the adjustment of PI

controllers, selection of a proper threshold adaptively based on the acknowledgement of the vehicle speed.

REFERENCES

[1] B V Brikle, "Railway vehcle dynamics". *Physics in Technology*, Vol.17, pp.181-186,1986

[2] Ion Boldea, S.A. Nasar, *Electric Drives*. CRC Press LLC, 1999.

[3] R.J. Hill, "Electric Railway Traction Part 2: Traction drives with three-phase induction motors", *Power Engineering Journal*, 1994

[4] Mehrdad. Ehsani, Yimin Gao, and Sebastien Gay, "Characterization of Electric Motor Drives for Traction Applications", IEEE Annual Conference of *Industrial Electronics Society*, Vol. 1, pp.891-896, November 2003.

[5] Satoshi, Kadowaki, Kiyoshi Ohishi, etc, "Re-adhesion Control of Electric Motor Coach Based on Disturbance Observer and Sensor-less Vector Control". *Proceedings of Power Conversion Conference*, Vol. 3, pp. 1020-1025, April 2002.

[6] Woo-seok Kim, Yong-Seok Kim, Jun-koo Kang and Seung-ki Sul. "Electro-Mechanical Re-adhesion Control Simulator for Inverter-Driven Railway Electric Vehicle", Conference record of *IEEE IAS annual Meeting*, Vol. 2, pp.1026-1032, 1999

[7] Ikuo Yasuoka, Takuma Henmi, Yooske Nakazawa etc, " Improvement of Re-adhesion for Commuter Trains With Vector Control Traction Inverter", *Proceeding of the Power Conversion Conference*, Vol. 1, pp. 51-56, August, 1997

[8] Hiroshi Miki, Haruki Yoshikawa, Michio Iwahori. "New AC Traction Drive System with Transistor VVVF Inverter", IEEE, 1991

[9] Finch, J.W., "Scalar and Vector: a Simplified Treatment of Induction Motor Control Performance", *IEE Colloquium on Vector Control Revisited (Digest No. 1998/199)*, pp. 2/1-2/4, 1998

[10] K. Hasse, "On the Dynamics of Speed Control of Static ac Drives with Squirrel-cage Induction Machines", PhD thesis, TH Darmstadt, 1969

[11] F. Blaschke. " The Principle of Field Orientation as Applied to the New Transvector Closed-loop Control System for Rotating Field Machines", *Siemens Review*, Vol. 34, pp.217-220, 1972

[12] Vas, P., *Vector Control of AC Machines*, Oxford University Press, 1990

[13] T. A. Lipo and K.C. Chang, " A New Approach to Flux and Torque-Sensing in Induction Machines", *IEEE Transaction On Industry Applications*, Vol. 30, pp. 441-447, 1994

[14] Tomoke Wananabe, Michihiro Yamashita. "A Novel Anti-slip Control Without Speed Sensor for Electric Railway Vehicles". Conference record of the Annual Conference of IEEE *Industrial Electronics Society*, Vol. 2, pp. 1382-1387, 2001

[15] Bo Jacobson, Joost J. Kalker, *Rolling Contact Phenomena*, Springer Wien New York, 2000

[16] Daniel Frylmark and Stefan Johnsson, *Automatic Slip Control for Railway Vehicles,* Master thesis

[17] Mei, T. X., Goodall, R. M., "Optimal Control Strategies for the Active Steering of Railway Vehicles", *IFAC World Congress*, 1999

[18] Goodall, R.M., Li, H., " Solid Axle and Independently-Rotating Railway Wheelset- a Control Engineering Assessment of Stability", *Vehicle System Dynamics*, Vol. 33, pp.57-67, 2000

[19] Hayashi, Y.; Tsunashima, H.; Marumo, Y., "Fault Detection of Railway Vehicles Using Multiple Model Approach", International Joint Conference of SICE-ICASE, pp. 2812-2817, 2006

[20] E. Andresen, R. Grimm, A. Jockel, etc, " Utilization of Wheel Conditioning for Adhesion Maximizing of Locomotives", *SPEEDAM*, Vol. 1, pp. B2-19

[21] O. Polach, "Creep Forces in Simulation of Traction Vehicles Running on Adhesion Limit", *Wear* , Vol. 258, pp. 992-1000, 2005

[22] Xiang Sun, "机车的传动、驱动、控制与粘着", *Journal of the China Railway Society*. Vol.16,1994

[23] T X Mei, J H Yu and D A Wilson, " Wheelset Dynamics and Wheel Slip Detection", *4th STECH symposium, 2006*

[24] Lewis R.1, Dwyer-Joyce R.S.1,Lewis J., "Disc Machine Study of Contact Isalation During Railway Track Sanding", *Proceeding of The I MECH E Part F Journal of Rail and Rapid Transit*, Vol. 217, pp. 11-24, 2003

[25] Tomoki Watanabe, Akihiro Yamanaka, etc, "Optimization of Readhesion Control of Shinkansen Trains with Wheel-rail Adhesion Prediction", *Proceedings of the Power Conversion Conference*, Vol. 1, pp. 57-50, 1997

[26] Tomoki Watanabe, Akihiro Yamanaka, " Adhesion Phenomena and Optimization of Readhesion Control for High Speed Trains with Wheel-rail Adhesion Prediction", World Congress on *Railway Research*, Italy, 1997

[27] T. Watanabe, M.Ogasa, " Realization of Anti-slip Control in Railway Motor Vehicle by Slip Velocity Feedback Torque Control", Proceeding of IEEE European Conference on Power Electronics Applications, Vol. 6, pp. 156-161, September, 1993

[28] Köck, F., Weinhardt,M., "Tractive Effort and Wheel Slip Control of Locomotive Type 120", IFAC 10th World Congress on Automatic Control, Vol. 3, pp. 259-267

[29] Doh-Young Park, Moon-Sup Kim, Don-Ha Hwang, etc, " Hybrid Re-adhesion Control Method for Traction System of High-Speed Railway", Proceedings of the International Conference on Electrical Machines and Systems, Vol.2, pp. 739-746, August, 2002

[30] H.J Ryoo, JS Kim, G.H Rim, etc, " Novel Anti-Slip/Slide Control Algorithm For Korean High-Speed Train", Conference Record of IEEE Annual Conference of *Industrial Electronics Society*, Vol. 3, pp. 2570-2574, November, 2003

[31] Atsuo Kawamura, Keiichi Takeuchi, Takemasa Furuya, etc, " Measurement of the Tractive Force and the New Adhesion Control by the Newly Developed Tractive Force Measurement Equipment", *Proceeding of the Power Conversion Conference*, Vol. 2, pp. 879-884, 2002

[32] Satoshi Kadowaki, Kiyoshi Ohishi, Shinobu Yasukawa, etc, " Anti-skid Re-adhesion Control Based on Disturbance Observer Considering Air Brake for Electric Commuter Train", Conference Record of IEEE International Conference on *Control Applications*, Vol. 2, pp. 1124-1129, September, 2004

[33] Kiyoshi Ohishi, Ken Nakano, Ichiro Miyashita, etc, "Anti-slip Control of Electric Motor Coach Based on Disturbance Observer", IEEE International Workshop on *Advanced Motion Control*, pp.580-585, June 1998

[34] Hideo Sado, Shin-ichiro Sakai, Yoichi Hori, " Road Condition Estimation for Traction Control In Electric vehicle", Proceeding of IEEE International Symposium on *Industrial Electronics*, Vol. 2, pp. 973-978, 1999

[35] Yoshiki Ishikawa, Atsuo Kawamura, " Maximum Adhesive Force Control in Super High Speed Train", *Proceeding of the Power Conversion Conference*, Vol. 2, pp. 951-954, August, 1997

[36] D. Iannuzzi and R. Rizzo, "Disturbance Observer for Dynamic Estimation of Friction Force in Railway Traction Systems", Conference Record of the IEEE *Industrial Electronics Society*, Vol.3, pp. 2979-2982, 2002

[37] Kiyoshi Ohishi, Yasuaki Ogawa, Ichiro Miyashita, etc, "Adhesion Control of Electric Motor coach Based on Force Control Using Disturbance Observer", IEE Technical Meeting on Industrial Instrumentation and Control, Vol. 11c-99, pp. 125-130, 1999

[38] Pieter M. De Koker, J. Gouws, L. Pretorius, " Fuzzy Control Algorithm For Automotive Traction Control Systems", 8th Mediterranean *Electrotechnical Conference*, Vol. 1, pp. 226-229, 1996

[39] Jian Xiao, Helmut Weiss, Hui Wang. "Locomotive Optimal Adhesion Control by Wavelet Analysis", Conference Record of the IEEE International Conference on *Industrial Technology*, Vol. 1, pp. 309-314, 2003

[40] Monica Malvezzi, Paolo Toni, Benedetto Allotta, etc. "Train Speed and Position Evaluation Using Wheel Velocity Measurements", Proceeding of IEEE/ASME International Conference on *Advanced Intelligent Mechatronics*, Vol. 1, pp. 220-224,2001

[41] B. Cai, X. Wang. " Train Positioning via Integration and Fusion of GPS and Inertial Sensors", Conference Record of International Conference on *Computers in Railway*, pp. 1217-1226, 2000

[42] A. Pilip, L. Bazant, H. Mocek, etc, "GPS/GNSS Based Train Position Locator For Railway Signalling", Conference Record of International Conference on *Computers in Railway*, pp1227-1242, 2000

[43] Kalman, R.E., " A New Approach to Linear Filtering and Prediction Problems", *Transactions of ASME-Journal of Basic Engineering*, Vol. 82, pp. 35-45, 1960

[44] Kalman, R.E., Bucy R.S., " New Results in Linear Filtering and Prediction Theory", *Transactions of ASME-Journal of Basic Engineering*, Vol. 83, pp. 95-107, 1961

[45] Grewal, M.S., Andrews, A.P., *Kalman Filtering: Theory and Practice,* Prentice-Hall Inc., New Jersey, 1993

[46] A. Geistler, F. Böhringer, "Robust Velocity Measurement for Railway Applications by Fusing Eddy Current Sensor Signals", IEEE Symposium of *Intelligent Vehicles*, pp. 664-669, 2004

[47] Ernest, P., Mazl, R.,Preucil, L., "Train Locator Using Inertial Sensors and Odomoter", IEEE Symposium of *Intelligent Vehicles*, pp. 860-865, 2004

[48] Mirabadi, A., Mort, N., Schmid, F., "Application of sensor fusion to railway systems", IEEE/SICE/RSJ International Conference on *Multisensor Fusion and Integration for Intelligent Systems*, pp. 185-192, 1996

[49] Osada, H, "Practical approach to designing Kalman filter for velocity and acceleration of Doppler radar", IEEE Pacific Rim Conference on *Communications, Computers and Signal Processing*, Vol. 2, pp. 847-849, 1997

[50] Saab, S.S.; Nasr, G.E.; Badr, E.A., "Compensation of axle-generator errors due to wheel slip and slide", *IEEE Transactions on Vehicular Technology* , Vol. 51(3), pp. 577-587,2002

[51] Spors, S., Rabenstein, R., Strobel, N., "Joint Audio-Video Object Tracking", *Proceedings of The International Conference on Image Processing,* Vol. 1, pp. 393-396, 2001

[52] P. Li, R. Goodall, P. Westion, etc, "Estimation of Railway Vehicle Suspension Parameters for Condition Monitoring", *Control Engineering Practice*, Vol. 15, pp. 43-55, 2006

[53] Mei, T.X., Goodall, R.M., Li, H., " Kalman Filter for the State Estimation of A 2-axle Railway Vehicle", *5th European Control Conference*

[54] Li, H., Goodall, R.M., "State Estimation for Active Steering of Railway Vehicles", *Proceedings of IFAC 99*, PP. 133-138, 1999

[55] Charles, Guy; Goodall, Roger, "Low Adhesion Estimation", *The Institution of Engineering and Technology International Conference on Railway Condition Monitoring*, pp.96-101, 2006

[56] Ion Boldea, S. A. Nasar, *Electric Drives*. CRC press LLC, 1999

[57] Werner Leonhard, *Control of Electrical Drives*, 2nd edition, Springer, Berlin-Heidelberg-New York 1996

[58] J. Chen, *Control of AC Motors*, National Defence Industry Press, 1989.

[59] Du, T., Brdys, M.A., "Shaft Speed, Load Torque and Rotor Flux Estimation of Induction Motor Drive Using an Extended Luenberger Oberver", Sixth International Conference on *Electrical Machines and Drives*, pp. 179-184, 1993

[60] Charles, V. Jones, *The United Theory of Electrical Machines*, Butterworth Co. Ltd., London, 1967

[61] H.C. Stanley, " An Analysis of the Induction Machine", *Transaction of AIEE*, Vol. 57, pp.751-757, 1938

[62] Hoang Le-huy, "Comparison of Field-Oriented Control and Direct Torque Control for Induction Motor Drives", Conference Record of the 1999 IEEE Conference of *Industry Applications* , Vol. 2, pp. 1245-1252, 1999

[63] A. Powell, T. Meydan, " Optimisation of Magnetic Speed Sensors", *IEEE Transaction on Magnetics*, Vol. 32, Part 2, pp. 4977-4979, 1996

[64] Daniel Foito, Antonio Roque, Jose Maia, etc, " Electric Vehicles-Improving the Performance With a Traction Control System"

[65] Leonard Meirovitch., *Principles and Techniques of Vibrations*, Prentice-hall press, 1997

[66] D. Fitzgeorge, F. W. Williams. " Compact Distributed Inertia Solution For Free Torsional Vibrations of Shaft and Rotor System", *Journal of Sound and Vibration*, Vol. 46(3), pp 311-322, 1976

[67] Micheal D. Greenberg, *Advanced Engineering Mathematics*, Prentice-hall press. 1998

[68] Mastinu G., Gobbi, M., Bon A.," A Railway Wheelset Optimally Designed for Cold Pressing Fitting", *JSME International Journal: Mechanical System, Machine Elements and Manufacturing*, Vol. 47, pp. 502-507, 2004

[69] Jaschinski A, Chollet H, and Iwnicki S D etc, " The Application of Roller Rigs to Railway Vehicle Dynamics", *Vehicle System Dynamics*, Vol. 31, pp345-392, 1999

[70] Olson, Garrard, " Model-follower Longitudinal Control for AGT", IEEE *Transaction On Vehicular Technology*, Vol.28, No.1, 1979

[71] E. Manges, J. Wilson, J. Clark, "Alignment, Ride Comfort and Guideway Beam Design for High Speed Maglev Systems: the Pennsylvania Project/Maglve. Inc. Appraoch", Transportation Research Board Annual Meeting, 2006

[72] David W.Love, Masayoshi Tomizuka. " Vehicle Longitudinal Control Using Discrete Markers". Research report, 1994

[73] G. Lu, N.A. Harwood, "Prediction of Torsional Vibration on Mass Transit", *Computers in Railways*, Vol.2, pp. 3-12, 1996

[74] Steven Senini, Frank Finders, Wardina Oghanna, " Dynamic Simulation of Wheel-Rail Interaction for Locomotive Traction Studies", Proceeding of the *IEEE/ASME Joint Railroad Conference*, pp. 27-34, 1993

[75] Harwood N.A., Keogh P.S, "Self-excited Oscillation in Locomotive Transmission Systems Under Loss of Adhesion", *Proceedings of Institution of Mechanical Engineers. 1991*

[76] Alfred Jaschinski, Hugues Chollet, Simon Iwnicki and etc, " The Application of Roller Rigs to Railway Vehicle Dynamics", *Vehicle System Dynamics*, Vol. 31, pp. 345-392, 1999

[77] Anon, "SAW-based Transducer for Non Contact Torque", Electronicstalk, 21 Feb. 2001

[78] A. E. Bryson, Jr. and Y. C. Ho, *Applied optimal Control*, Hemisphere publishing, 1975

[79] Ken Dutton, Steve Thompson, Bill Barraclough, *The Art of Control Engineering*, Addison Wesley Longman Limited, 1997

[80] Nam-Joom Kim, Dong-Seok Hyun. "Very Low Speed Control of Induction Machine by Instantaneous Speed and Inertia Estimation", Conference Record of 20th International Conference on *Industrial Electronics, Control and Instrumentation*, Vol. 1, pp. 605-610, 1994

[81] George Ellis, *Control System Design Guide: a Practical Guide,* ELSERIER , Academic Press.

[82] Mei, T.X., Nagy Z., Goodall R.M. and etc., " Mechatronic Solutions for High-speed Railway Vehicles", Control Engineering Practice, Vol. 9, pp. 1023-1028, 2002

APPENDIX A

Copy of the paper:

"Re-adhesion control based on wheel set dynamics in railway traction system",

J H Yu, T X Mei, D A Wilson

Published at *UKACC (United Kingdom Automatic Control Council) Control Conference*, August, 2006

RE-ADHESION CONTROL BASED ON WHEELSET DYNAMICS IN RAILWAY TRACTION SYSTEM

J H Yu, T X Mei, D A Wilson

The University of Leeds, UK

Abstract: This paper demonstrates how wheelset dynamics is affected by wheel-rail contact nonlinearities. Based on vibration phenomena due to wheel slip, two detection methods are proposed, both utilizing wheel speed information. One uses a running FFT to detect spectrum variation of a particular frequency component while the other uses bandpass and low pass filters to obtain magnitude information of the frequency interest. A re-adhesion scheme which is based on slip detection is developed. The simulation results show that this re-adhesion control scheme can detect slip effectively and improve traction stability.

Keywords: re-adhesion control, wheelset dynamics, vibration, nonlinearity, stability

1. INTRODUCTION

The knowledge of adhesion force through wheel-rail contact is of primary importance in railway traction systems. Generally, adhesion force has nonlinear features which are related to the creep value and are strongly affected by wheel-rail contact conditions such as dry/wet, dust/leaves and so on. When the mechanical torque transmitted to the wheel is much higher than the maximum adhesion torque that can be obtained from wheel-rail contact, the wheel will lose adhesion, and slip will occur. Slip is harmful in traction operations since it will increase the wear of wheel and rail, increase mechanical stress in the system, affect stability and, furthermore, lead to poor traction performance. Therefore re-adhesion schemes are required to reduce the risk of slip.

Disturbance observers are often used to detect slip conditions (Kadowaki, *et al.*, 2002; Woo-Seok Kim, *et al.*, 1999). In these papers, traction torque is treated as a disturbance torque, and estimated either through zero/first-order observers (Kadowaki, *et al.*, 2002) or through state observers (Woo-Seok Kim, *et al.*, 1999) using motor speed and torque information. Besides, hybrid anti-slip methods, which used slip speed, wheel speed and acceleration information, were introduced in some papers (Don-Young Park.. *et al.*, 1999; Hyoun-Chul Choi and Suk-Kyo Hong, 2002). Those controllers have difficulty obtaining satisfactory performance, and also require accurate measurement of wheel slip. On the other hand, most disturbance observers are established on the assumption of rigid shaft connection, and the performances of such anti-slip schemes based on a disturbance observer are to a large extent affected by noise in the system.

In this paper, a wheelset model is established and its dynamics under stable and slip conditions are studied and compared. Based on this, novel slip detection methods are proposed. In addition, a torque control unit is adopted for a vector controlled three phase induction motor to achieve re-adhesion.

2. WHEELSET MODEL

In order to analyse slip phenomenon in the traction system, a wheelset model is established as shown in Fig.1. The right side driving wheel is driven by an inverter-fed induction motor and connected to the other wheel through a shaft, which is considered to have finite torsional stiffness.

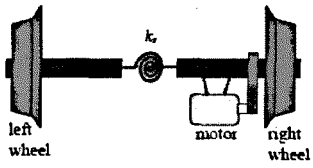

Fig. 1 Diagram of simplified wheelset

The dynamics of the system are governed by equations (1) to (3). Equation (1) describes the dynamics of the right wheel, which is driven by an induction motor through a gear box; (2) describes the motion of left wheel; (3) is the description of the torsional torque, and (4) gives the general form of the traction torque.

$$T_m - T_s - T_{tr} = J_r \frac{d\omega_r}{dt} \tag{1}$$

$$T_s - T_{tl} = J_l \frac{d\omega_l}{dt} \tag{2}$$

$$T_s = k_s \int (\omega_r - \omega_l) dt + c(\omega_r - \omega_l) \tag{3}$$

$$T_t = \mu \cdot M_v g \cdot r \tag{4}$$

where, T_m is the driving torque transmitted from the motor through a gearbox, T_s is the torsional torque, T_{tr} is the traction torque contributed by the right side wheel-rail adhesion, T_{tl} is the traction torque contributed by the left side wheel-rail adhesion, J_r and J_l are moment of inertias of right and left side respectively, k_s is the torsional stiffness of the shaft, c is the viscous damping of the shaft, and ω_r and ω_l are the angular velocity of the right and the left wheel respectively. μ is called the traction coefficient, and its maximum value is called adhesion coefficient. M_v is the equivalent vehicle mass of each wheel. In this paper it is assumed that each wheel shares vehicle mass evenly.

Since the damping of the system is very small, we assume that $c = 0$ .Then the state equation of this two inertia system is given by (5) where the state variables are chosen as $\mathbf{x} = [\omega_r \ \omega_l \ \theta_s]^T$ with θ_s defined as $\theta_s = \int (\omega_r - \omega_l) dt$:

$$\begin{bmatrix} \dot{\omega}_r \\ \dot{\omega}_l \\ \dot{\theta}_s \end{bmatrix} = \begin{bmatrix} 0 & 0 & -\frac{k_s}{J_r} \\ 0 & 0 & \frac{k_s}{J_l} \\ 1 & -1 & 0 \end{bmatrix} \begin{bmatrix} \omega_r \\ \omega_l \\ \theta_s \end{bmatrix} + \begin{bmatrix} \frac{1}{J_r} \\ 0 \\ 0 \end{bmatrix} T_m + \begin{bmatrix} -\frac{1}{J_r} & 0 \\ 0 & -\frac{1}{J_l} \\ 0 & 0 \end{bmatrix} \begin{bmatrix} T_{tr} \\ T_{tl} \end{bmatrix} \tag{5}$$

Then, the natural frequency f_n of the two inertia system is given by:

$$f_n = \frac{1}{2\pi} \sqrt{\frac{k_s}{J_l} + \frac{k_s}{J_r}} \tag{6}$$

In equation (10), the traction torques T_{tr} and T_{tl} have nonlinear properties and are determined by wheel-rail contact characteristic, which can be expressed as group of slip curves as shown in Fig.2. Each slip curve gives a rule for how the traction coefficient varies with slip ratio, which is defined in equation (7) where λ is slip ratio, ω_v is equivalent angular speed of the vehicle at the contact point.

$$\lambda = \frac{\omega_w - \omega_v}{\omega_v} \tag{7}$$

In Fig.2, curve I with the higher adhesion coefficient, can be considered as a dry condition which indicates a good contact, and curve II represents a very wet/snowy condition as a poor case. It can be seen that the traction coefficient varies nonlinearly with slip ratio. The left side of the maximum point is a stable region where the slip curve has a positive slope, and on the other side, the traction coefficient decreases as the slip ratio increases. Hence, a slip condition is associated with negative slope.

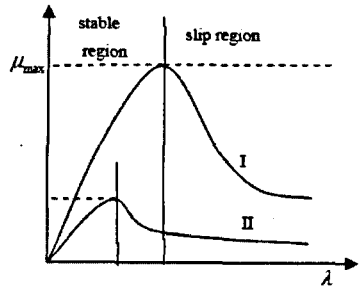

Fig. 2 Profile of adhesion characteristics

An approximation of traction torque can be obtained through linearization of the slip curves. Equation (8) and (9) give such approximation of the right and left hand side traction torque:

$$\Delta T_{tr} = k_1 \Delta\omega_r \tag{8}$$

$$\Delta T_{tl} = k_2 \Delta\omega_l \tag{9}$$

here, k_1 and k_2 are values related to slopes at the operating points of the right and left wheel on their respective slip curves.

Using (8) and (9), the small signal model is given as:

$$\begin{bmatrix} \Delta\dot{\omega}_r \\ \Delta\dot{\omega}_l \\ \Delta\dot{\theta}_s \end{bmatrix} = \underbrace{\begin{bmatrix} -\frac{k_1}{J_r} & 0 & -\frac{k_s}{J_r} \\ 0 & -\frac{k_2}{J_l} & \frac{k_s}{J_l} \\ 1 & -1 & 0 \end{bmatrix}}_{A} \begin{bmatrix} \Delta\omega_r \\ \Delta\omega_l \\ \Delta\theta_s \end{bmatrix} \tag{10}$$

It is clear from equation (10) k_1 and k_2 add extra damping to the system, and their values are closely related to the stability of the system. Generally, positive k_1 and k_2 values indicate a stable condition, and negative ones denote an unstable condition, which give rise to self-excited vibrations.

A simulation model was built in SIMULINK together with the SimPowerSystems toolbox to model the induction motor vector control unit as shown in Fig. 3.

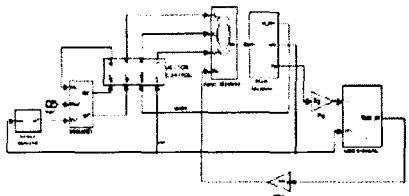

Fig. 3 Simulink diagram of inverter-fed induction motor traction system

3. SLIP PHENOMENON AND DETECTION METHOD

In this section, the results of simulation are given to study wheelset dynamics in slip condition, and based on that two detection methods are presented.

3.1 Slip phenomenon

In all simulations, the torque demand of motor T_e^* was as shown in Fig.4.

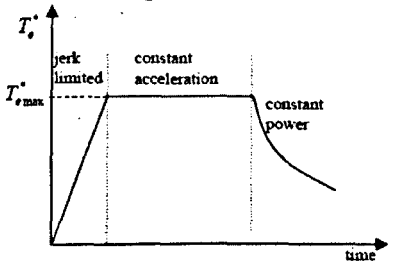

Fig 4 Torque demand profile

At a specified time e.g. *t=4.5s*, the wheel-rail contact condition is changed from a dry case to a poor case to develop a slip condition. Fig. 5 gives the wheel-rail wheel rail adhesion data used in the simulation. At *t=4.5s* the contact curves of both wheels are switched from curve ① to curve ②.

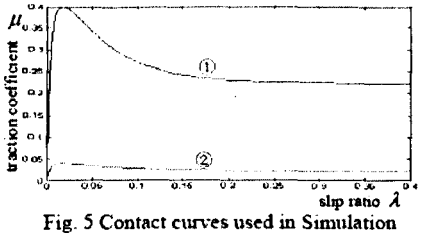

Fig. 5 Contact curves used in Simulation

Table 1 gives the motor and vehicle parameters used in simulation. All the results are given and analysed with a shaft natural frequency of 40 Hz unless stated otherwise.

Table 1 Simulation parameters

T_{emax}^*	J_r	J_l	c	f_n
1500 *Nm*	133.2 kgm^2	62.8 kgm^2	0	40*Hz*

Fig.6 shows speeds of both wheels and vehicle from the simulation results. It is obvious that after *t=4.5s* when the contact condition is switched to a poor one, wheel speed rises much faster than that of vehicle, and slip happens.

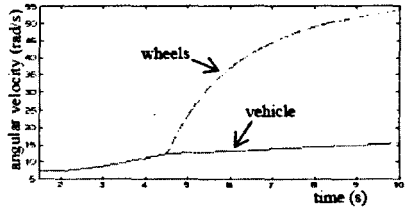

Fig. 6 Angular speeds of wheels and vehicle

Fig.7 shows the torsional torque. It can be seen that when slip occurs a vibration appears. The frequency of this vibration is 40Hz, which is the natural frequency of the two inertia torsional system.

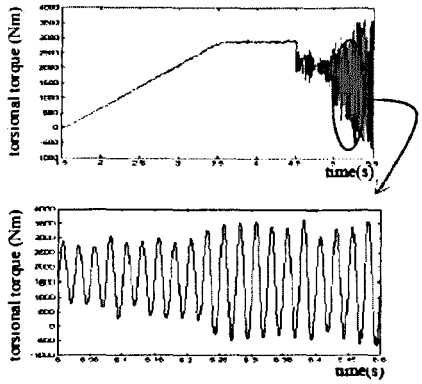

Fig.7 Torsional torque

From equation (10), it is known that k_1 and k_2 affect system stability. In the simulation, two sets of k_1 and k_2 were used. Table 2 gives one set of k_1 and k_2 values. They are obtained from the stable operating conditions in the simulation. The corresponding engenvalues of matrix A1 in (10) are also given in the table. It is clear that all engenvalues are real and negative, and this confirms that the system is stable.

Table 2 k_1 and k_2 values and eigenvalues (stable)

k_1	k_2	eigenvalues
2.43e5	2.43e5	-22.39, -1813, -3835

Table 3 gives the other set of k_1 and k_2, and they are obtained from slip operation condition. One of the eigenvalues is positive real, and the others are complex conjugate with positive real part. Hence, the system is unstable. The oscillation frequency obtained from the imaginary part of complex eigenvalues is

40Hz, and this agrees with the natural frequency of the torsional system.

Table 3 k_1 and k_2 values and eigenvalues (slip)

k_1	k_2	eigenvalues
-2175.8	-2175.8	$22.23, 14.38 \pm 250.77i$

In practice, when a vehicle is built, the natural frequency of wheelset axles is fixed. So this typical vibration can be used as a indication of slip condition.

3.2 Slip detection method using running FFT

When a torsional vibration occurs, the speeds of two wheels are directly affected. Such vibrations can be detected from speed information. Fig. 8 shows the difference between the right wheel and left one. It shows that the torsional vibrations affect the speeds, and that makes it possible to detect the slip.

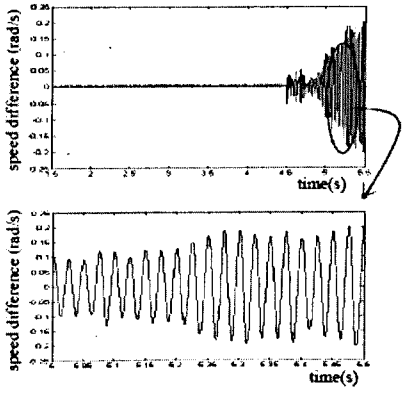

Fig.8 Waveform of speed difference

In this section, a running FFT is used to detect the vibration from information of the speed difference between the right wheel and left wheel. The running FFT uses a 0.2s window to extract the information. From the FFT, the magnitude of the natural frequency component is determined. When the value exceeds a threshold, slip has been assumed to occur. Fig.9 shows magnitude of the natural frequency component. When slip occurs, the magnitude increases due to torsional vibration. Setting a magnitude of 0.1 as the threshold, slip can be detected after 0.2s, which would be satisfactory in practical situation.

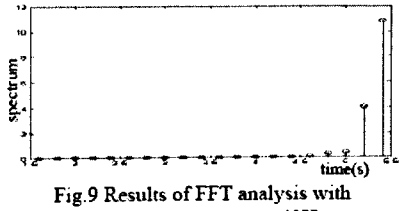

Fig.9 Results of FFT analysis with shaft natural frequency 40Hz

To demonstrate that frequency of the vibration when slip occurs is directly determined by the shaft parameters. The shaft natural frequency is changed to 60Hz. Fig.10 shows the speed difference of the two wheels. The result shows the vibrations of this frequency at slip condition.

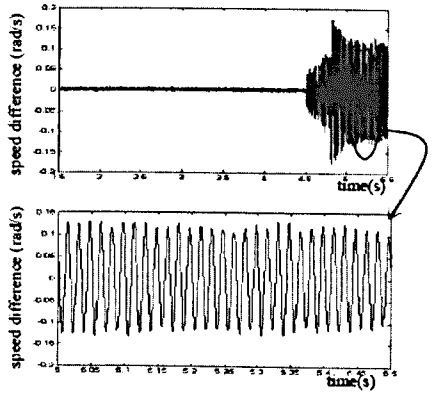

Fig.10 speed difference with shaft natural frequency 60Hz

Fig. 11 gives the magnitude of 60Hz component. And once again, the slip condition can be determined after 0.2s.

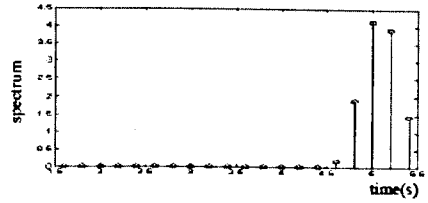

Fig.11 Results of FFT analysis with shaft natural frequency 60Hz

3.3 Slip detection method using filters

In this section, another method is introduced to obtain vibration magnitude as shown in Fig.12. A band-pass filter is used to extract the signals of the shaft natural frequency. Then, the absolute values are obtained. After that a low pass filter with a very low cut off frequency is used to catch the magnitude augment due to torsional vibration.

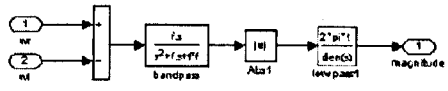

Fig. 12 Slip detection

Fig. 13 and 14 show the results applying this method with the shaft frequency 40 Hz and 60Hz. In both cases, the results show the magnitude increase in slip condition and they agree well with running FFT analysis. With appropriate threshold values, the slip condition could again be rapidly detected.

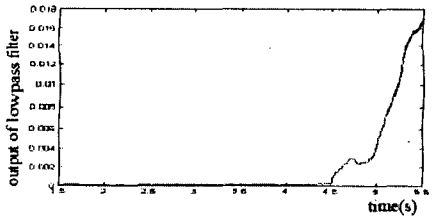

Fig. 13 Estimation of vibration magnitude with shaft natural frequency 40Hz

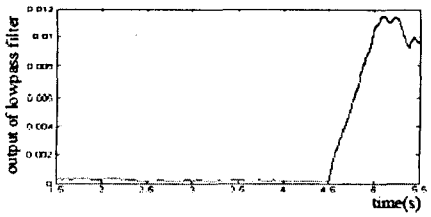

Fig. 14 Estimation of vibration magnitude with shaft natural frequency 60Hz

3. RE-ADHESION CONTROL

A torque control unit is added to correct the motor torque demand such that when slip condition is detected, the demand is reduced.

When re-adhesion is achieved which is indicated by the disappearance of vibrations, the present torque demand is kept to maintain this stable traction level. The amount of toque reduction is determined by applying the slip ratio which is obtained from equation (7) to a PI unit as shown in equation (11):

$$T_{red}(s) = (K_P + \frac{K_I}{s})\lambda(s) \qquad (11)$$

Here, K_P and K_I are the proportional and integral parameters respectively, and need to be tuned appropriately.

Fig.15 gives the wheels and vehicle speeds, and shows that rapidly increasing wheel speeds are drawn back to vehicle's within 3 seconds due to the action of re-adhesion scheme, and then increase stably in the new contact condition. Fig.16 gives the torsional torque, and shows that the torsional vibration disappears when re-adhesion is achieved.

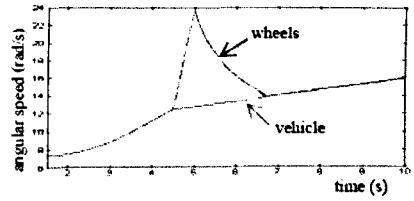

Fig.15 Angular speeds of both wheels and vehicle with shaft natural frequency 40Hz

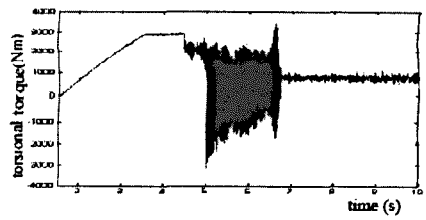

Fig.16 Torsional torque with shaft natural frequency 40Hz

Fig.17 shows magnitude of the natural frequency component from the running FFT analysis results, and this is used to indicate slip and re-adhesion condition in the simulation. Fig. 18 shows the estimation of vibration magnitude using filter method and it agrees well with running FFT results.

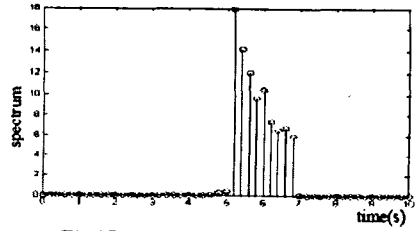

Fig.17 Results of FFT analysis with shaft natural frequency 40Hz

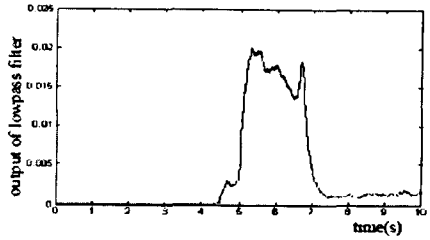

Fig 18 estimation of vibration magnitude with shaft natural frequency 40Hz

4. CONCLUSION AND FURTHER WORK

In this paper, a wheelset model has been presented. Based on the study of its dynamics, it is observed that a typical self-excited torsional vibration appears in slip conditions. Then effective slip detection methods have been developed using this vibration information. The first method uses a running FFT to determine the spectrum of the speed difference at a given instance. The magnitude of the specified frequency component is then selected from the FFT data. The second method uses a combination of bandpass and low pass filters to obtain magnitude information of the specified frequency component. Simulation results show that both methods indicate the slip condition in a timely fashion. Based on the slip detection scheme, a torque control scheme was introduced to reduce the torque to enable the wheelset system to regain

adhesion after a slip condition is indicated. The simulation results show that the re-adhesion scheme can bring the slipping system back to a stable condition within 3 seconds, and then exert appropriate traction effort after re-adhesion.

The planned future work will concentrate on two aspects: one is to study the possibility of detecting the shaft vibration from the motor operating parameters such as stator currents, and the other issue of interest is to try using vibration parameters directly to adjust the motor torque demand.

REFERENCES

Doh-Young Park, Moon-Sup Kim, Don-Ha Hwang, Joo-Hoon Lee, Yong-Joo Kim; (2001). Hybrid re-adhesion control method for traction system of high-speed railway, *Proceedings of the International Conference on Electrical Machines and Systems*, **Volume 2**, p739 – 742.

Hyoun-Chul Choi, Suk-Kyo Hong (2002). Hybrid control for longitudinal speed and traction of vehicles, *IEEE 2002 Annual Conference of the Industrial Electronics society*, **Volume 2**, p1675 – 1680.

Kadowaki,S., Ohishi, K., Miyashita I. and Yasukawa (2002). Re-adhesion control of electric motor coach based on disturbance observer and sensor-less vector control, *Proceedings of the Power Conversion Conference*, **Volume 3**, p1020 – 1025.

Woo-Seok Kim, Yong-Seok Kim, Jun-Koo Kang and Seung-Ki Sul (1999). Electro-mechanical re-adhesion control simulator for inverter-driven railway electric vehicle, *Conference Record of the 1999 IEEE Industry Applications Conference*, **Volume 2**,p1026 – 1032.

APPENDIX B

Copy of the paper:

"Wheelset dynamics and wheel slip detection"

T X Mei, J H Yu, D A Wilson

Published at *4th International Symposium on Speed-up and Service Technology for Railway and Maglev Systems,* July, 2006

WHEELSET DYNAMICS AND WHEEL SLIP DETECTION

T X Mei, J H Yu and D A Wilson
School of Electronic and Electrical Engineering
The University of Leeds, LS2 9JT, UK
Corresponding email address: t.x.mei@leeds.ac.uk

Abstract: This paper proposes a radically new approach for the detection of wheel slip/slide, which may provide an important alternative and advantageous technique in traction/braking control systems to maximise the use of adhesion in poor contact conditions. Instead of the direct measurement of speed difference between wheels and the train, the proposed concept explores the variations in wheelset dynamic properties caused by condition changes at the wheel-rail contact and therefore detects slip conditions from the dynamic behaviour of a wheelset indirectly. In this study, the configuration of a typical traction system is used, consisting of an induction traction motor (with associated power inverter and field-orientated control) connected to a wheelset via a gearbox, but the developed technique may be also applied to braking control systems. Non-linear wheel-rail contact laws are used in the simulations, and linearised models at different contact conditions are developed to enable a detailed analysis of the key dynamic properties. Simulation results are produced to support the proposed idea. The main aim of the study is to present the basic principle and theoretical background of the novel concept, although some of the fundamental issues for practical implementations are also discussed.

1. INTRODUCTION

Wheel slip/slide is caused by the tractive or braking effort exceeding the maximum adhesion available at the wheel-rail contact, which typically occurs in poor weather conditions and/or due to contaminations on track surface. It is a serious problem in railway, not only because it may compromise vehicle/passenger safety, but also cause operational difficulties and increase the cost of maintenance for flat/damaged wheels.

Tackling the problem involves two fundamental issues, which are the slip/slide detection and anti-slip control. Conventional techniques for the detection of wheel slip/slide rely on the direct measurements of slip ratio (relative speed between a wheel and the train) and/or wheel rotational acceleration [1-4]. However, there are a number of practical constraints of the detection approaches, e.g.

- The requirement of robust/reliable sensors for the harsh working environment limits the accuracy of position/speed measurement. Typically the resolution of position encoders used in traction applications is less than 100 pulses per revolution, which is particularly problematic for low speed measurement.
- The output of the encoders can be affected by the vertical dynamics of the wheelset/bogie, because the way the sensors are normally mounted
- The absolute speed of the train is normally obtained from a trailer bogie (or axle), but the provision of a reliable train speed is a problem when all axles are affected, e.g. in braking.
- Contact conditions at the wheel-rail interface are subject to large variations and the relation between the creepage and contact force (the slip curve, or the creep - creep force curve) can be very different in different conditions. Therefore it is difficult to identify the precise point of the slip ratio for the maximum adhesion.

It must be noted that the overall approach to detect and control the slip is in fact not the ideal option. It would be much more valuable to detect the adhesion available at the wheel-rail interface so that appropriate tractive or braking may be applied without causing the wheel slip/slide at all. However, this would be also scientifically much more challenging and so far there are no feasible solutions.

Once a slip/slide condition is detected, anti-slip/slide measures are normally applied to reduce tractive/braking effort to below the adhesion level until the adhesion is restored. The control can be achieved with the feed-forward approach using a predefined pattern for traction effort reduction, or with a feedback method to control the slip ratio (to a pre-determined value), or a combination of both [1-4]. However, there is no guarantee that the use of available adhesion at the wheel-rail interface is optimised in practice because of the difficulties to detect/identify the maximum adhesion and corresponding slip ratio. The detection based on the estimation of the slope at different operating points of a slip curve studied in a number of papers is probably the most relevant technique to date, but there seems to be little report on the practicality and effectiveness of the approach [5, 6].

Additional measures may be used to improve the adhesion level at the wheel-rail interface. The use of sand machines, often installed on locomotives, has been for many years a popular and effective means to

increase the traction. More recently specially formulated chemicals (friction modifiers) are reported to have the effect of adhesion enhancement, although some tests have produced results that are less supportive [7, 8]. At the system (infrastructure) level, it is also possible to improve the track conditions (e.g. by removing the contaminations), although currently known techniques are in general expensive and/or impractical for implementation.

This paper studies an indirect approach for the wheel slip detection which explores how a wheelset reacts dynamically to changes in contact conditions. The study will provide a detailed analysis on how the changes in contact conditions can substantially affect the dynamic properties of a wheelset, and propose and assess a technique to detect wheel slip by identifying the variations in wheelset behaviours. There is no need for the measurement of slip ratio and/or estimation of creep forces at the wheel-rail interface.

The paper is organised as follows. The configuration of the traction system used in the study is presented and mathematical models are provided in section 2. Section 3 describes the fundamental properties of wheel-rail contact forces and how the contact laws are modelled. Section 4 provides a detailed theoretical analysis on how wheelset dynamic behaviour may be affected by different contact conditions. Simulation results and performance evaluation are presented in section 5. A novel concept for the detection of wheel slip/slide derived from the studies is presented in section 6, and key conclusions are drawn in section 7.

2. SYSTEM AND MODELLING

For the basic study, a simple single wheelset is used which involves a conventional solid axle wheelset powered by an AC traction motor. A three-phase induction motor is connected to one side of the wheel via a gearbox for the provision of traction (for the wheelset and ¼ of a typical vehicle). Connections between the wheelset and the bogie/vehicle in the longitudinal direction are assumed to be solid, as the stiffness is normally very high and the associated dynamics is not of significant relevance to this study.

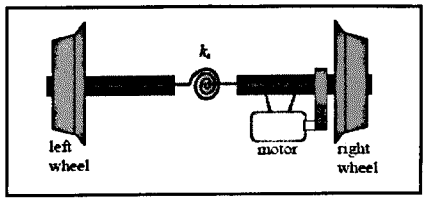

Fig. 1 Wheelset configuration used in the study.

However, the axle flexibility is considered in this study and the resonant frequency of the axle torsional mode typically ranges between 40-80Hz. This is different from many other studies, where the stiffness of the wheelset axle is often neglected and a rigid axle is assumed. The significance to include the torsional dynamics will become clear in the following sections.

Fig. 2 gives a schematic diagram of the models developed (in SIMULLINK) for the study. The models for the induction motor and power inverter are standard and available from the Matlab power toolbox. A vector control scheme (as shown in the dotted box) is also implemented to ensure good responses in the control of motor torque and flux, which is commonly used in modern traction systems.

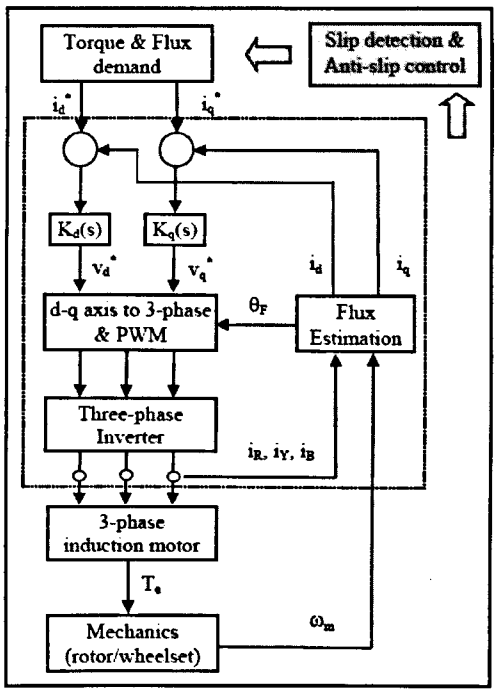

Fig. 2 Block diagram of the system model.

In the study of the proposed slip detection technique (indicated in the shaded black in Fig. 2), the focus is the mechanical dynamics of the wheelset and the relevant mathematical models are given in equations 1-3.

$$\left(J_w + n^2 J_{mg}\right)\dot{\omega}_R = n \cdot T_e - T_{tor} - r_R \cdot F_{R\_crp}(\gamma_R, t) \quad (1)$$

$$J_w \dot{\omega}_L = T_{tor} - r_L \cdot F_{L\_crp}(\gamma_L, t) \quad (2)$$

$$\left(m_w + \frac{m_b}{4}\right)\dot{V} = F_{R\_crp}(\gamma_R, t) + F_{L\_crp}(\gamma_L, t) \quad (3)$$

Equation 1 represents the rotational mode of the wheel on the right hand side, which also includes the rotor mechanics of the traction motor. Equation 2 is for the

rotational mode of the left wheel and Equation 3 represents the forward motion of the wheelset and a quarter of the vehicle. Mechanical losses or backlash of the gearbox are considered insignificant for the study and are not included in the model [9]. The lateral and yaw motions of the wheelset are not modelled for simplicity, but additional longitudinal creepages due to track irregularities are considered in the form of random disturbances.

The link between the wheel rotations and the forward motion is established via the contact forces at the wheel-rail interface which is explained below.

3. WHEEL-RAIL CONTACT

The wheel-rail contact mechanics involves the contact forces caused by so-called "creepages" between the wheel and rail surfaces which are small relative velocities resulted from elastic deformation of the steel at the point of contact. The overall creep force at the contact point is a non-linear function of the creep and limited by the adhesion available. Typically, a creep – creep force curve can be partitioned into three different sections as illustrated in Fig 3 – the low creep or the linear section (before F_o); the large creep or the non-linear section (between F_o and F_m); and the slip or unstable region (beyond F_m).

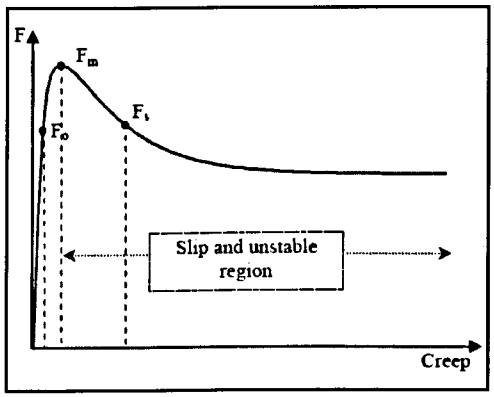

Fig. 3 A typical (idealised) creep – contact force curve.

However, the properties of the curves are subject to large and uncertain variations due to condition changes at the two contacting surfaces, such as contaminations, weather, wheel dynamic loading, and vehicle speed. Not only the maximum adhesion available and the corresponding creep are difficult to predict, but also the initial slope in the linear region can be seriously affected.

Furthermore, the curve in Fig. 3 presents a rather idealised contact force characteristics. Measurements from many experimental studies have indicated that the creep – creep force relations in practice broadly conform to the ideal curves, but there appear to be a degree of randomness in the variation of actual creep forces as shown in Fig 4 [10].

For computer simulations in the study, look-up tables are generated and use to represent different contact conditions where random variations may be included.

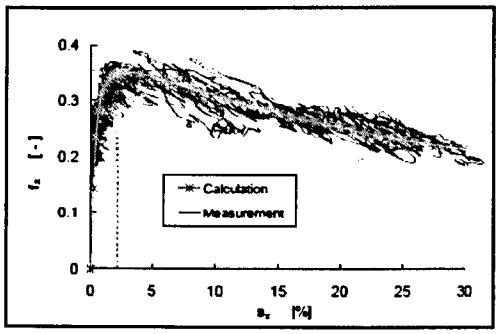

Fig. 4 Measured vs ideal curves

4. WHEELSET DYNAMICS AND SLIP DETECTION

The contact forces play a key role in providing the basic wheelset functions such as the guidance control and the delivery of tractive effort, but also are a dominant factor affecting wheelset behaviours. However those effects are highly dependent upon the creep characteristics which may vary considerably due to the above mentioned uncertainties in contact and track conditions, and different wheelset motions react differently to the changes.

In normal conditions where adhesion level is high, contact forces at the wheel-rail interface are principally proportional to creepages (operating in the low creep and linear region) and the creep coefficients are normally of large values. The large creep coefficients (in the order of MNs) result in very effective damping to all dynamic motions of a wheelset, with the exception of the kinematic mode (not modelled in the study) which must be stabilised using additional measures in suspensions. In low adhesion conditions, on the other hand, it is much more likely that a wheelset would operate in the non-linear or even the unstable region of the slip curve, where the damping effect is significantly lower (or becomes negative). Consequently the stability margins of the dynamic motions are much weakened.

A stability analysis based on the linearization of the creep - creep force curves (as illustrated in Fig 3) at individual operating points is used to study how the wheelset dynamic behaviours are affected by different contact conditions. Fig. 5 shows the migration of eigenvalues with the increase of the creep, where the two wheels are assumed to have the same creepage, the wheelset speed is 30m/s and the resonant frequency of

the torsional mode is set to a lowly 40Hz. In the linear (low creep) region of the creep curve, the positive damping keeps all the modes concerned clearly stable (as indicated by '*'). However, once the creep is increased beyond the peak value (as indicated by 'o'), there are potentially two unstable modes. One is the torsional mode of the axle which is indicated by the pair of the unstable conjugate poles. The other is the common rotation of the two wheels indicated by the unstable pole on the real axis.

The use of a more rigid axle will obviously increase the frequency of the torsional mode, but the general trend of the destabilising effect in large creep remains similar as evidently shown in Fig 6.

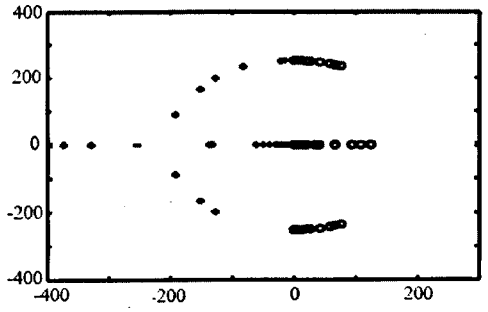

Fig. 5 Eigenvalue migrations with contact conditions (Vs=30m/s; f=40Hz; adhesion coeff=0.1)

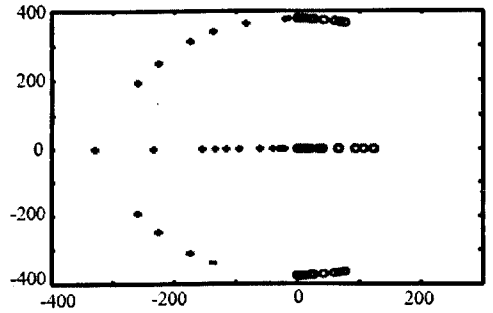

Fig. 6 Eigenvalue migrations with contact conditions (Vs=30m/s; f=60Hz; adhesion coeff=0.1)

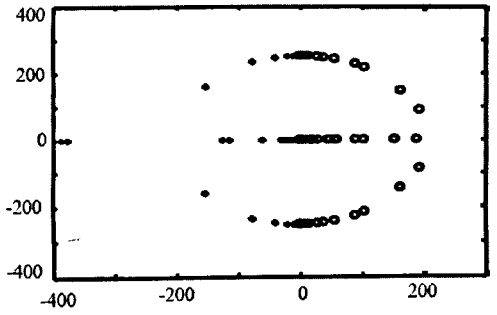

Fig. 7 Eigenvalue migrations with contact conditions (Vs=1m/s; f=40Hz; adhesion coeff=0.1)

The adhesion coefficient at low speeds is in general is higher than that at high speeds on comparable track conditions, but the when pushed towards the adhesion limit and/or the slip region, the torsional mode of a wheelset appears to encounter the similar instability problem as indicated in Fig 7.

When the two wheels of a wheelset are in different creep conditions, e.g. running on curves track where a different longitudinal creep forces are often produced. it is possible that one side of the wheelset experiences a positive damping and the other side negative. The stability will be determined by the overall effect of the contact forces and it is possible that the wheelset becomes unstable even if one of the wheels may still be operating in the stable region of the contact curve as shown in Fig 8.

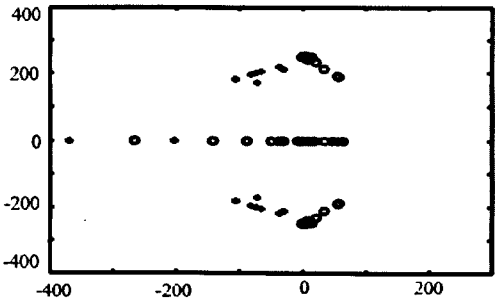

Fig. 8 Eigenvalue migrations – two wheels on different points of the creep curve (Vs=30m/s)

A system becoming unstable or marginally stable would obviously lead to undesirable oscillations. Even when a wheelset is lightly damped, sustained vibrations may still be produced in practice because disturbances present in the system (in particular those related to the track roughness) would keep exciting the torsional mode before previous responses die out.

There have been a number of reports that, when operating in slip regions, locomotives as well as EMU vehicles may experience severe mechanical vibrations in the wheelset assembly and transmission systems [9]. For example, a study based on Class 91 locomotives in the UK reveals an unstable torsional mode for the wheelset axles under the loss of adhesion [11]. However the vibrations have been largely considered as a 'problem', because they may lead to component failure or rail corrugation. There have been attempts to design away the problem, e.g. via the use of damping in the gearbox suspensions [9].

5. SIMULATION RESULTS

Based on the models presented in sections 2 and 3, simulation results are produced to support the theoretical studies. No anti-slip control is used in the computer simulations so that a comparison of the wheelset dynamic behaviours in different contact

conditions is not hindered by additional external interferences.

Figs 9 and 10 show the responses in the torsional torque of the wheelset axle at a starting speed of 1m/s and 30m/s respectively. A low level of the adhesion is used and a tractive effective is gradually increased (from zero). In Fig 9, an oscillation clearly develops at around t=1.2s, where the applied tractive effort starts to exceeds the adhesion available at the wheel-rail interface. The oscillation is sustained but not divergent as the creep curve used in the simulation become almost flat in very large slips and the damping effect become negligible. At a higher speed, a similar trend of oscillations can be observed as shown in Fig 10 and the magnitude of the oscillation appear to grow with the increase of the tractive effort, although there seems to be a less clear cut between the stable and unstable conditions.

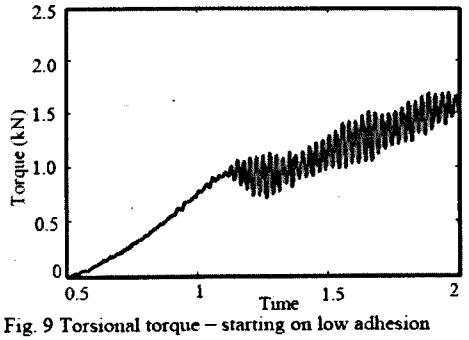

Fig. 9 Torsional torque – starting on low adhesion (Vs = 1m/s)

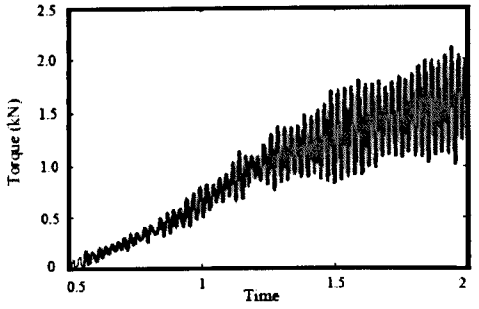

Fig. 10 Torsional torque – starting on low adhesion (Vs = 30m/s)

When a wheelset/vehicle experiences a sudden change of contact conditions, e.g. going through a bad patch where the adhesion is substantially lower than other track sections, the incited oscillations can be much more dramatic as shown in Figs 11 and 12 – the peak-to-peak variation of the torsional torque can be as high as 2/3 of that of the applied tractive effort.

The high level of sensitivity of the wheelset torsional mode to changes in contact conditions makes the monitoring of the axle oscillations an ideal means to detect wheel slip/slide. A direct measurement of the torsional torque would be desirable and straight-forward for implementation, if the issue of practical sensing can be satisfactorily resolved.

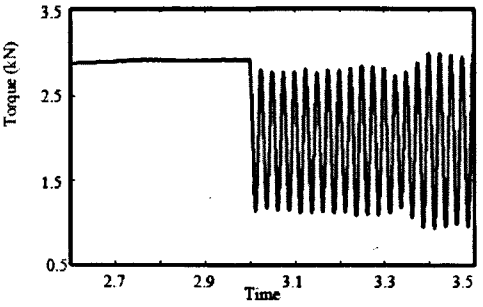

Fig.11 Torsional torque - sudden reduction of adhesion (Vs = 1m/s)

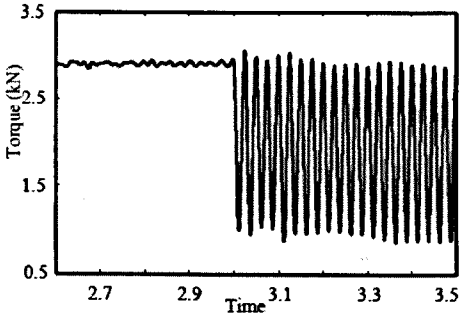

Fig. 12 Torsional torque - sudden reduction of adhesion (Vs = 30m/s)

Alternatively, it is possible to consider the development of appropriate estimation solutions that would only require more conventional sensor measurements such as the motor current and/or speed. Figs 13 and 14 demonstrate how the q-axis current of a vector controlled traction motor can be affected by the wheel slip. The oscillations are still present, but the magnitude is at such a low level that a more sophisticated use of the current measurement will probably have to be developed to improve the sensitivity for slip detection.

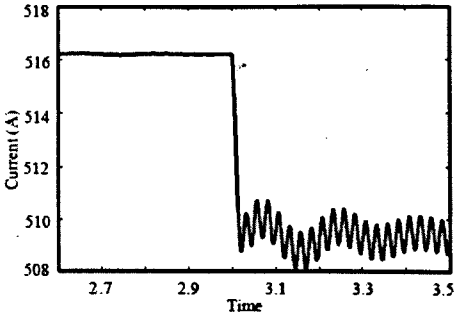

Fig. 13 q-axis current of the traction motor (Vs = 1m/s)

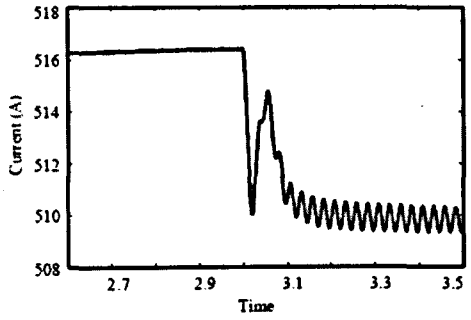

Fig. 14 q-axis current of the traction motor (Vs= 30m/s)

6. PROPOSED DETECTION SCHEME

Whilst the desire to overcome the 'unwanted' and potential damaging oscillations is natural in mechanical design, the link between the level of damping (or stability) for the torsional mode of a wheelset and the wheel-rail contact conditions provides an excellent opportunity for control engineers to explore in the pursuit of alternative slip detection and anti-slip control methods, which is the basis of this study. As long as the wheel slip/slide is effectively prevented, there will be no long lasting oscillations and associated damages to be expected.

No detailed solutions are offered in the study, but two possibilities are proposed below. Fig 15 shows a basic scheme for the detection for wheel slip/slide. In the simplest form, the torsional torque in the wheelset axle would be measured and processed to retain the signals at the frequency of the torsional oscillations only. The vibrations may then be used to reduce the traction demand (in a pre-defined manner) until the re-adhesion is restored. One of the big challenges for this scheme would be the issue of reliable and cost effective sensing and transmission of the axle torque because of the harsh working environment. However, this is achievable with recent advances in sensing technologies, e.g. a rotary torque transducer based on the so-called Surface Acoustic Wave technology (which is essentially 'frequency dependent' strain gauges to measure the change in resonant frequency caused by an applied shaft strain) is reported to offer a low cost and non-contact solution that appears to meet all the measurement requirements in terms of accuracy, bandwidth, robustness and EMC issues [12].

Alternatively, it is possible to explore the use of measurements that are easier to obtain, e.g. motor speed and/or current, as the axle vibrations will affect the wheel/motor speed and the generation of the back emf in the motor. However those signals are expected to be far less sensitive than the direct measurement of the axle torque and more sophisticated data processing techniques such as the use of state observers will be needed to amplify/estimate relevant parameters. Fig. 16 indicates how a state-observer may be constructed, where either the estimated states or the residuals may be explored for the slip detection.

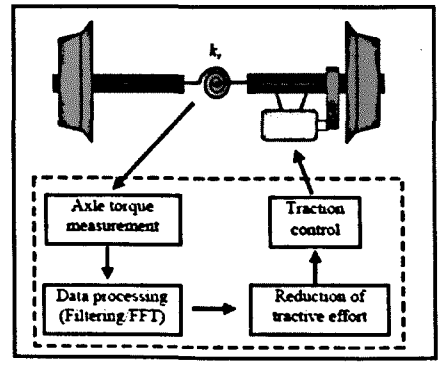

Fig. 15. Basic detection scheme

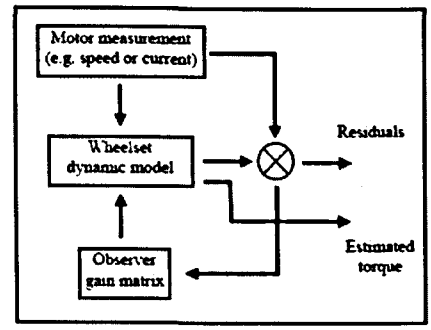

Fig. 16 The use of state observers

7. CONCLUSIONS

A new concept for the detection of wheel slip/slide for railway applications has been presented in this paper. With the help of theoretical analysis and computer simulations, the study has clearly established an explicit link between the dynamic behaviour of wheelset axles and conditions changes at the wheel-rail contact which forms the critical foundation for the proposed detection concept.

Although the paper is not focussed on the development of a final 'solution' that can be readily applied to railway vehicles, it has demonstrated the potentials and advantages of the new scheme that are not possible with the current practices:

- No need for accurate measurement of absolute vehicle speed or the slip ratio
- Maximum (or near maximum) adhesion is ensured regardless of the uncertainties.
- The potential for a fast and reliable detection of wheel slip/slide

Further studies are clearly required to tackle practicalities and other implementation issues.

REFERENCES

1. Watanabe T, and Yamanaka A et al "Optimisation of readhesion control of Shinkansen Trains with wheel-rail adhesion", IEEE Power Conversion Conference (PCC'97), 1997.
2. Schwartz H J, and Krebe R "Implementation of an advanced wheel creep control with searching strategy on a light rail vehicle". European Power Electronics Conference (EPE'97), 1997.
3. Yasuoka I, and Henmi T et al "Improvement of re-adhesion for commuter trains with vector control traction inverter" IEEE Power Conversion Conference (PCC'97), 1997.
4. Park D, and Kim M S et al "Hybrid re-adhesion control method for traction system of high speed railway" IEEE International Conference on Electrical Machines and Systems (ICEMS'01), 2001
5. Ohishi K, and Ogawa Y et al "Anti-slip re-adhesion control of electric motor coach based on force control using disturbance observer", IEEE IA Conference, 2000
6. Matsumoto Y, and Eguchi N et al "Novel re-adhesion control for train traction system of the Shinkansen", IEEE IECON 2001
7. Waring JR "Adhesion modification tests 1993, Part 4: Centrac HPF results", BR Research, March, 1994, pp160.
8. McEwen, I J "Review of the use of chemicals in the management of low adhesion", RSSB report, April, 2003
9. Lu G, and Harwood N A "Prediction of torsional vibration on mass transit vehicle", Computers in Railways'96, Volume 2: Railway Technology and Environment, 1996
10. Polach O "Creep forces in simulations of traction vehicle running on adhesion limit", 6th International conference on contact mechanics and wear of rail/wheel systems (CM'2003), 2003
11. Hardwood N A, and Keogh P S "Self-excited oscillation in locomotive transmission systems under loss of adhesion", Institute of Mechanical Engineers, C414/063, 1991.
12. Anon "SAW-based transducers for noncontact torque", Electronicstalk, 21 Feb 2001

APPENDIX: SYMBOLS

F_{L_crp}	Creep force at the left wheel
F_{R_crp}	Creep force at the right wheel
i_d	d axis current of the motor
i_q	q axis current of the motor
i_d^*	d axis current demand
i_q^*	q axis current demand
i_R, i_Y, i_B,	Motor phase current
J_{mr}	Moment of inertia of the rotor and gearbox
$K_d(s)$	Controller for d-axis current
$K_q(s)$	Controller for q-axis current
k_s	Torsional stiffness
m_b,	Mass of the vehicle
m_w,	Mass of the wheelset
n	Gear ratio
r_L	Radius of the left wheel
r_R	Radius of the right wheel
T_e	Motor torque
T_{tor}	Torsional torque
V	Vehicle speed
v_d^*	d axis voltage demand
v_q^*	q axis voltage demand
ω_L	Rotational speed of the left wheel
ω_R	Rotational speed of the right wheel
γ_L	Creepage of the left wheel
γ_R	Creepage of the right wheel

APPENDIX C

Copy of the paper:

"A Mechatronic Approach for Anti-slip Control in Railway Traction"

T X Mei, J H Yu, D A Wilson

To be published at 17th International Federation of Automatic Control World Congress, July, 2008, invited and submitted

A Mechatronic Approach for Anti-slip Control in Railway Traction

T X Mei*‡ J H Yu*, D A Wilson*

* *School of Electronic and Electrical Engineering, The University of Leeds, Leeds LS2 9JT, UK (‡Tel: 44 113 3432066; e-mail: t.x.mei@leeds.ac.uk).*

Abstract: This paper presents a novel mechatronic approach for the detection of wheel slip/slide and anti-slip control in railway traction systems, to enable an optimal use of adhesion in poor contact conditions. The proposed technique explores the variations in wheelset dynamic properties caused by condition changes at the wheel-rail contact and detects slip conditions from the torsional resonant vibrations of the wheelset axle indirectly. The modeling of a typical traction system, consisting of an induction traction motor (with associated power inverter and field-orientated control) connected to a wheelset via a gearbox, is introduced. The development of the slip detection and control scheme is presented, and the effectiveness of the proposed technique is demonstrated using computer simulations.

1. INTRODUCTION

Railway traction is a complex mechatronic system, as the traction motors and the associated controls have to work in harmony with the complex mechanical loads especially at the wheel-rail interface. Wheel slip/slide occurs when applied tractive effort exceeds the level of maximum adhesion available at the wheel-rail interface, e.g. in poor weather conditions or with contaminated tracks. Apart from the potential impact on normal operations of a rail network, the wheel slip/slide causes undesirable wear to both wheel/track surfaces and increases the requirements/costs of maintenance. Most conventional wheel slip protection schemes involve measures to limit the amount of slip ratio (relative speed between a wheel and the train) to a set value that is sometimes necessary to be tuned on line, and in more extreme cases to control the wheel rotational acceleration below a pre-defined threshold [Park et al, 2001; Schwartz et al, 1997; Watanabe et al, 1997; and Yasuoka et al, 1997]. The performance of those schemes is affected by the limited accuracy of the encoders used in the traction systems, which is typically less than 100 pulses per revolution, as well as difficulties related to a reliable measurement of vehicle absolute speed in slip/slide conditions.

Furthermore, the wheel-rail contact characteristics are subject to large variations, and it is difficult to ensure optimal use of the available adhesion because there is no fixed relationship between the slip ratio and the maximum adhesion. There have been studies on the use of so-called disturbance observers to detect the longitudinal creep forces and hence to derive the rate of change on the slip curve [Kadowaki, et al., 2002; Kim, et al., 1999] with the aim to optimise the control of slip ratio. However there seems to be little reported on the practicality and effectiveness of the approach.

Additional measures may be used to improve the adhesion level at the wheel-rail interface. The use of sand machines, often installed on locomotives, has been for many years a popular and effective means to increase the traction. More recently specially formulated chemicals (friction modifiers) are reported to have the effect of adhesion enhancement, although some tests have produced results that are less supportive [McEwen, 2003; and Waring, 1994]. At the system (infrastructure) level, it is also possible to improve the track conditions, e.g. by removing the contaminations, although currently known techniques are in general expensive and/or impractical for implementation.

This study investigates an indirect approach for the wheel slip detection which explores how the wheelset dynamics are affected by changes in contact conditions. The study demonstrates how the torsional mode of a conventional solid axle wheelset may be linked to the wheel slip/slide and consequently proposes a novel technique to detect wheel slip by identifying the variations in wheelset torsional vibrations. There is no need for the measurement of slip ratio and/or estimation of creep forces at the wheel-rail interface.

Some of the findings have been published previously. A fundamental examination of the concept and the feasibility for real applications was discussed in [Mei et al, 2006], followed by a study on possible control solutions in [Yu et al, 2006]. This study presents the latest results from the research project, in particular the development of practical slip detection and re-adhesion control strategies.

The paper is organised as follows. The configuration of the traction system used in the study is presented and mathematical models are provided in section 2. Section 3 describes the fundamental properties of wheel-rail contact forces and gives an analysis on how wheelset dynamic behaviour may be affected by different contact conditions. The development of a novel anti-slip control scheme and performance assessment is presented in section 4, and key conclusions are drawn in section 5.

2. SYSTEM AND MATHEMATICAL MODELS

A standard configuration as illustrated in Fig 1 is used in the study, which involves a conventional solid-axle wheelset

connected to an AC traction motor through a traction gearbox. A typical three-phase induction motor is used for the provision of traction for the wheelset and ¼ of a typical vehicle. Connections between the wheelset and the bogie/vehicle in the longitudinal direction are assumed to be solid, as the stiffness is normally very high and the associated dynamics is not of significant relevance to this study.

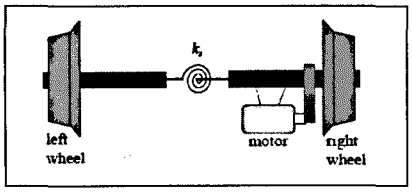

Fig. 1. Wheelset configuration

The spring k_s in Fig. 1 represents the equivalent stiffness for the first torsional mode of the wheelset. The frequency is typically about 60Hz, but can vary between perhaps 40Hz for a soft axle and to around 80Hz for a more rigid one.

An overall diagram of the mathematical models is shown in Fig 2. The models for the induction motor, the power electronics and the associated vector control scheme are fairly standard, some of which are available from SIMULINK SimPower toolbox [Yu et al 2006].

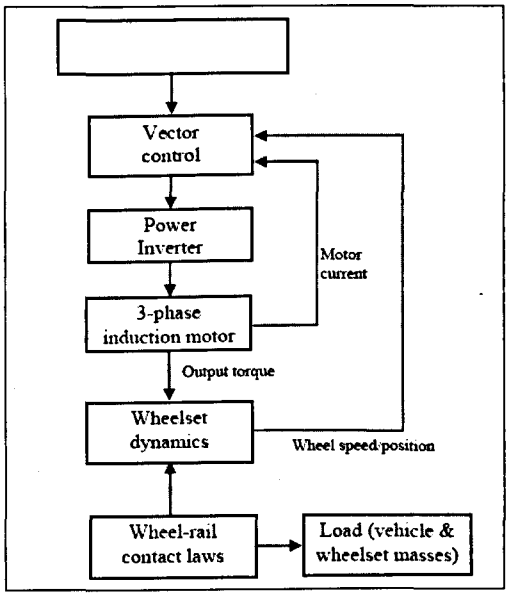

Fig. 2. Block diagram of the system models

However, the mechanical models of the systems are much more complex. One of the key issues is the modelling of the wheel-rail contact forces, as it provides the essential link between the output of the traction motor and the mechanical load. The wheel-rail contact mechanics involves the contact forces caused by so-called creepages between the wheel and rail surfaces which are small relative velocities resulted from elastic deformation of the steel at the point of contact. The overall creep force at the contact point is a non-linear function of the creepage and limited by the available adhesion. Measurements from many experimental studies have indicated that the creep – creep force relations follow a general trend as indicated in Fig. 3 [Polach, 2003]. Typically, a creep – creep force curve can be partitioned into three different sections – the low creep or the linear section (of the initial slope); the large creep or the non-linear section (before the peak point); and the slip or unstable region (beyond the peak point).

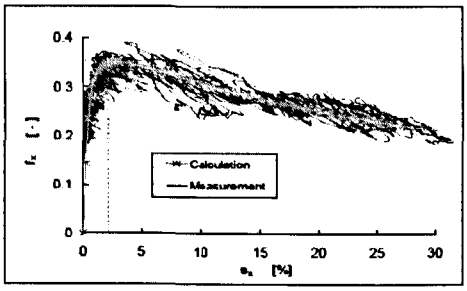

Fig. 3. Creep – creep force curve

Also, the overall contact force at the wheel-rail interface is affected by creepages in both longitudinal and lateral directions. Apart from the creep forces necessary to produce the tractive effort which are in the longitudinal direction only and are largely equal between the two wheels of a powered axle, there are additional creepages due to the wheelset motions (e.g. yaw and lateral) and contact geometries. The longitudinal creep forces of the two wheels of the same wheelset in this case produce a yaw toque but no net traction effort. Because all the creepages are developed at the same contact patch, there will obviously be dynamic interactions and the overall contact force is constrained by the adhesion.

Furthermore, the properties of the curves are subject to large and uncertain variations due to condition changes at the two contacting surfaces, such as contaminations, weather, wheel dynamic loading, and vehicle speed. Not only the maximum adhesion available and the corresponding creepages are difficult to predict, but also the initial slope in the linear region can be seriously affected.

For computer simulations in the study, a number of look-up tables are generated and used to represent different contact conditions. Those are somewhat idealised, but they provide essential features of wheel-rail contact laws [Polach, 2003].

The dynamics of the wheelset axle in the rotational direction should strictly be modelled using a distributed parameter model, but it can be readily demonstrated that the only two

dominant modes are necessary to be included in the study – the common rotation of the wheelset (rolling forward) and the first torsional mode between the two wheels. A simplified mechanical model is given in equations 1-4, representing the rotation of the right wheel, rotation of the left wheel and longitudinal motion of the wheelset (and the vehicle).

$$\left(J_w + n^2 J_{mg}\right)\dot{\omega}_R = n \cdot T_e - T_{tor} - r_R \cdot F_{R\_crp}(\gamma_R, t) \quad (1)$$

$$J_w \dot{\omega}_L = T_{tor} - r_L \cdot F_{L\_crp}(\gamma_L, t) \quad (2)$$

$$\left(m_w + \frac{m_b}{4}\right)\dot{V} = F_{R\_crp}(\gamma_R, t) + F_{L\_crp}(\gamma_L, t) \quad (3)$$

$$T_{tor} = k_s \cdot \Delta\theta_s + c_s(\omega_R - \omega_L) \quad (4)$$

where, T_e is the driving torque transmitted from the motor through a gearbox. T_{tor} is the torsional torque, $F_{R\text{-}crp}$ is the creep force at the right wheel and $F_{L\text{-}crp}$ is that at the left wheel, J_w and J_{mg} are moment of inertias of wheel and motor/gearbox respectively, m_w and m_b are wheelset and vehicle masses respectively, n is the gearbox ratio, k_s is the torsional stiffness and c_s represents the material damping of the axle, ω_R and ω_L are the angular velocity of the right and the left wheel respectively, $\Delta\theta_s$ is the relative rotation between the two wheels, γ_R and γ_L are the creepages at the right and left wheels.

The interactions with the lateral and yaw motions of the wheelset are considered in the full performance assessment, although the models are not given in the paper as they are not concerned with the control design.

3. WHEEL-RAIL CONTACT AND SYSTEM DYNAMICS

The contact forces are essential in the provision of the guidance control and the delivery of traction for railway vehicles, but can produce undesirable dynamic effects under more extreme contact conditions. When the adhesion level is high, contact forces at the wheel-rail interface are approximately a linear function of the creepages (i.e. in the low creep and linear region) and the creep coefficients are normally large. The large creep coefficients (in the order of MNs) provide a high level of damping to all dynamic motions of a wheelset, with the exception of the kinematic mode (related to the yaw and lateral modes of the wheelset) which are in practice stabilised as a part of the design for primary suspensions. In low adhesion conditions, it is much more likely that a wheelset would operate in the non-linear or even the unstable region of the slip curve, where the damping effect is significantly lower (or becomes negative).

A stability analysis to study how the wheelset dynamic behaviours are affected by different contact conditions is carried out based on the linearization of the creep - creep force curves at individual operating points. Fig. 4 shows the migration of eigenvalues with the increase of the creepage, where the two wheels are assumed to have the same creepage, the wheelset speed is 30m/s and the resonant frequency of the torsional mode is set to 60Hz. In the linear (low creep) region of the creep curve, the positive damping keeps all the modes concerned clearly stable (as indicated by '*'). However, once the creep is increased beyond the peak value (as indicated by 'o'), there are potentially two unstable modes. One is the torsional mode of the axle which is indicated by the pair of the unstable conjugate poles. The other is the common rotation of the two wheels indicated by the unstable pole on the real axis. Similar observations may be made with axles at different torsional frequency and at different speed/contact conditions [Mei et al, 2006].

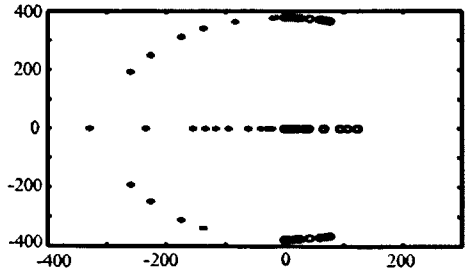

Fig. 4. Eigenvalue migrations with contact conditions (Vs=30m/s; f=60Hz; adhesion coeff=0.1)

Because the existence of sustained external disturbances to the railway vehicles, in particular those related to the track inputs, an unstable or even lightly damped wheelset would lead to potentially damaging oscillations at a frequency that is very high for a mechanical system. In the railway industry, the vibrations have been largely considered as a 'problem' that must be overcome, because they may lead to component failure or rail corrugation [Hardwood et al, 1991 and Lu et al, 1996].

However, the link between the level of damping (or stability) for the torsional mode and the wheel-rail contact conditions provides an excellent opportunity for control engineers to explore in the pursuit of alternative slip detection and anti-slip control methods. This paper will build upon the general principle of the novel slip detection that have been introduced before [Mei et al 2006 and Yu et al 2006], and present more technical detail on the control design and performance assessment.

4. CONTROL SYSTEM DESIGN AND ASSESSMENT

4.1 Slip detection with axle based sensor

If a reliable sensor can be provided to measure directly the torsional torque in the axle, the vibration signals at the resonant frequency would clearly provide an easy solution to for detecting wheel slip. This may be achieved by the use of some fairly standard data processing techniques as shown in Fig. 5. The band pass filter can be designed to provide a narrow pass band for the frequency of the torsional mode to

avoid possible interferences from other dynamic modes in the system. The low pass filter is used to remove the effect of the change of traction effort from the traction motor. The threshold will have to be carefully tuned to provide a reliable detection of wheel slip and in the meantime avoid false detection.

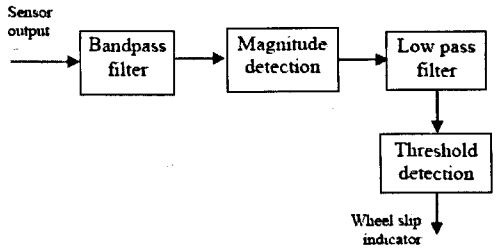

Fig. 5. Wheel slip detection with axle based sensors

Figure 6 shows how the magnitude of the torsional vibration (the output of the low pass filter) is linked to the wheel slip, where the maximum adhesion coefficient is changed from 0.4 to 0.05 at the time of 4s.

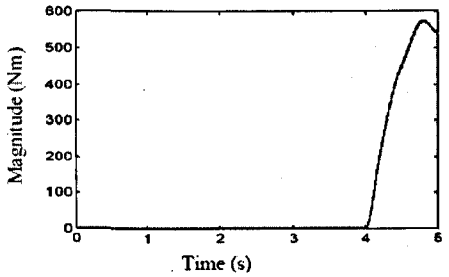

Fig. 6. Magnitude change of the torsional motion

One of the main practical challenges for this scheme would be the issue of reliable and cost effective sensing and transmission of the axle torque, because of the harsh working environment. This may become possible with recent advances in sensing technologies, e.g. a rotary torque transducer based on the so-called Surface Acoustic Wave technology (which is essentially 'frequency dependent' strain gauges to measure the change in resonant frequency caused by an applied shaft strain) is reported to offer a low cost and non-contact solution [Anon, 2001].

4.2 Slip detection with speed sensor

For practical applications, however, it is obviously desirable to minimise the use of sensors and reduce costs. In this study the measurement of the axle speed, which is normally provided in rail traction systems, is explored in the development of a Kalman filter that estimates the torsional vibrations.

To reduce the complexity of the Kalman filter, a linearised model is derived to represent the key features of the wheelset dynamics as given in equations 5 and 6.

$$\begin{bmatrix} \dot{\Delta\omega_R} \\ \dot{\Delta\omega_L} \\ \dot{\Delta\theta_s} \end{bmatrix} = \begin{bmatrix} -\frac{k_1}{J_R} & 0 & -\frac{k_s}{J_R} \\ 0 & -\frac{k_2}{J_L} & \frac{k_s}{J_L} \\ 1 & -1 & 0 \end{bmatrix} \begin{bmatrix} \Delta\omega_R \\ \Delta\omega_L \\ \Delta\theta_s \end{bmatrix} + \begin{bmatrix} \frac{1}{J_R} \\ 0 \\ 0 \end{bmatrix} \cdot \Delta T_e \qquad (5)$$

$$Y = \begin{bmatrix} 1 & 0 & 0 \end{bmatrix} \cdot \begin{bmatrix} \Delta\omega_R \\ \Delta\omega_L \\ \Delta\theta_s \end{bmatrix} \qquad (6)$$

where additional variables J_R ($=J_w + n^2 J_{mg}$) and J_L ($=J_w$) are moment of inertias of right and left wheels respectively, and Y represents the output measurement; and k_1 and k_2 are the rate of change on the creep-creep force curve corresponding to the creepages at the two wheels.

This is clearly a small signal model which, in a strict sense, is only valid at defined operating point(s) on a particular creep-creep force curve and therefore a Kalman filter obtained from the model should ideally only be used to provide estimations under the particular condition. It is possible to design and use a bank of Kalman filters to cover a wide range of contact conditions, but this would substantially increase the system complexity. For simplicity, a single Kalman filter is designed using the model given in eqs 5 and 6 in the proposed scheme, but the values of k_1 and k_2 are tuned to provide balanced estimations in the saturation region of the creep – creep force curves that is critical for a fast slip detection.

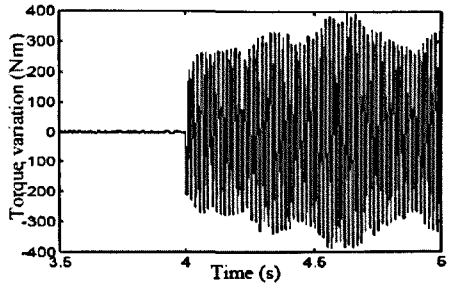

Fig. 7. Torsional motion from full simulation model

A comparison of the original and estimated torsional motions is given in Figs 7 and 8. Although a close match is not achieved in this case, the Kalman filter provides an estimation that captures the essential vibrations which is sufficient to detect the occurrence of a wheel slip.

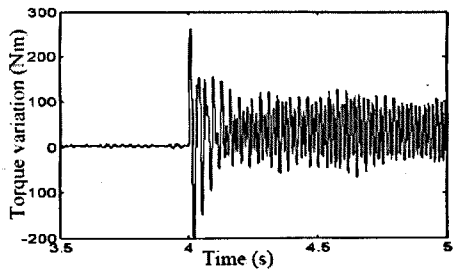

Fig. 8. Estimated torsional motion from Kalman filter

4.3 Re-adhesion control

The overall readhesion control scheme is shown in Fig. 9. The Kalman filter provides an estimation of the torsional torque of the wheelset axle from the measurement of the rotational speed of one of the wheels. An additional input of the output torque from the traction motor may also be needed, which can be provided from the motor torque controller. The output of the Kalman filter is processed to obtain the magnitude of the torsional vibrations at the resonant frequency (as shown in Fig. 5). Once a wheel slip is deemed to have occurred by the threshold detector, the torque reduction control will be switched on to reduce the torque demand below the adhesion available at the wheel-rail interface. The level and speed of the torque reduction are made to be dependent on the level of the magnitude of the estimated torsional torque, and an integral term is also needed to help and maintain the torque demand at an appropriate level even after a re-adhesion is achieved and there is no longer a wheel slip. A hysteresis control for the switching would help to increase/restore the original torque demand after the contact condition has improved.

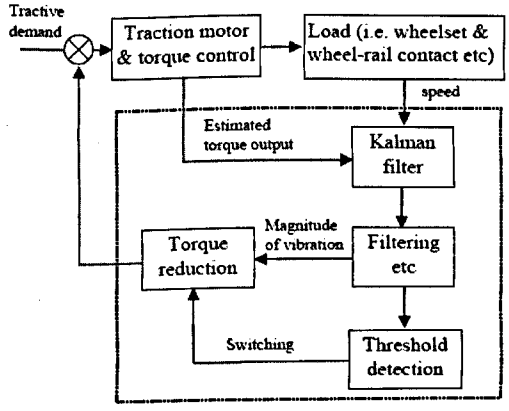

Fig. 9. Readhesion control scheme

4.4 Performances in different conditions

The worst case scenario for wheel slip is if there is a sudden reduction of adhesion on the track when there is a high level of tractive effort applied. Fig. 10 compares wheel and (equivalent) vehicle angular velocities during the vehicle acceleration from an initial speed of 10km/h. At the time t=4s, the adhesion of the track is reduced to well below the tractive effort, and consequently a severe wheel slip occurs and the slip ratio reaches as much as 60% in less than 0.5s before being detected. The re-adehsion control is clearly effective in reducing the torque output from the motor rapidly and the recovery time takes about 1.5s.

If the adhesion is already low when a tractive effort is applied and increased gradually, the wheel slip (when it occurs) tends to be less severe as the net torque driving on the wheelset is relatively low. On the other hand the torsional vibrations will also be smaller and less sensitive to slip conditions. However, the proposed control scheme appears to deliver a robust performance in different conditions as illustrated in Figs. 11 and 12. At the low (initial) speed of 10km/h, the peak slip ratio reaches approximately 20% and the wheel slip is quickly detected and a complete re-adhesion is achieved within a fraction of a second. At the higher speed of 100km/h, the peak slip ratio is about 14% but the recovery time takes somewhat longer as the system has to overcome a higher level of kinematic energy stored in the wheelset.

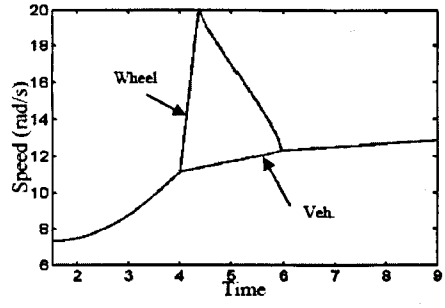

Fig. 10. Re-adhesion control – reduced adhesion at t=4s (initial vehicle speed of 10km/h)

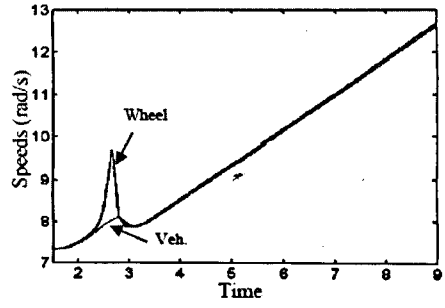

Fig. 11. Re-adhesion control – low adhesion from t=0s (initial vehicle speed of 10km/h)

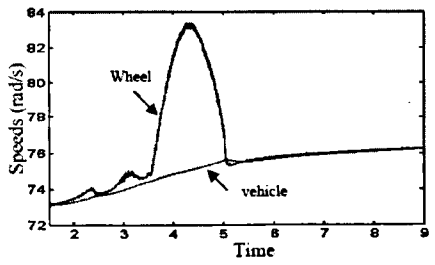

Fig. 12. Re-adhesion control – low adhesion from 0s (initial vehicle speed of 100km/h)

For the wheelset with a different axle stiffness, the centre frequency of the bandpass filter used for detecting the resonant vibration of the axle must obviously be tuned to coincide with the different torsional frequency. Fig 13 shows the simulation results using a more rigid axle where the torsional frequency is changed from 60 to 80Hz. Again the detection of a wheel slip and a complete re-adhesion are achieved in less than 2s. In this, a second (smaller) wheel slip is observed which is quickly detected and eliminated by the controller – a clear evidence that the system operates very closely to the maximum adhesion region on the creep-creep force curve which is expected.

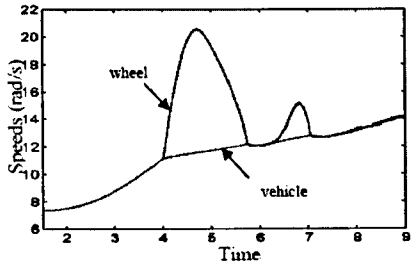

Fig. 13. Re-adhesion control – reduced adhesion at t=4s (a more rigid axle, initial vehicle speed of 10km/h

5. CONCLUSIONS

Effective use of the maximum adhesion available without causing any damaging wheel slip is an important and challenging requirement in railway traction. A new concept for the slip detection and re-adhesion control has been presented in this paper. Unlike conventional anti-slip control techniques, the new control strategy does not require the measurement of train speed or the slip ratio, which can be problematic to obtain in practice. Because the slip detection is based on the observation that the wheel slip is closely linked to the wheelset torsional vibrations, it inherently enables an optimal use of the adhesion regardless of the uncertainties/variations of the contact characteristics.

REFERENCES

Watanabe T, and Yamanaka A et al (1997), Optimisation of readhesion control of Shinkansen Trains with wheel-rail adhesion, *IEEE Power Conversion Conference (PCC'97)*.

Schwartz H J, and Krebe R (1997), Implementation of an advanced wheel creep control with searching strategy on a light rail vehicle, *European Power Electronics Conference (EPE'97)*.

Yasuoka I, and Henmi T et al (1997), Improvement of re-adhesion for commuter trains with vector control traction inverter, *IEEE Power Conversion Conference (PCC'97)*.

Park D, and Kim M S et al (2001), Hybrid re-adhesion control method for traction system of high speed railway, *IEEE Power Conversion Conference (PCC'97)*.

Kadowaki,S., Ohishi, K., Miyashita I. and Yasukawa (2002). Re-adhesion control of electric motor coach based on disturbance observer and sensor-less vector control, *Proceedings of the Power Conversion Conference*, Volume 3, p1020 – 1025.

Kim W S, Kim Y S, Kang J K and Sul S K (1999). Electro-mechanical re-adhesion control simulator for inverter-driven railway electric vehicle, *IEEE Industry Applications Conference*, Volume 2, p1026 – 1032.

Waring J R (1994), Adhesion modification tests 1993, Part 4: Centrac HPF results, *BR Research*, March, 1994, pp160.

McEwen, I J (2003) Review of the use of chemicals in the management of low adhesion, *RSSB report*, April, 2003

Mei T X, Yu J H and Wilson D A (2006), Wheelset dynamics and wheel slip detection, *STECH2006*, Chengdu, China.

Yu J H, Mei T X and Wilson D A (2006), Re-adhesion control based on wheelset dynamics in railway traction system, *UKACC2006*, Glasgow, UK

Polach O (2003), Creep forces in simulations of traction vehicle running on adhesion limit", *6th International conference on contact mechanics and wear of rail/wheel systems* (CM'2003)

Hardwood N A, and Keogh P S (1991), Self-excited oscillation in locomotive transmission systems under loss of adhesion", *Institute of Mechanical Engineers*, C414/063.

Lu G, and Harwood N A (1996), Prediction of torsional vibration on mass transit vehicle", *Computers in Railways'96*, Volume 2: Railway Technology and Environment.

Anon (2001), SAW-based transducers for non contact torque, *Electronicstalk*, 21 Feb 2001